

**Ministry of Higher Education and Scientific Research
University of Baghdad
Institute of Laser for Postgraduate Studies**



Modified Nanomaterial for Multiwavelength (Yb, Er) Doped Fiber Lasers

**A Thesis Submitted to the Institute of Laser for Postgraduate Studies,
University of Baghdad in Partial Fulfillment of the Requirements for
the Degree of Doctor of Philosophy in Laser / Electronic and
Communication Engineering**

By

Ansam Majid Salman

B.Sc. Laser and Optoelectronics-2006

M.Sc. Laser and Optoelectronics-2009

Supervisor

Prof. Dr. Abdulhadi M. Al-Janabi

2021AD

1442AH

Certification

I certify that this thesis was prepared under our supervision at the Institute of Laser for Postgraduate Studies, University of Baghdad, in a partial fulfillment of requirements for the degree of a Doctor of Philosophy in Laser/ Electronic and Communication Engineering. Signature:

Signature:

Name: **Dr. Abdulhadi M. Al-Janabi**

Title: Professor

Address: Institute of Laser for Postgraduate Studies, University of Baghdad.

Date: // 2021

(Supervisor)

In view of the available recommendation, I forward this thesis for debate by Examining Committee.

Signature:

Name: **Asst. Prof. Dr. Hanan J. Taher**

Title: Head of the Scientific Committee.

Address: Institute of Laser for Postgraduate Studies,
University of Baghdad.

Date: // 2021

Examination Committee Certificate

We certify that we have read this thesis “**Modified Nanomaterial for Multiwavelength (Yb, Er) Doped Fiber Lasers**” and as examination committee we examined the student in its contents and in our opinion it is adequate with standards as a thesis for the degree of Doctor of Philosophy in Laser/ Electronic and Communication Engineering.

Signature:

Name: **Dr. Hussein A. Jawad**

Title: Professor

Address: Institute of Laser for
Postgraduate Studies,

University of Baghdad

Date: //

(Chairman)

Signature:

Name: **Dr. Jassim K. Hmood**

Title: Professor

Address: optoelectronics engineering,
University of Technology

Date: //

(Member)

Signature

Name: **Dr. Evan T. Salim**

Title: Professor

Address: Applied Sciences department,
University of Technology

Date: //

(Member)

Signature:

Name: **Dr. Mohamed K. Dhahir**

Title: Assistant Professor

Address: Institute of Laser for
Postgraduate Studies,

University of Baghdad

Date: //

(Member)

Signature:

Name: **Dr. Hanan J. Taher**

Title: Assistant Professor

Address: Institute of Laser for
Postgraduate Studies,

University of Baghdad

Date: //

(Member)

Signature:

Name: **Dr. Abdulhadi M. Al-Janabi**

Title: Professor

Address: Institute of Laser for
Postgraduate Studies,

University of Baghdad.

Date: //

(Supervisor)

Approved by the deanship of Institute of Laser for Postgraduate Studies,
University of Baghdad, Signature:

Name: **Prof. Dr. Hussein A. Jawad**

Title: Dean

Address: of Institute of Laser for Postgraduate Studies, University of Baghdad.

Date: //

ACKNOWLEDGMENT

Firstly, I would like to present thanks and appreciation to my mentor and supervisor, **Prof. Dr. Abdulhadi Al-Janabi**, for being an excellent advisor. Even when he was the dean of the Institute of Laser for Postgraduate Studies, he still gives some of his precious time to me. Without his guidance, creative thinking, experimental research experience and patience in technical writing, this work would not have been possible. I will be in his debt forever.

I am deeply grateful to **Asst. Prof. Dr. Hussein A. Jawad**, Dean of the Institute of Laser for Postgraduate Studies, for his support.

Special thanks go to, Asst. Dean of the Institute of Laser for Postgraduate Studies **Dr. Mahmud S. Mahmud**.

My sincere thanks to **Asst. Prof. Dr. Mohamed K. Dhahir**, head of the Engineering and Industrial Applications Department for generously providing the oscilloscope.

I want to express my sincere thanks to the faculty members and staff of Institute of Laser for Post graduate Studies, University of Baghdad, especially to, **Asst. Prof. Dr. Zaineb Fadhal**, **Asst. Prof. Dr. Shelan Khasro**, and **Dr. Jawad A. Hasan** from whose lectures I benefited greatly.

Most importantly, big thanks to my entire family especially, my parents and my husband for helping me to get through the difficult times, for all their emotional support, understanding, encouragement over the past years, and care they provided.

I am deeply indebted to all my friends and colleagues at the ILPS during my Ph.D. for their great support and kind advice.

Ansam

DEDICATION

TO:

MY PARENTS

MY DEAR BEST FRIEND (MY HUSBAND)

And

MY LOVELY CHILDREN

*Whose advice, patience, love, encouragement and prayers
day and night make me able to get such success and honor*

ABSTRACT

This thesis focuses on the design and construction of a multiwavelength fiber laser that operates in both Ytterbium-doped fiber (YDF) and Erbium-doped fiber (EDF) using newly developed highly nonlinear nanomaterials as gain equalizer and stabilizer. Three types of nanomaterials have been utilized in this work namely nickel nanoparticles (Ni-NPs) and Ferro oxide (Fe_2O_3 -NPs) and silica (SiO_2 -NPs), which were fabricated in simple, straight, and cost-effective methods with two different forms: liquid form and freestanding polymer composite for later used in the laser cavity as optical modulator. They were incorporated inside the laser cavity. Four-wave mixing assists multi-channel oscillation, alleviation mode competition, and mode hopping in rare-earth-doped fiber lasers used the aforementioned nanomaterials was investigated. Besides that, fiber lasers with different operation regimes (continuous wave, Q-switched, and mode-locked) have been successfully demonstrated.

Multiwavelength was simply generated in the L-band and 1 μm region with channel spacing of 0.8 nm and 1.2 nm when a Ni-thin layer was integrated with the YDF and EDF laser cavities, respectively. While, as a small piece of the Ni-thin flim sample was integrated into a ring cavity of both YDF and EDF laser cavities; passively Q-switching multiwavelength with pulse duration of a 1.5 μs and 138 ns were realized, respectively. Besides, mode-locking pulse was realized in YDFL too.

Five-lasing channel perceived around 1040 nm region, operated in CW regime, and dual- lasing channel detected around 1563 nm, operated in Q-switching mode with smallest pulse duration of 7.18 μs and utmost repetition frequency of 30.74 kHz have been obtained when Fe_2O_3 -PVA was incorporated in both EDFL and YDFL cavities, respectively. Also, multiwavelength operated in the mode-locked regime has been detected around 1 μm induced by the high nonlinear effect of Fe_2O_3 -NF.

Q-switched pulses having minimum pulse duration of 4 μs induced by SiO_2/PVA have been generated from the EDFL cavity. Besides, the SiO_2/PVA and $\text{SiO}_2\text{-NF}$ modulators induce CW dual-wavelength, and pulse quadruple-wavelength in the 1 μm band.

Multiwavelength emitted in CW, Q-switched, as well as mode-locked, were realized from EDFL based on $\text{Fe}_2\text{O}_3/\text{SiO}_2$ nanocomposite. Also, more than 20 lines with SNR between 9 dB and 46 dB with many numbers of side modes lasing in mode-locking operation were realized from YDFL based on $\text{Fe}_2\text{O}_3/\text{SiO}_2$ nanocomposite.

The proposed fiber lasers can be exploited in several fields of application such as wavelength division multiplexing, spectroscopy, and sensing.

LIST OF CONTENTS

CONTENTS	PAGE
Abstract	I
List of Contents	iii
List of Symbols	vi
List of Abbreviations	viii
List of Tables	x
List of Figures	xi
Chapter One: Introduction and Basic Concepts	1
1.1 Background	1
1.2 Principles of Fiber Lasers	5
1.3 Optical Components With Fiber Lasers	6
1.3.1 WDM	7
1.3.2 Optical Isolators	7
1.3.3 Polarization Controller	8
1.3.4 Fiber Output Coupler	9
1.3.5 Optical Filters	10
1.3.6 Fiber-Coupled Diode Laser	10
1.4 Fiber Laser Cavity Configurations	11
1.4.1 Linear Cavity	11
1.4.2 Ring Cavity	12
1.5 Spectroscopic Properties of Trivalent Rare Earth Ions-Doped Fibers	14
1.5.1 Ytterbium Ion-Doped Fiber (YDF)	15
1.5.2 Erbium Ion-Doped Fiber (EDF)	17
1.6 Modeling of Fiber Laser	20
1.7 Propagation of Optical Signals In A Fiber	22
1.7.1 Four-Wave Mixing (FWM) Process	24

1.8	Operating Regimes Of Fiber Lasers	25
1.8.1	CW Fiber Laser Operation	26
1.8.2	Passive Q-Switched Mechanism	27
1.8.3	Mode-Locking Mechanism	29
1.9	Saturable Absorbers	30
1.9.1	Characterization of Saturable Absorber	34
1.10	Thin Film Materials	37
1.10.1	Pure Metal (Nickel Nanoparticles)	38
1.10.2	Transition Metal Oxide (Iron Oxide " Hematite")	39
1.10.3	Silica Nanoparticles	41
1.11	Literature Survey	42
1.12	Aim of The Work	47
1.13	Thesis Outline	47
Chapter Two: Experimental Design of Ring Cavity Doped Fiber Laser And Saturable Absorbers Synthesis		49
2.1	Introduction	50
2.2	Theoretical Design Consideration	50
2.2.1	CW-YDFL	51
2.2.2	CW-EDFL	54
2.3	Experimental Setups and The Characterization of The System	54
2.3.1	YDF Emission Spectra	55
2.4	Preparation, and Characterization of Optical Modulators	58
2.4.1	Ni-NPs Optical Modulator	58
2.4.2	Fe ₂ O ₃ Optical Modulator	63
2.4.3	SiO ₂ Optical Modulator	67
2.4.4	Fe ₂ O ₃ /SiO ₂ Nanocomposite Optical Modulator	71
Chapter Three: Results and Discussion: Multiwavelength Ytterbium Doped Fiber Laser		75
3.1	Introduction	75

3.2Ni-NPs Optical Modulator	76
3.1.1 Ni Thin Layer Based-NF	76
3.2.1 Ni-PVA Freestanding Film (0.75% Volume)	86
3.2.2 Ni-PVA Freestanding Film (1% Volume)	92
3.3Fe ₂ O ₃ Optical Modulator	100
3.3.1 Fe ₂ O ₃ -PVA Freestanding Film	100
3.1.2 Fe ₂ O ₃ Thin Layer Based NF	102
3.4SiO ₂ Optical Modulator	109
3.4.1 SiO ₂ -PVA Freestanding Film	109
3.4.2 SiO ₂ Thin Layer Based-NF	110
3.5Fe ₂ O ₃ /SiO ₂ Optical Modulator	114
Chapter Four: Results and Discussion: Multiwavelength Erbium Doped Fiber Laser	123
4.1 Introduction	123
4.2Ni-NPs Optical Modulator	123
4.2.1 Nickel Thin Layer Based-NF	123
4.2.2 Ni-PVA Freestanding Film (0.35% Volume)	128
4.3Fe ₂ O ₃ Optical Modulator	134
4.4SiO ₂ Optical Modulator	137
4.5Fe ₂ O ₃ /SiO ₂ Optical Modulator	140
Chapter Five: Conclusions and Suggestions for Future Work	144
5.1 Conclusions	144
5.2 Suggestions for Future Work	146
References	147

LIST OF SYMBOLS

SYMBOLS	DESCRIPTION	UNITS
a	Constant	-
A	Absorbance	-
A_{eff}	Effective area	m^2
c	Speed of light in free space	m/s
E_g	Band-gap energy	ev
$E(t)$	Applied optical field	V/m
g	Small-signal fiber gain	dB/m
G_{max}	Maximum gain in the active fiber	-
h	Planck constant	$m^2 \text{ kg} / \text{s}$
I	Intensity	W/cm^2
I_s	Saturation intensity	W/cm^2
k	Cavity total loss	dB
L	Overall length	m
L_{min}	Minimum length of gain fiber	m
L_{opt}	Optimum length of gain fiber	m
L_s	Thickness of the thin film	m
M	Integer	-
n	Refractive index coefficient	RIU
n_2	Nonlinear refractive index coefficient	Cm^2/W
$n(I)$	Refractive index- intensity dependent	-
P	Optical power	W
P_{th}	Threshold pump power	W
P_{out}	Laser output power	W
P_p	Pump power	W
P_p^{sat}	Saturation pump power	W
P_s^{sat}	Saturation signal power	W

$P_{lin}(t)$	Linear polarization	C/m^2
$P_{nl}(t)$	Nonlinear polarization	C/m^2
T_{eff}	Transmission factors	%
$T(I)$	Nonlinear transmission	-
t_c	Cavity lifetime	s
t_p	Pulse width	s
u_j	Propagation direction of the pump or signal	-
α	Linear absorption	cm^{-1}
α_2	Nonlinear absorption coefficient	cm/W
α_{ns}	Non-saturable loss	-
α_s	Absorption coefficient at signal wavelength	dB/m
α_p	Absorption coefficient at pump wavelength	dB/m
γ	Nonlinear coefficient	Rad/W.m
δ	Saturation power ratio	-
ΔT	Modulation depth	%
ϵ_0	Free space permittivity	F/m
ϵ	Actual cavity transmission	-
ϵ_2	Loss from the output of the doped fiber to the laser output coupler	-
H	Efficiency	-
λ_s	Signal wavelength	nm
λ_p	Pump wavelength	nm
σ	Absorption cross-section	cm^2
τ	Relaxation time	S
ν	Frequency	Hz
χ^1	Linear susceptibility	-
χ^2	Second nonlinear coefficient	esu
χ^3	Third nonlinear coefficient	esu

LIST OF ABBREVIATIONS

Abbreviations	Description
ASE	Amplified spontaneous emission
C-band	Conventional band
CW	Continuous wave
dB	Decibel
dBm	Decibel per milliwatt
EDF	Erbium-doped fiber
EDFA	Erbium-doped fiber amplifier
EDFL	Erbium-doped fiber laser
EDX	Energy dispersive x-ray
FBG	Fiber Bragg Grating
FC/PC	Fiber connector/ physical contact
Fe ₂ O ₃ -NPs	Iron oxide nanoparticles
FFT	Fast fourier transform
FWHM	Full width at half maximum
FWM	Four-wave mixing
Fs	Femtosecond
GVD	Group velocity dispersion
ISO	Isolator
KHz	Kilohertz
L-band	Long band
MHz	Megahertz
Ms	Millisecond
μs	Microsecond
mW	Milliwatts
μW	Microwatts
NIR	Near infrared

Ni-NPs	Nickel nanoparticles
Nj	Nanojoule
NPR	Nonlinear polarization rotation
NPs	Nanoparticles
Ns	Nanosecond
OC	Output coupler
OSA	Optical spectrum analyzer
OSC	Oscilloscope
PC	Polarization controller
PEO	Polyethylene glycol
PMMA	Poly (methyl methacrylate)
PRR	Pulse repetition rate
Ps	Picosecond
PVA	Polyvinyl alcohol
RF	Radio frequency
SBS	Stimulated Brillouin scattering
SDS	Sodium dodecyl sulfate
SEM	Scanning electron microscope
SiO ₂ -NPs	Silica nanoparticles
SMF	Single-mode fiber
SNR	Signal to noise ratio
SRS	Stimulated Raman scattering
SPM	Self-phase modulation
WDM	Wavelength division multiplexing
XRD	X-ray diffraction
XPM	Cross-phase modulation
YDF	Ytterbium doped fiber
YDFL	Ytterbium doped fiber laser

LIST OF TABLES

TABLE NO.	TITLE	PAGE
1.1	Rare-Earth Ions with their Absorption and Emission Wavelength Ranges	14
2.1	Ytterbium-doped single-mode fiber specifications	52
2.3	The linear parameters of Ni-NPs samples	61
2.4	The nonlinear parameters of Ni-NPs samples	63
2.5	The linear parameters of Fe ₂ O ₃ -NPs samples	68
2.6	The nonlinear parameters of Fe ₂ O ₃ -NPs samples	67
2.7	The linear parameters of SiO ₂ -NPs samples	69
2.8	The nonlinear parameters of SiO ₂ -NPs samples	69
2.9	The linear and nonlinear parameters of Fe ₂ O ₃ /SiO ₂ nanocomposite	74
4.1	The output performance comparison of multiwavelength fiber lasers based on FWM	127
4.2	Performance comparison of different types of saturable absorbers in <i>Q</i> -switched EDFL	133

LIST OF FIGURES

FIGURE NO.	TITLE	PAGE
1.1	Isolator operation	7
1.2	Polarization controller, (a) three puddle PC, (b) in-line PC	9
1.3	Schematic Diagram of Fiber Output Coupler	10
1.4	Fiber laser linear cavity configuration based on (a) two dielectric mirrors, (b) FBG	11
1.5	Fiber laser ring cavity configuration	13
1.6	Yb^{3+} energy level structure	15
1.7	Absorption and emission cross-sections of Yb^{3+} - doped glass	16
1.8	Absorption and emission cross-sections of the Er^{3+} - doped, PKBA Er glass	18
1.9	Energy levels of Erbium ions in silica glass host	19
1.10	Energy level diagram for the two-level system	21
1.11	Schematic diagram of a fiber ring laser	21
1.12	Mechanism of Q-switching	28
1.13	Superposition of three longitudinal modes leading to repetitive pulse generation	30
1.14	Two-level saturable absorber	32
1.15	Z-scan experimental setup	35
1.16	Twin detector setup	36
1.17	Bleaching curve of the two-level system	36
1.18	Absorbance of Ni-PVA at different concentrations of Ni NPs	39
1.19	The linear and nonlinear transmission of $\text{Fe}_2\text{O}_3/\text{PVA}$ thin film	41

2.1	The structure of chapter two.	50
2.2	Schematic diagram of the standard ring laser	51
2.3	Calculated the shortest lengths and the optimum lengths of YDF as a function of different coupling efficiencies	52
2.4	Calculated output power as a function of active fiber length for YDF	53
2.5	Experimental setup for ASE measurement of EDF/YDF	55
2.6	Measured ASE of YDF at different input pumping powers	56
2.7	Measured optical spectrum of the CW-YDFL at the threshold of 65 mW and at 127 mW input pump power	57
2.8	Comparison between theoretical and experimental results of CW-YDFL output power	57
2.9	The absorption spectrum of Ni-NPs in the range 200-2000 nm (highlighted is lasing operation region)	60
2.10	Tauc plot of the three samples of Ni-NPs	60
2.11	Normalized transmission of (a) closed aperture, (b) open aperture	61
2.12	Nonlinear absorption of Ni-NPs for: (a) Ni-NF of 75% volume ratio, (b) Ni:PVA film (0.75% volume ratio), and (c) Ni:PVA film (1% volume ratio)	62
2.13	The absorption spectrum of prepared Fe ₂ O ₃ -NPs samples in the range 200-2000 nm (highlighted is lasing operation region)	64
2.14	Tauc plot of Fe ₂ O ₃ -NPs	65
2.15	Normalized transmission of Fe ₂ O ₃ for: (a) closed	66

	aperture, (b) open aperture	
2.16	Nonlinear absorption for: (a) Fe ₂ O ₃ -NF, (b) Fe ₂ O ₃ :PVA film	66
2.17	The absorption spectrum of prepared SiO ₂ -NPs samples in the range 200-2000 nm (highlighted is lasing operation region)	68
2.18	Tauc plot of SiO ₂ -NPs	68
2.19	Normalized transmission of SiO ₂ for: (a) closed aperture, (b) open aperture	70
2.20	Nonlinear absorption for: (a) SiO ₂ -NF, (b) SiO ₂ :PVA film	70
2.21	The absorption spectrum of Fe ₂ O ₃ /SiO ₂ nanocomposite in the range 200-2000 nm (highlighted is lasing operation region)	72
2.22	Tauc plot of Fe ₂ O ₃ /SiO ₂ nanocomposite	72
2.23	Normalized transmission of Fe ₂ O ₃ /SiO ₂ nanocomposite for: (a) closed aperture, (b) open aperture	73
2.34	Nonlinear absorption for Fe ₂ O ₃ /SiO ₂ nanocomposite film	73
3.1	Optical spectra of YDFL based-Ni-NF at pump power of: (a) 126 mW, (b) 153 mW, (c) 160mW, (d) 182 mW, (e) 235 mW, and (f) 300 mW	77
3.2	Optical spectra of YDFL based-Ni-thin layer at pump power of: (a) 130 mW, (b) 174 mW, and (c) 300 mW	78
3.3	Oscilloscope trace at a different pump power of (a) 193 mW and (b) 280 mW	79
3.4	(a) Pulse width and repetition rate vs. pump power, and (b) Average power and pulse energy vs. the pump	80

	power	
3.5	(a) RF pattern, and (b) The single-pulse form of Q-switching based on Ni-NF at 300 mW	80
3.6	Optical spectra of YDFL based-Ni-NF at pump power of: (a) 60 mW, (b) 71.4 mW, and (c) 85 mW	81
3.7	Oscilloscope trace of unstable pulsed YDFL based on Ni-NF	82
3.8	Optical spectra of YDFL based-Ni-NF at pump power of: (a) 71 mW, (b) 85 mW, and (c) 102 mW	83
3.9	Oscilloscope trace at fundamental mode-locked dark pulses based on Ni-NF	83
3.10	Oscilloscope trace at 3 rd harmonic mode-locked dark pulses based on Ni-NF	84
3.11	RF spectra for the (a) fundamental and (b) 3 rd harmonic generations of the dark pulse mode-locked based on Ni-NF	85
3.12	Average power vs. the pump power	86
3.13	The optical signal with Ni-NPs SA at (a) threshold, (b) maximum pump power	87
3.14	Oscilloscope trace at: (a) 185 mW, and (b) 288 mW	88
3.15	(a) RF signal and (b) The single pulse envelope at 288 mW	88
3.16	The effect of the boost input power on (a) the repetition frequency and pulse duration, and (b) the output power and pulse energy	99
3.17	Optical spectra of YDFL based on Ni-PVA at pump power of: (a) 65.7 mW, (b) 85 mW, and (c) 96.4 mW	90
3.18	Oscilloscope trace at pump power of: (a) 107.7 mW, and (c) 170 mW	91

3.19	(a) Optical spectrum, (b) RF spectrum, and (c) Single pulse profile at 170 mW	91
3.20	The effect of the boost input power on (a) the repetition frequency and pulse duration, and (b) output power and pulse energy	92
3.21	Optical spectra at different pump powers: (a) 120, (b) 185, (c) 250 and (d) 260 mW	93
3.22	Oscilloscope trace at (a) 144 mW, (b) 290 mW	95
3.23	(a) The repetition rate and pulse width, and (b) the average output power and pulse energy as a function of pump power	95
3.24	(a) RF spectrum, and (b) optical spectra stability at a maximum pump power of 290 mW	96
3.25	The optical signal based Ni-PVA SA at threshold pump power	97
3.26	(a) The optical, and (b) the temporal signals based Ni-PVA SA at 144 mW	98
3.27	Optical spectra at different pump powers: (a) 178.5 mW, (b) 210 mW, and (c) 250 mW	99
3.28	(a) Oscilloscope trace, (b) single pulse envelope, and (c) RF spectrum at 260 mW	99
3.29	(a) The average output power and pulse energy, and (b) the repetition rate and pulse width as a function of pump power	100
3.30	Optical spectra of YDFL based on Fe_2O_3 -PVA thin film at (a) 102 mW, (b) 107.7 mw, (c) 117.4 mW, (d) 127 mW, (e) 135.5 mW, and (f) 170 mW	101
3.31	Optical spectra of YDFL based on Fe_2O_3 -NF at (a) 85 mW, and (b) 150	102

3.32	(a) Oscilloscope trace, (b) RF spectrum, and (c) single pulse envelope at 120 mW	103
3.33	(a) Oscilloscope trace, (b) RF spectrum, and (c) single pulse envelope at 200 mW	104
3.34	Average power vs. the pump power	105
3.35	Optical spectra of YDFL based on $\text{Fe}_2\text{O}_3\text{-NF}$ at (a) 85 mW, (b) 102 mW, and (c) 187 mW	106
3.36	(a) Oscilloscope trace, (b) single pulse envelope, and (c) RF spectrum at 250 mW	107
3.37	Optical spectra of YDFL based on $\text{Fe}_2\text{O}_3\text{-NF}$ at 250 mW with different PC states	108
3.38	Average power vs. the pump power	108
3.39	Optical spectra of YDFL based on $\text{SiO}_2\text{/PVA}$ thin film at (a) 90.7 mW, (b) 102 mw, (c) 121.3 mW, and (d) 170 mW	109
3.40	Optical spectra of YDFL based on SiO_2 suspension at (a) 90.7 mW, (b) 102 mw, (c) 121.3 mW, and (d) 170 mW	111
3.41	Oscilloscope trace of YDFL based on SiO_2 suspension	111
3.42	Optical spectra of YDFL based on SiO_2 suspension and polarization controller at (a) 90.7 mW, (b) 102 mw, (c) 121.3 mW, and (d) 170 mW	112
3.43	Average power vs. the pump power	114
3.44	Optical spectra of YDFL based on $\text{Fe}_2\text{O}_3\text{/SiO}_2$ nanocomposite film at (a) 85 mW, (b) 93 mw, (c) 127 mW, (d) 162 mW, and (e) 187 mW	116
3.45	Oscilloscope trace of YDFL based on $\text{Fe}_2\text{O}_3\text{/SiO}_2$ nanocomposite film	117

3.46	Multiwavelength spectrum at a different pump power of (a) 93 mw, (b) 110 mw, (c) 152 mw, (d) 187 mw, (e) 202 mW, and (d) 250 mW	118
3.47	Polarization dependence on multiwavelength at 290 mw	119
3.48	The characterization of temporal behavior, (a) the recorded pulsed train, (b) the corresponding single pulse profile (c), and (d) RF spectrum of the laser at different polarization states	122
3.49	Average power vs. the pump power	122
4.1	The optical spectrum of EDFL (a) without and, (b) with Ni-NF	124
4.2	The optical spectrum of erb ium-doped fiber at a different pump power (a) 52 mW, (b) 88 mW (c) 101.6 mw, (d) 160 mW, and (e) 300 mW	125
4.3	(a) Output spectra measured with 30 minutes, (b) wavelength shift, and (c) Power fluctuations	126
4.4	The optical spectra of the CW laser in comparison with Q-switched pulsed at threshold pump power	128
4.5	Oscilloscope trace at (a) 85 mW, and (b) 375 mW (the inset figure is a single pulse profile)	129
4.6	RF spectrum at maximum pump power	130
4.7	(a) Pulse width and pulse repetition rate, and (b) Output power and pulse energy as a function of pump power	130
4.8	The optical spectra at different pump power	131
4.9	Output spectra measured at the maximum pump power of 275 mW for 30 minutes	132
4.10	The optical spectrum of EDFL based on Fe ₂ O ₃ thin	134

	film at threshold pump power	
4.11	Oscilloscope trace at (a) threshold pump power and (b) maximum applied pump power	135
4.12	(a) Pulse width and pulse repetition rate, and (b) Output power and pulse energy as a function of pump power	136
4.13	(a) RF spectrum, and (b) single pulse profile at maximum pump power	136
4.14	The optical spectrum of EDFL based on SiO ₂ thin film at threshold pump power	137
4.15	(a) Pulse width and pulse repetition rate, and (b) Output power and pulse energy as a function of pump power	138
4.16	Oscilloscope trace at (a) threshold pump power and (b) maximum applied pump power	139
4.17	(a) Single pulse envelope, and (b) RF spectrum of EDFL based on SiO ₂ -NF	139
4.18	The optical spectrum of EDFL based on SiO ₂ thin film at threshold pump power	139
4.19	The optical spectrum of EDFL based on SiO ₂ thin film at threshold pump power	139
4.20	Oscilloscope trace at (a) threshold pump power and (b) maximum applied pump power	140
4.21	(a) Pulse width and pulse repetition rate, and (b) Output power and pulse energy as a function of pump power	141
4.22	(a) Single pulse envelope, and (b) RF spectrum of EDFL based on Fe ₂ O ₃ /SiO ₂ thin film	142
4.23	(a) Oscilloscope trace, (b) single pulse envelope, and	142

	(c) RF spectrum of EDFL based on $\text{Fe}_2\text{O}_3/\text{SiO}_2$ thin film at 250 mW	
4.24	Optical spectra of EDFL based on $\text{Fe}_2\text{O}_3/\text{SiO}_2$ thin film at pump power of: (a) 96.3 mW, (b) 144 mW, and (c) 250 mW	143

CHAPTER ONE
INTRODUCTION AND BASIC
CONCEPTS

Chapter One

Introduction and Basic Concepts

1.1 Background

Since 1960, when Theodore Maiman had demonstrated the first Ruby laser operation [1], the story of the success of different inventions of new laser sources continues which can create an intense light with amazing features of a single- and later multiple-wavelength. The unique features of the emerged coherent light had opened up numerous new areas for scientists, including nonlinear optics, fiber optics, and optoelectronics. Shortly thereafter, the prototype of the fiber laser was also proposed in 1961 when Snitzer published his well-known manuscript on oscillation of the laser in glass [2] and later reported on the prospect of fiber laser action [3]. Little times after, in 1964, the amplification of fiber laser generation in a gain fiber was experimentally proved by Koester and Snitzer [4]. After that several attempts were made by many research groups, but many issues placed earnest fiber laser exploration stop for many years. It is noteworthy that numerous facilitating technologies have been responsible for the fast performance scaling of fiber laser techniques and their enormous market prosperity in various applications. The suitable pump source and the homogeneously doped fiber active mediums still challenging issues for many years later. Passive and active techniques were employed to generate short pulses in the μs and ns pulse and ultrashort pulses in the ps and fs pulse widths since the early times of the first laser demonstration. Fiber lasers were also capable to generate such short and ultrashort durations but need a suitable pump power in the sense of power and adaptation.

After the 1980s, with the development of optical fiber technology and the evolution of relatively influential, reliable and powerful semiconductor lasers and semiconductor-pumped laser techniques, fiber

laser technique has been promoted quickly. It was escorted via the employment of fiber laser technique in optical communication that utilized a fiber amplifier instead of a fiber laser idea. The fundamental phenomena and innovations built thru the first communication era acted —and are remaining acting —an essential job in the improvement of fiber laser/amplifier techniques. It is also exciting to notice how progress in fiber optics have revolutionized laser science technique, specifically for ultra-fast optical devices and networks [5].

A fiber laser employs rare-earth-doped fiber to play a function of a gain medium. Many types of rare-earth ions have been doped into the fiber to deliver gain in diverse wavelength bands (0.4-4 μm) [6–8] including neodymium (Nd^{3+}), erbium (Er^{3+}), ytterbium (Yb^{3+}), thulium (Tm^{3+}), praseodymium (Pr^{3+}) and holmium (Ho^{3+}) [5,9]. It noteworthy, that historically the first fiber laser demonstrated utilizing the Nd^{3+} ion; and then a lot of researches have been accomplished using this active doped ion type in fiber laser which has shown good spectral and temporal characteristics. However, engineers and researchers transferred their attention to Yb^{3+} and Er^{3+} , in which the features of these rare-earth ions were increased by the development of the technology of 970-980 nm laser diodes which utilized for exciting the fiber lasers. Furthermore, Yb^{3+} exhibits excellent conversion efficiency, wide tuned range around 1000 nm spectral region, as well as fast power storage period. Additionally, Yb^{3+} -doped fiber lasers drawn more consideration after 2000 of the current century due to their ability for delivering high power levels. On the other side, with more progress in the development of optical telecommunication, Er^{3+} -doped fiber lasers happen to be the topic of extreme focus due to low loss in the 1.55 μm which makes it attractive in optical communications systems [5].

Nowadays, multiwavelength fiber lasers have attracted noteworthy study concentration owing to their wide field of applications in distributed

multiplexing, laser ranging, spectral analysis, sensing, and so on [10,11]. Up to the present time, many techniques have been proposed to generate multiwavelength fiber laser with different spectral ranges of operation. Consequently, several kinds of multiwavelength fiber lasers based on various gain mediums have been reported, in which the choice of gain medium notably influences the stability of the multiwavelength lasing in fiber systems. Usually, inhomogeneous gain media are more widespread options compared with homogeneous media as the earlier participates in the stability of the multiwavelength fiber laser system [12,13]. Homogeneous gain medium such as the doped fiber experiences from large instability at room temperature process owing to large gain broadening and mode competition between neighboring modes [14,15]. Therefore, many techniques based on the stimulating inhomogeneity within the gain medium have been developed that made the multiwavelength lasing more stable at room temperature. These techniques can be categorized in terms of lasing techniques being employed as: either 'passive' techniques which based on the interferometric filter such as Mach-Zehnder [16], Fabry-Perot filters [17], and Sagnac loop mirrors [18]; or 'active' nonlinear phenomena such as four-wave mixing (FWM) [15], stimulated Raman scattering (SRS) [12], stimulated Brillouin scattering (SBS) [19], and nonlinear polarization rotation (NPR) [12]. On the other side, inhomogeneous gain based on the nonlinear medium is popular technique for generating multiwavelength lasers, which these techniques deliver a good stability regardless of demanding high power supply and highly long length gain media for the influence to obvious [12,15,20]. Thus, the combining of the homogeneous and inhomogeneous gain media in the fiber system can be proposed for the generation of multiwavelength fiber lasers [21,22].

In recent times, nanostructure materials have become a principal element of particular laser cavities and drawing important functions in all areas of engineering. The optical features of such innovative materials

should meet the conditions of the laser cavity. Moreover, employing such passive elements into the fiber oscillator can employ them to simultaneously or separately function as gain stabilizers for a multiwavelength generation as influenced by the real part of the third-order optical susceptibility. Whereas, the imaginary part of the third-order optical susceptibility influences the modulation character for pulse operation regimes [23–25]. Generally, the nonlinear influences are mainly dependent on the type, size, and geometry of the nanoparticles themselves [26,27]. Accordingly, multiwavelength fiber lasers based on nanostructure materials can be emitted in different temporal operations including the continuous wave (CW) [28], Q-switched [29], and mode-locked [30] operation regimes. For the CW regime, the laser emits an optical wave of steady output power, a narrow linewidth emission, and good coherence. While in the pulse regimes; the emitted signal has a pulsed profile shape, described by parameters including pulse repetition rate, pulse duration, and pulse energy. The Q-switching fiber lasers which could produce short pulses with high energy up to several milli-joules has a wide range of application in many aspects, such as range finding, remote sensing, ladar, telecommunication spectroscopy, and biotechnology. Instead, mode-locking is the second method for pulse generation with lasers. It generates ultrashort pulses on the range of nanoseconds to femtoseconds. But, related to the mode-locking, Q-switching creates much lower pulse repetition rates, much longer pulse durations, and much higher pulse energies. Both techniques are important in the progress of laser technology and sometimes applied together [5,8]. In this regard, the investigation of new nanomaterials is one of the essential matters of modern science and technology. A numerous of these nanomaterials including carbon-based nanomaterial [31,32], black phosphorus [33,34], and semiconducting transition metal dichalcogenides (e.g. WS_2 , MoS_2 , $MoSe_2$, and WSe_2) [35–

38] have been experimentally investigated and demonstrated in many fiber laser cavities.

Recently, more focus on the transition metals[29,31,39,40] and transition metal oxides[11,30,41–44] nanomaterials have been observed to assist as effective nonlinear materials for many kinds of fiber lasers-based on different structures/mechanisms, owing to their notable optical features like great 3rd susceptibility, wideband absorption, wideband surface plasmon resonance and short response time. In particular, the transition metals are tunable over a wideband spectral region covered to several hundreds of nanometers, leading those promising elements for various developments in the area of photonics like saturable absorber for pulse generation, wavelength conversion, and wavelength comb generation [45–47].

1.2 Principles of Fiber Lasers

Fiber lasers are a distinctive type of solid-state lasers that possess many promising physical features that differentiate them from other types of lasers in regards to performance, functionality, and practicality. Fiber lasers have confirmed the advantage of good beam quality, high brightness, quite an excellent wavelength stability with environmental effects, great opto-optical efficiency, and improved heat dissipation owing to their bigger surface to volume ratio of the gain medium [48,49].

Even after the demonstration of the fiber laser, a series of laser structures has been engineered utilizing ions-doped fiber [2], optical nonlinear effects [50], or the combination of these two techniques as the optical gain medium [51]. Even though active laser practice has been witnessed from optical nonlinearity inside the fiber lasers oscillator, the utmost study assurance has been employed on the perfection of ions-doped techniques. That has been encouraged through the remark that considerable ions concentrations could be hosted into the core of traditional communications fiber void of reducing the promising features of the fiber

[5]. Typically, the rare-earth ions are doped in the core of silica glass host to be an active fiber, which these doping rare-earth ions make the fiber to be a distinctive medium that exhibits a low attenuation loss, as well as high gain, can accomplish [52]. Intense absorption ranges are constructed via the doped ion, whereas the little waste wave guiding features of the fiber are preserved at the lasing peak of the rare earth ion. This rare-earth is optically active; therefore it can absorb light at one wavelength and emit light at another. Generally, fiber lasers are pumped by cost-effective laser diodes. The emitted wavelength of the laser should be matching with the exciting wavelength of the designated dopant ions of the fiber gain medium. Accordingly, fiber lasers become able to lase above a large spectral band extended from 0.4 to 2.9 μm with a somewhat narrow beam output laser [8,53]. Usually, the emitted wavelength of fiber lasers is specified by the transitions among the energy states of the doped rare-earth ions, in which the absorption and emission transitions wavelength are independent of the fiber host matter. Moreover, the active gain fiber matter is somewhat long, which the signal and pump so appreciably over the total length of the doped fiber [52,53].

1.3 Optical Components with Fiber Lasers

In addition to the amplifying gain medium, there is a difference in passive fiber optics elements that are utilized in optical fiber laser systems to implement the precise job. These passive elements split, redirect or combine the light signals. The most popular passive fiber optics elements that commonly utilized are wavelength division multiplexing (WDM), isolator (ISO), fiber filters, polarization controller (PC), and coupler. Each of these passive elements has functions which are described in detail in the next sub-sections. Then, the subsequent subsections explain probable cavity structures employed for the fiber lasers and then the explaining the

spectroscopy of the most potential doped-ions that have been employed to function in a host fiber is present.

1.3.1 Wavelength Division Multiplexing (WDM)

Often, it is wanted to split or combine different signals in fibers corresponding to their wavelength [54]. WDM elements are specified coupler kinds that permit light from two or more optical sources of various spectral wavelengths to be propagated in parallel into a single optical fiber. In a fiber laser, WDM is an ideal solution to combine signal and pump with little insertion attenuation, permitting the combined signal and pump to be traveled within the same gain fiber without interference [55].

1.3.2 Optical Isolators (ISO)

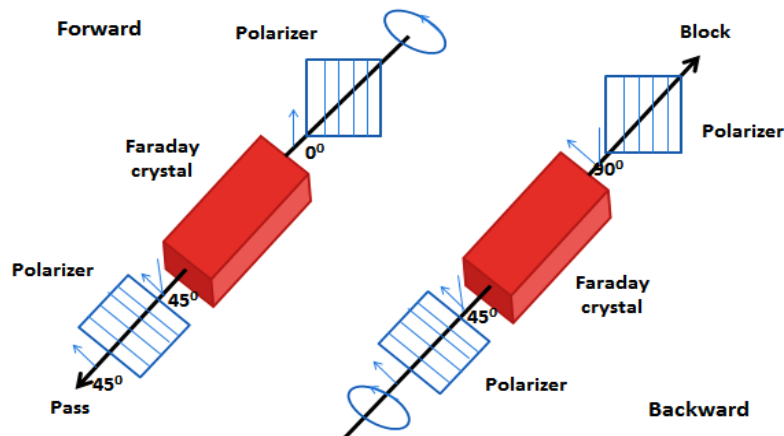


Fig.(1.1): Isolator operation [55].

When light propagates through fiber splices, connectors, and other optical elements there are several probabilities for back reflection. These reflections typically materialize after light propagates via an interface vertical to the direction of the light path. But, an isolator is utilized to save the signal and pump sources from back-reflections. Generally, the optical isolator is a two-port passive element that permits light (in a specific wavelength band) to travel through with little loss in one direction, although isolating (giving a high loss for) light traveling in the reverse

direction [55,56]. The operation principle of the isolator is illustrated in Fig. (1.1).

1.3.3 Polarization Controller (PC)

PC is a device that allows adjusting the state of polarization of light within a fiber. The fiber polarization controller enables the induced birefringence by bending a fiber. In all-fiber systems, the polarization state can be adjusted by the fiber itself which can operate as a birefringent retarder plate. Generally, as the axes of the circular core fibers are straight, there are not birefringent which is, the two orthogonally polarized LP_{01} modes possess identical effective indices. That is because the birefringence can be induced when a fiber is exposed to stress. Then bending such a fiber initiates stresses in the fiber and forces the fiber linearly birefringent with the fast and slow axes in the plane and vertical to the plane of the loop, respectively [57,58].

Fig. (1.2) shows two types of PC. The first one composes of optical fiber wrapped in a circle around three plates with a variable number of fiber loops. This type of PC employs these coils in a sequence, where the middle coil functions as a half waveplate and the other two as quarter waveplates. Each coil can be rotated around an axis coordinated with the input and output fibers, which state of polarization can be adjusting by the orientations of the three coils. The other PC employs a mechanical fiber squeezer by rotating it to adjust an arbitrary input polarization to any required output polarization. Through tightening the knob on the fiber squeezer, the pressure will be applied to the fiber which is sandwiched between two pressure plates in the center portion of the device. This leads to induce a linear birefringence in this portion of the fiber with its slow axis in the direction of applied pressure. Also, through the rotating of the fiber squeezer about the fiber, the induced birefringent axis can be changed [59,60].

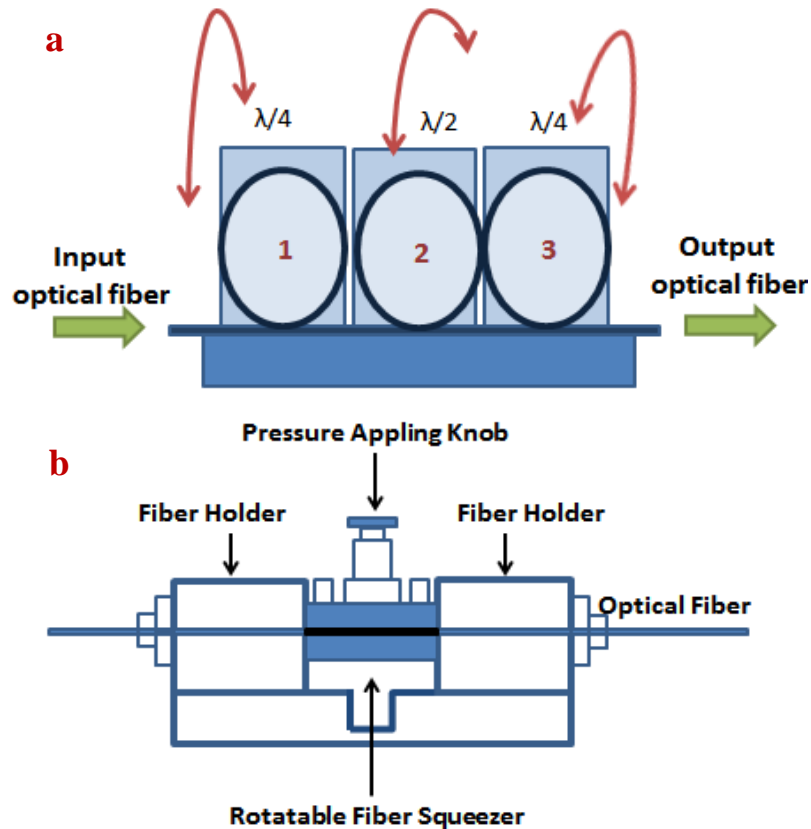


Fig.(1.2): Polarization controller, (a) three puddle PC [59], (b) in-line PC[60].

1.3.4 Fiber Output Coupler (OC)

OCs are generally utilized for light coupling between various fibers. The opportunity for a division between various fibers frequently demands that a signal be dividing into two (or more) ports or two (or more) ports are to be joint into one fiber. OCs are generally bidirectional and exhibit little back reflection and insertion attenuations. The most forms 2x2 or 1x2 ports couplers with various dividing are employed for the output of laser generations of the fiber laser[55]. The simplest form of this device is a 2×2 coupler as depicted in Fig. (1.3). In general, those couplers are manufactured by twisting two SMFs together in which their cores become so close over a specific length of the fiber. As light guided in one fiber may then the evanescent fields leak over to the other one. This is a coherent approach that is greatly wavelength-dependent [57].



Fig. (1.3): Schematic Diagram of Fiber Output Coupler [57].

1.3.5 Optical Filters

Optical filters are utilized in widespread fields of application within optics and optical fiber systems. Optical filters are frequency domain systems that chosen weaken or pass specific wavelengths. The common parameter in all-optical filters is their reliance on particular wavelength-sensitive influence. Generally, optical filters are dependent either on interference or diffraction phenomena [55]. There is a huge variety of optical filter configurations. The next filters are the most familiar [56]: Mach-Zehnder, Fabry-Perot, Fiber Bragg grating (FBG), and Saganc loop mirror.

1.3.6 Fiber-Coupled Diode Laser

Fiber lasers are optically pumped by a diode laser of an appropriate wavelength. The crucial benefit of diode pumping is the excellent optical conversion efficiency due to there is excellent matching between diode laser central wavelength and the absorption spectrum of the fiber gain medium [49]. Generally, the fiber gain medium is longitudinally pumping which the pump signal can be guided along the fiber length through either the core itself, as the classical single-mode fiber laser, or an inner cladding that surrounding the core-that is term as double-clad fiber laser, this scheme delivering high output power. Depending on the coupling technique, the most common pump structure is the end pumping structures [5].

1.4 Fiber Laser Cavity Configurations

Different laser cavities can be employed to operate the fiber laser. Depending on the design parameters and the intended laser output in terms of quality, wavelength, and/or power. For instance, to operate the laser with a single longitudinal mode, linear cavities are subject to spatial hole burning, so, the best alternative is to use ring cavity configuration.

1.4.1 Linear Cavity

Fiber laser with a linear cavity can be fabricated by positioning a length of doped fiber between two reflectors such as dichroic dielectric mirrors, fiber Bragg grating, or fiber loop mirrors. Also, this cavity consists of some other intracavity optical components that are used to determine the spectral and temporal characteristics of the output fiber laser [5,61]. The typical schematic diagram of the linear cavity fiber laser is depicted in Fig. (1.4).

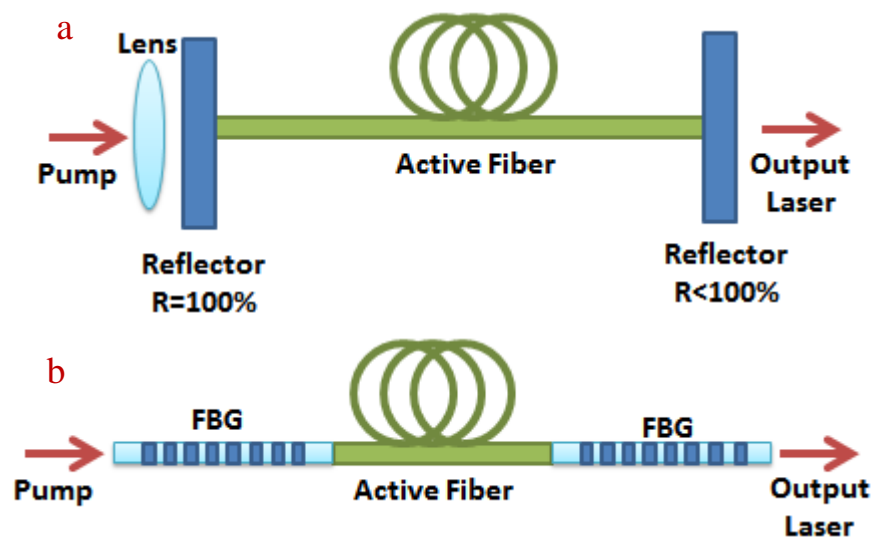


Fig.(1.4): Fiber laser linear cavity configuration based on (a) two dielectric mirrors [5], (b) FBG [57].

In these types of cavities, the cavity modes are typically theorized as an overlap of double electromagnetic signals propagating in reverse paths among reflectors of the cavity. Hence, standing waves are generated, that after some cycles possess maximum and minimum interfering amplitudes. Then, the resonant frequencies can be given as [5]:

$$\nu = M \times \left(\frac{c}{2nL} \right) \quad (1.1)$$

where, M is an integer, c is the speed of light in free space, n is the refractive index of the core fiber which the light travels along the laser cavity of length L . Hence, the frequency difference among two longitudinal (consecutive) modes can be expressed as [5]:

$$\Delta\nu = \frac{c}{2nL} \quad (1.2)$$

The minimum amplitudes of the standing wave are accountable for the spatial hole-burning influence that is generated inside the laser cavity, which influences the laser spatial gain distribution, and then supports the multispectral mode oscillation of the laser. So, this type of fiber design with a somewhat lengthy cavity and great gain-bandwidth experiences prompt mode hopping influence resulted from the spatial hole burning [5]. Besides, owing to the roundtrip character of the light path within the laser cavity, as well the light travels twice per roundtrip cycle via the gain medium, and then the laser gain/loss is considered twice per cycle. In this cause, the gain medium attains deep saturation, and the spectral profile of the output power above the entire amplified spontaneous emission (ASE) span becomes flat, denoting that the peak power alternative is quite small [62]. That is a vital property of the linear laser cavity, distinguishing it from the one-directional ring laser cavity, which exhibits no spatial hole-burning influence. Linear-cavity fiber lasers also possess some benefits in comparison to ring-cavity fiber lasers such as accomplishing higher output power readings with great signal to noise ratio (SNR) [63,64].

1.4.2 Ring Cavity

A ring resonator is an essential form of the fiber laser cavity, in which the intracavity light propagates through the loop of fibers in one direction; therefore the ring cavity may be accomplished using a folded form. An integrated ring fiber laser system built from a fiber ISO can be spliced into the cavity to produce the unidirectional lasers, the exciting

source is injected into the oscillator via a WDM and the emitted laser is extracted from the oscillator by employing a simply fiber fused OC. As the light signal propagating unidirectional through the cavity, then less roundtrip gain will create and the gain/loss will be counted once in this cavity structure [5,61]. On the other side, to realize a phase shift situation for the propagating light signal per round-trip cycle of the oscillator to be match 2π , as alike condition of the linear resonator case, then the resonant frequency expression can be given as [5]:

$$v = M \times \left(\frac{c}{nL} \right) \quad (1.3)$$

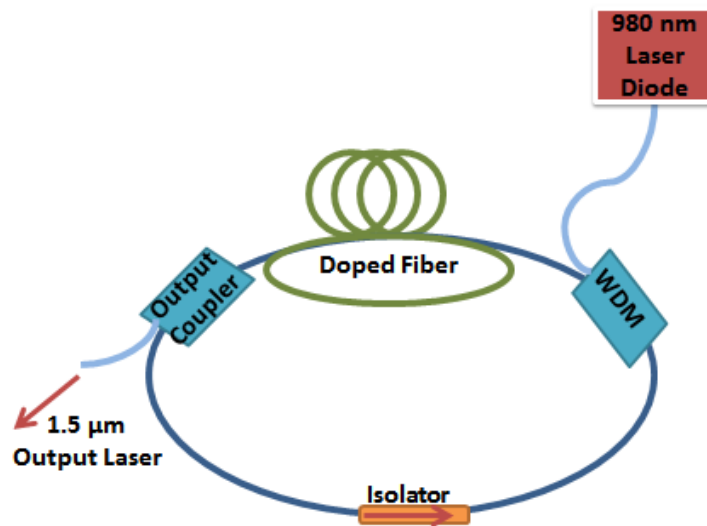


Fig. (1.5): Fiber laser ring cavity configuration [57].

In the ring cavity, the hole-burning influence does not stimulate [65], which assists to accomplish a very narrow, lone longitudinal mode of laser generation. Fig. (1.5) shows a typical form of an integrated ring cavity. As in the state of a linear cavity, this type requires some intracavity components to achieve the desired performance and to determine the spectral and temporal characteristics of the output fiber laser. Generally, a PC is required inside the fiber laser oscillator to control the state of polarization inside the cavity against the physical movement and pendulum [66]. Ring fiber lasers are known to be susceptible to power fluctuations. However, the laser output power stability can be improved through an

appropriate choice of laser parameters like the doped fiber lengths, the coupling ratio on the output, and the total cavity length [67].

1.5 Spectroscopic Properties of Trivalent Rare Earth Ions-Doped Fibers

The transitions of rare-earth ion reveal in the spectroscopic spectrum as narrow bands that differ slightly in energy level from one to another (like crystals and glass), that is owing to a transmission of the ion by the electron shells 5s and 5p. In glasses, the active media of fiber lasers, rare-earth ions have spectroscopic features which are extremely identical to crystals. But, they exhibit little fundamental variances related to the environment glass character wherever the doped ion is hosted. Generally, glass classified as disordered matter that exhibits an inhomogeneous spectral broadening; thus, it demonstrates wide absorption/emission spectrum of specific absorption/emission transition [5,8]. The subsequent sub-units explain the spectroscopic properties of the greatest utilized rare-earth ions (Yb^{3+} and Er^{3+}) in the plan and demonstration of latest fiber lasers.

Table (1.1) displays the most prevalent rare-earth ions occupied in fiber lasers with their host glasses and emission wavelengths [5,52,68].

Table (1.1): Rare-Earth Ions with their Absorption and Emission Wavelength Ranges [5,52,68].

Ion	Absorption Wavelength (nm)	Emission Wavelength (nm)
Nd^{+3}	520, 590, 820	1000-1100
Yb^{+3}	860, 920, 976	1000-1100
Er^{+3}	520, 650, 800, 980, 1480	1500-1600
Tm^{+3}	800	1700-2100
Ho^{+3}	2040, 2076	2100,2900

1.5.1 Ytterbium Ion-Doped Fiber (YDF)

Ytterbium ions are one of the most popular and promising dopant based silica host media. It won more attention like a laser ion in the structure of ytterbium-doped fiber lasers (YDFL). Ytterbium is a motivating scheme as it possesses a simple energy level with just two manifolds: the $^2F_{7/2}$ ground state and the $^2F_{5/2}$ excited state, which the ground state splits into four stark states, and the excited state splits into three stark states. The little difference between absorption and emission spectrum causes little quantum defect (which leads to reduce thermal load per pump power unit) that participating in excellent optical-to-optical efficiency (>90%). The energy state schema of the utmost significant laser transitions associated with Yb^{3+} is illustrated in Fig. (1.6). While the absorption/emission spectrum of the Yb^{3+} -doped fiber are depicted in Fig. (1.7). Yb^{3+} -doped fiber possesses broad and intense absorption ranges around 976 and 915 nm which are fit for InGaAs laser diodes exciting. These two absorption peaks belong to the shift from the lowest Stark sub-levels of $^2F_{7/2}$ level to the first and second Stark sub-levels of $^2F_{5/2}$ state, respectively.

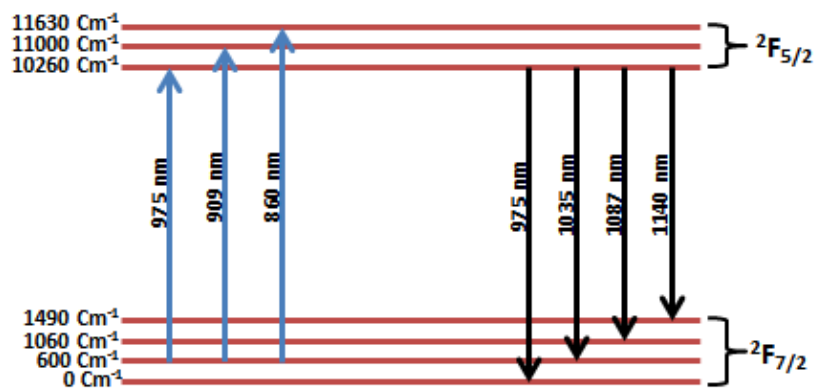


Fig.(1.6): Yb^{3+} energy level structure [5].

Besides, Yb^{3+} -doped fiber possesses wide and appropriately strong emission ranges around 950-1200 nm spectral band, as well as at 976 nm with a zero-phonon line. YDF exhibits a quasi-three-state or four-state

pattern depends on the pump wavelengths. For wavelengths emit in the region shorter than 1080 nm, the lower laser transition level is very close to the ground level, which this case alike to a quasi-three-level regime. While, the wavelengths located in the region that higher than 1080 nm, the laser transitions happen at energy states higher than ground-level, consequently the system exhibits a four-level scheme behavior [69].

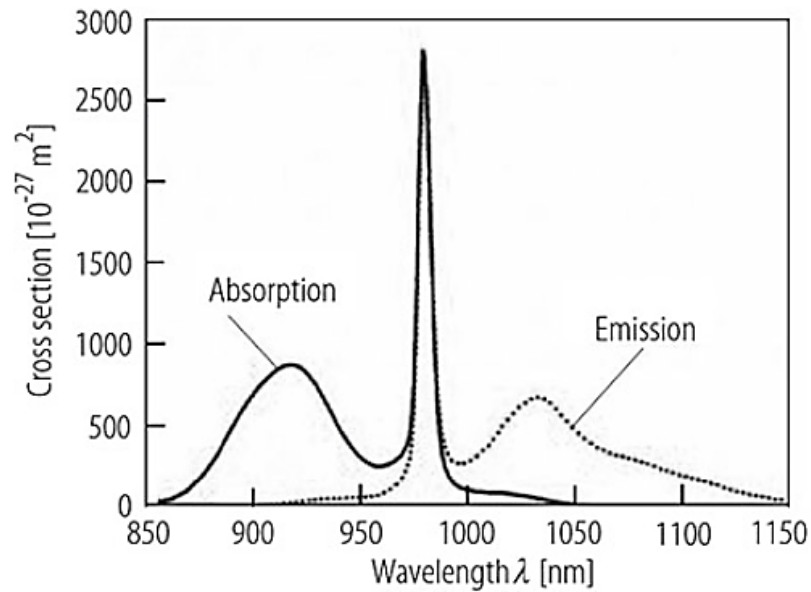


Fig. (1.7): Absorption/emission spectrum of Yb^{3+} -doped glass [5].

The broadened exhibition of YDF initiates due to the ion-host lattice interaction that provides wide levels which in turn permits for tunability of laser action with a broad spectral range between 980-1150 nm. On the other side, the wide gain bandwidth of YDF makes it desirable for an ultra-short pulse and high power generation [69]. But, there is a challenge associated with the Yb^{3+} -doped fibers laser operation at huge-power states and big intense excitation states which are typically related to the so-called photo-darkening effect of Yb^{3+} -doped fibers that has been ascribed for the creation of color-centers in the doped fiber. Photo-darkening acts as a sequential upsurge in wide-band absorption within the visible-region peak of the absorption spectrum of the fiber [5,70].

Moreover, Yb^{3+} -doped silica fibers exhibit promising features including longer excited-state lifetime (~ 1 ms), absence of quenching, and

nonappearance of the pumped level absorption and up-conversion wastes due to a simple energy-state structure. As the YDF operates within the 1 μm band, this gains advantages since the laser generates in the normal dispersion. Consequently, there is no demand for the external component to compensate for the normal dispersion and to switch back the cavity into an anomalous dispersion as in the case of employing EDF of TDF. But, to generate a stable pulse, YDFL design should take into consideration the nonlinearity influences like self-phase modulation (SPM) and group velocity dispersion that result in instability and pulse broadening, respectively. Generally, the influence of these two reversing effects requires to balance out so which the cavity could generate soliton laser with stable and ultrafast pulse [71].

1.5.2 Erbium Ion-Doped Fiber (EDF)

Erbium ion (Er^{3+}) is generally employed as a gain part as it can function at a little attenuation band of 1.5 μm which appropriate for the optical-communication field. The EDF can be utilized in laser (Erbium-doped fiber laser "EDFL") and amplifier (erbium-doped fiber amplifier "EDFA") systems, together, in which the function of both systems depends on the same mechanism. Generally, EDFA can be converted to the EDFL system by integrating a feedback arrangement in the design [72].

Fig. (1.8) displays the absorption/emission spectrum of EDF. The absorption/emission wavelength peaks appear in the region around 1530 nm; so, the operating wavelength must be selected in the region in which the absorption cross-section much smaller than the emission cross-section, which is nearby 1550 nm. On the other side, the emission is broad which covers the band from 1450 to 1650 nm. Additionally, EDF possesses many absorption peaks that located at 520, 650, 800, 980, and 1480 nm. Consequently, the optical excitation at each of these peaks has been examined, but some of this pumping show a serious drawback that is credited to the strong excited absorption state that results in an unwanted

waste of pump photons. And so, 980 and 1480 nm the pumping wavelengths are the most commonly employed, due to them because of the absence of excited-state absorption [73].

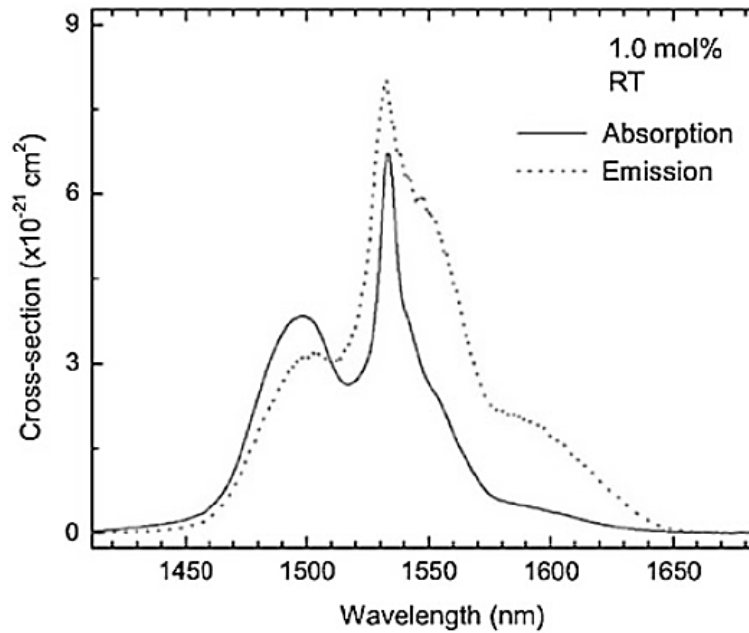


Fig. (1.8): Absorption/emission spectrum of the Er^{3+} -doped fiber (PKBA Er glass) [5].

Fig. (1.9) displays the energy level diagram of Er^{3+} doped in silicate glass with an optical transition of the $4f$ shell. From this figure, it can notice that the lowest energy state $^4\text{I}_{15/2}$ regards a ground state for EDFL transition. EDFL can be characterized as a three-state or quasi-three state behavior [53]. The energy level of Er^{3+} is splitting into multiple sub-states owing to stark influence. This splitting leads to the broad emission bandwidth. As the pump photon is absorbed, EDF is excited to a state of $^4\text{I}_{11/2}$ or $^4\text{I}_{13/2}$, reliant on the pump wavelength utilized. Indeed, EDF possesses two laser transitions that are practically detected through the pumping process. The first one is the $^4\text{I}_{15/2}$ - $^4\text{I}_{11/2}$ transition which corresponds to wavelength ~ 980 nm. While, the other is the $^4\text{I}_{15/2}$ - $^4\text{I}_{13/2}$ transition, which corresponds to wavelength ~ 1480 nm. The relaxation action among the $^4\text{I}_{11/2}$ and $^4\text{I}_{13/2}$ energy states exhibits quick (μs) non-radiative decay [74]. In the present work, EDF has been agitated by

pumping wavelength around ~ 980 nm that possesses a non-radiative transition to a $^4I_{13/2}$ state. Generally, the $^4I_{13/2}$ - $^4I_{15/2}$ radiative transition is the main and the most popular transition of EDF which is exploited to generate the wavelength in the band around 1530-1600 nm. This transition has a long fluorescence lifetime of ~ 10 ms. This feature is very vital, due to the system quantum efficiency is reliant on time it can remain in that excited level. If it recovers extremely fast, additional photons are demanded to sustain it excited, denoting additional incident pump power is demanded to create the amplifier action [75]. The 980 nm pumping is the most popular scheme, owing to the better gain efficiency and SNR) for small signal amplifiers. Also, it provides better quantum conversion efficiencies and noise Figures for power amplifiers. Despite this, EDFs show little pump/lasing conversion efficiency which about 60–70 % from the incident pump power can be waste in the heat form. Such a low optical-to-optical efficiency makes the challenged researchers employ long-wavelength pumping devices, mainly those located around the resonant absorption range of the EDF energy state scheme close to $1.53 \mu\text{m}$. This method utilizes the application of 1.46 – $1.5 \mu\text{m}$ diodes laser [53].

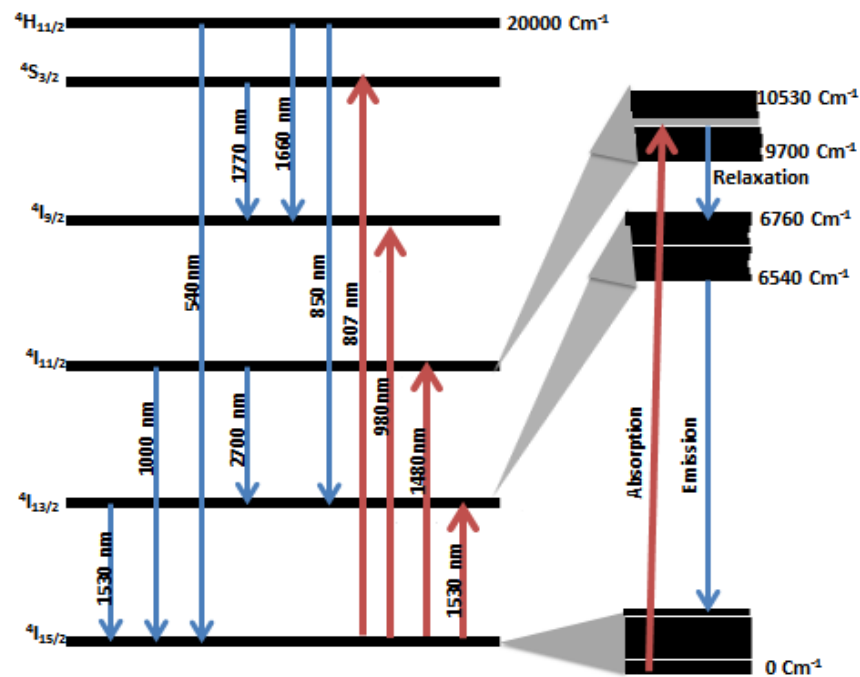


Fig. (1.9): Energy levels of Erbium ions in silica glass host [5,73,76].

Moreover, as the EDF exhibits a broad spectrum band, this spurred to generate different laser systems for practical application in a telecommunication band around 1550 nm, such as multiwavelength lasers, tunable lasers, and pulsed lasers. Also, the fiber dispersion at 1550 nm is irregular (anomalous), so the EDF has helpful for ultrashort pulse fiber lasers generation, which the anomalous dispersion functions with nonlinearity in the fiber that assists to generate good self-stable pulses especially the soliton pulse regime of mode-locking fiber lasers [71].

1.6 Modeling of Fiber Laser

Based on three-energy-state schemes or quasi-three-energy-state schemes (identical to the situation of greatest commonly utilized Yb^{3+} - and Er^{3+} -fiber lasers), requiring to consider reabsorption wastes of laser emission at the emitted spectral line. The characteristics of the fiber laser can be described by employing the propagation equations and rate equations. The rate equations are dependent on the energy level diagram in Fig. (1.10), in which the three-level regimes can be explained utilizing a reduced two-level scheme, as the non-radiative transitions to the meta-stable state are very quick [77]. Barnard et al. [61] established an mathematical prototype for fiber-doped lasers. This prototype offers formulations for the key laser factors stated in somewhat simple calculable optical factors of the scheme. The current theoretical scheme is related to a fiber ring resonator with L length, as shown in Fig. (1.11). Herein, the small-signal fiber gain (g) and the maximum gain (G_{max}) as stated by Barnard et al. [61], can be given as:

$$g = \left(\alpha_s + \frac{1}{P_s^{sat}} \sum_{j=P..s} u_j \frac{\lambda_j}{\lambda_s} \frac{\partial s_j}{\partial z} \right) \quad (1.4)$$

$$G_{max} = \exp \left[\left(\frac{\alpha_p}{\delta} - \alpha_s \right) L \right] \quad (1.5)$$

P_s^{sat} is the signal saturation power that denotes the factor describing the conversion of power from the absorbed excited power to the laser

output. α_s, α_p are terms as the small-signal absorption coefficients at the emitted laser λ_s and pump λ_p wavelengths, respectively. The relating quantities of u are 1, as the ring laser works unidirectional, (the backward signal power has been ignored). Then, the intrinsic-threshold pump power P_{th} is expressed as [5]:

$$P_{th} = \frac{h\nu_p P_s^{sat} [\alpha_s L - \ln(\epsilon k)]}{1 - (G_{max} \epsilon k)^{-\delta}} \quad (1.6)$$

where k is denoted as the fraction of the energy that comes back to the ring oscillator via the OC. ϵ is the actual cavity transmission, δ is the proportion of the output laser cross-saturation energy factor to the excited real saturation energy factor.

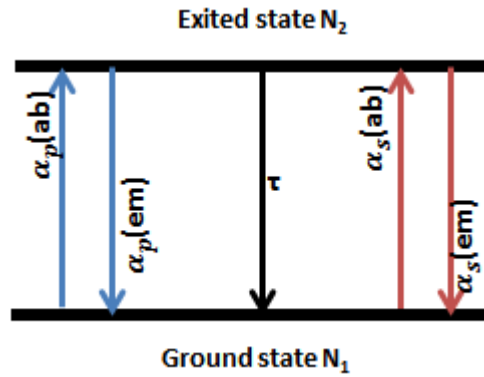


Fig. (1.10): Energy state scheme for the two-level system [78].

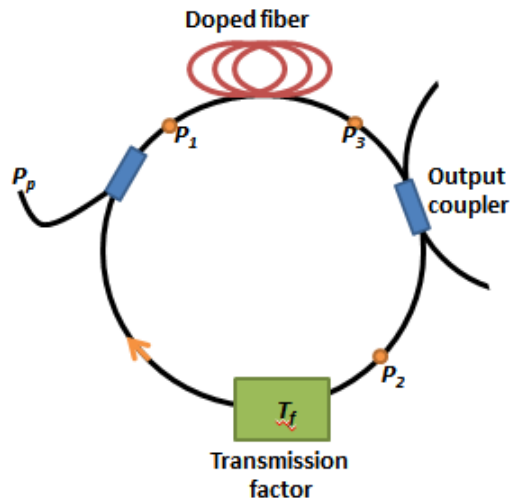


Fig. (1.11): Schematic diagram of a fiber ring laser [79].

The OC with a precise coupling ratio is required to adjust the feedback and output ratios. The stability and the efficiency of laser output

power are influenced by many factors, including the active medium length (the doped fiber), the output coupling ratio, and the overall cavity length. It can be enhanced via suitable adjusted laser parameters [74].

Accordingly, if the effective transmission of the ring cavity T_{eff} , then the slope-efficiency of the fiber laser ring cavity is expressed as:

$$\eta_{ring} = \frac{\lambda_p \varepsilon_2 (1-k) P_s^{sat}}{\lambda_s T_{eff} P_p^{sat}} [1 - (G_{max} \varepsilon k)^{-\delta}] \quad (1.7)$$

Based on this formula, it may find the laser output power of the fiber ring cavity utilizing the following typical relation:

$$P_{out} = \eta_{ring} (P_p - P_{th}) \quad (1.8)$$

The influence of pump beam decline lengthways of the gain fiber causes from the non-uniform medium inversion. The gain fibers will absorb the laser beam while not being reversed; the gain fibers will be lost at laser wavelengths that exceed a certain length [61,77]. So, for a specified pump power, there is an optimum length of gain fiber that enlarges the output power. For a fiber laser ring cavity, it is expressed by [61]:

$$L_{opt} = \frac{1}{\alpha_p - \delta \alpha_s} \ln \left[\frac{P_p (\alpha_p - \delta \alpha_s)}{P_s^{sat} \alpha_s (\varepsilon k)^\delta} \right] \quad (1.9)$$

The fiber must be extended to the length at which the full round-trip gain matches the round-trip losses. This minimum length L_{min} is determined by putting the slope expression in eq. (1.7) equivalent to zero. For a ring laser cavity, the minimum length is expressed by:

$$L_{min} = \frac{-\ln(k\varepsilon)}{(\alpha_p - \delta \alpha_s)} \quad (1.10)$$

1.7 Propagation of Optical Signals in a Fiber

The propagation of light through an optical fiber structure can be studied utilizing the ray and electromagnetic wave theories in a dielectric waveguide. Herein, it essential to considered the refractive index of the dielectric matter. Owing to the difference among the refractive indices of the core and the cladding of the optical fiber, it is possible to propagate

light through the fiber. The refractive index of the core must be always much greater than the cladding refractive index. The key features of this signal guiding within the optical fiber (waveguide) are dependent on total internal reflection [80,81].

Any intense light pulse that particularly in the linear region, while propagating in an optical fiber, experiences the influence of time dispersion, which initiates its broadening and may produce interference among symbols that can significantly border the bandwidth of the wave to be transmitted. But, pulse propagation in the nonlinear region is influenced by the optical Kerr effect. Generally, the nonlinear effects occur in the dielectric medium as a consequence of the variation of the optical features of a material structure by applying appropriate intense laser light. The optical nonlinearity relies on the interaction among the polarization of a material $P(t)$ and the intensity of the applied optical field $E(t)$. Firstly, linear polarization can be expressed as [82]:

$$P_{lin}(t) = \epsilon_0 \chi^1 E(t) \quad (1.11)$$

where χ^1 is the linear susceptibility and ϵ_0 is the free space permittivity.

While the nonlinear polarization can be expressed by the subsequent power series:

$$P_{nl}(t) = \epsilon_0 [\chi^2 E(t)^2 + \chi^3 E(t)^3 \dots] \quad (1.12)$$

where χ^2 and χ^3 are recognized as the second and third nonlinear coefficients.

In fibers, the refractive index of the silica glass varies with intensity [80]:

$$n(I) = n + n_2 I \quad (1.13)$$

$$n_2 = \frac{3}{8n} \text{Re}(\chi^3) \quad (1.14)$$

$$I = P/A_{eff} \quad (1.15)$$

where n is the linear refractive index, n_2 is the nonlinear refractive index, I is the intensity, P is the optical power and A_{eff} is the mode area.

All nonlinear effects that happen in fiber optics can be classified into dual chief groups: nonlinear scattering effects (including SBS and SRS) and nonlinear power dependence based on the fiber refractive index (including Four-Wave Mixing (FWM), self-phase modulation (SPM), and cross-phase modulation (XPM)). From an applied opinion, FWM, SRS, and SBS typically influence energy distribution amongst a number of spectral channels related to discrete transmitting signals, while SPM and XPM typically influence spectral boundaries of the guiding signals [83]. Due to the vital significance of the FWM effect in present multiwavelength fiber lasers engineering and implementation, its nonlinear effects are explained in more describe in the next sub-section.

1.7.1 Four-Wave Mixing (FWM) Process

FWM is a 3rd nonlinear influence. This influence leads to redistribution of energy amongst several spectral channels that generate through propagated of the intense light signal in the optical fiber. Consequently, optical fibers work a passive function except for mediating the interaction between various optical signals. FWM can appear in optical fiber when two-wavelength lines propagate and then two new wavelength lines are created in the condition of energy and phase matching conservation.

FWM can appear with two frequency components propagate mutually in a nonlinear medium like optical fiber where two added frequency components forms. In order to conserve energy:

$$\omega_1 + \omega_2 = \omega_3 + \omega_4 \quad (1.16)$$

Phase matching is a key parameter that determines the FWM conversion efficiency. To generate high conversion efficiency, the phase-matching condition must be satisfied:

$$k = \Delta k_l + \Delta k_{nl} \approx 0 \quad (1.17)$$

Where, Δk_l is the linear phase mismatch related to dispersion condition, and $\Delta k_{nl} = 2\gamma P$ is the nonlinear phase mismatch which is related to self-phase modulation and cross-phase modulation [84,85].

In an optical fiber, it is the possibility of degenerate FWM when two photons with the same frequency ($w_1 = w_2$) are absorbed and two new photons ($w_3 = 2w_1 - w_2$ and $w_4 = 2w_2 - w_1$) are created [84,86].

FWM can be accomplished above lengthy spaces of single wave transmitting in situations of phase matching by selecting the suitable dispersion dependence of the fiber. Different approaches to achieve FWM by using several meters of high nonlinear fiber [15,20], photonic crystal fiber [87], dispersion shift fiber [20], and single-mode fiber [15] have been investigated. However, the employment of nanomaterial-based thin film to encourage FWM can be gainful in terms of dispersion. The dispersion of light-transmitting across a few micron-layers is impalpable and can be ignored. FWM efficiency depends on nonlinear coefficient γ , pump power P , and the effective fiber length L as [28]:

$$\eta_{FWM} \propto \gamma PL \quad (1.18)$$

More importantly, the nonlinear coefficient plays a dominant role in enhancing the FWM occurrence, which is governed by [28]:

$$\gamma = \frac{2\pi n_2}{A_{eff}\lambda} \quad (1.19)$$

1.8 Operating Regimes of Fiber Lasers

The fiber lasers have been classified according to temporal operation regimes to CW or pulsed operations. The pulsed operation can be achieved by Q-switching and mode-locking mechanisms. Q-switching is realized by modulating the intra-cavity losses and delivers fast pulses with high peak power and energy. But, in the state of mode-locking, multiple longitudinal modes are oscillating with phased locked as to produce ultrashort pulses in the range of nanosecond to femtosecond durations. Both regimes of pulses

can be achieved in fiber laser actively or passively [88]. The active one can be done generally utilizing a modulator (electro-optic modulator, acousto-optic modulator, semiconductor electro-absorption modulator, or Mach–Zehnder integrated-optic, etc.) that is often incorporated at one end of the laser cavity. Whereas a passive scheme is achieved via incorporating a saturable absorber (SA) within a laser cavity to modulate the laser cavity losses, so delivering short/ultrashort pulses [89].

Passive Q-switching laser generation bases on the SA to modulate the Quality factor (Q) within the laser cavity and generate pulses accordingly. Whereas the passive mode-locking scheme, instead, employs SA in a laser cavity as a mode-locker to generate ultra-short pulses, i.e. constant-phase relationship is made among the longitudinal modes of the resonant laser cavity. Fiber lasers are perfect for pulsed generation, owing to the broadband emission of doped fibers that permits producing short/ultra-pulses with tunable wavelength [5]. In the following subsection, the fundamentals behind fiber laser with CW and pulses based-SA generations as well as SA operation principles are addressed.

1.8.1 CW Fiber Laser Operation

Fiber lasers have been usually operating in the CW regime, in which the light intensity is fixed with time. Generally, the fiber laser is excited continuously and lasing in single or multiple transverse or longitudinal modes. As with other lasers kinds, particularly solid-state lasers, physics and theory of the CW fiber lasers regime are identical. But, the principal distinction that must be taken into consideration through the engineering and demonstration of CW fiber lasers is the nonlinear effects, for instance, the FWM, self-focusing, and Kerr effect. These nonlinear effects, generally, are based on the nonlinear refractive index generated due to the high-power intensity traveling through the fiber core. Furthermore, the damage threshold and thermal management of the silica fiber and side fiber

areas are too vital thru fiber laser engineering [5]. The greatest attempts regarding the demonstration of CW fiber lasers concentrate on power scaling, that is associated with the chosen high-power fiber coupled elements including pump couplers, isolators, and active fibers of proper core diameter and clad diameter, and numerical apertures [90]. CW fiber laser is one of the supreme significant and requisite lasers for various scientific, industrial, and military applications.

1.8.2 Passive Q-switched Mechanism

Q-switching is a method for producing optical short pulses with a time scale in the order of μs -ns and kHz repetition rates. This can be accomplished by modulating the Q-factor of the laser cavity. The Q-factor is described as the rate of energy accumulated in the oscillator/energy lavished in every roundtrip cycle. Accordingly, the Q-factor signifies the attribute of the laser cavity in terms of losses thereby the great Q-factor signals little intra-cavity loss and vice versa. The Q-factor of the cavity can be expressed in the equivalent form as [91,92]:

$$Q = 2\pi\nu t_c \quad (1.20)$$

where ν is a central frequency of laser and t_c is the cavity lifetime. Modulating the Q-factor of the cavity can be fulfilled by hosting an optical loss switcher within the laser cavity. A passive Q-switching is the method of self-adjusting the loss of the cavity and frequently lasing high-intensity pulses without external modulating devices. This method can be established by employing a thin film as SA inside the laser cavity to switch a CW output into a periodic pulse train. The process can be explained as follows. At the starting of laser generation, the huge cavity loss results in the great threshold of laser initiating, this leads to approximately zero output intensity. This due to the output laser is restrained by retaining Q-factor is held at a low value (high losses). Consequently, the energy accumulates in the gain medium via pumping of the active medium, and then raising the population inversion will be caused. Afterward, the Q-

factor is modulated to a high value (i.e. the cavity loss reduces suddenly) which a specific quantity of energy is collected in the oscillator. This saturates the active medium, leading the swift release of energy in the shape of laser pulses, which drains the gain and method iterates. Through cycling the loss switching, a series of short pulses are generated which called Q-switched pulses equivalent to the upper-level lifetime, as illustrated in Fig. (1.12) [93,94].

Then, the 3 dB pulse width (t_p) can be guessed by:

$$t_p = 4 \cdot 6 t_r / (g - k) \quad (1.21)$$

$$t_r = nL/c \quad (1.22)$$

Where : t_r is the round trip time, g is the gain, k is the resonator loss, L is the overall length of the laser cavity, and n is the refractive index at laser operating wavelength [92].

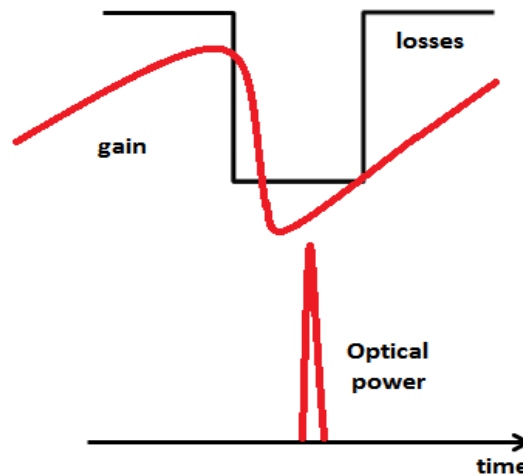


Fig. (1.12): Mechanism of Q-switching [92].

Passive Q-switching laser operation is usually more effective in terms of designing cost and works as it demands less control of the cavity factor. Passive Q-switching is mostly practical, simple, and does not demand any complex component and external trigger to force the modulator, however the pulse duration and repetition frequency of the emitted laser is power-reliant.

1.8.3 Mode-Locking Mechanism

Mode locking is a method of producing laser pulses with ultrashort duration. Mode-locking comprises cyclic modulation of cavity loss. As the cavity loss is modulated, all the longitudinal modes can easily oscillate in synchronism, in which the phases of all modes are locked in a fixed relationship via superposition of these longitudinal modes (constructive/destructive interference). Consequently, the coherent interference of a large number of longitudinal modes extending above a broad spectrum results in a very short pulse realization at every round-trip time. The frequency spacing among modes, gain bandwidth and the group velocity are all accountable for limiting the total of modes that can lase [95,96]. Fig. (1.13) shows three longitudinal modes in the laser cavity. Locking the phase of these multiple longitudinal modes in the laser cavity initiates constructive interference that consequently generates a whole field amplitude and intensity output, which has distinctive repetitive pulse character. Usually, the repetition rate of the mode-locking pulses is related to the cavity length, which can be given for the ring cavity as [96,97]:

$$PRR = \frac{1}{t_r} = \frac{c}{nL} \quad (1.23)$$

The cavity configuration for a mode-locked laser is frequently much further complex than a Q-switched laser owing to the that the ultrashort pulse generation is relevant to dispersion, and nonlinearity processes such as SPM, XPM, etc. [83,98]. As well as the spectral filtering influence of a limited gain saturation, gain bandwidth, and loss are contributed in the mode-locked generation [99].

Usually, Passive mode-locking is more operative and has more practical significance than the active method. Passive mode-locking can be accomplished by incorporating an SA with appropriate features into the laser cavity and is relying on the SAs and cavity characteristics. The SA initiates some loss to the intra-cavity laser emission that is comparatively

big for low intensities but significantly reduced for high intensities. Intended, a short pulse will produce a loss modulation while the high intensity (peak of the pulse) will saturate the SA, but low intensity (leading and trailing edges) would be absorbed by the SA. On the other side, the gain will enlarge the intensity of the pulse, but other low-intensity will have their losses more than their gain, and they will die out [96,100]. In general, the passive mode-locked laser based on SA can achieve very short pulses, since the recovery time of the SA can be very short [96], causing a quick loss modulation. Recently, the passive mode-locked laser based on SAs can generate ultrafast pulses in the range between nanoseconds to femtoseconds reliant on the SA parameters [101,102]. More details about the SA operation are in the next sub-section.

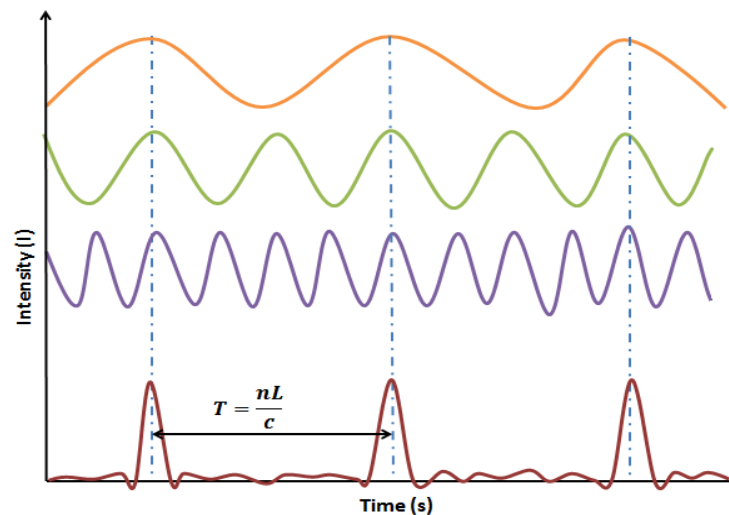


Fig. (1.13): Superposition of three longitudinal modes leading to repetitive pulse generation [103].

1.9 Saturable Absorbers

Saturable Absorber (SA) is a nonlinear optical substance that acts as a passive optical modulation system to convert CW output into a cyclic pulse train. It reveals an intensity-dependent transmission, which at a specific bleaching threshold, the transmission of the SA rises nonlinearly with intensity [49,104]. So that, SAs possess low transmission at low-intensity light while the transmission increases at a higher intensity of light.

This is owing to the occurrence that in this state of high intensity, more photons will be provided to the matter that has a limited number of electrons [105]. As the photon numbers become much greater than the electrons in the SA, the matter becomes opaque for a low-intensity light pulse and transparent for a high-intensity light pulse. Intended, the optical pulse peak propagates in fiber has big intensity and saturates (bleach) the SA further than its wings with low intensity. This also happens once multiple longitudinal modes are in synchronism and superpose constructively. So, the SA represents a key component of any passive pulsed laser structure to deliver self-starting and stable short/ultrashort pulses laser [96,106].

The basic principle of SA's function can be explained by employing a simplified two-electronic-level scheme, where SA is proportioned to gain saturation, as illustrated in Fig. (1.14) [49]. Firstly, the electrons in the ground state can annihilate photons once the energy of these photon is matching the difference between the two states then it will be exciting to higher energy state. When the intensity upsurges more, huge photo-excitation leads the upper state to be filled and blocking more absorption. Significantly the absorption saturates and discontinue and the matter turns into transparent to signal at high intensity. The key source of the SA is owing to state-filling. After a certain lifetime, the carriers at the upper level return to the ground state, and this routine continuously repeated. The two-level scheme is expressed as [107]:

$$T(I) = 1 - \Delta T \exp\left(\frac{-I}{I_s}\right) - \alpha_{ns} \quad (1.24)$$

where $T(I)$ is the nonlinear transmission, ΔT is the modulation depth, I is the incident intensity, I_s is the saturation intensity, and α_{ns} is the non-saturable absorption.

Generally, nonlinear absorption (SA) is related to the imaginary part of the third-order coefficient(χ^3), which can be given as:

$$\alpha_2 = \frac{3w_0}{4nc} \text{Im}(\chi^3) \quad (1.25)$$

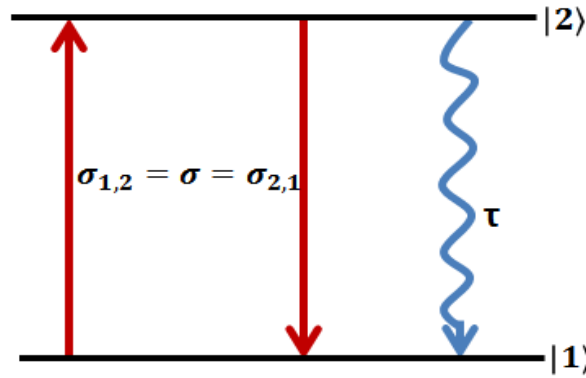


Fig. (1.14): Two-level saturable absorber [49].

The figure of merits for SAs is its absorption wavelength band, modulation depth, recovery time, saturation intensity, and damage threshold [102,108,109]. Worthy note, the pulse duration relies on the modulation depth and recovery time of the SA. Generally, for any substance to be suitable for SA:

1. The absorption wavelength of the SA band of operation must be harmonized with the gain bandwidth of the related lasing medium. Also, the substance should have naturalistic absorption that will induce nonlinear absorption at the operating wavelength [49].
2. The modulation depth is described as the maximum feasible modification of nonlinear transmission. According to Honninger *et al.* rules (1999) [110], the ΔT , saturation energy of both absorption (E_A), and the laser active material (E_L) and the energy within the cavity (E_p) have a large influence on the pulse operation regime. Relating to these rules, the laser will deliver mode-locked pulses if criteria $E_p > E_L E_A \Delta T$ must be satisfied. Otherwise, Q-switched pulses will be accomplished. Also, rising the ΔT beyond the Q-switched regime, the laser will only deliver CW laser and by raising it more the laser will not function [88,110]. Interestingly, the pulse operation regime can be adjusting by controlling the modulation depth, which represents one of the most effective factors that

determining pulse dynamics. Generally, for the passively Q-switched fiber laser, the pulse width is related to modulation depth as given by the expression [111]:

$$t_p = \frac{3 \cdot 25 t_r}{\Delta T} \quad (1.26)$$

While, in the case of mode-locked, the influence on the pulse dynamics depends on the SA if it slows or fasts SA, which the pulse duration can be estimated from [112]:

$$\text{- Slow SA: } t_p = \frac{1 \cdot 07}{\Delta f_g} \sqrt{\frac{g}{\Delta T}} \quad (1.27)$$

$$\text{- Fast SA: } t_p = \frac{0 \cdot 9}{\Delta f_g} \sqrt{\frac{g}{\Delta T}} \quad (1.28)$$

Where Δf_g is the FWHM gain bandwidth, and g is the power gain coefficient that equivalent the total cavity losses.

3. The Recovery time puts a limit on the switching time of the system that can influence the time duration of the attainable pulses. The electrons after excitation to the upper state must go back to the ground state during the cavity roundtrip time so that the circulating pulse could again confront a similar or significant quantity of nonlinear absorption [88].
4. The demanded light intensity in the system to saturate the absorption is denoting the saturation intensity. In other words, the saturation intensity signifies the light intensity that essential to decrease the absorption to 1/2 of its unbleached quantity. It is expressed as [113]:

$$I_s = \frac{h\nu}{\sigma\tau} \quad (1.29)$$

where $h\nu$ is the photon energy, σ is the absorption cross-section of the SA at the operation wavelength, and τ is the relaxation time.

5. The damage threshold is the maximum light intensity that the system can withstand before damage happen.

6. Besides these factors that determining pulse dynamics, other features are also vital in selecting SAs like the environmental stability and the fabrication easiness, and its cost. As well, it must be easy to incorporate within the laser cavity. The SA should be prepared in a certain technique that performs easily with the designing of the laser cavity [105]. Generally, drop-casting and spin coating are the most used techniques to fabricate the SA. On the other side, in fiber lasers, SA is usually blended with a host material such as PVA, dehydrated at room temperature and a tiny part is integrated between two fiber ferrule [114–116].

Finally, short/ultrashort laser based on SAs has gained enormous concentration owing to the compact scheme, beam quality, adaptable application, cost-effectiveness, and excellent compatibility. Particularly, SA is a key component for adjusting the laser cavity loss, the discovery and investigation for a new one should not be ignored.

1.9.1 Characterization of Saturable Absorber

In general, precise linear, spectroscopic, and nonlinear characterizations are the key essential step to verify if a specified material can be considering as a prospective optical modulator. These characters rely on the chemical composition, the thickness of the fabricated thin film, and the structure of the synthesis SA. The important factors of a SA influence in defining the output performance for fiber laser are linear absorption coefficient, band-gap, nonlinear absorption coefficient, nonlinear refractive coefficient, nonlinear transmission (which is known as the modulation depth, non-saturable absorption, and saturation intensity), and the absorber recovery time.

The linear absorption coefficient can be estimated from the spectrophotometer data using the following expression [117]:

$$\alpha = \left[(2.303) \times \left(\frac{A}{2} \right) \right] / L_s \quad (1.30)$$

where α is the linear absorption coefficient, A is the absorbance, L_s is the thickness of the thin film.

While band-gap energy of the sample can be determined utilizing the Tauc relation [117]:

$$\alpha h\nu = a(h\nu - E_g)^q \quad (1.31)$$

where $h\nu$ is the energy (eV), E_g is the band-gap energy, and a is a constant. The factor q is denoting the nature of transition and equal to $1/2$ for the direct bandgap and 2 for the indirect bandgap [118].

The nonlinear absorption and refraction coefficients can be determined using the z-scan technique introduced by Sheik Bahae *et al.* [119]. The Z-scan technique is dependent on the spatial beam broadening and narrowing of the Gaussian beam in far-field owing to the occurrence of optical nonlinearity. This experiment consists of an intense laser with suitable wavelength, beam diameter, and intensity which is utilized as the excitation source of this experiment. Then the laser beam focused utilizing a specific lens into the sample. The sample must be fixed on a linear, translation stage to shifting it around the focus of the lens to investigate the variation of the pulsed laser intensity. Also, this setup has an aperture with a suitable pinhole size was settled after the samples to study closed aperture signals. The schematic diagram of the Z-scan technique is depicted in Fig. (1.15). The alteration in the transmitted laser intensity is verified utilizing an optical detector as a function of the sample location.

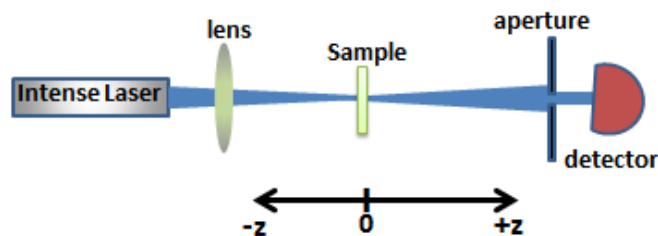


Fig. (1.15): Z-scan experimental setup [119].

Finally, the nonlinear transmission curve for the SA can be investigated using the twin detector method (as shown in Fig. (1.16)). The

scheme is based on the principle differential detection, which consists of an intense laser with suitable wavelength and intensity, which is used as the pump light. Then, a 50:50 fiber coupler is used to split the laser power between a sensing arm and a reference arm, and separate photodiodes are used to measure each. The two powers are then measured. The sense beam propagates via the specimen to be measured, while the reference beam is uninfluenced (i.e. to observe the power). By constantly adapting the attenuator, the transmitted power is registered versus incident optical power on the SA film. With no alteration in sample transmission, the two transmitted powers are nulled. Lastly, the dataset from a twin-detector examination can be well fitted with a two-level SA model. From this experiment, it can be determined the modulation depth that is defined as the difference in the transmission between the maximum and minimum values (Fig.(1.17)). The α_{ns} should be preserved at small value and it initiates from scattering and absorption of the SA material itself [120,121].

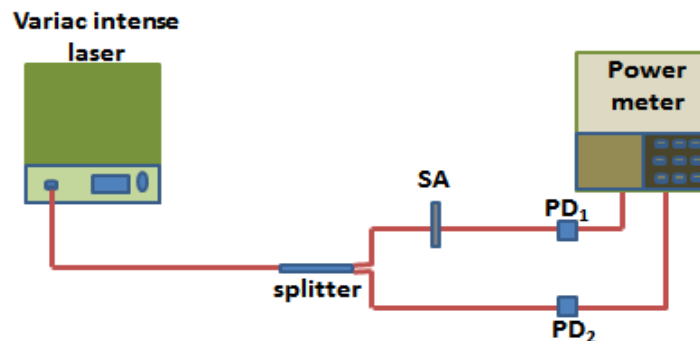


Fig. (1.16): Twin detector setup [113].

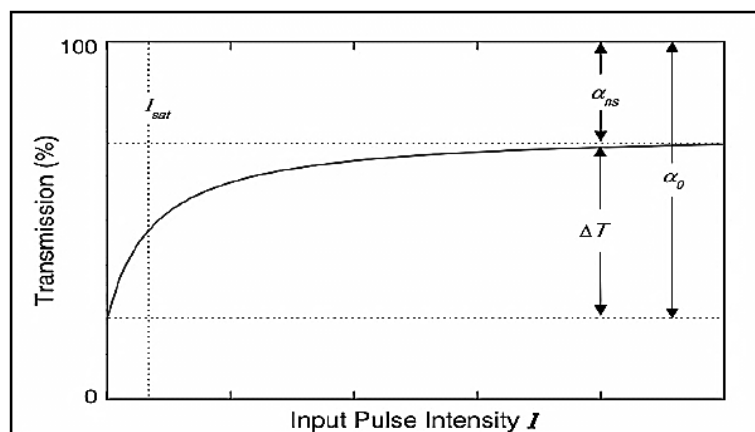


Fig. (1.17): Bleaching curve of the two-level system[107].

1.10 Thin Film Materials

The multiwavelength passive pulse fiber laser can be realized utilizing various nonlinear nanomaterials hosted in various dielectric materials. Nonlinear absorption effects e.g., saturable [122,123] and multiphoton [124,125] absorption are widely existing in nanoparticle-based material. In general, these nonlinear effects are particularly reliant on the type, size, and shape of the nanomaterials themselves [26,27]. In this regard, the exploration of new nanostructured materials is one of the crucial issues of modern science and technology. A range of these materials such as: carbon-based nanomaterial [126–128], metal oxide (e.g. copper oxide, aluminum oxide, zinc oxide, nickel oxide, titanium dioxide, Ferro-oxide, and tungsten oxide) [11,28,39–42,124–129], and semiconducting transition metal dichalcogenides [35–38] have been proposed for use in photonic and optoelectronic applications.

Furthermore, different freestanding polymer films were exploited in the assembly of SA thin film for instance Polyvinyl Alcohol (PVA), Poly (methyl methacrylate) (PMMA), and Polyethylene glycol (PEO). These are transparent polymer, which possess a refractive index comparable to that of silica glass of the fiber. Also, numerous surfactants were employed as dispersing agents deposited into a solution to augment the separation of nanoparticles and to restrain clumping. For instance, sodium dodecyl sulfate (SDS). Generally, the improvement of linear and nonlinear optical parameters such as linear/nonlinear refractive index, linear/nonlinear absorption coefficient, third-order nonlinear susceptibility as well as optical band gap of the nanomaterial materials is the chief goal for considering the optoelectronic matters [135]. These parameters can be improved and tuned through the varying of the geometrical shape of the nanoparticles and their distribution in a host matrix [136]. The subsequent sub-sections describe in detail the materials utilized in this research and their features.

1.10.1 Pure Metal (Nickel Nanoparticles)

Transition metal nanoparticles have attracted much interest due to their distinguished optical properties such as large third-order nonlinearity, broadband plasmon resonance absorption, and ultrafast response time, which make them have potential applications in electronic and optic applications [137]. Many research groups have reported the employment of metal NPs as an SA in fiber laser-like silver, gold, aluminum, and copper [18,29,39,40,138]. Ni is one of the transition metals, having a high response to the magnetic field, catalysis, good electrical properties, good thermal conductivity, large surface area, strong electron mobility, high surface energy levels, good absorption coefficient, broadband near-infrared (NIR) absorption/emission, abundance in nature, environmental friendliness, operational simplicity, and cost-effective advantages [139–144]. It has enticed increasing concentration owing to its possible/prospective use in a variety of applications such as optical filters, sensors, electronics, imaging, magnetic storage, energy technology, biochemical, biomedical, ferrofluids applications, etc. [140,145,146]. Yet, some attention was giving to Ni-NPs in the field of ultrafast optics. Recently, the linear and nonlinear properties were stated by Soliman et al. [147]. The absorption spectra of the Ni-PVA thin films for different Ni concentration are depicted in Fig. (1.18). It was clear that the absorption of these films rises as the Ni-NPs concentration rises too, and the absorption peak shifts toward longer wavelengths (redshift).

Furthermore, the absorption of all films does not vary almost at longer wavelengths. On the other side, the same authors were estimated the nonlinear refractive index and third-order nonlinear coefficient using Wemple–Di Domenico single-oscillator model, which n_2 equal to $\sim 10^{-7}$, while $\chi \sim 10^{-8}$. Also, the band gap of the PVA matrix was varied with the Ni-NPs concentration in the thin film which increases as the concentration

decreases, then the indirect bandgap ranged between 3.4-4.8 eV while the direct bandgap is between the range of 5.15-5.8 eV [147].

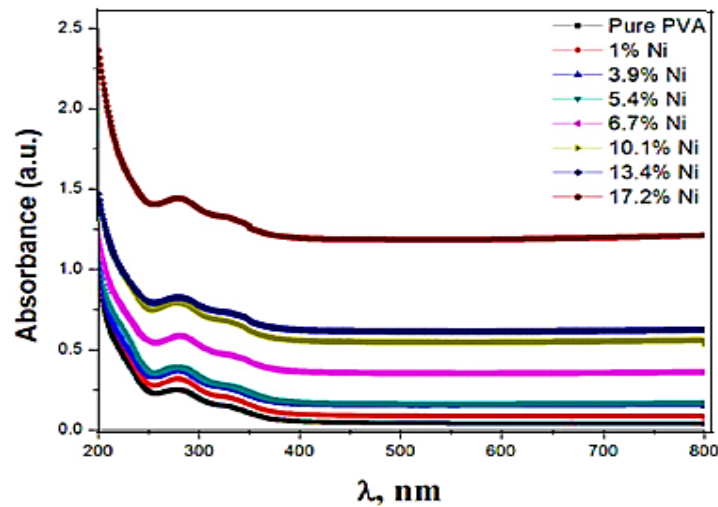


Fig. (1.18): Absorbance of Ni-PVA at different concentrations of Ni NPs [147].

1.10.2 Transition Metal Oxide (Iron Oxide " Hematite")

The importance in the preparation of oxide nanoparticles has persisted to develop over the latest decades due to their distinctive optical, electrical, and magnetic features [1, 2]. Iron oxides look another brilliant and efficient choice for a short pulse and multiwavelength generation. Iron oxides, usually existent with different chemical forms such as Fe_3O_4 , and Fe_2O_3 , which are representing transition-metal oxides with strong electron-electron correlation and electron-phonon coupling [148]. Generally, Iron oxides gain more significance to be utilized as optical modulator inside fiber laser owing to their promising optical features, such as great third-order nonlinear coefficient, broadband absorption, broadband surface plasmon resonance, swift response time, and low saturation intensity [129,134,149–153]. Notably, Hematite ($\alpha\text{-Fe}_2\text{O}_3$) is considered as the greatest stable iron oxide and environmental friendliness semiconductor with low cost, biocompatibility, and non-toxicity [154]. The $\alpha\text{-Fe}_2\text{O}_3$ -NPs reveals good physical and paramagnetic property, high thermodynamically stable structure, extreme catalytic feature, with a bandgap ranged between

2.0–2.2 eV [155,156]. Generally, their features rely mostly on the geometry of the particles as well the dispersion of the substances, which several surveys mentioned that the controlling hematite nanoparticles properties depend fully on size, morphology, the surfactant, pH solution, the concentration of reactant, temperature, and timely reaction, and so on [154,156].

Owing to their intriguing features, Fe_2O_3 -NPs have enticed an immense deal of research attention and applied in different fields of application such as bio-applications, catalysis, sensing, etc. [154,157]. Some previous reports proven that the Fe_2O_3 reveals a considerable nonlinear response with a good high third absorption coefficient of $\sim 10^{-10}$ m/W and a relatively third-order nonlinear susceptibility in orders of 10^{-11} to 10^{-8} esu [150,151], polarization-insensitive with a response time in tens of ps, this makes it an innovative optical modulator competitor for nonlinear usages [152,158–161]. Remarkably, the linear and nonlinear optical properties of Fe_2O_3 -NPs film can be adjusted by tuning their geometrical shape, size and the composite film materials [138,149,162]. The linear and nonlinear transmission of Fe_2O_3 /PVA thin film is depicted in Fig.(1.19). As the real and imaginary part of third-order susceptibility is often associated with nonlinear refraction and nonlinear absorption, therefore it can have exploited their features in the nonlinear photonic system, especially the multiwavelength pulse laser generations. Despite this, only one work proposed the use of Fe_2O_3 -NPs as broadband SA and can be employed as an optical modulator for producing Q-switching laser at $\sim 1 \mu\text{m}$, $1.5 \mu\text{m}$, and $2 \mu\text{m}$ regions [149]. But, Fe_2O_3 has gained less focus and stayed undiscovered matter for a multiwavelength generation.

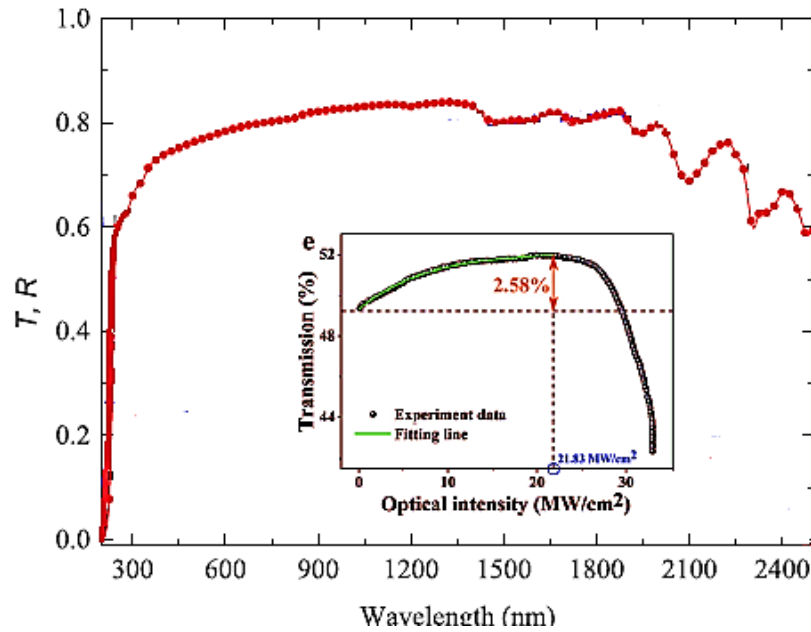


Fig. (1.19): The linear and nonlinear transmission of $\text{Fe}_2\text{O}_3/\text{PVA}$ thin film [149,156].

1.10.3 Dielectric (Silica Nanoparticles)

The reaction of every dielectric to intense light turns into nonlinear behavior, and Silica nanoparticles (SiO_2 -NPs) are no exception. On a basic idea, the source of nonlinear behavior corresponds to the anharmonic activity of bound electrons under the impact of an exciting field. SiO_2 attracts significant interest in the optoelectronics proposed studies. SiO_2 is one of the most motivating materials that offer a certain characteristic to be employed a good optical activity with a large bandwidth [163,164]. Despite SiO_2 nanoparticles exhibit a good optical limitation based on nonlinear light scattering at which this feature is particularly effective for mitigating unwanted laser intensity instabilities as well as for pulse and beam reshaping [165]. But it still exhibits low refractive and absorption optical nonlinearity coefficients with about $10^{-17} \text{ m}^2/\text{W}$ and $10^{-11} \text{ m}/\text{W}$ [166]. Generally, silica as nanocomposite with different nanomaterials was employed as an efficient nonlinear material with a fiber laser cavity [167–170]. Still, pure SiO_2 -NPs has gained less concentration and remained undiscovered matter as optical modulator inside fiber laser for pulsed and

multiwavelength generation. Usually, SiO_2 can be utilized as a polymer film, which the reason for that originates mostly from its excellent thermal stability and the promising strength features of the resulting composites.

1.11 Literature Survey

Multiwavelength generations as nonlinear phenomena have been established by many methods. Previous reports concerning multiwavelength operations in $1\mu\text{m}$ and $1.5\mu\text{m}$ wavelength regions are reviewed and epitomized in the subsequent survey in chronological order.

Multiwavelength EDFL based on FWM using graphene was reported by **Luo et al. in 2011**, [28]. Eleven lines were realized at room temperature with a SNR of 57 dB as the pump power attained 178 mW. Sagnac loop filter was combined with EDFL based on ring cavity and line spacing of 0.54 nm was achieved. EDFL was working at the CW regime without Q-switching or mode-locking pulses.

Later in 2011, Luo et al. [171] also proved FWM induced by graphene in EDFL and YDFL by monitoring the spectral broadening. At $1.5\mu\text{m}$ region, a stable twenty-three lines were produced with a Q-switching pulse possessing a spacing of 0.2 nm. The minimum pulse width, maximum repetition rate, and maximum pulse energy were $2.5\mu\text{s}$, 63kHz, and 72.5 nJ, respectively. Whereas in the $1\mu\text{m}$ band, five lines were detected with simultaneous Q-switching pulses possessing a duration of 3 μs and a repetition rate of 56.2 kHz.

Multiwavelength EDFL based on a nonlinear amplifying loop mirror and assistance by un-pumped EDF was demonstrated by **Liu et al. in 2012** [14]. As the pump power reached 70 mW and with adjusting the polarization controllers, fifty-one lines output within 3dB bandwidth. But as the pump power increased to 110 mW, the output decays in terms of lines number and SNR, this is due to the saturation influence of the ASE absorption via the un-pumped EDF with big intra-cavity power.

In 2013, Wang et al. [15] proposed multiwavelength generation in EDF based on FWM in SMF and HNL. A multiwavelength comb was generated with the assistance of FWM that enhance the mitigation of the mode competition resulting from the homogenous gain broadening in the ring cavity in Er ions. At maximum pumping power of 300 mW, five lasing lines were generated utilizing the single-mode fiber. For comparison, the SMF was substituted by 110m high nonlinear fiber and at 300 mW seven lines were observed. The power fluctuation in HNL and SMF were 0.18, and 3.18 dB, respectively, this confirming that FWM induced by HNL has more stability.

In 2014, Liu et al. [172] demonstrated multiwavelength EDFL based on a microfiber knot resonator. This structure comprised 5 m of EDF, 85 m of highly nonlinear fiber, and a knot of ring diameter of ~ 2.84 mm which was fabricated using 5 μm diameter of SMF microfibers. Via adjusting the polarization controller at a pump power of 275 mW, eleven channel lines with channel spacing of 0.184-nm were achieved.

In 2015, Xueyuan et al. [12] reported multiwavelength generation in a 1 μm region based on SRS. This structure involves a fiber loop mirror (FLM) encompassing a 5.5 m of polarization maintaining, and a 1 km-long passive fiber. At 1W, multiwavelength laser output with 35 nm bandwidth, 0.75 nm line spacing, and OSNR ~ 10 dB is obtained.

Xu-De Wang et al. in 2015 [169] utilized gold nanorod/ SiO_2 core-shell configuration as SA for delivered fs pulse in a fiber laser.

Rashid et al. in 2016 [34] reported on the generation of dual-wavelength with Q-switching operation regime from YDFL based on the black phosphorus. The system comprised a D-shaped fiber as a wavelength-selective filter. The dual lasing lines were at 1038.68 and 1042.05 nm. Besides, the repetition rate tuned from 52.52 to 58.73 kHz with the rise of the pump power. The lowest pulse width was about 1.16 μs while the greatest pulse energy of 2.09 nJ was realized.

Xude Wang et al. in 2016 [167] utilized the silica-encased gold nanorods as an efficient optical modulator inside the fiber laser to generate wavelength-switchable with femtosecond pulses in the 1.5 μm region.

Then, the generation of dual-wavelength passively Q-Switched YDFL based on aluminum oxide nanoparticles was demonstrated by **Sarah et al. in 2017** [131]. The dual-wavelength pulse generation was observed at 1050 and 1060.7 nm as the pump power reached 80 mW. When the pump power increased from the threshold to 300 mW, the repetition rate tuned from 16.23 to 59 kHz, and the pulse width was reduced from 19 to 6 μs .

Later in 2018, Sarah et al. [43] proposed the generation of triple-wavelength passively Q-switched YDFL based on zinc oxide nanoparticles. The output laser was tuned from single, dual to triple wavelengths as the pump power increases 143, 250, and 330 mW, respectively. These triple wavelengths were observed at 1054.7, 1058, and 1065.9 nm. Also, this laser delivered pulses with maximum pulse repetition and shortest pulse duration of 87.9 kHz and 2.7 μs , respectively.

Also later in the same year (2018), Sarah et al. [129] reported on the dual-wavelength passively Q-switched YDFL based on Fe_3O_4 -nanoparticle. The dual-wavelength was observed at 1048.9 and 1053.3 nm. While the pulses output was realized at a threshold pump of 80 mW with the highest output pulse energy, repetition rate, and lowest pulse width of 38.8 nJ, of 73.4 kHz and 3.4 μs , respectively.

In 2018, Dong et al. [149] synthesized Fe_2O_3 NPs by a co-precipitation technique, then the prepared NPs was incorporated into PVA host to form Fe_2O_3 -PVA thin film. The prepared thin film revealed broadband saturable absorption with a modulation depth of 2.83%. This thin film was employed as SA to achieved single wavelength, Q-switched operations in a YDFL, an EDFL, and a TDFL. The minimum pulse duration was about 2.2, 5.7, and 3.5 at 1038 nm, 1557 nm, and 1942 nm, respectively.

In March 2019, Salman et al. [18] reported on the generation of multiwavelength *Q*-switched EDFL based on aluminum nanoparticles as SA, and a Sagnac loop filter. By simply adjusting the polarization controller, eleven lasing channels in the *Q*-switching regime were achieved with a line spacing of 0.48 nm and SNR of ~ 30 dB. This laser delivered the lowest pulse width of 2.36 μ s and the highest pulse repetition rate of 33.45 kHz at a maximum pump power of 300 mW.

Shi Li et al. in 2019 [173] reported on the generation of a dual-wavelength soliton mode-locked EDFL utilizing SnS₂ nanoparticles. The laser generates two lasing lines at 1536.7 and 1562.6 nm, with a pulse duration of 5.3 ps. The dual lines were simply achieved at low threshold power of 75 mW.

Salman et al. in 2019 [11] demonstrated a passively *Q*-switched multiwavelength EDFL applying tungsten oxide nanoparticles as SA combined with a Sagnac loop filter. The high optical nonlinearity of tungsten oxide nanoparticles was induced dual influence in the cavity, an SA which induced pulsed operation and four-wave mixing effects which assist of multiwavelength generation. The laser delivered 15 emission lines with a spacing of 0.48 nm and pulses with the lowest pulse width of 4.24 μ s and the highest repetition rate of 52.49 kHz at a higher pump power of 300 mW.

In July of 2019, Pengfei et al. [174] reported the generation of Raman Mode-Locked YDFL based on MoS₂ as an optical modulator. By adjusting the polarization states, stable single- or dual-pulse Raman soliton operations were obtained at a threshold pump power of 220 mW. Two lasing lines with central wavelengths of 1029.2 and 1082.5 nm, and mode-locked with pulse repartition rate of 683.5 kHz, SNR of ~ 50 dB, 15.96 ns pulse duration, and good optical efficiency of 5.16 were achieved.

In 2020, Salman et al. [24] reported the emission of three wavelengths in passively *Q*-switched YDFL employing SA based on

tungsten oxide nanoparticles. The triple wavelength operation was located at 1030.01, 1032.122, and 1036.21 nm, respectively. In the Q-switching regime, the laser-produced the largest repetition rate of 71.3 kHz and a minimum pulse width of 2.92 μs .

In 2020, CHEN et al. [175] applying the Fe_3O_4 nanoparticle as an optical modulator inside YDFL. This cavity consisted of a section of 5 m YDF as a linear gain has 4dBm^{-1} absorption coefficient at 975 nm and the suspension of Fe_3O_4 nanoparticle with a modulation depth of 6.6% at $1\mu\text{m}$ spectral region as a nonlinear absorber. This laser operated at a pump threshold of 100 mW, but as the pump power increased to 150 mW, and by justly regulating the polarization controller state, the system exhibited three various laser dynamics (CW, Q-switched, and Q-switched mode-locked operation). Also, the lasing spectrum switched from dual-wavelength to single wavelength and then triple wavelength, respectively. The triple lasing lines were observed around $1.08\mu\text{m}$, while the Q-switched pulse operation at 150 mW possesses a pulse width of 4 μs and a repetition frequency of 16.1 kHz. But at the laser switched to Q-switched mode-locked operation, the pulse repetition rate became equal to 11.1 MHz, while the pulse width was less than 900 ps.

In 2020, Sun et al. [176] utilized a piece of unpumped erbium–ytterbium co-doped fiber as an SA to generate a multiwavelength Q-switched fiber laser in the region of $1.5\mu\text{m}$. Ten wavelengths with line spacing of 100 GHz and 200 GHz were achieved. A wave shaper filter was used in this experiment to tune the wavelength-spacing. In the Q-switching regime, the repetition rate tuned between the range of $\sim 15\text{-}55$ kHz and pulse duration tuned between the ranges of $\sim 7\text{-}2\mu\text{s}$ in the excited power range of 17.6-140 mW.

In 2020, Wenxiong Sun et al. [177] utilized Bismuthene nanosheets as SA inside EDFL. A dual-wavelength located at 1531.6 and 1543.2 nm,

and 52nd harmonic mode-locked with a repetition frequency of 208 MHz and a pulse width of 1.58 ps realized as the pump power reached 402 mW.

In 2020, Xude Wang et al. [168] employed silica-encased gold nanorods to generate mode-locked soliton, harmonic soliton, dual-wavelength bound soliton, and soliton bundle.

In 2020 S. Liu et al. WS₂/SiO₂ was utilized as SA to generate an ultrafast pulse in both YDFL and EDFL [170].

1.12 Aim of the Work

The main objective of this research is to implemented compact, ring cavity, multiwavelength fiber lasers using active nonlinear technique. The research is validated via the characterization, and examining the nonlinear functionality of various new materials namely Ni NPs, Fe₂O₃ NPs, and SiO₂ NPs at 1 μ m and 1.5 μ m spectral regions using both YDFL and EDFL.

1.12 Thesis Outline

This thesis comprises of five chapters, starting from the introduction chapter as **Chapter one** including the chief basic and technological ideas that employ in this thesis. The remainder of the thesis is organized as follow:

Chapter Two focuses on the construction and the experimental implementation of YDFL and EDFL with ring cavity design operated in CW regimes. The experimental laser output characteristics including output power and slope efficiency and the laser output performance are discussed. Besides, it explores the preparation and characterization of the SA's: Ni-NPs, Fe₂O₃ NPs, SiO₂ NPs, and Fe₂O₃/SiO₂ nanocomposite as a new type of nonlinear nanomaterial.

Throughout **Chapter Three**, the successful assembled SAs that integrated into a YDFL ring cavity to generate multiwavelength operation

are given. The spectral and temporal output laser characteristics are reported and discussed.

In **Chapter Four** multiwavelength operation, as well as CW and pulsed operation in EDFL based on the different assembled SAs, are reported and discussed.

Chapter Five highlights the general conclusions based on the found results. Then, some suggestions and recommendations to enhance and develop this work in the future are given.

CHAPTER TWO

EXPERIMENTAL DESIGN OF

RING CAVITY DOPED FIBER

LASER AND SATURABLE

ABSORBERS FABRICATION

CHAPTER TWO

EXPERIMENTAL DESIGN OF FIBER LASER RING CAVITY AND SATURABLE ABSORBERS SYNTHESIS

2.1 Introduction

Planning an effective fiber laser demands a full understanding of its functioning under various operation conditions. Fiber lasers are usually engineered utilizing general numerical formulations and optimizations. Theoretical and analytical studies of such laser are extremely vital to prevent time and cost consuming of trial and error experimental methods. It is frequently the case that a wide range of factors demands to be covered to determine the optimal factors for good performance. An analytical solution is particularly useful for multi-factor optimization in engineering a fiber laser. The optimization factors contain the selection of the fiber geometry mainly the length, rare earth doping concentration, mirror and so on. In this chapter, three-ring cavities of fiber lasers (2-YDFL and EDFL) workings in the CW regime were proposed and experimentally demonstrated. Based on the rate equations given in chapter one, numerical estimates are executed by utilizing MATLAB 12 software to determine the cavity parameter. These methods studied the influences of pump power and active fiber length on the output power for CW operation mode in YDFL and EDFL ring cavities. To support these theoretical studies, experimental examinations are done to clarify the laser performance and to more examine the laser output. The theoretical model gave into consideration the losses made by the optical components, fiber cord patch (FC/PC) connectors, and the splicing practice.

Additionally, on the road to implementation a stable multiwavelength fiber laser, three kinds of nanomaterials are utilized separately to assemble seven nonlinear samples to act simultaneously as an optical modulator for both YDFL and EDFL with ring cavity. These are Ni NPs, Fe₂O₃ NPs, and

SiO₂ NPs. Two various techniques are utilized for optical modulator assembly: sonication-assisted liquid-phase agitation and drop-cast technique. Because of the synthesis easiness, nonexistence of costly apparatus, and less fabrication stages, they are facile and affordable ways to prepare the optical modulator. Then, the linear and nonlinear absorption of these nonlinear materials are characterized using spectrophotometer, Z-scan techniques and balance twin detector technique. The structure of chapter two is presented in Fig. (2.1).

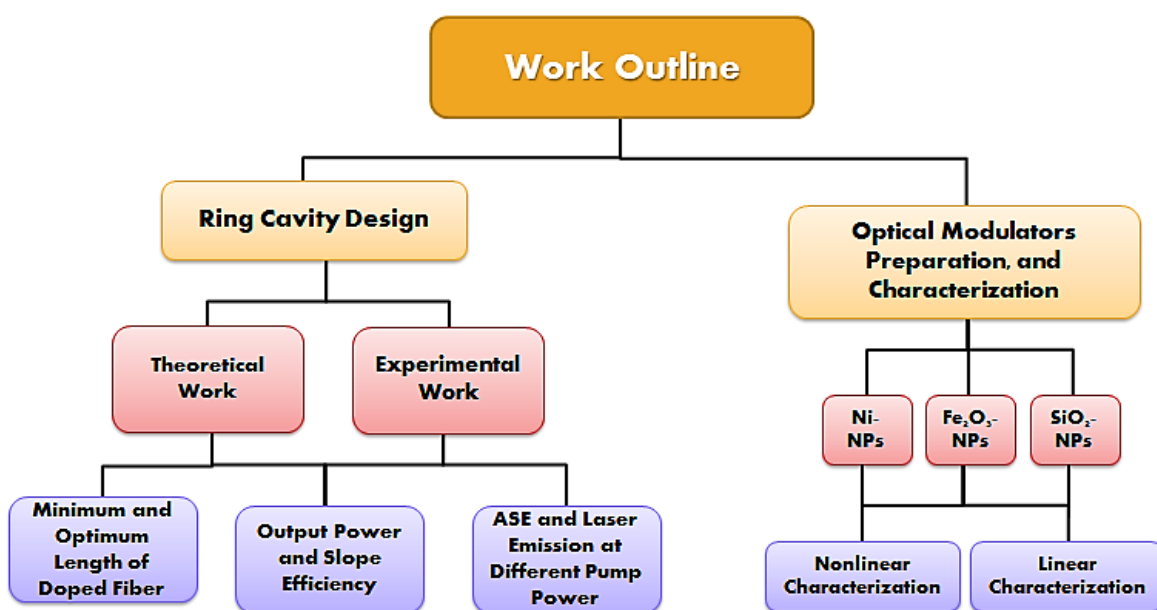


Fig.(2.1): The structure of chapter two.

2.2 Theoretical Design Consideration

In our work, three cavities are employed to generate multiwavelength from both YDFL and EDFL. Two of them were previously planned by our group team. The other one has been carried out using a short length of high absorbed doped fiber. The theoretical configuration of the suggested typical ring fiber laser (YDFL/EDFL) is portrayed in Fig. (2.2).

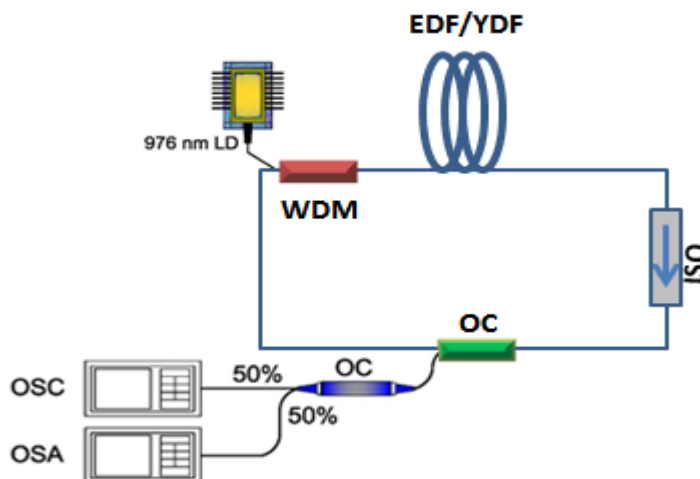


Fig.(2.2): Schematic diagram of the fiber ring laser.

2.2.1 CW-YDFL

Two schemes of YDFL ring cavities are implemented; the first is based on Yb^{3+} concentration of 326000 ppm and ~ 250 dB/m absorption coefficient at 976 nm pump wavelength, while the second based on Yb^{3+} concentration of 16300 ppm and ~ 1200 dB/m absorption coefficient of at 976 nm pump wavelength. Generally, the optimal length of the active fiber is dependent on the doping concentration of the Yb/Er ion, central wavelength, and absorption coefficient at the pump and emission wavelength as well as the pump power. Consequently, optimal length of active fiber is determined according to all these parameters.

The characterization and the optimum length of the first ones were reported by Sarah et al. [178], which was found that the slope efficiency ~ 4.3 % if the optimum length of the active medium was ~ 1.5 m. The other one has been carried out according to the input factors are as follows: The exciting source is a laser diode (LD) with a center wavelength of 976 nm and a maximum power of 300 mW. Table (2.1) provides the active medium factors of YDF considered in the theoretical modules. The overall loss within the ring cavity symbolizes the sum of the insertion loss of each of the intra-cavity optical elements, splicing losses, and FC/PC connectors. So, the proposed overall

cavity loss is about 4 dB. The simulated output of the CW-laser is estimated utilizing a 10 % port of 90:10 output coupler.

To design CW-YDFL ring cavities, the minimum and optimum length of YDF are determined theoretically using Eq.(1.9) and Eq.(1.10). The results show that at 300 mW pump power the minimum and optimum lengths of YDF were 0.11 and 1.226 m respectively, as shown in Fig.(2.3).

Table (2.1): Ytterbium-doped single-mode fiber specifications.

Parameter	Value	Parameter	Value
λ_p (nm)	976	λ_s (nm)	1064
α_p (dB/m)	1200	α_s (dB/m)	19
$\sigma_p^{ab,em}$ (m ²)	$25 \cdot 10^{-25}$	Numerical Aperture	0.2
σ_s^{ab} (m ²)	$1.25 \cdot 10^{-25}$	σ_s^{em} (m ²)	$2.36 \cdot 10^{-25}$
Core Diameter (μm)	4	Cladding Diameter (μm)	125
Mode Field Diameter (μm)	4.4	Yb ³⁺ Concentration (ppm)	16300

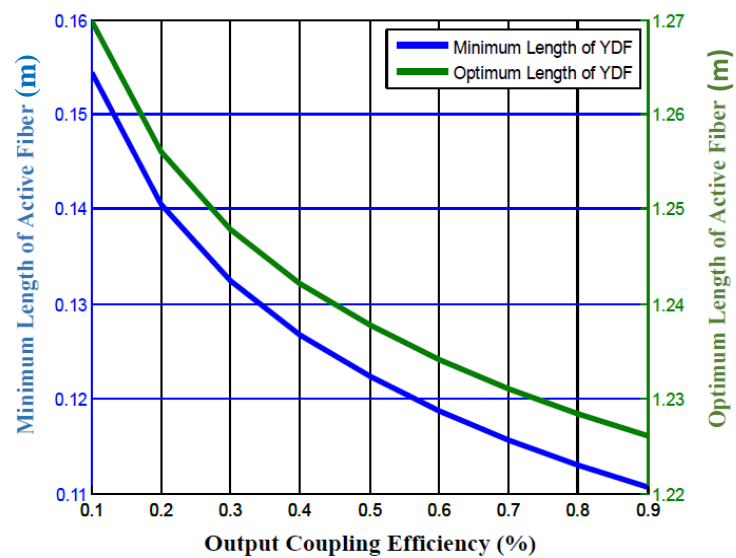


Fig.(2.3): The shortest lengths and the optimum lengths of YDF as a function of different coupling efficiencies.

After that, all other fiber laser parameters were preserved to be constant to investigate the effect of fiber length on the output power only. Fig.(2.4) explains the function of laser output power versus the active fiber length. From this figure, it is obvious that before such a minimum length of 0.11 m, there is no laser output even if launching a high pump power to active fiber. At these fiber lengths, the gain is little and the loss in the cavity is still bigger than the gain. The other range on length in Fig.(2.4) the laser output power upsurges up to a specific length (optimum length) of the fiber, to be exact 1.226 m. Then for lengthier lengths, the losses override the gain, and attenuation is predominating, so the output power will become reduced. Therefore, the effective length of YDF that must be applied is the value between the minimum and optimum lengths.

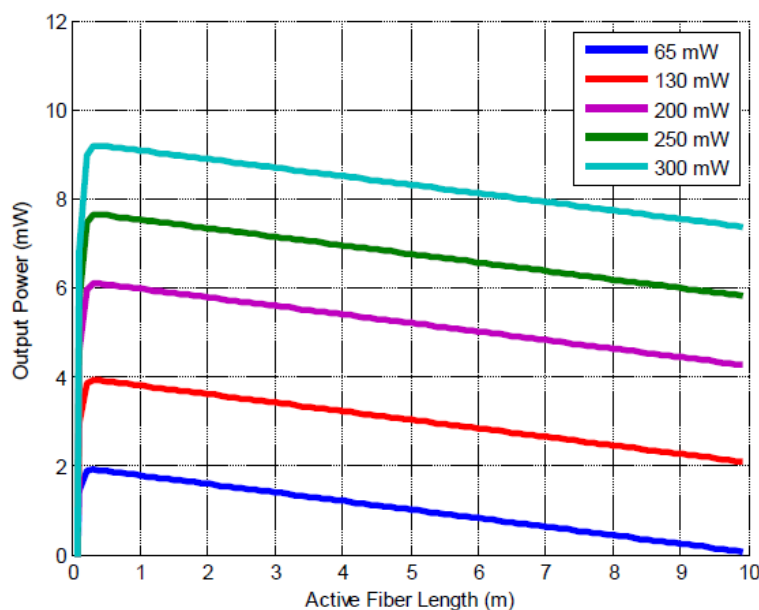


Fig.(2.4): The output power as a function of active fiber length for YDF.

In this setup, highly absorbed with ytterbium ions of 16300 ppm is desired as the gain medium owing to its excellent features, like low pump threshold which the great threshold of light-induced darkening. Additionally, it possesses intense absorption which shortens the overall cavity length and

consequently decreases the resonator loss; reduce resonator round-trip time, in addition to shorten the generated pulse width.

2.2.2 CW-EDFL

The EDFL is also built. The ring cavity comprises of 2 m length of EDF (Liekki ER-4/125) as a gain medium with a doping concentration of 3000 ppm, 0.2 core numerical aperture, 27 dB/m absorption coefficient at 975 nm, and 6.5 μm mode field diameter at 1550 nm. EDF is pumped by a 975 nm laser diode with a maximum output power of 300 mW through a 980/1550 wavelength division multiplexer. A Polarization-independent isolator is used to ensure the unidirectional operation. The output coupler with 90/10 is used which 10% portion of laser power is coupled out from the cavity.

The characterization and the optimum length of the first ones were reported by Wurood A. et al. [179], Dunya Z. et al. [180], and Sarah et al. [178]. They have found that the slope efficiency $\sim 6.7\%$ if the optimum length of the active medium was ~ 2 m.

2.3 Experimental Setups and the characterization of the system

Firstly, transmission spectra of the doped fibers are studied separately before splicing them to the ring cavity. These spectra represent the characteristics of the doped fiber and typically well-known as the amplified spontaneous emission (ASE) profile of doped fiber. Fig. (2.5) illustrates the principal optical elements utilized for measuring the ASE of doped fiber gain media, which can be simply executed by opening the loop of the ring cavity and connecting lead-out of the active medium to ISO. For examining the YDF's ASE spectrum, the setup is constructed utilizing optical elements that are compatible with the 980/1060 nm operation spectra. But, to examine the ASE spectrum of EDF, all optical elements that utilized are fitted with 980/1550 nm operation spectra.

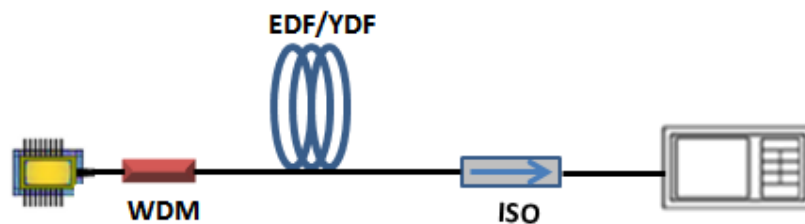


Fig. (2.5): Experimental setup for ASE measurement of EDF/YDF.

Then, the ring cavity has been accomplished by incorporating a fiber coupler into the setup as displayed in Fig. (2.2). The planned ring cavity encompasses a segment of doped fiber (YDF or EDF) that acts as the gain media, which is pumped via WDM coupler, a polarization-independent isolator to enforces the unidirectional laser propagation in the ring cavity and to suppress any unabsorbed pump light out of the system, a fused 10/90 fiber-based output coupler was employed to draw out about 10% of the laser from the oscillator for laser property measurement and allow 90% of the energy for further amplification. A 976 nm semiconductor laser with highest pump power of 300 mW is employed as exciting device. The laser output was examined OSA (Yokogawa AQ6370C, 0.02 nm resolution) for spectral analysis and a 1 GHz Oscilloscope (Tektronix MDO3102) for temporal analysis. The EXFO FPM-300 power meter was used to measure the average output power.

The ASE of the YDF based on 1.5 m and EDF based on 2 m were reported in [178–180]. While, the ASE of YDF based on 0.6 m is illustrated in the next sub-section.

2.3.1 YDF emission spectra

Firstly, the ASE spectra of 60 cm YDF at various exciting powers were examined, as depicted in Fig. (2.6). These results show that the ASE bandwidth can be more broadened as the exciting power rises. Also, the profile of the ASE spectrum is altered with the pump power alteration. At

exciting power of ~23 mW, the profile of ASE spectra possesses a bell curve form. As the exciting power boosted, the spectra increased slightly rising before plateauing and next falling again. This is owing to the reabsorption of ASE emission by the high concentration of Yb^{3+} . At 250 mW excited power, it can be observed that the ASE spectrum has a one peak around 1030 nm. Furthermore, it was perceived that the pump signal at 980 nm is entirely absorbed by the 0.6 m of YDF, which there is no any sign of excited power detected on OSA.

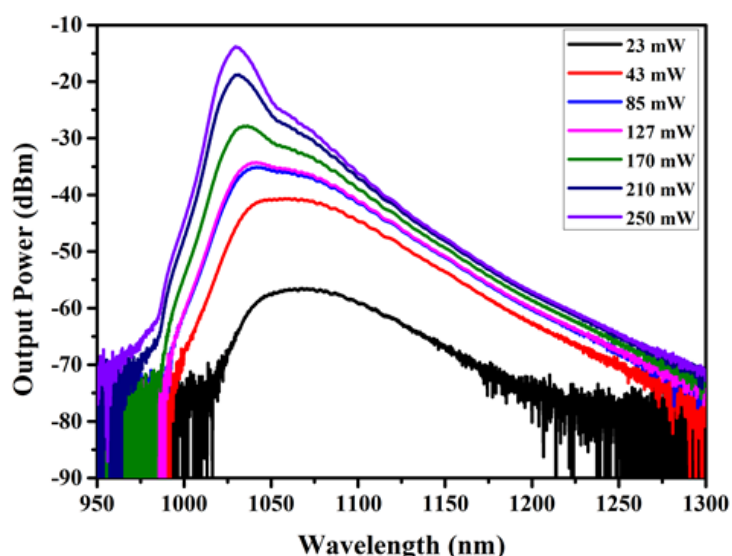


Fig.(2.6): Measured ASE of YDF at different input pumping powers.

Thereafter, the output port of ISO was connected with the input port of OC, and the 90 % port of OC was connected to the signal input port of WDM. Accordingly, the all-fiber ring cavity is closed and the CW-YDFL operation began at the input excited power threshold of 65 mW. No lasing signal was detected below 65 mW. The optical spectrum of CW-YDFL is illustrated in Fig. (2.7). The center wavelength at the threshold pump power was 1057.43 nm, while the FWHM and optical signal to noise ratio (SNR) was 0.11 nm and 30.4 dB respectively. While the center wavelength at the pump power of about 127 mW was 1058.25 nm with FWHM and SNR were 0.21 nm and 41.4 dB respectively.

Additionally, it is obvious that the peak output power of the laser is higher and sharper contrasted with the ASE signal. This is due to the ASE signal is amplified via each round trip. Besides, the center lasing wavelength is located in the region of ASE's peak center, which the ASE spectrum can be supposed as a gain band of the generated laser. So, as the cavity is closed (complete the ring cycle) the laser action will be beginning. Also, the modes closed to the peak of ASE are stronger and gain furthermore amplification.

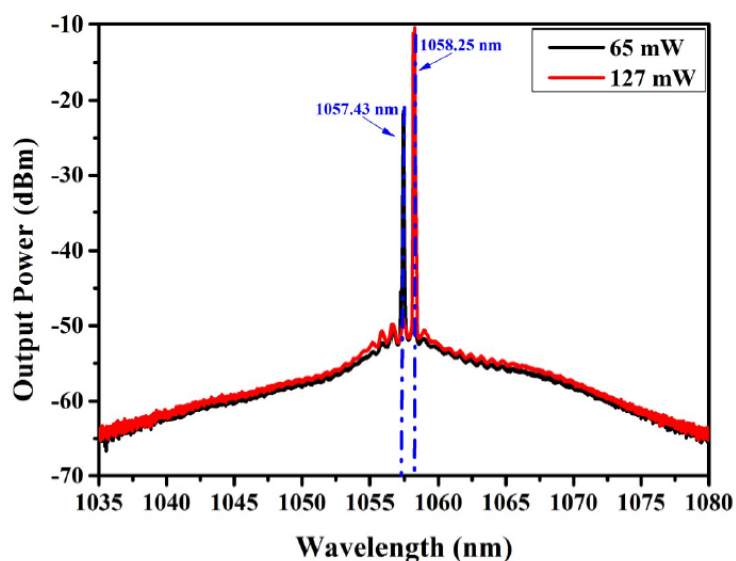


Fig.(2.7): Measured optical spectrum of the CW-YDFL at the threshold of 65 mW and at 127 mW input pump power.

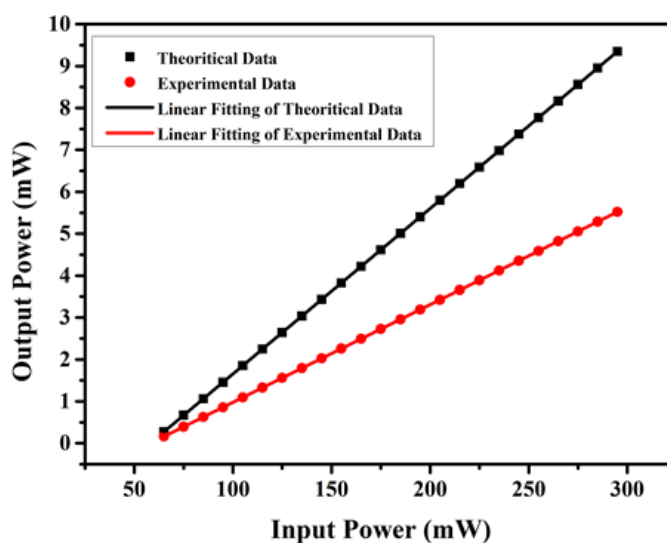


Fig. (2.8): Comparison between theoretical and experimental results of CW-YDFL output power.

Afterward, the laser output power as a function of the input excited power was measured; this relation is shown in Fig.(2.8). This figure shows the comparison between the theoretical and experimental results of the output laser power. The calculated theoretical and experimental slope efficiencies were 3.95% and 2.33%, respectively.

2.4 Preparation, and Characterization of optical modulators

Ni, SiO₂, and Fe₂O₃ NPs were utilized to assemble optical modulators for a multiwavelength fiber laser. These samples were prepared in two forms: as nano-suspensions and/or freestanding PVA composite films. During the fabrication of the optical modulator based nanomaterials, the operation spectrum range, recovery time as well modulation depth have great relevance in the present application, so, all these parameters will be determined or estimated. The following sections contain the film preparation and characterization of all mentioned materials.

2.4.1 Ni-NPs optical modulator

To prepare Ni-NPs in the suspension form, sodium dodecyl sulfate (SDS) aqueous solution was first prepared by adding 1 g of SDS to 100 ml of deionized water and mixed thoroughly for 15 min; SDS was used as a negatively charged surfactant to functionalize the nanoparticle and prevent further aggregation and surface binding. Then, Ni-NPs (from Hongwu International Group Ltd) with 99.9% purity and particle size of 40–60 nm were dispersed in SDS solution with different volume ratios (0.75% and 1%). The aqueous solution was further processed by an ultrasonic homogenizer to obtain a controlled dispersion with high homogeneity. To waste unwarranted hotness during sonication, the sample container was submerged in a water bath. The prepared surfactant-dispersed solution exhibited good stability reaching up to several days without any sedimentation of particle agglomeration. This fabrication process is proven to be simple and effortless.

While the freestanding Ni-PVA nanocomposites were prepared using casting methods in four main steps. Since Ni-NPs cannot be dissolved in water directly, this type of nanoparticles was functionalized firstly by using SDS surfactant to be dispersed easily in water. Then, a PVA aqueous solution with a ratio of ~10 mg/mL was also prepared. After that, the Ni-NPs fluid was further dispersed in a PVA aqueous solution at the volume ratio of 1:1 for 10 hours using an ultrasonic device. The resultant suspension is dropped into a clean petri dish and kept to dehydrate at room temperature for 4-6 days until Ni-polymer film is formed.

Precise linear, spectroscopic, and nonlinear characterizations are the key essential step to verify if a specified material can be considering as a prospective optical modulator or switcher. The absorption spectra (200-2000 nm) of prepared Ni-based optical modulator samples were investigated using a spectrophotometer. Due to plasmon resonance arising from the metallic characteristics, Ni-NPs exhibits a broadband absorption over a wide range covering UV to NIR regions with a notable absorption in the 1 and 1.5 μm region as depicted in Fig. (2.9).

From the data of absorption spectrum, the value of the optical band-gap is appraised via applying the Tauc relation. Fig.(2.10) displays the plot of $(\alpha_0 h\nu)^2$ versus $h\nu$, in which the optical band-gap of the prepared sample is achieved by linear extrapolating the Tauc plot. From this plot, the Ni-matrix samples reveal a sharp absorption edge, and a narrow range for the band-gap value is estimated as 3.25-5.1 eV. Noteworthy, strong spin-orbit coupling in assisted with high thermal conductivity of Ni results in absence of excited state absorption, up-conversion mechanism, minimize re-absorption loss and thermal phonon vibrations during lasing action [27,38]. The linear parameters (including the absorption coefficient, absorption cross-section, band-gap

energy, insertion loss, and the recovery time) of the three samples of Ni-NPs are shown in Table (2.3).

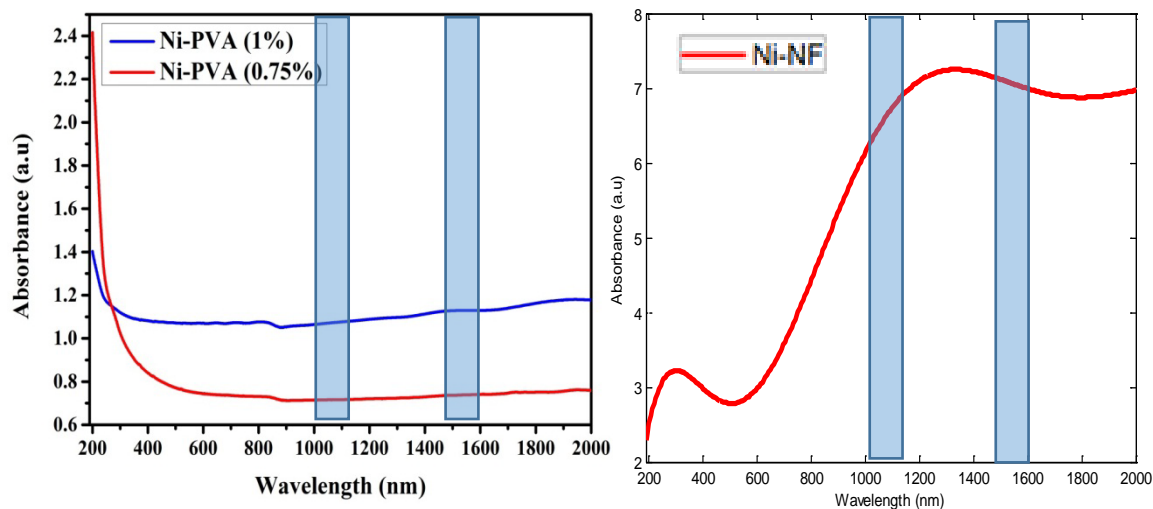


Fig. (2.9): The absorption spectrum of Ni-NPs in the range 200-2000 nm (highlighted is lasing operation region).

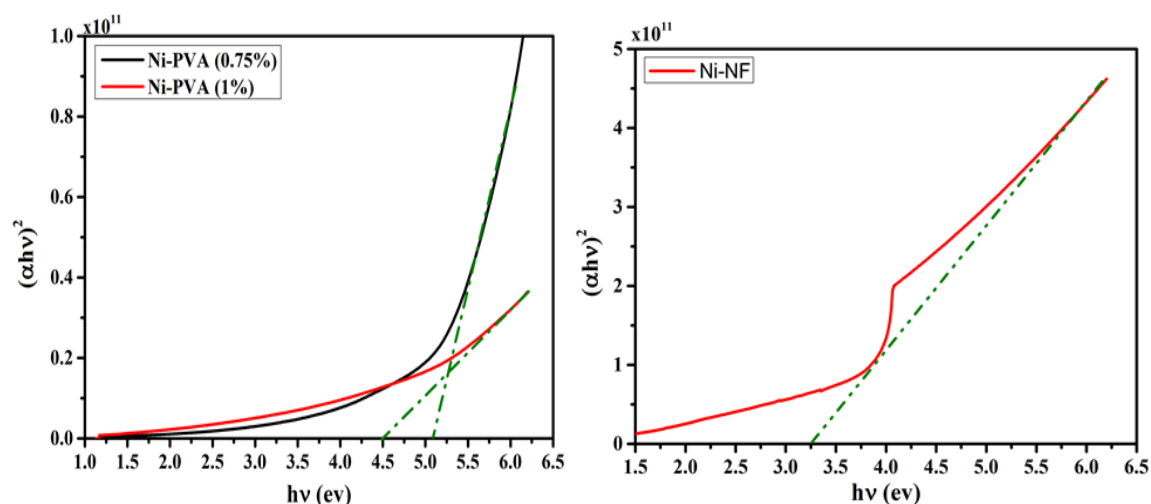


Fig. (2.10): Tauc plot of the three samples of Ni-NPs.

Furthermore, the nonlinear optical properties of Ni-NPs suspension were characterized using the Z-scan technique. A CW Nd: YAG laser with a power of 100 mW, beam diameter < 1.5 mm and beam divergence of 1.2 mrad was used in this experiment. A 10 cm focal length lens was used to focus the laser beam into the sample. The Ni-NPs suspension was put in a cuvette of 1 mm path length to use in this study. The closed aperture and open aperture were used for the determination of the nonlinear refractive index (n_2)

and the nonlinear absorption coefficient (β). The Z-scan profile for both closed aperture and open aperture is depicted in Fig.(2.11). From this figure, Ni-NPs suspension shows a wide range of nonlinear properties such as self-defocusing and saturable absorption.

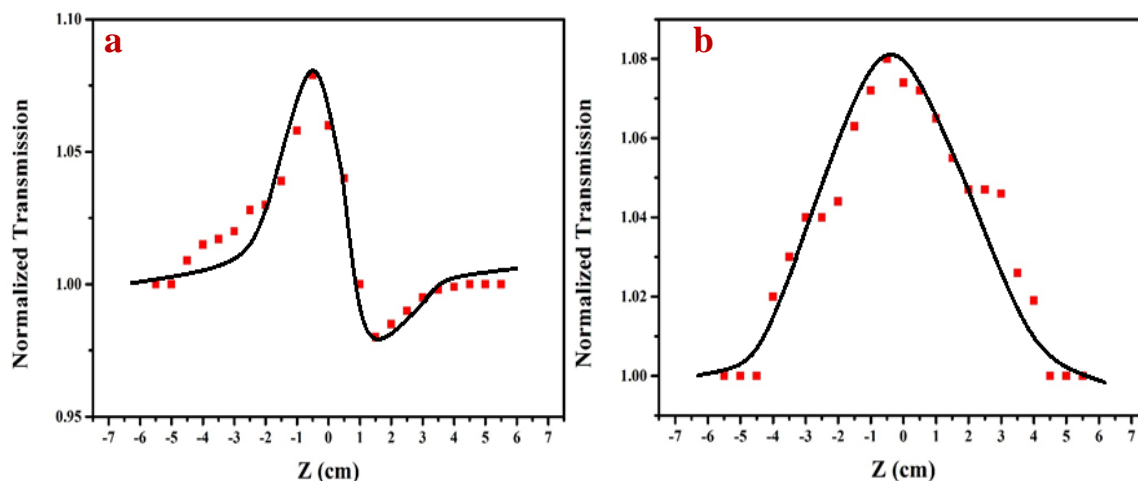


Fig.(2.11): Normalized transmission of (a) closed aperture, (b) open aperture.

Table (2.3): The linear parameters of Ni-NPs samples.

Sample	α at 1030 nm (cm^{-1})	σ_a at 1030 nm (cm^2) $\times 10^{-16}$	α at 1550 nm (cm^{-1})	σ_a at 1550 nm (cm^2) $\times 10^{-16}$	E_g (ev)	τ (ps)	Insertion loss (dB)	L_s (μm)
Ni-NF (0.35)	28.57	0.273	97.05	0.927	3.25	3	1.227	-
Ni-PVA/ 0.75%	39.248	1.7497	40.526	1.8066	5.1	5.43	2.63	21
Ni-PVA/ 1%	87.887	2.9385	92.911	3.1064	4.5	39.81	2.372	14

Moreover, the intensity-dependent optical absorption of Ni-PVA film was investigated by a twin-detector measurement technique. The resultant characteristic of various Ni-NPs samples is depicted in Fig.(2.12). From these nonlinear measurements, it is found that Ni-NPs samples exhibit a significant

saturable absorption property with a very large nonlinear absorption coefficient, nonlinear refractive index coefficient, and strong 3rd susceptibility. The nonlinear properties of Ni-NPs samples are shown in Table (2.4).

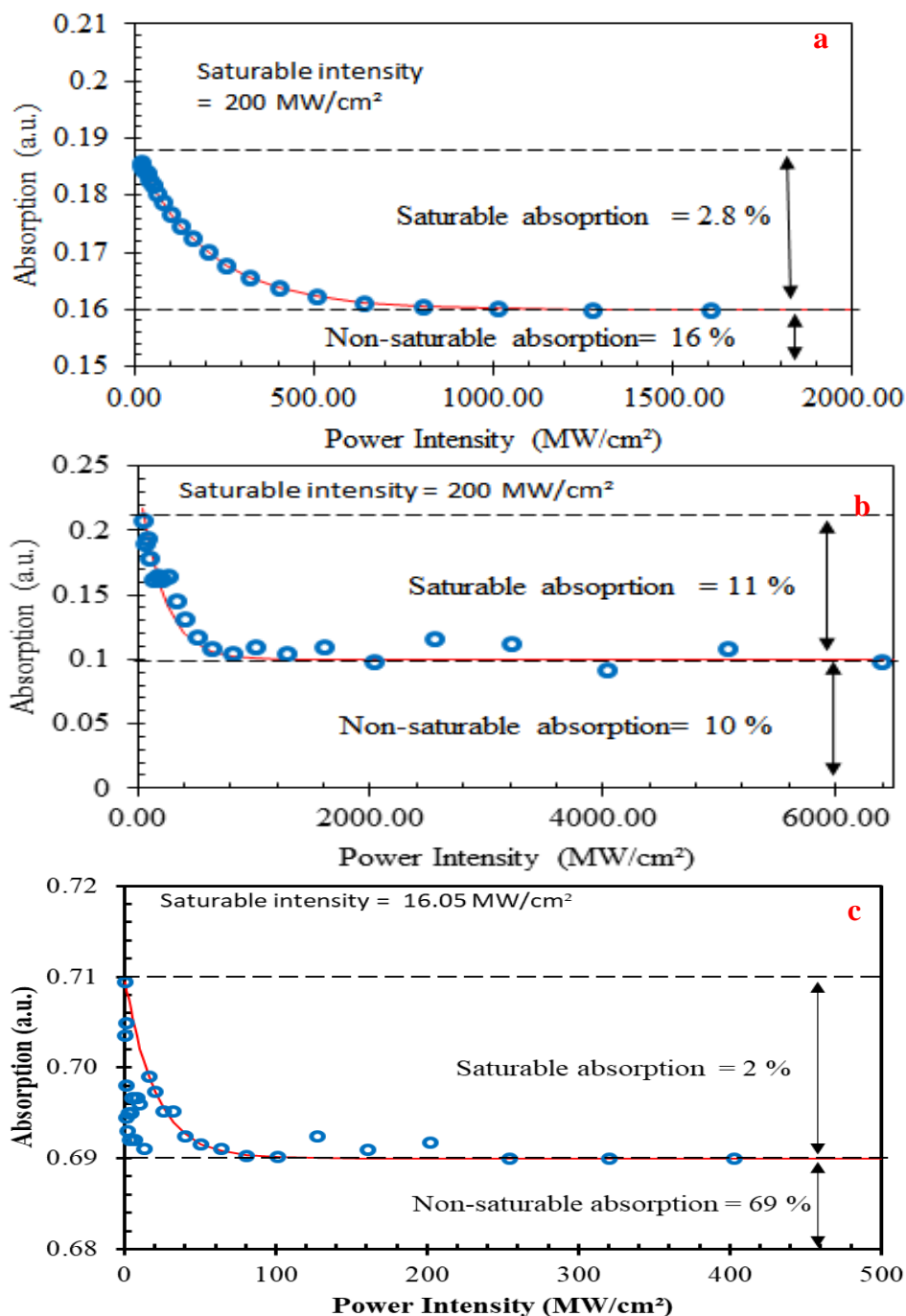


Fig.(2.12): Nonlinear absorption of Ni-NPs for: (a) Ni-NF of 75% volume ratio, (b) Ni:PVA film (0.75% volume ratio), and (c) Ni:PVA film (1% volume ratio).

Table (2.4): The nonlinear parameters of Ni-NPs samples.

Sample	ΔT (%)	α_{ns} (%)	I_s (MW/cm ²)	α_2 cm/W	n_2 (cm ² /W)	χ^3 (esu)
Ni-NF	2.8	16	200	-0.012	-5.83x10 ⁻⁸	1.29x10 ⁻⁵
Ni-PVA/ 0.75%	11	10	200	-	-	-
Ni-PVA/ 1%	2	69	16.05	-	-	-

Notably, Ni-NPs has a reasonably large saturation intensity, which this property attributed to the transition metals behavior [181]. The recovery time is estimated to be in the range between 3-39.81 ps. These parameters indicate that Ni-NPs is suitable to be used as an optical modulator for enhancing the stability of multiwavelength oscillation as well as for a fast and ultrafast pulse generation, which is superior to many other nonlinear materials.

The optical absorption can mainly be accomplished from the plasmonic characteristic of the metallic Ni-NPs. The nonlinear optical influence of metallic Ni-NPs material can be described as follows: as the pump light incident on these metallic NPs, the free electrons are collectively excited. Owing to the massive amplification of the local electric field at the surface of Ni-NPs, the nonlinear optical absorption can be improved and subsequently results in excited electrons up to the conductive band until it reaches saturation [45,182]. The transition action of an electron in the NIR region is a key role in both linear absorptions as well as nonlinear absorption phenomena.

2.4.2 Fe₂O₃ optical modulator

Firstly, Fe₂O₃ optical modulator was prepared in a water-based magnetic fluid using sonication assisted liquid-phase agitation. Fe₂O₃-NPs (nanoshell) possess 99 % purity with an average diameter of about 45 nm dispersed in SDS solution with a 3 mg/ml concentration to process the NPs

and avert further aggregation as well as surface binding. The aqueous solution was further functionalized using an ultrasonic homogenizer to get a regulated dispersion with great homogeneity. To waste unwarranted hotness during sonication, the sample container was submerged in a water bath. Finally, the resulting rust orange solution was kept in a plastic container for future using.

Later, Fe_2O_3 optical modulator was also assembled as a freestanding thin film using drop-casting process followed by dehydration. 5 mg of Fe_2O_3 -NPs was mixed to 5 ml of polymer solution (concentration of 10 mg/ml) giving a mass to the volume ratio of 1 mg/ml. The mixture was agitated under a sonication homogenizer for 2 h. Next, the prepared nano-suspension was dropped into a plastic plate and let to dehydrate at the ambient room temperature for 4 days to form a uniformly distributed freestanding film. Subsequently, the resultant Fe_2O_3 /PVA film was removed from the dish and chopped into small parts to be employed as an optical modulator for a fiber laser. The deposition of Fe_2O_3 film by drop-casting is a simple physical method without complex equipment needed.

After that, the absorption spectra (200-2000 nm) of prepared Fe_2O_3 -based optical modulator samples were investigated using a spectrophotometer, as shown in Fig (2.13). The prepared samples exhibit good absorption in the 1 μm and 1.5 μm .

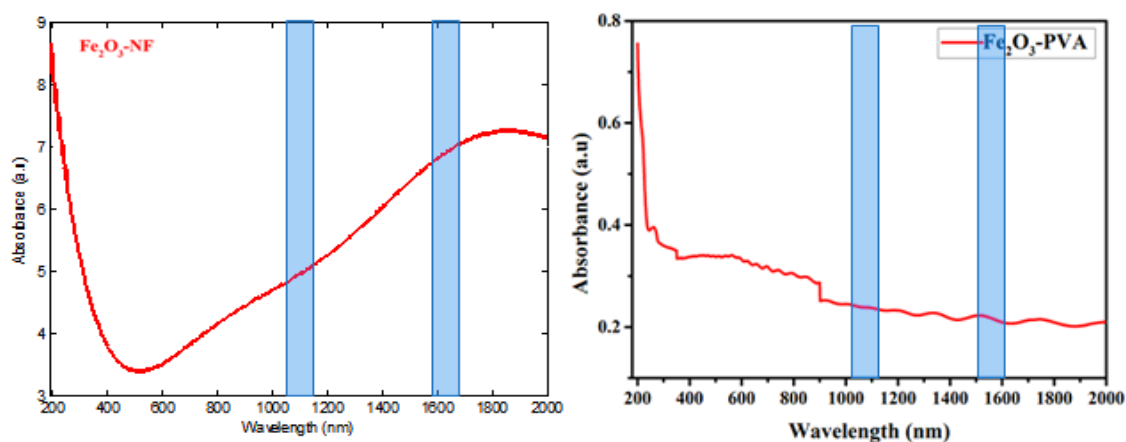


Fig. (2.13): The absorption spectrum of prepared Fe_2O_3 -NPs samples in the range 200-2000 nm (highlighted is lasing operation region).

The absorption coefficient and absorption cross-section of each of these samples at the two regions are illustrated in Table (2.5). Moreover, the band-gap energy also has been estimated using the Tauc relation. Fig.(2.14) illustrates the Tauc plot at $n=2$. From this plot, the Fe_2O_3 -NPs samples reveal a wide adsorption edge, and a wide range for the band-gap value is estimated as 3.5-4.96 eV.

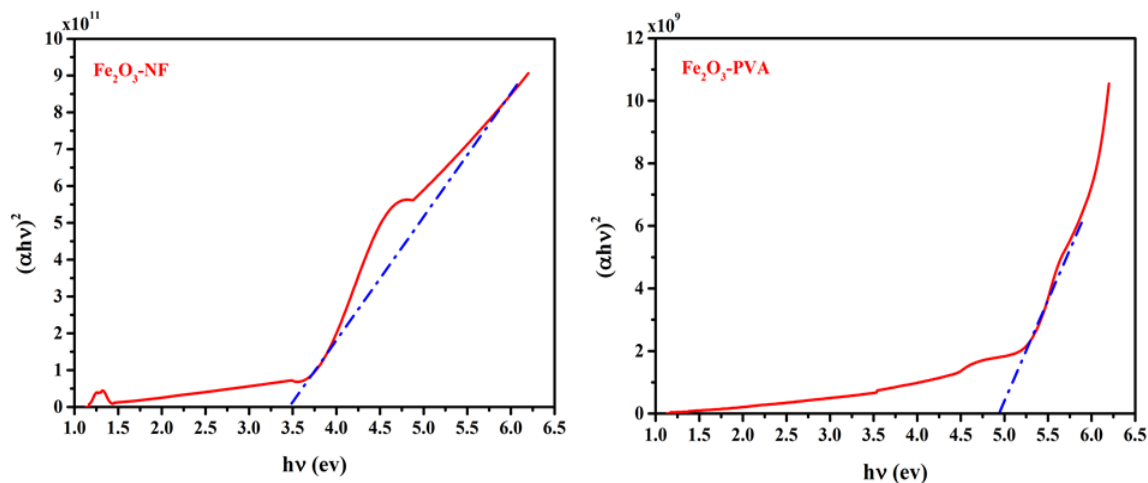


Fig.(2.14): Tauc plot of Fe_2O_3 -NPs.

Table (2.5): The linear parameters of Fe_2O_3 -NPs samples.

Sample	α at 1030 nm (cm^{-1})	σ_a at 1030 nm (cm^2) $\times 10^{-18}$	α at 1550 nm (cm^{-1})	σ_a at 1550 nm (cm^2) $\times 10^{-18}$	E_g (eV)	τ (ns)	Insertion loss (dB)	L_s (μm)
Fe_2O_3 -NF	535.7	512	806.1	770	3.5	1.94	1.327	-
Fe_2O_3 -PVA	91.3	0.611	168.04	1.124	4.96	1.66	4.02	15

Thereafter, the nonlinear features of the Fe_2O_3 -based optical modulator samples were explored using the Z-scan and twin-detector measurement techniques. The Z-scan technique was done using a nanosecond Nd: YAG with Gaussian profile, beam divergence of 0.711 mrad, beam diameter <1.5 mm, and maximum energy of 140 mJ as the excitation source of this

experiment. This laser was focused into the sample utilizing a convex lens of 20 cm focal length. In the closed-aperture examination part, the prepared sample is moved laterally the z-axis and the transmitted energy was recorded through a narrow aperture in the distant-area. The Z-scan resultant characteristics of closed/open apertures for the prepared Fe_2O_3 -NPs sample are depicted in Fig.(2.15). While the intensity-dependent optical absorptions of various Fe_2O_3 -NPs samples are depicted in Fig.(2.16). From these nonlinear measurements, it is found that Fe_2O_3 -NPs samples exhibit a significant saturable absorption property with a good nonlinear absorption coefficient, large nonlinear refractive index, and strong 3rd susceptibility. Additionally, the recovery time is estimated to be in the range between 1.66-194 ns. The linear and nonlinear properties of prepared Fe_2O_3 -NPs samples are shown in Table (2.5) and Table (2.6), respectively.

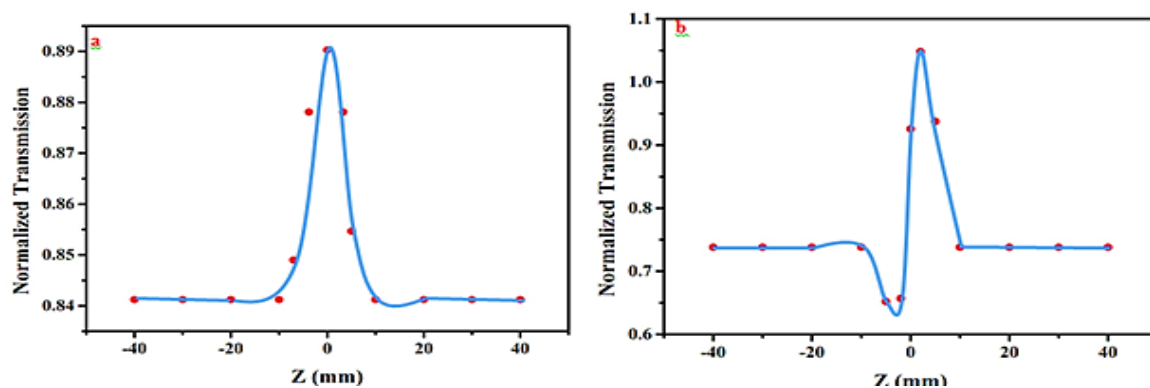


Fig.(2.15): Normalized transmission of (a) open aperture, (b) closed aperture.

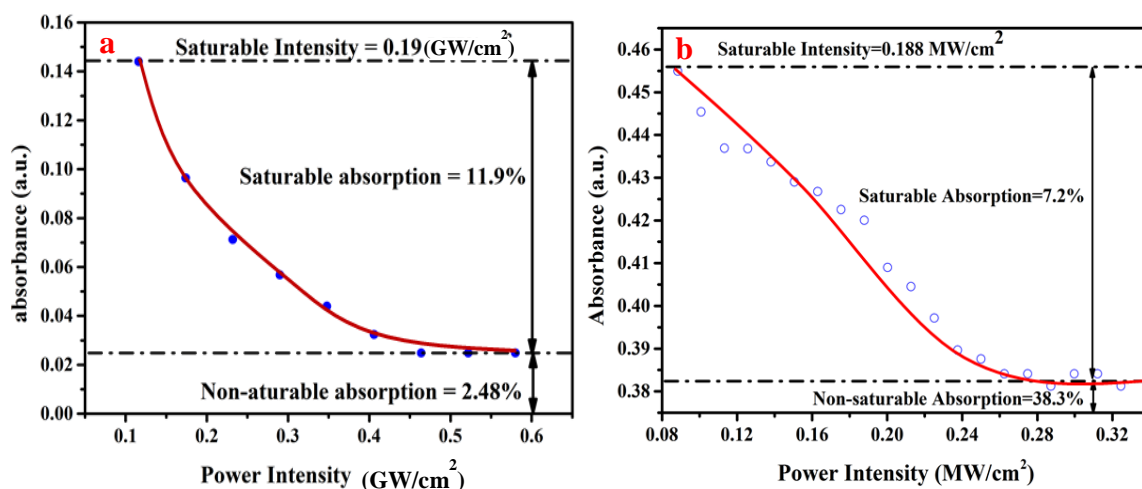


Fig.(2.16): Nonlinear absorption for: (a) Fe_2O_3 -NF, (b) Fe_2O_3 :PVA film.

Table (2.6): The nonlinear parameters of Fe₂O₃-NPs samples.

Sample	ΔT (%)	α_{ns} (%)	I_s (MW/cm ²)	α_2 cm/W	n_2 (cm ² /W)	χ^3 (esu)
Fe ₂ O ₃ - NF	7.2	38.3	0.188	-	-	-
Fe ₂ O ₃ - PVA	11.9	2.48	190	-8.598× 10 ⁻⁶	9.457× 10 ⁻¹¹	8.695× 10 ⁻⁹

2.4.3 SiO₂ optical modulator

As in the previous nanoparticles, SiO₂ is also prepared in two forms. Firstly, SiO₂ nano-suspension was prepared via dispersed nanoparticle (SiO₂ with uniform tetrahedral structures or near-spherical shape with an average diameter of about 32 nm from Nanjing Nano Technology Co., Ltd.) SDS solution with a 3 mg/ml concentration. At the first, the mixture was continuously blended at modest speed for 1 h with the aid of a magnetic blender. Then, the resultant nanofluid was further functionalized using ultrasonic agitation for ~ 2 h to get a homogenous dispersion of the NPs. Due to the easiness of the assembling, the absence of costly tools and fewer fabrication steps give rise to a straightforward and economical technique to assemble the optical modulator. Lastly, the resultant milky color suspension was preserved in the plastic cuvette.

Then, SiO₂-PVA film is assembled via mixed 5 mg with 5 ml of polymer solution using a magnetic stirrer at moderate speed for 1 h. Then the resultant mixture was emptied carefully into plastic Petri dishes and left to be dried at room temperature for about 4 days. Dried thin films were produced due to dehydrating the evaporation process.

As the optical qualities are the figures of merit to verify if a precise substance can be recommending as a tolerable optical modulator, the prepared samples are exposed to a spectrophotometer, z-scan technique, and twin-

detector techniques. The linear absorption spectra of the prepared SiO₂-NPs samples in the 200-2000 nm region are measured using the spectrophotometer as shown in Fig. (2.17). These spectra indicated that the SiO₂-NPs samples possess a good absorption value at the lasing bands of 1 and 1.5 μm , where the highlight regions show the wavelength range in 1 and 1.5 μm regions. While, the insertion losses of the SiO₂-NPs samples based optical modulator are measured ~ 0.11 and 3.468 dB, for the liquid and thin-film samples, respectively. This quantity contains the absorption of optical modulator matter itself and the misalignment among the coupled ferrules produced via the integration of the optical modulator matter. The big loss can put a number of limitations on the cavity gain and restricts the pulse duration [183].

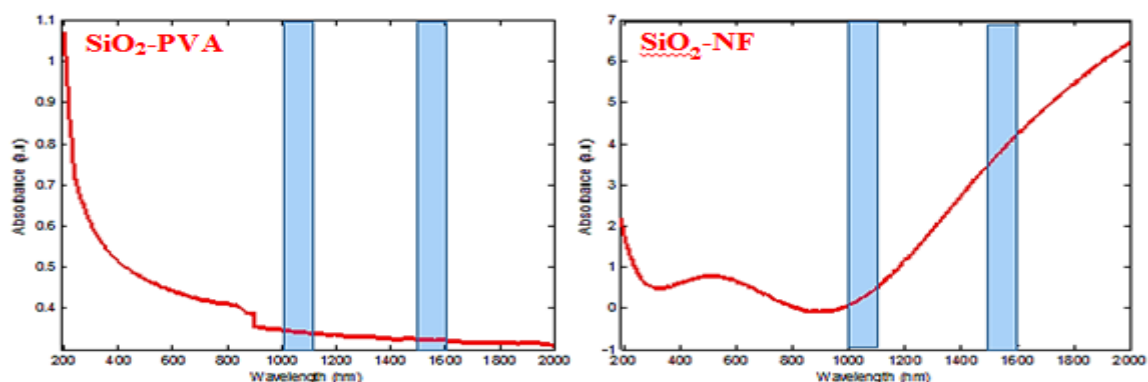


Fig. (2.17): The absorption spectrum of prepared SiO₂-NPs samples in the range 200-2000 nm (highlighted is lasing operation region).

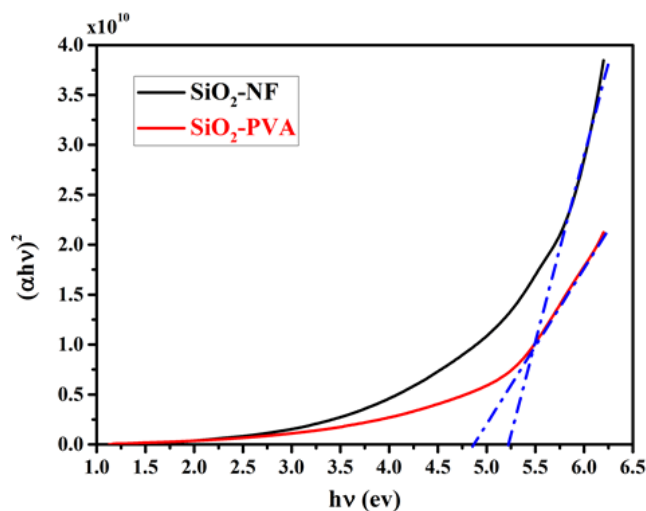


Fig.(2.18): Tauc plot of SiO₂-NPs.

Additionally, the band-gap energy also has been determined as depicted in Fig.(2.18). The linear properties of prepared SiO₂-NPs samples are shown in Table (2.7).

Table (2.7): The linear parameters of SiO₂-NPs samples.

Sample	α at 1030 nm (cm ⁻¹)	σ_a at 1030 nm (cm ²) × 10 ⁻¹⁸	α at 1550 nm (cm ⁻¹)	σ_a at 1550 nm (cm ⁻²) × 10 ⁻¹⁶	E_g (ev)	τ (ns)	Insertion loss (dB)	L_s (μm)
SiO ₂ -NF	29.26	19.567	806.05	5.39	4.86	38.4	0.11	-
SiO ₂ -PVA	111.9	0.748	158.77	0.01062	5.21	1.17	3.468	23.5

The nonlinear properties of prepared SiO₂-NPs samples are shown in Table (2.8), in which the same setup that is used in the nonlinear examination for the Fe₂O₃ was employed here also. The resultant characteristics of Z-scan (closed and open apertures) and the intensity-dependent optical absorption for the prepared SiO₂-NPs sample are depicted in Fig.(2.19) and Fig.(2.20), respectively. From these measurements, it is found that SiO₂-NPs samples exhibit a significant saturable absorption property with a good nonlinear absorption coefficient, good nonlinear refractive index, and a strong 3rd susceptibility. Additionally, the recovery time can be estimated to be in the range between 1.17-38.4 ns.

Table (2.8): The nonlinear parameters of SiO₂-NPs samples.

Sample	ΔT (%)	α_{ns} (%)	I_s (MW/cm ²)	α_2 cm/W	n_2 (cm ² /W)	χ^3 (esu)
SiO ₂ -NF	8	34.1	0.126	-	-	-
SiO ₂ -PVA	24.68	3.82	220	-3.072×10^{-11}	1.1562×10^{-6}	1.238×10^{-8}

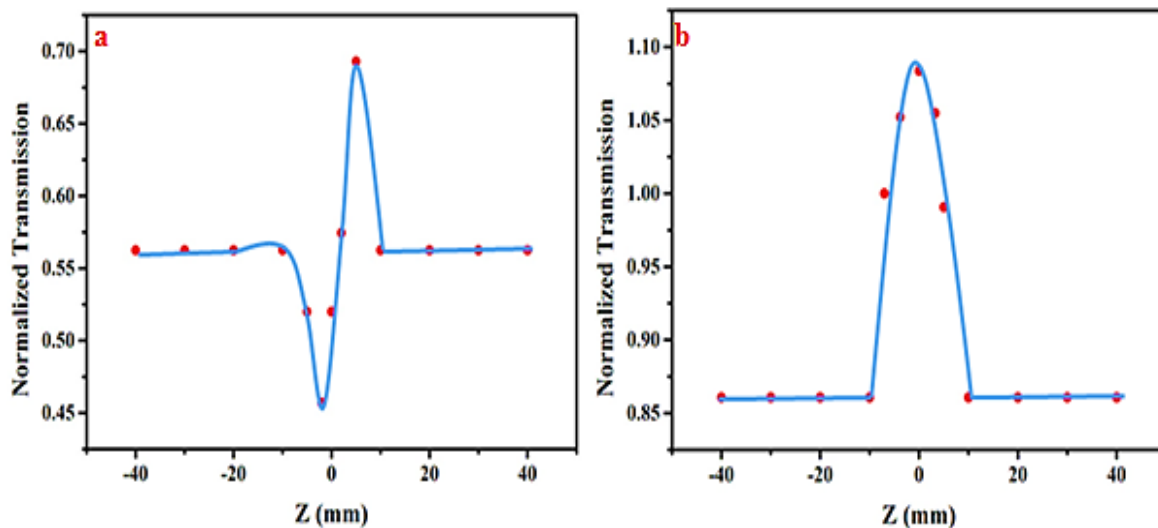


Fig.(2.19): Normalized transmission of (a) closed aperture, (b) open aperture.

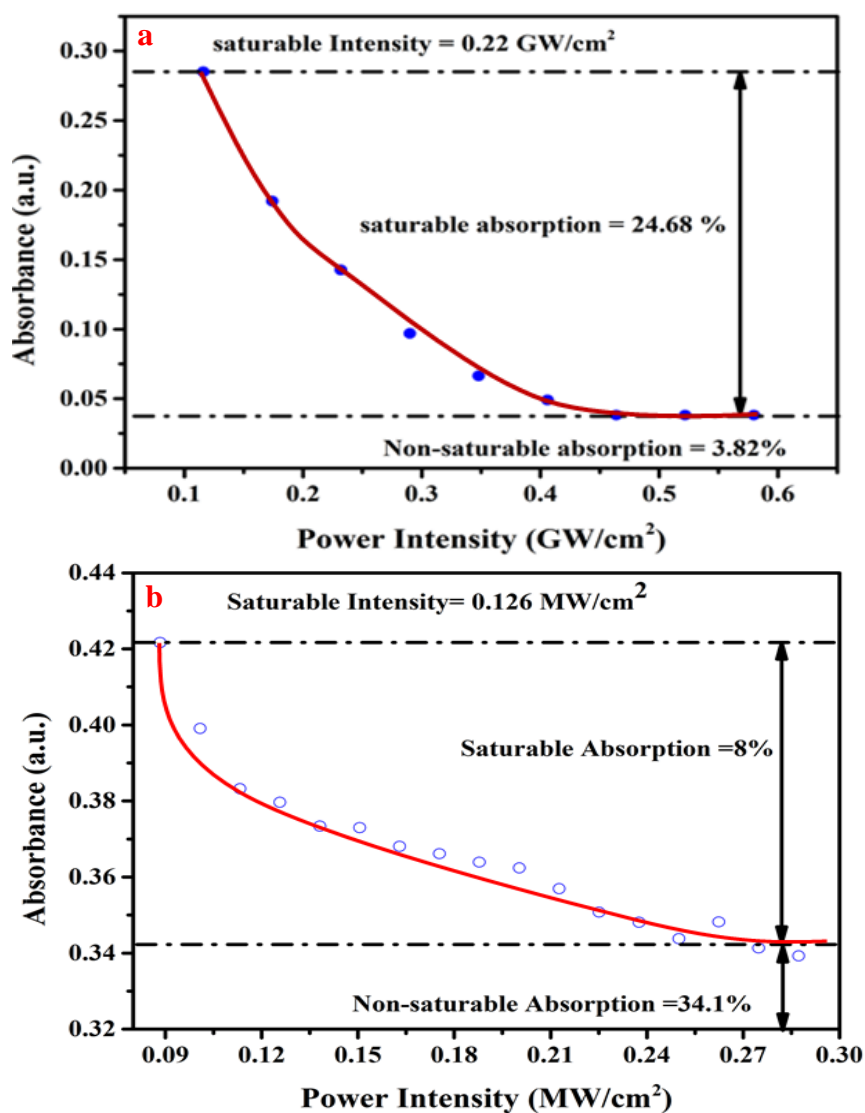


Fig.(2.20): Nonlinear absorption for: (a) SiO₂-NF, (b) SiO₂:PVA film.

2.4.4 Fe₂O₃/SiO₂ nanocomposite optical modulator

By fabricating a ferroelectric-dielectric composite, a new approach is proposed to realize the unique optoelectronic features under field coupling. Due to that the performance of optical modulators considerably relies on the crystal building, morphology of the surface, and the NPs composition of the film. Therefore, a mixture Fe₂O₃-NPs and SiO₂-NPs were prepared and then examined its performance as an optical modulator. An equal amount of Fe₂O₃-NPs and SiO₂-NPs were mixed and then dispersed in PVA solution with a concentration of 1 mg/ml. The product of mixture was agitated under an ultrasonic vibration (40 kHz frequency, and 60 W ultrasonic power) for 10 hours to produce a uniform suspension. The prepared nanocomposite solution displays a rust orange color. The resultant nanocomposite solution is dropped into a clean petri dish, and then left till the freestanding nanocomposite polymeric film is formed. Finally, the dried thin film with a thickness of about 23 μm was obtained and then carefully peeled off from the petri dish substrate to later use.

The Vis-NIR spectrum of the nanocomposite is studied by using a spectrophotometer in the wavelength band of 200-2000 nm covering the visible and near-infrared bands. The detected transmittance spectrum is presented in Fig.(2.21). It can be observed from this figure that the nanocomposite exhibits a broadband linear transmittance with good absorption character in the entire mentioned regions. This nanocomposite is almost possessing an appropriate absorption in the band between 1000 and 1500 nm. From the absorption spectrum values, the optical band-gap quantity can be appraised via applying the Tauc relation. Fig. (2.22) displays the plot of $(\alpha_0 h\nu)^2$ versus $h\nu$, in which the optical bandgap of the prepared sample was achieved by linear extrapolating the Tauc plot. From this plot, the Fe₂O₃/SiO₂ nanocomposite sample reveals a broad absorption edge, and a wide span for the band-gap quantity is estimated as 2.702-4.53 eV.

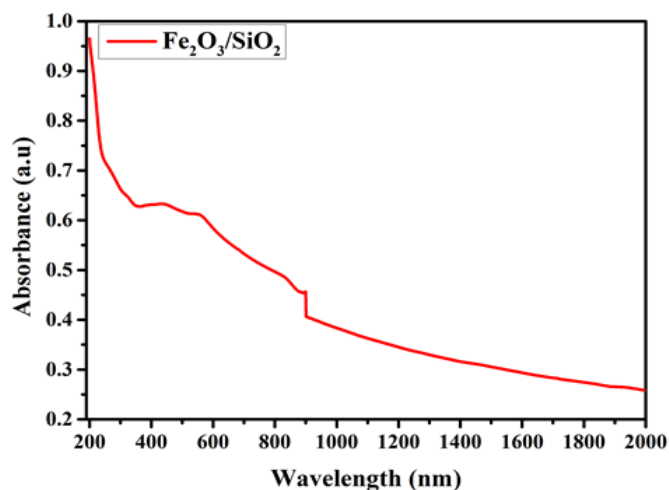


Fig. (2.21): The absorption spectrum of $\text{Fe}_2\text{O}_3/\text{SiO}_2$ nanocomposite in the range 200-2000 nm (highlighted is lasing operation region).

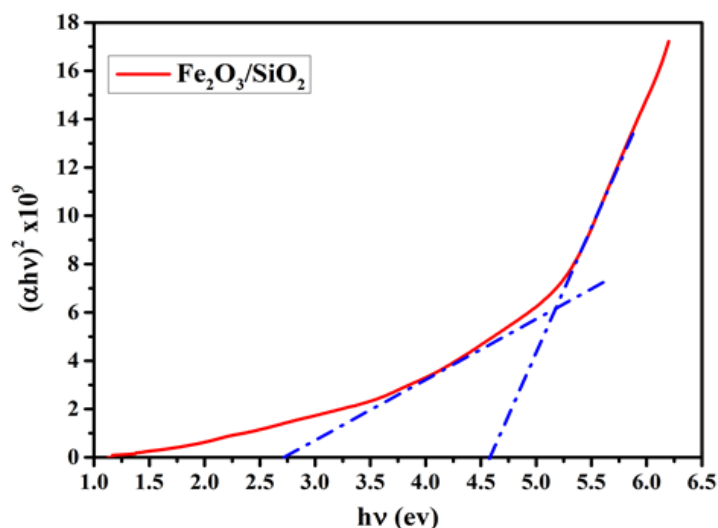


Fig.(2.22): Tauc plot of $\text{Fe}_2\text{O}_3/\text{SiO}_2$ nanocomposite.

The normalized transmittance (Fig.(2.23)) is plotted against the z sample location that is estimated concerning the focal plane. Fig.(2.23a) shows the closed aperture behavior of the nanocomposite thin film, in which the curves of the prepared sample revealed a valley after a peak, this means that the sign of n_2 is negative. This state denotes that the present nanocomposite work as self-defocusing material. An open-aperture examination is accomplished via the elimination of the aperture; so, the transmitted beam reaches the photo-detector once transmitting the prepared specimen. The normalized transmittance is graphed against the z -location of

the specimen, which the signature of $\text{Fe}_2\text{O}_3/\text{SiO}_2$ nanocomposite is presented in Fig.(2.23b). From this figure, $\text{Fe}_2\text{O}_3/\text{SiO}_2$ nanocomposite shows a saturable absorption property. Also, from this measurement, it is found that $\text{Fe}_2\text{O}_3/\text{SiO}_2$ nanocomposite has a big nonlinear absorption coefficient - 1.1562×10^{-5} cm/W, good nonlinear refractive index coefficient -3.8234×10^{-11} cm²/W, and a strong third order susceptibility $\sim 1.7955 \times 10^{-7}$ esu.

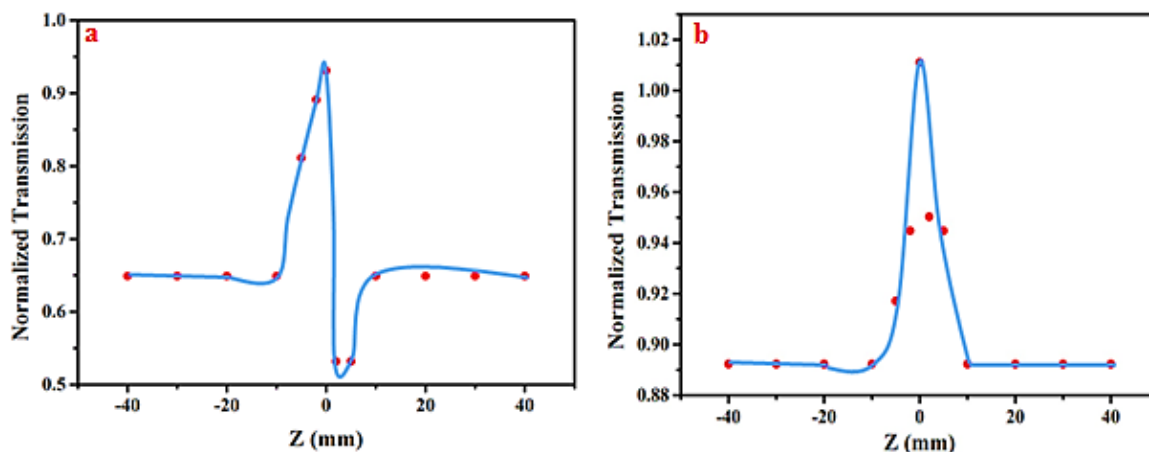


Fig.(2.23): Normalized transmission of $\text{Fe}_2\text{O}_3/\text{SiO}_2$ nanocomposite for: (a) closed aperture, (b) open aperture.

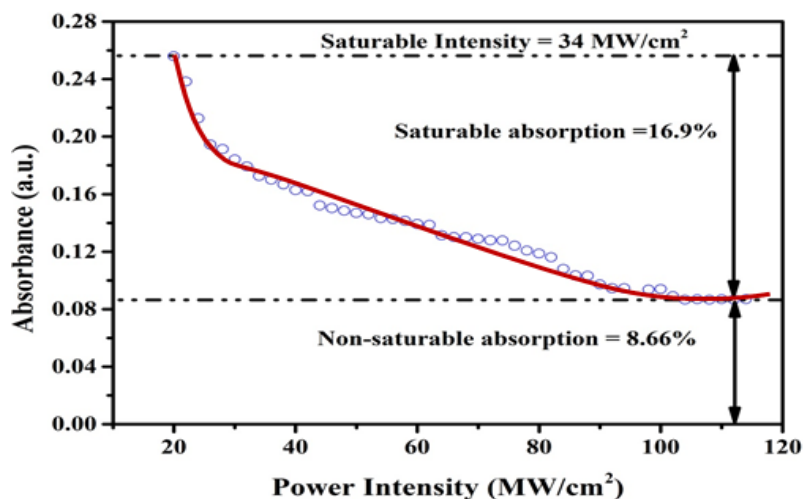


Fig.(2.24): Nonlinear absorption for $\text{Fe}_2\text{O}_3/\text{SiO}_2$ nanocomposite film.

Besides, the intensity-dependent optical absorption for the prepared $\text{Fe}_2\text{O}_3/\text{SiO}_2$ nanocomposite film was investigated by a twin-detector measurement technique. The resultant characteristic of the $\text{Fe}_2\text{O}_3/\text{SiO}_2$

nanocomposite sample is depicted in Fig.(2.24), these results clearly indicate that the $\text{Fe}_2\text{O}_3/\text{SiO}_2$ nanocomposite film exhibits a significant saturable absorption property. The as-prepared $\text{Fe}_2\text{O}_3/\text{SiO}_2$ nanocomposite film has a modulation depth of 16.9 %, a nonsaturable absorber of 8.66 %, and a saturation intensity of 34 MW/cm^2 .

To further investigate the property of the prepared sample, the recovery time was also estimated to be about 7.65 ns. The linear and nonlinear properties of the prepared $\text{Fe}_2\text{O}_3/\text{SiO}_2$ nanocomposite sample are shown in Table (2.9).

Table (2.9): The linear and nonlinear parameters of $\text{Fe}_2\text{O}_3/\text{SiO}_2$ nanocomposite.

α at 1030 nm (cm^{-1})	σ_a at 1030 nm (cm^2)	α at 1550 nm (cm^{-1})	σ_a at 1550 nm (cm^2)	E_g (ev)	τ (ns)	Insertion loss (dB)
111.014	7.423×10^{-19}	99.98	6.685×10^{-19}	2.702-4.53	7.65	1.026
L_s (μm)	ΔT (%)	α_{ns} (%)	I_s (MW/cm^2)	α_2 cm/W	n_2 (cm^2/W)	χ^3 (esu)
34.5	16.9	8.66	34	- 1.1562×10^{-5}	- 3.8234×10^{-11}	1.7955×10^{-7}

CHAPTER THREE

Results and Discussion:

Multiwavelength Ytterbium Doped

Fiber Laser

Chapter Three

Results and Discussion: Multiwavelength Ytterbium Doped Fiber Laser

3.1 Introduction

Nonlinear influences based on nanomaterials have a vital role in current photonic employment, containing control over the wavelength spectrum of laser signal, initiation of short/ultrashort pulses, and ultra-swift switching. In this chapter, highly nonlinear nanomaterials are employed to generate a steady multiwavelength ytterbium fiber laser in various operation conditions. Three different nonlinear nanomaterials based on optical modulators (Ni, Fe₂O₃, and SiO₂ NPs) are employed in the ring cavity to generate a multiwavelength in a 1 μm region. These nanomaterials are a comparatively simple and cost-effective alternative compared to other techniques utilized in a multiwavelength generation. Besides, the exploiting of these nanomaterials averts the radical alternatives to the oscillator length and consequently averts the trouble of the specific balance of the losses in the laser cavity. This is strangely crucial for the controlling of the nonlinear effects in the laser cavity to achieve multiwavelength generation. On the other hand, at precise conditions, these nanomaterials assist to induce a pulsed generation. In this work, two different types of YDF are used as an active medium, one with length of 1.5 m while the other with 0.6 m. The experimental setup of the proposed multiwavelength YDFL is shown previously in chapter two in Fig. (2.1). Characterization of the obtained results including optical spectrum, stability, average power, pulse energy, PRR, and pulse width with the employment of the fabricated optical modulators are discussions.

3.2 Ni-NPs Optical Modulator

This section includes the details about the experimental setup, results, and discussion of the proposed multiwavelength YDFL based on Ni thin film.

3.2.1 Ni Thin Layer Based-NF

Firstly, an ultra-thin layer of Ni-NF was embedded inside the YDFL based on 1.5 m of the gain medium. As the pump reached about 126 mW, lasing emission centered 1036.104 nm was realized. As the absorbed pump power was upraised gradually above the threshold, the cavity nonlinearity was more promoted and the lasing emission switched from one line to multiple-lines where the new lasing wavelengths appeared as the pump power increased due to the mode hopping effect inside the cavity. Dual-emission lines located at 1037.388 nm and 1038.06 nm with wavelength spacing of 0.722 nm began at the excited power of 153 mW. Sequentially, via gradually adapting the excited power to 160 mW and then to 182 mW, the multiwavelength was switched to triple- wavelength (1035.48, 1037.516, and 1038.028 nm), and quadruple-wavelength (1034.84, 1035.012, 1037.528, and 1037.92 nm), respectively. The optical spectra at different pump power are shown in Fig(3.1).

From this figure, it can be observed that as the incident pump power was continued to increase between 235 mW and 300 mW, a significant broadening was noticed with multiple-lines reached to more than 15 peaks with lines spacing of about 0.188 nm. This is owing to the augmentation of YDF gain concerning rising pump power. Also, this condition permits significant signal power for the nonlinear effects (such as FWM) assistance by the high nonlinearity of Ni thin layer to generate new lines at the neighborhood lasing wavelengths. The broadening effect may be attributed to some nonlinear processes generated in the YDFL ring cavity such as the self-phase modulation effect. In the meantime, the temporal signal of the

multiwavelength YDFL output was examined, which was no pulse-like output was found, indicating that the multiwavelength YDFL output is operated in the CW state. This might be accredited to the deposited Ni-thin layer does not meet the prerequisites of the pulse laser operation [28,184].

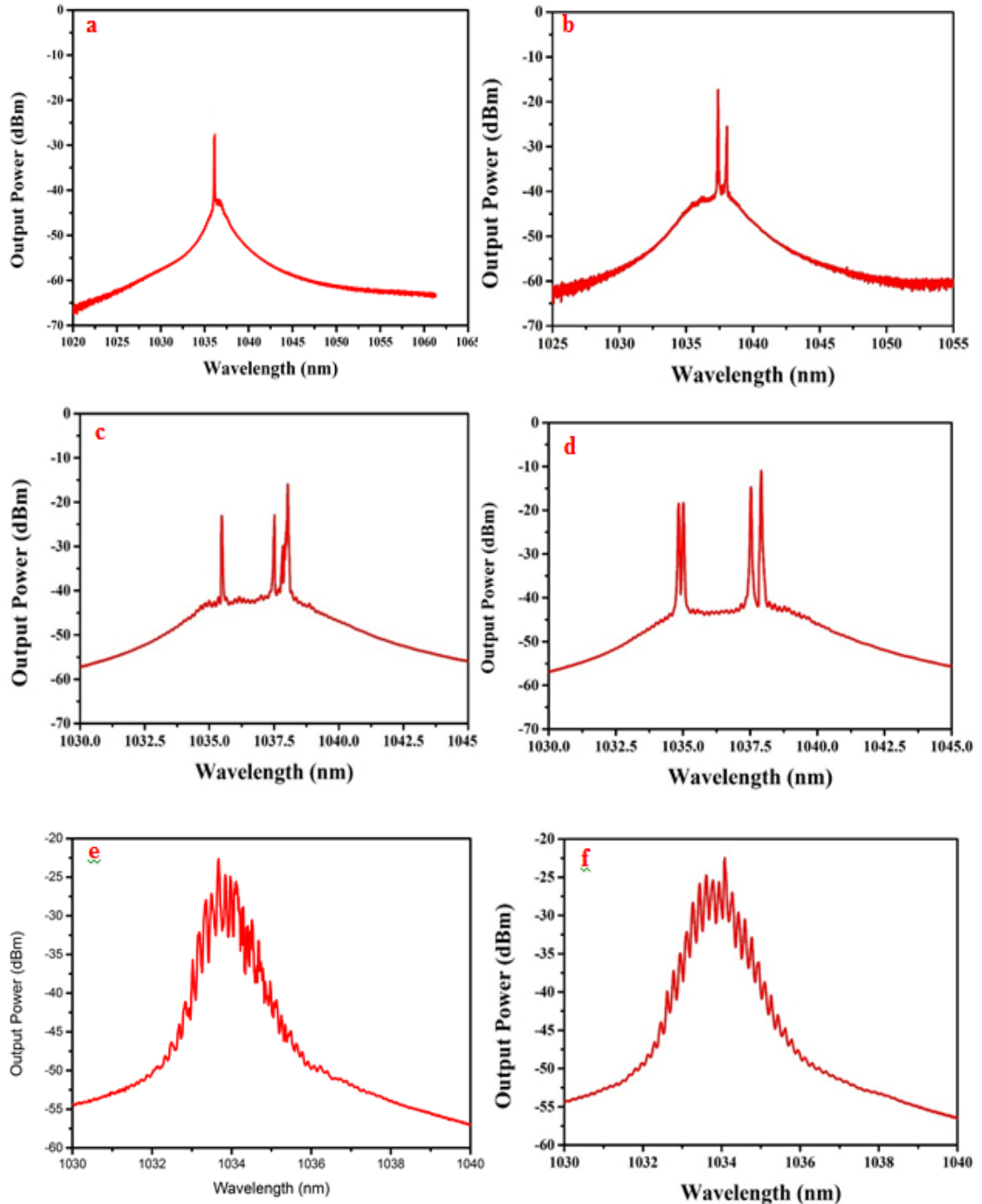


Fig (3.1): Optical spectra of YDFL based-Ni-thin layer at pump power of: (a) 126 mW, (b) 153 mW, (c) 160mW, (d) 182 mW, (e) 235 mW, and (f) 300 mW.

To more examination of the operation characteristic of the fiber laser based on Ni-thin layer, two successive thin layers of the coating were smeared by dripping the Ni-thin layer onto the tip of the fiber and subsequent desiccation at room temperature. After embedding the Ni-thin layer inside the YDFL, the cavity nonlinearity was enhanced and lasing emission was realized at a threshold pump power of about 130 mW centered at 1036.104 nm. But, as the pump power increases to about 174 mW, dual-emission with wavelengths of 1035.692 nm and 1037.932 nm was appeared. It noteworthy that as the pump power exceeds the 230 mW, the emitted laser was switched to a single line centered at 1037.544, which showed a significant broadening due to the high nonlinearity inside the cavity. The optical spectra at different pump power are depicted in Fig.(3.2).

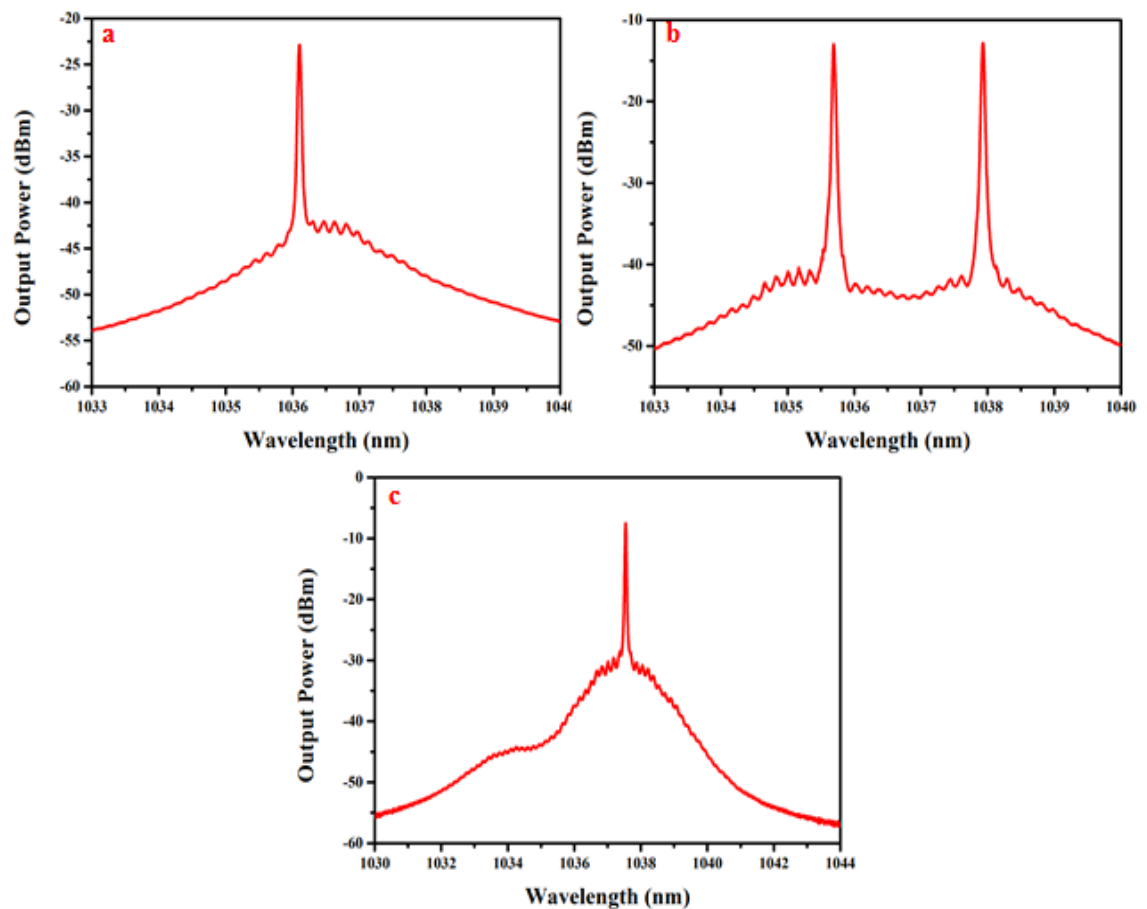


Fig (3.2): Optical spectra of YDFL based-Ni-thin layer at pump power of: (a) 130 mW, (b) 174 mW, and (c) 300 mW.

In the meantime, once the bleaching threshold of about 193 mW, the self-starting Q-switching pulse was achieved and its stable generation was maintained up to the uppermost exciting power of 300 mW. Fig. (3.3) presents the stable pulse trains at the lowest and uppermost exciting power.

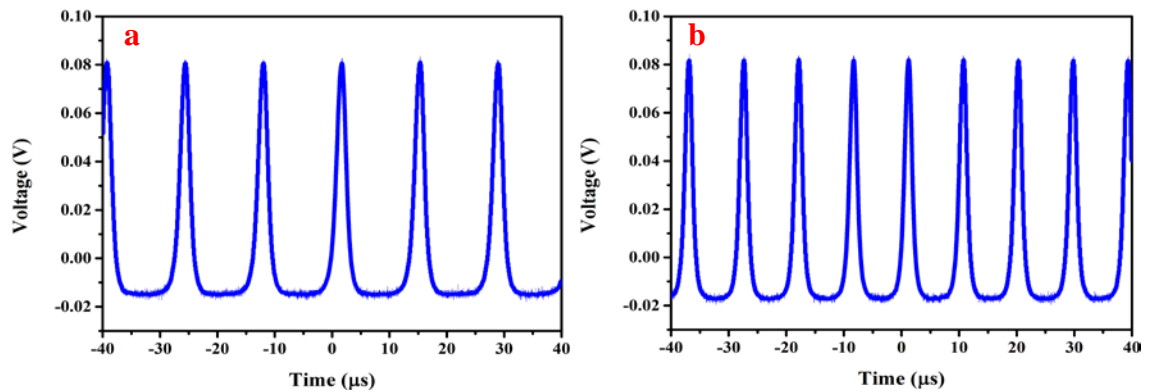


Fig. (3.3): Oscilloscope trace at a different pump power of (a) 193 mW and (b) 280 mW.

The repetition rate and pulse width as a function of the pump power are depicted in Fig.(3.4a), while, the average output power and pulse energy of the proposed laser as a function of the input pump power are depicted in Fig.(3.4b). Fig.(3.4a) and Fig.(3.4b) show a near-linear dependence of the repetition rate, pulse width, average output power, and the pulse energy on the pump power. During this operation, the pulse width was tuned between 1.88-1.31 μs , repetition frequency was varied between 74-130.6 kHz. From Fig. (3.4a), it can be observed that at the pump power of about 253 mW, the pulse duration was increased to about 1.38 μs and then became decreases as the pump power increased more. While at the maximum repetition rate of about 137 kHz was observed at a pump power of about 267 mW, but after that became decreases to about 131 kHz and then 10 130.7 kHz. This is due to the oversaturation effect of the Ni SA.

On the other side, the recorded output power raised linearly up to 1.271 mW, whereas the pulse energy varied from 1.014 nJ to 9.732 nJ as the pump power increased across the range 193–280 mW. Temporarily, the maximum peak power of 7.43 mW was achieved at the maximum pump

power of 280 mW. The Q-switched fiber laser has a slope efficiency of 1.38 %.

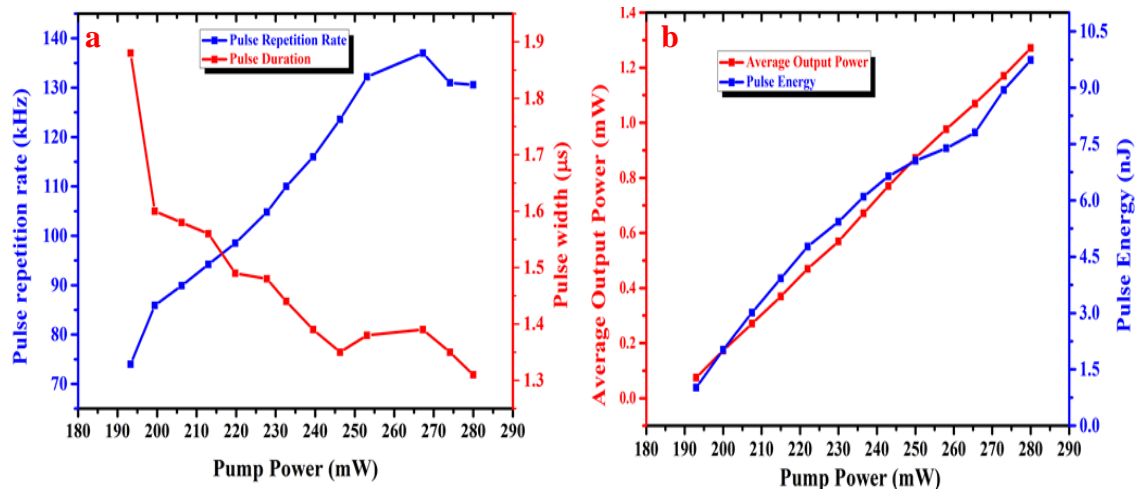


Fig. (3.4): (a) Pulse width and repetition rate vs. pump power, and (b) Average power and pulse energy vs. the pump power.

The fundamental frequency was stated by the RF spectrum to be ~ 130.6 kHz, which can be achieved from Fourier transform. A signal to noise ratio (SNR) ~ 50 dB within a 500 kHz span of frequency, which is obviously offered in Fig.(3.5). This designates the great stability of the emitted pulses. Adopting the exciting emission among minimum and maximum allowable magnitudes does not influence the performance of the generated Q-switched pulses confirming that the optical modulator matter continued intact.

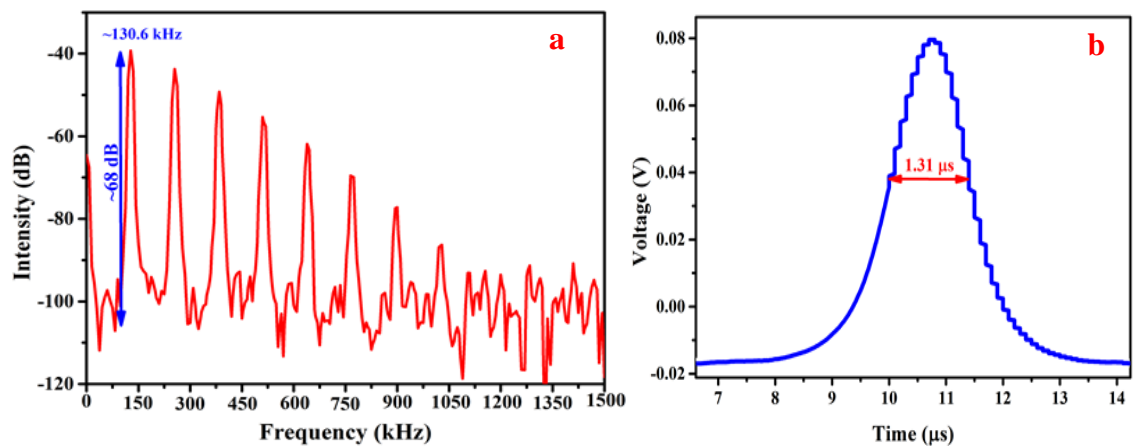


Figure (3.5): (a) RF pattern, and (b) The single-pulse form of Q-switching based on Ni-thin layer at 300 mW.

After that, the Ni-thin layer performance was examined using the YDFL cavity based on 0.6 m of the gain medium. In the present case, the lasing starting for single line generation was verified at 60 mW placed at 1062.9 nm. By progressively adjustment of the laser diode pump power up to 71.4 and 85 mW and without any intracavity filtering, stable dual-, and triple-lasing lines have been observed at 1062.9 nm, 1063.7 nm, and 1064.5 nm, respectively, with a SNR \sim 36.5 dB. The optical spectra at different pump power are shown in Fig.(3.6).

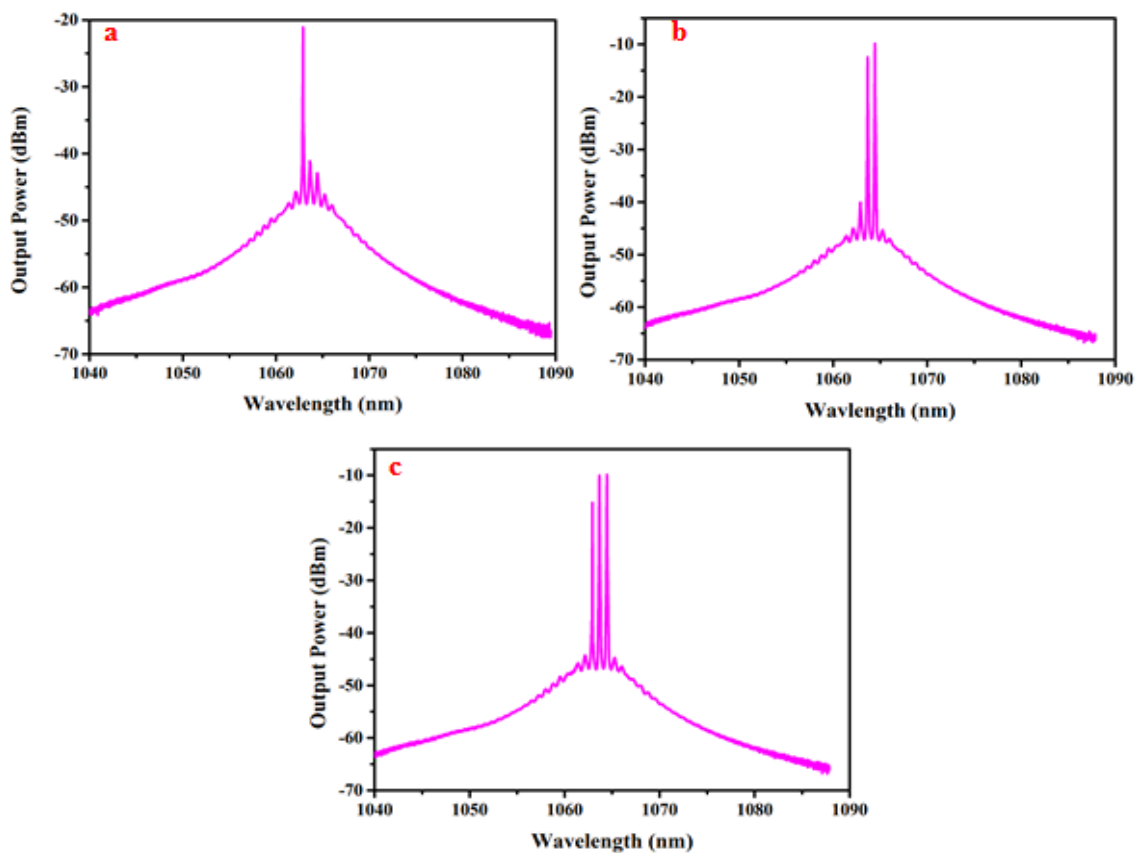


Fig (3.6): Optical spectra of YDFL based-Ni thin layer at pump power of: (a) 60 mW, (b) 71.4 mW, and (c) 85 mW.

These multiwavelength generations were realized with constant spacing with the assistance of the FWM effect. The FWM effect can efficiently exert control over the YDF gain profile, which leads to the mitigation of the mode competition resulting from the homogenous gain broadening in the ring cavity; this is due to the high third-order nonlinearity

of Ni-thin layer. On the other hand, as the number of wavelength lines depends on the pump power, therefore additional peaks might appear if the pump power increases further.

Meanwhile, the temporal examination proved that Ni-thin layer induced a pulse generation within the cavity. The mode-locking signal was achieved at a bleaching power of 66 mW, but its process was suffered from instability issues (Fig. (3.7)) and then disappeared at the pump power exceeded the 170 mW. To further stabilized the pulse operation and sustained it, it must be balanced between the linear and nonlinear parameters of the cavity.

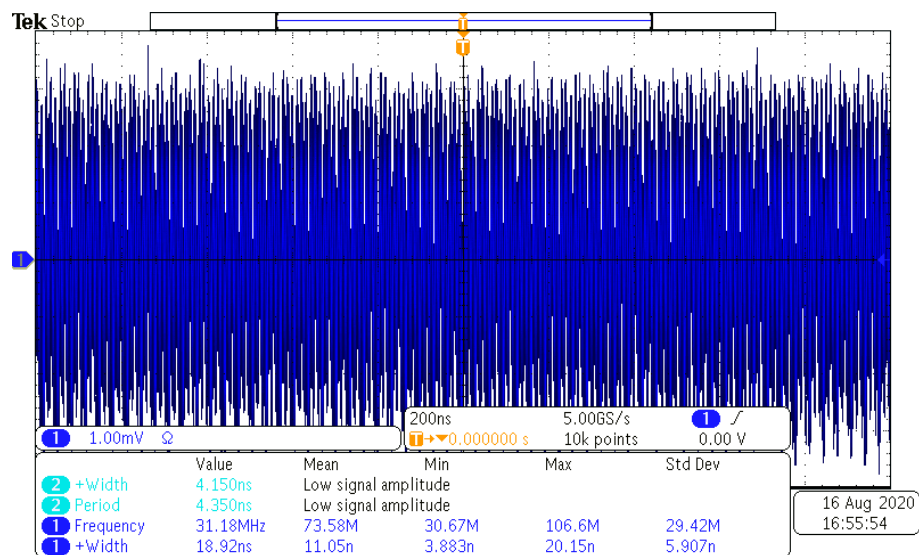


Fig. (3.7): Oscilloscope trace of unstable pulsed YDFL based on Ni thin layer.

To more compassion with the first YDFL cavity, two successive Ni-NF layers were applied on the fiber tip using the dropping method. In this experiment, the lasing process begun at a threshold of about 71 mW with a single wavelength located at 1064.4 nm. Then, dual- and triple-wavelength were observed at 1064.4 nm, 1063.6 nm, and 1062.8 nm as the pump power increased up to 85 and 102 mW, respectively. The optical spectra at different pump power are depicted in Fig.(3.8). In the meantime, the mode-locked operation was begun at a threshold pump power of about 108 mW.

By progressively adopting the rotational and compression forces of in-line PC, dark pulse radiation generating in a fundamental repetition frequency of 30.5 MHz (which corresponding to the fiber laser ring length) is perceived as presented in Fig. (3.9a).

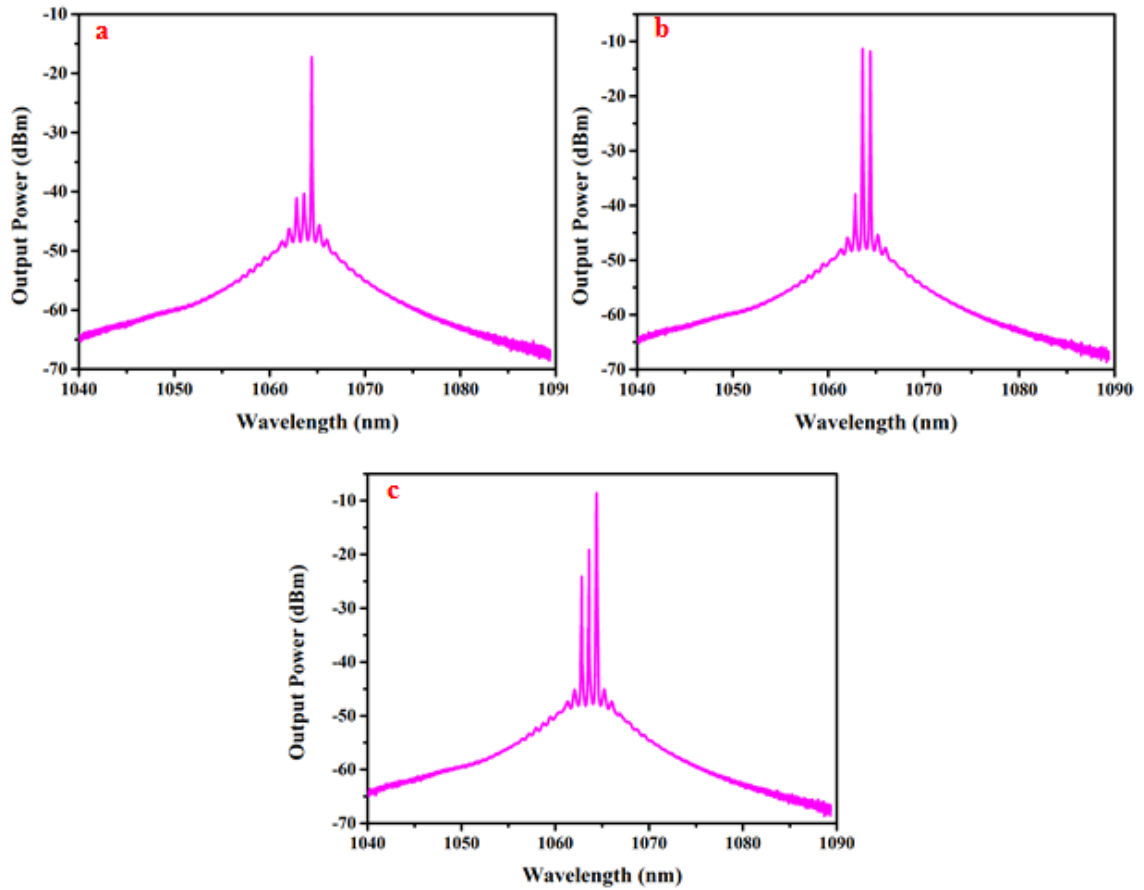


Fig (3.8): Optical spectra of YDFL based-Ni-thin layer at pump power of: (a) 71 mW, (b) 85 mW, and (c) 102 mW.

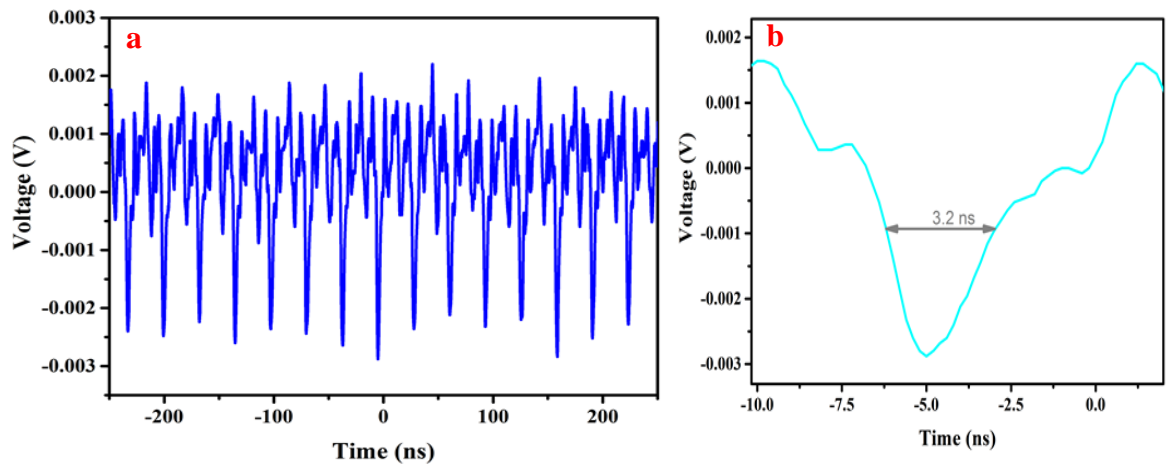


Fig. (3.9): Oscilloscope trace at fundamental mode-locked dark pulses based on Ni-thin layer.

As exhibited in the oscilloscope trace, the dark pulse is characterized via the narrow intensity dip in the CW lasing radiation background. The pulse duration of the resulted pulse was ~ 3.5 ns, as shown in Fig (3.9b). For more studied the polarization mechanisms of the dark pulse, the PC was more carefully adopted together at 200 mW, the 3rd harmonic generation of dark pulses was detected, as displayed in Fig.(3.10a).

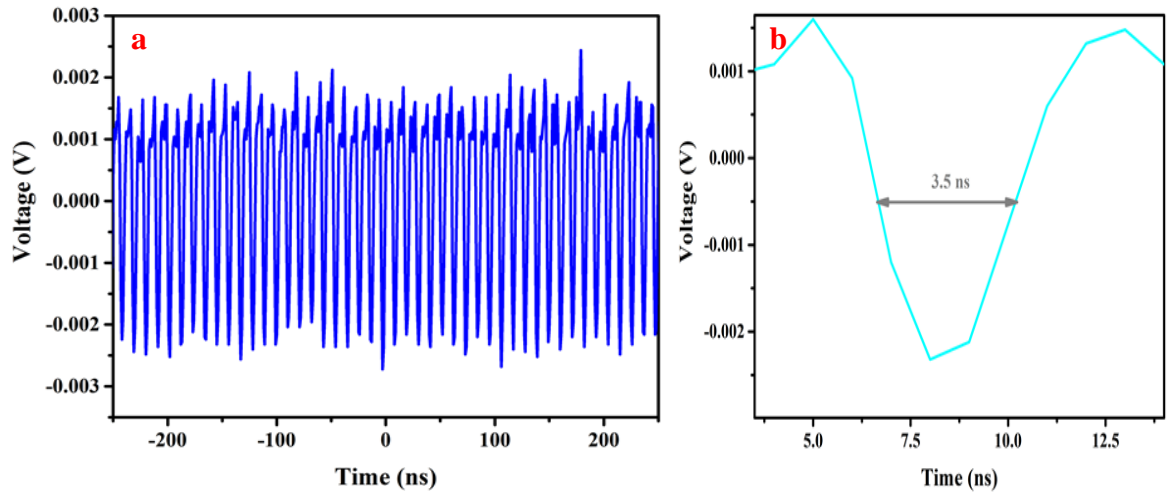


Fig.(3.10): Oscilloscope trace at 3rd harmonic mode-locked dark pulses based on Ni-thin layer.

It ought to be observed that the switching from the fundamental mode-locking to the 3rd harmonic mode-locking of the dark pulses was achieved by just adapting the PCs in the cavity, without any additional variations in the experimental states. Also, it might be realized another harmonic generation of the dark pulses through the adjusting of the PC, as well higher harmonic order can be risen with an upsurge in the pump power, as mentioned in previously published reports [185,186]. Additionally, it can be perceived that pulse splitting takes place in the practice of changing the PC compression and rotational strengths, this leads to the interface among the pulses. Correspondingly, the repetition frequency multiplies and converts to higher. On the other side, it can be observed that when the harmonic order upsurges to the 3rd one, the optical spectrum exhibit no noticeable variations.

Fig.(3.10b) shows the zoomed-in pulse of the 3rd harmonic generation, which the time pulse duration equal to ~3.2 ns. The central frequencies of both the fundamental and harmonic generations were verified through the RF spectra using the FFT algorithm which were about 30.5 and 91.5 MHz with supermode suppression ratio of more than 31 and 47 dB, respectively, as shown in Fig.(3.11), which signifies the moderately little peak fluctuations and good-performed mode-locking stability.

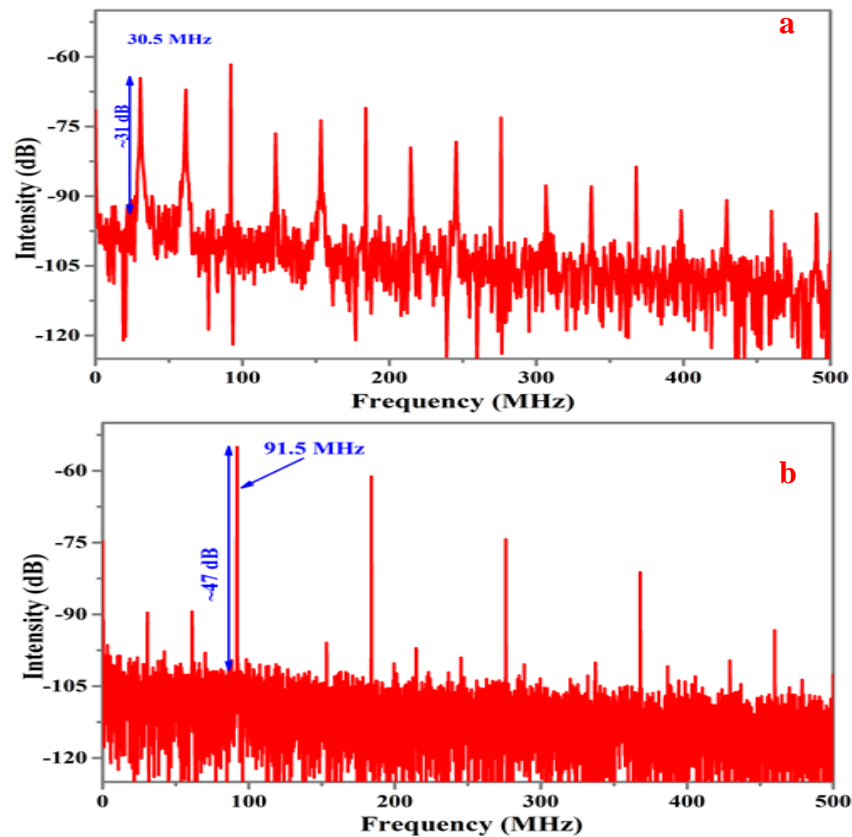


Fig.(3.11): RF spectra for the (a) fundamental and (b) 3rd harmonic generations of the dark pulse mode-locked based on Ni-thin layer.

Besides, the OSC signal one more time experienced from instability problems in the time domain which can be more enhanced via addition intracavity elements. Generally, the dark pulse generation condition is different from other pulse generation forms (e.g. bright pulse generation), which is difficult to sustain. This is owing to the laser noise and/or small environmental disturbance that permit diverse dark pulses to arise automatically in the oscillator. This leads the laser to work in a condition of

multiple dark pulses (harmonic generation). Finally, the average output versus the pump power was examined, which the recorded output power rises linearly up to 3.65 mW as the pump power was increased to about 200 mW, as illustrated in Fig.(3.12). The pulsed fiber laser has a slope efficiency of 2.69 %.

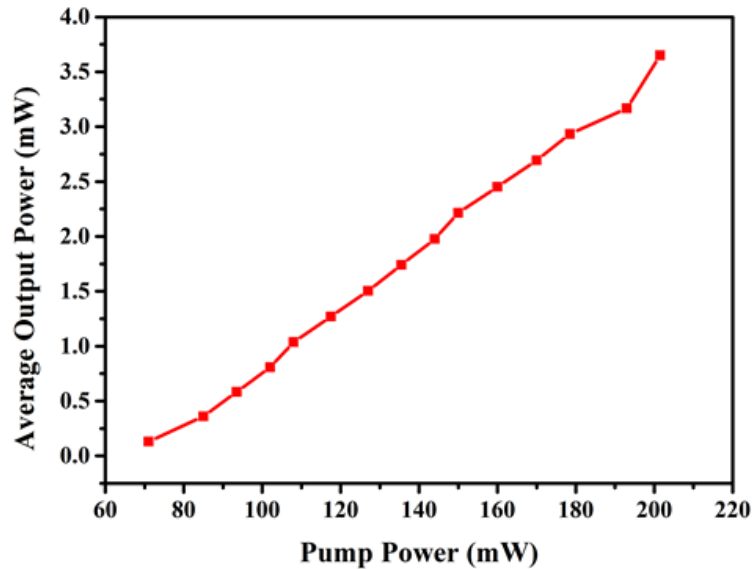


Fig. (3.12): Average power vs. the pump power.

Compare to the monolayers of Ni-thin layer, the increase in the number of layers means that the dripped NPs' concentration on the fiber end is somewhat greater that consequently persuades further absorption. So, the modulation depth could be changed with the number of coated layers on the fiber tip. The above-mentioned method can significantly have recognized by low insertion loss as well as decrease the stating bleaching power.

3.2.2 Ni-PVA Freestanding Film (0.75% volume)

To verify the functionality of the Ni-PVA as optical modulation, this thin film was incorporated inside two different cavities of YDFL. First, the Ni-PVA was adopted inside YDFL based on 1.5 m of YDF. As the input pump power was boosted to 144 mW, a CW operation was observed at a central wavelength of 1038.5 nm. Compared to the YDFL cavity without

Ni-PVA, it can be observed that the emitted laser exhibited a blue-shifted behavior. This blue shift might be ascribed to the insertion loss added by the Ni-PVA thin film. The emission spectrum at threshold pump power is depicted in Fig.(3.13a). Then, dual-wavelength peaks were generated with a line spacing of 5 nm as the pump power reached 195 mW. The dual-wavelength spectrum of the proposed laser at a maximum pump power of 288 mW is depicted in Fig.(3.13b). This figure displays two lasing lines at 1038.5 and 1043.5 nm with peak powers of about -13.556 and -19.135 dBm, respectively.

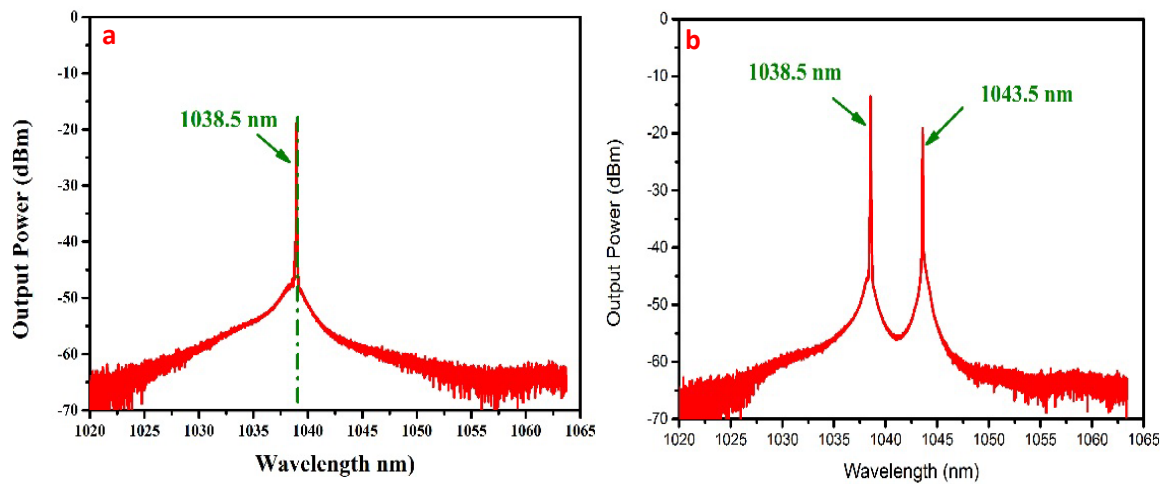


Fig. (3.13): The optical signal with Ni-NPs SA at (a) threshold, (b) maximum pump power.

In the meantime, as the pump power was gradually boosted in the values between 185 and 288 mW, stable self-started Q-switched pulses with broadly tunable repetition frequencies varying from 58.7 to 100.1 kHz were achieved. The pulse width declines nearly monotonously from 4.31 to 1.44 μ s corresponding to the achieved repetition rate. These are the distinctive property of passive Q-switching laser. The temporal characteristics of the proposed YDFL at threshold and maximum pump powers are depicted in Fig.(3.14).

In order to further analysis of the features of the proposed YDFL, the frequency characteristics of the Q-switched pulses were verified at the highest pumping power of 288 mW. The fundamental RF at maximum

output pulse of about 100.1 kHz which matched to the repetition rate of Fig.(3.14b), SNR ~ 57.3 dB with no spectral modulation, and more than eight harmonics frequency was observed with a frequency span of 1000 kHz are depicted in Fig.(3.15a). This confirms the good stability of the generated pulses. The corresponding single pulse envelope at maximum pump power is displayed in the inset of Fig.(3.15b). It shows the full half-width maximum of about 1.44 μs .

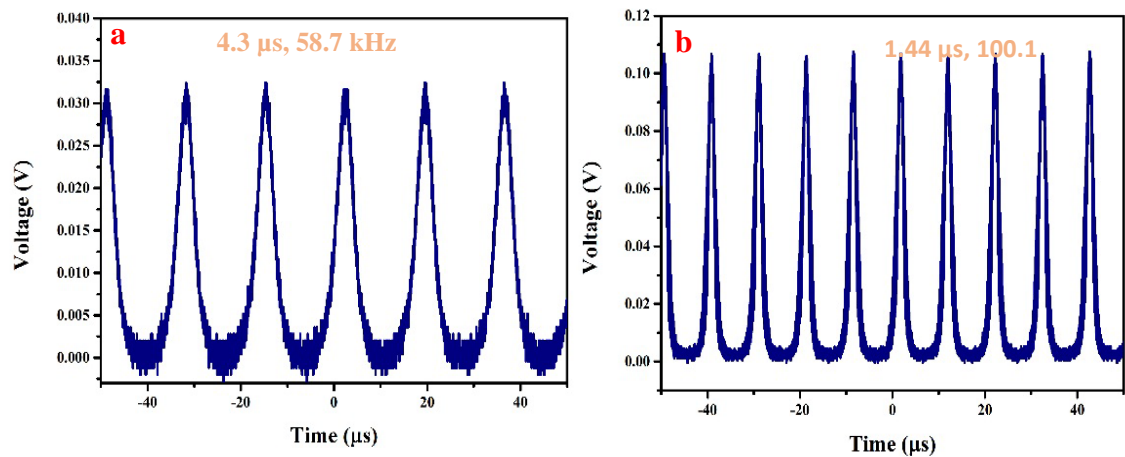


Fig.(3.14): Oscilloscope trace at: (a) 185 mW, and (b) 288 mW.

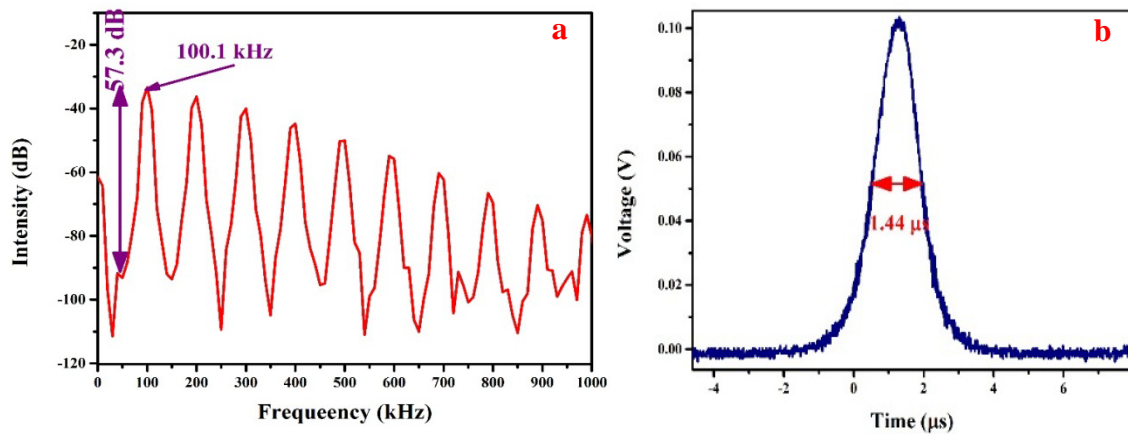


Fig. (3.15): (a) RF signal and (b) The single pulse envelope at 288 mW.

On the other hand, the effect of the boost input power on the repetition frequency and pulse duration are depicted in Fig.(3.16a). While the effect of the boost input power on the output power and pulse energy are presented in Fig.(3.16b). These results show that as the pump power boosting in the range 185-288 mW leads to boosting in the average output

power and the pulse energy between 107.15 to 445.45 μW and 1.825 to 4.45 nJ, respectively.

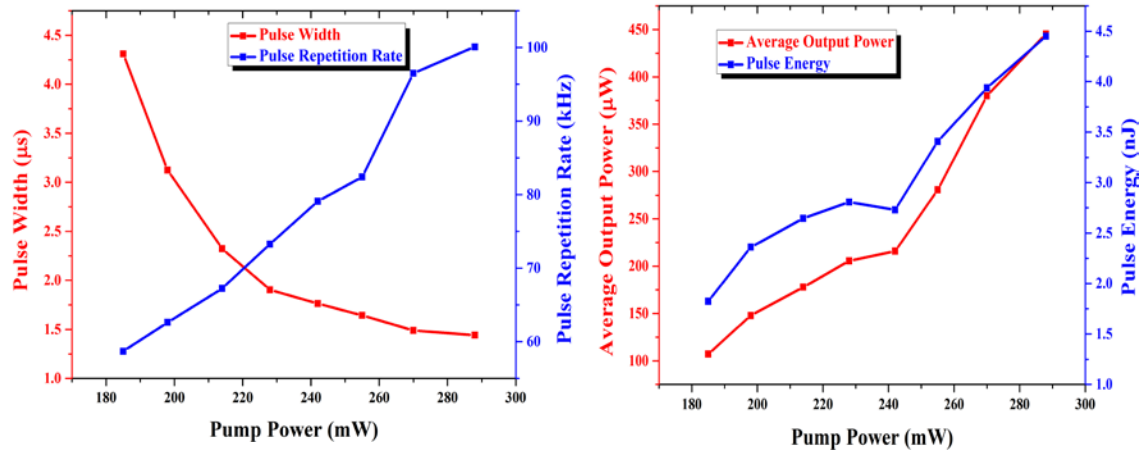


Fig.(3.16): The effect of the boost input power on (a) the repetition frequency and pulse duration, and (b) the output power and pulse energy.

The lasing lines and minimum pulse duration are related to cavity parameters such as the nonlinearity of the cavity which is controlled by the optical fiber and Ni-NPs thin film properties. Further enhancements, such as more lasing lines, narrowing the lasing lines spacing, better mode suppression, and wavelength selectivity can be achieved by optimizing the cavity parameters, as well as by adding the wavelength selective filter.

Accordingly, the piece of 1 mm \times 1 mm Ni-PVA (0.75%) was adopted inside YDFL based on 0.6 m of YDF to examine the effect of the cavity with a thin part of this nonlinear material. YDFL cavity based on Ni-PVA ran in CW regime at 65.7 mW, whereas Q-switched pulses began at a threshold pump power of 107.7 mW. Firstly, at the threshold pump power wavelength peak was detected at 1066.4 nm as presented in Fig.(3.17a). At the power increased to about 85 mW, triple wavelengths were observed which centered at 1058 nm, 1066.4 nm, and 1067.94 nm. Then, at exciting power of 96.4 mW, quadruple wavelength located at 1058 nm, 1061.5 nm, 1066.4 nm, and 1067.94 nm were detected (Fig.(3.17b)). For more progressively increased pump power, at 107.7 mW multiwavelength pulsed operation was started with a pulse width of 2.7 μs and peak to peak space

among two contiguous pulses of $16.1 \mu\text{s}$. The repetition rate raised to 91.55 kHz , however, the pulse width reduced to $1.32 \mu\text{s}$ with the rise of pump power to 170 mW . Fig.(3.18) shows the pulses train of Q-switched generation at the threshold and the maximum available pump power. The symmetric and smooth pulses were monitored at the oscilloscope with no noticeable amplitude and/or shape fluctuations in pulses, specifying the stability of the Q-switched process.

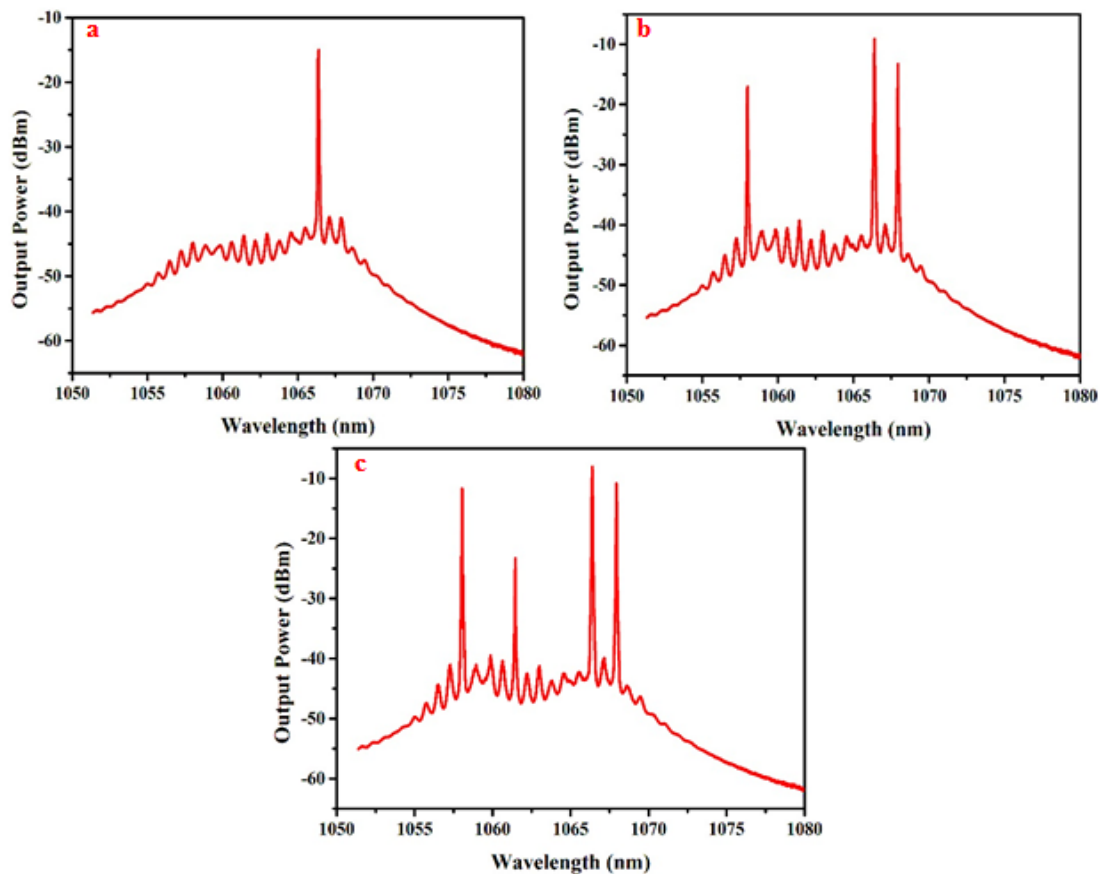


Fig.(3.17): Optical spectra of YDFL based on Ni-PVA at pump power of:
(a) 65.7 mW , (b) 85 mW , and (c) 96.4 mW .

The full characteristics of spectral, frequency domains, as well as single pulse envelope at the utmost available excited power of 170 mW are illustrated in Fig.(3.19). Whereas regarding the spectral examination, at the pump power reached about 163 mW , quintuple wavelengths were observed at peak locations 1057.4 nm , 1058 nm , 1061.5 nm , 1066.4 nm , and 1067.98 nm , as shown in Fig. (3.91a). Fig.(3.91b) offers the RF spectrum of the

proposed Q-switched laser, which possessing a fundamental frequency of 91.45 kHz with an SNR of about 54 dB. Several frequency peaks perceived in RF at the period of 1200 kHz confirm stable Q-switched generation.

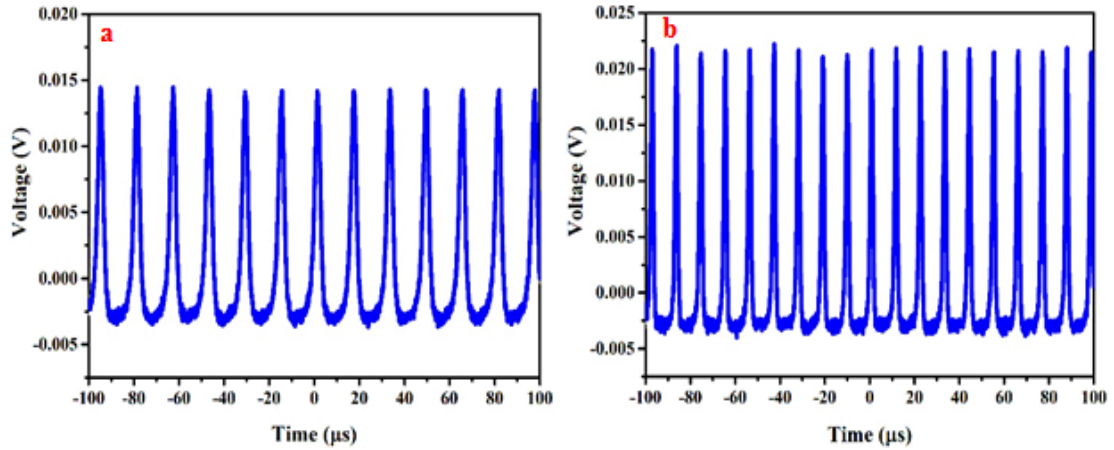


Fig.(3.18): Oscilloscope trace at pump power of: (a) 107.7 mW, and (c) 170 mW.

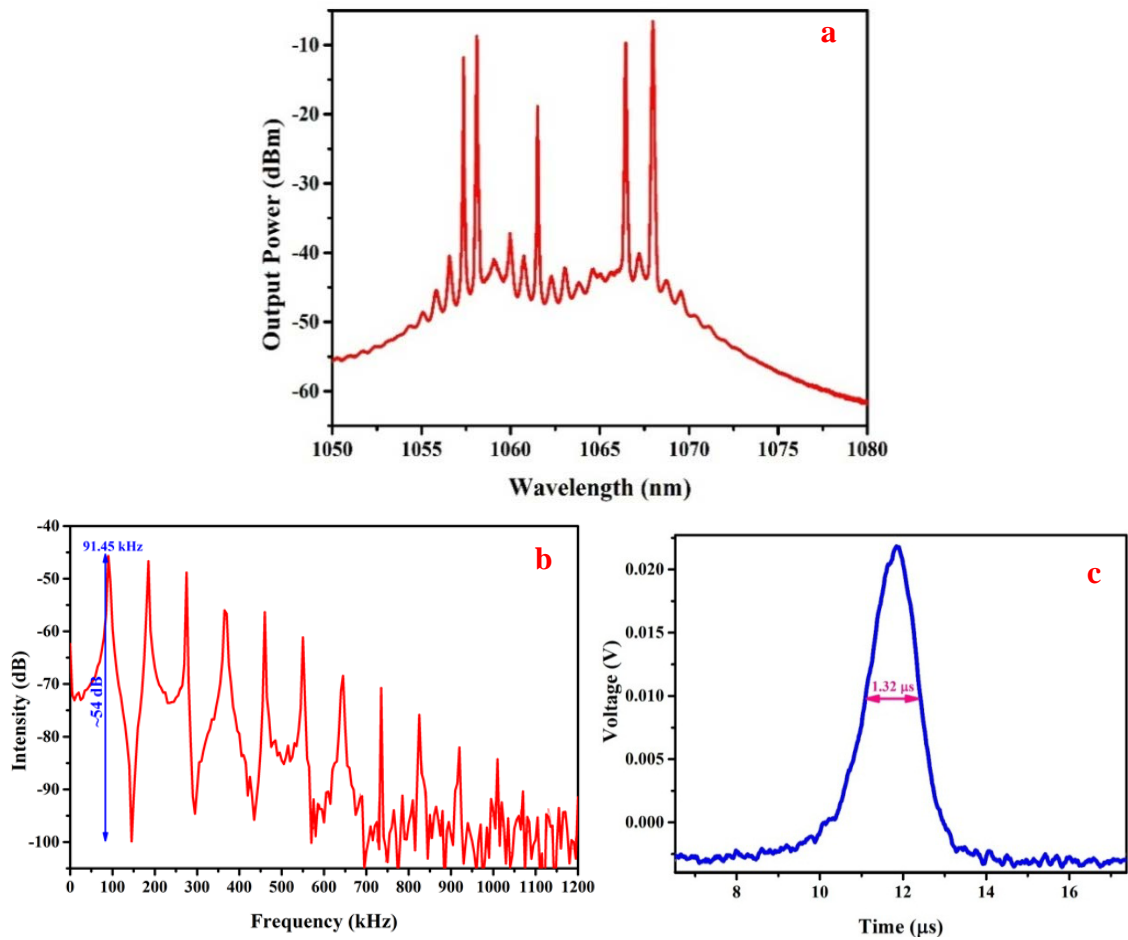


Fig.(3.19): (a) Optical spectrum, (b) RF spectrum, and (c) Single pulse profile at 170 mW.

Moreover, the largest pulse energy was registered to be 8.97 nJ, rising linearly from 0.92 nJ to 8.97 nJ, whereas, the recorded output power rises linearly up to 777.14 μW as the pump power was increased across the range 107.7-170 mW, as illustrated in Fig. (3.20a). The upsurge in the repetition frequency and reduction of pulse duration with risen exciting power is harmonious with the Q-switched process of the proposed YDFL as revealed in Fig. (3.20b). Q-switching process of the YDFL is also workable within a range exceeded the applied in the present experiment. The high nonlinear effect simultaneously with broadband absorption, good modulation depth, and low insertion loss of Ni-PVA film may improve both the stability of the multiwavelength generation and Q-switching quality, as well as it can be used in different photonics applications [187,188].

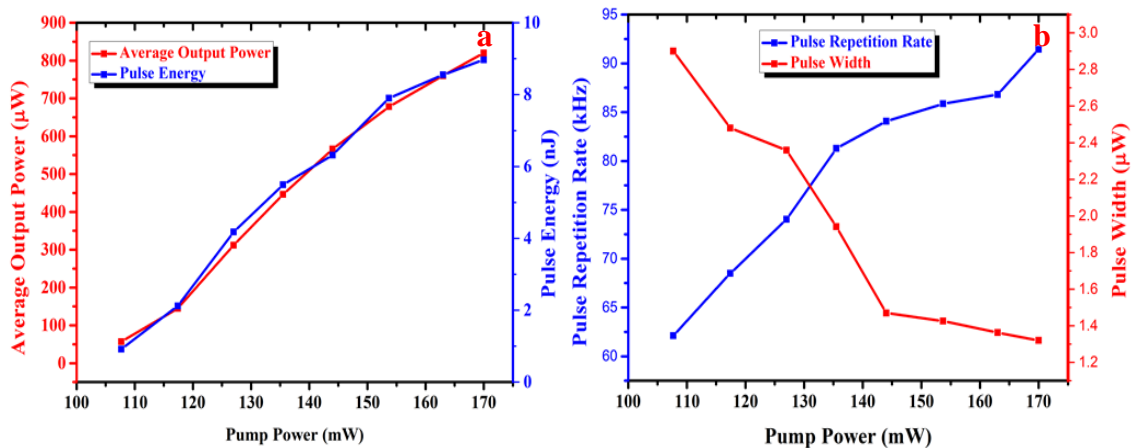


Fig.(3.20): The effect of the boost input power on (a) the repetition frequency and pulse duration, and (b) output power and pulse energy.

3.2.3 Ni-PVA Freestanding Film (1% volume)

The lasing lines and minimum pulse duration are related to cavity parameters such as the nonlinearity of the cavity which is controlled by the optical fiber and Ni-NPs thin film properties. As the linear and nonlinear properties (including absorption) are related to the doping concentration of nanoparticles in the host material, therefore, Ni-NPs is deposited with a 1% volume ratio in the PVA host to form a freestanding thin film having

different properties in comparison with the previous one. As the Ni-PVA thin film was integrated inside the YDFL ring cavity (1.5 YDF), the cavity nonlinearity was enhanced, and CW operation with a central wavelength of 1039.7 nm was generated at a threshold pump power of about 120 mW. Also, the emitted laser exhibited a blue-shifted behavior in comparison with the CW YDFL without Ni-PVA. At the pump power attained to 185 mW, dual-wavelength was observed at 1039.7 nm and 1039.1 nm. While, as the pump power reached 250 mW and 260 mW, newly switched triple- and quadruple lines appeared, respectively. Those triple- and quadruple-lines are oscillations at 1037, 1037.7, 1038.4, and 1039.1 nm. The related emission spectrum of the proposed YDFL for different pump powers is depicted in Fig.(3.21). The single-, dual-, triple-, and quadruple-line oscillations were observed with a combination of five wavelengths, namely 1039.7, 1039.1, 1038.4, 1037.7, and 1037 nm.

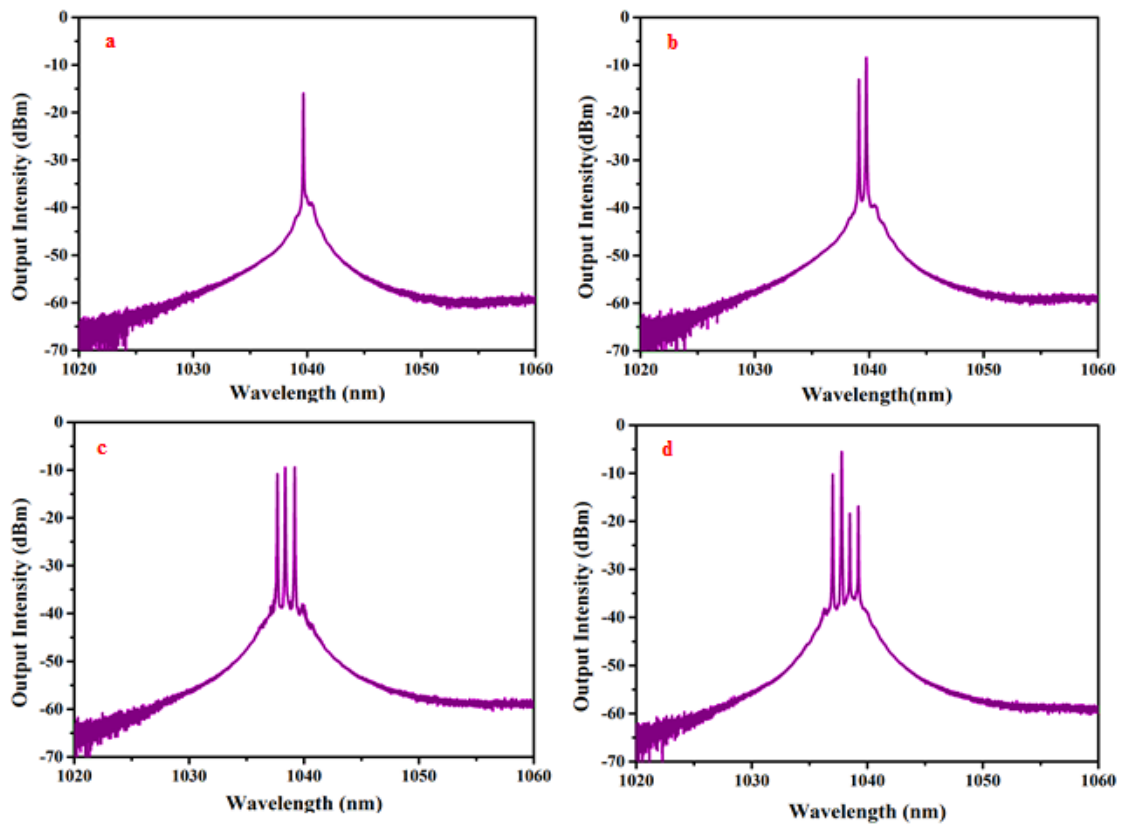


Fig.(3.21): Optical spectra at different pump powers: (a) 120, (b) 185, (c) 250 and (d) 260 mW.

These multiwavelength generations were realized with constant spacing with the assistance of the FWM effect. The FWM effect can efficiently exert control over the YDF gain profile, which leads to the mitigation of the mode competition resulting from the homogenous gain broadening in the ring cavity. The FWM effect leads to energy redistribution of various oscillating lines and then enhances the stability of multiwavelength operation. The following occurrence verifies the presence of FWM: first, the number of wavelength lines depends on the pump power, in which additional peaks might appear if the pump power increases further. This due to FWM efficiency increasing as the pump power increases. Second, all the wavelength lines are separated by a constant channel spacing of ≈ 0.7 nm. This effect resulted from the high nonlinearity of Ni-PVA thin film. Noteworthy, the wavelength spacing is determined by the lengths and the effective group indices of both the optical fiber and the nonlinear material (Ni-NPs) [25].

After that, the temporal characterization of this system was examined. Through this experiment, as the pump power reached 144 mW, a stable Q-switched pulse train self-started with a repetition rate of about 35.99 kHz and pulse duration of about 5.21 μ s. The Q-switched operation was increasingly preserved as the pump power boosts more to the maximum available pump power of 290 mW, at which the repetition rate linearly increased to 82.4 kHz and the pulse width narrowed to 138.7 ns. These are distinctive characteristics of passive Q-switching that are ascribed to the nonlinear mechanisms in both the gain medium and the saturable absorber. Fig.(3.22) shows the oscilloscope trace at 144, and 290 mW pump power, in which the corresponding pulse durations are about 5.21 μ s and 138.7 ns, respectively. The repetition rate and pulse width as a function of the pump power are depicted in Fig.(3.23a). On the other hand, the average output power and pulse energy of the proposed laser as a function of the input pump power are depicted in Fig.(3.23b).

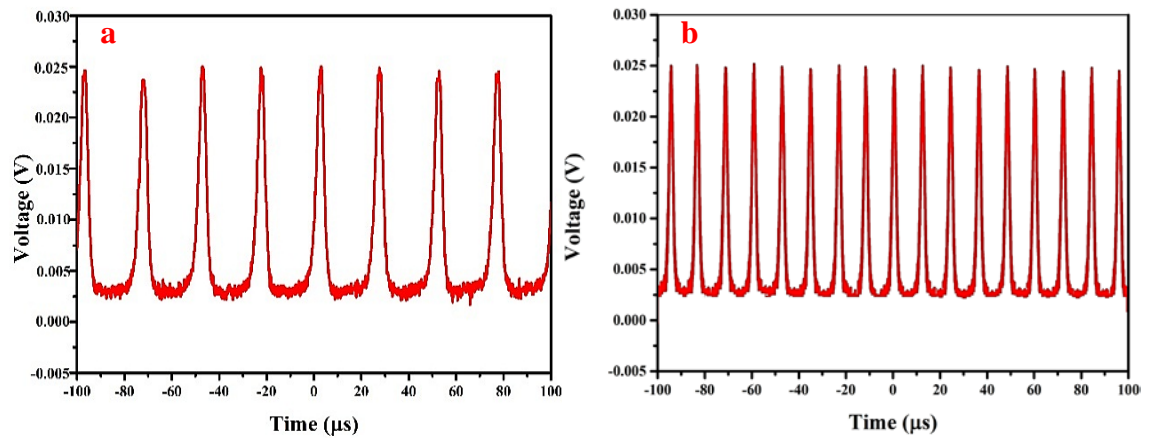


Fig.(3.22): Oscilloscope trace at (a) 144 mW, (b) 290 mW.

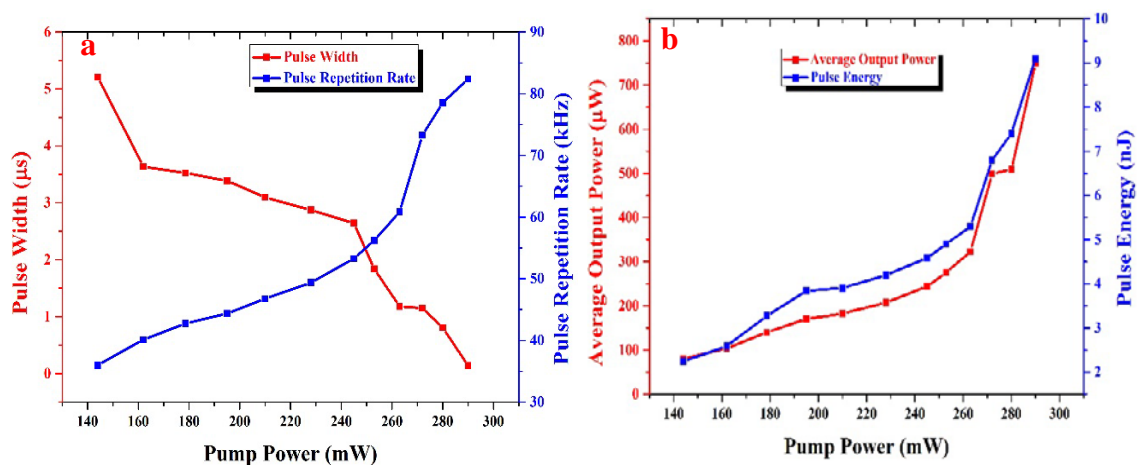


Fig.(3.23): (a) The repetition rate and Pulse width, and (b) The average output Power and pulse energy as a function of pump power.

Fig.(3.23) shows a near-linear dependence of the repetition rate, pulse width, average output power, and the pulse energy on the pump power. On the other side, the recorded output power rises linearly up to $777.14 \mu\text{W}$, whereas the pulse energy varied from 2.24 nJ to 9.1 nJ as the pump power was increased across the range $144\text{--}290 \text{ mW}$. Temporarily, the maximum peak power of 65.94 mW was achieved at the maximum pump power of 290 mW . The Q-switched fiber laser has a slope efficiency of 0.26% . The output efficiency could be improved by optimizing the cavity parameters such as reducing the insertion loss made by the SA and by adjusting the laser cavity design in terms of splice loss and fiber length [29].

Furthermore, the stability of the proposed laser can be verified by observing the RF output spectrum as well as scanning the optical spectra for a period of half an hour. Fig.(3.24a) shows the frequency characteristics of the Q-switching pulses at a pump power of 290 mW. At maximum pump power, the fundamental RF was observed at 82.40 kHz with SNR of more than 54 dB with no spectral modulation. The inset of Fig.(3.24a) shows the resultant single-pulse envelope, which displays a symmetrical, Gaussian-like shape. Fig.(3.24b) shows the laser spectrum scanning at 5-minute intervals for half an hour at a maximum pump power of 290 mW. Consequently, a stable multiwavelength with a wavelength drift and a power fluctuation of less than 0.2 nm and 3 dBm, respectively. Also, these multiwavelength generations have side mode suppression ratio (SMSR) of more than 32 dB, which can be achieved at room temperature and without the necessity for any additional intracavity filtration.

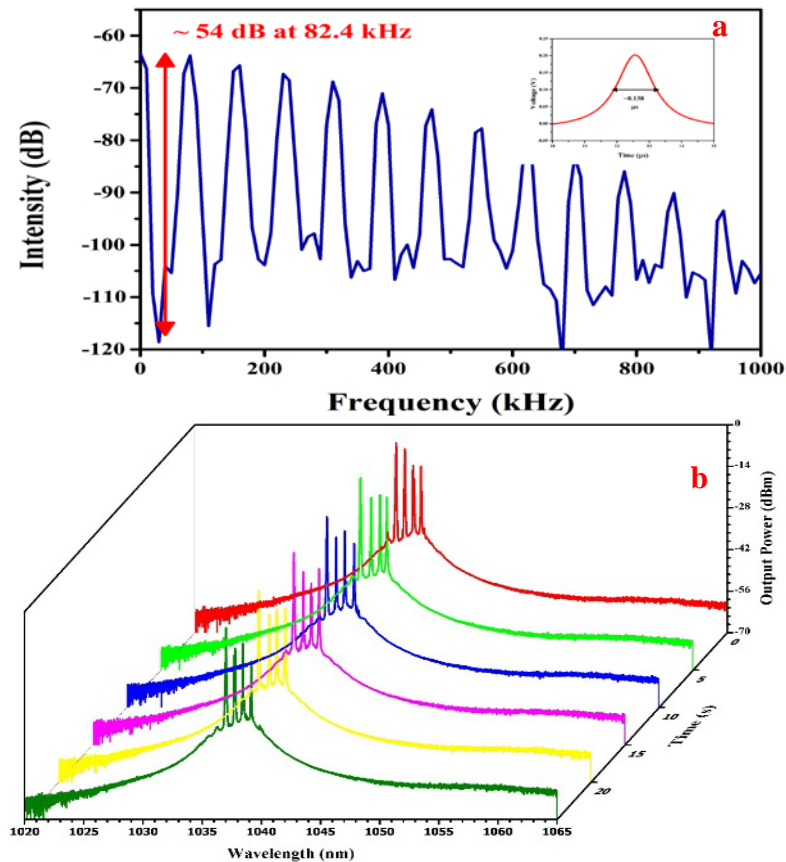


Fig. (3.24): (a) RF spectrum, and (b) optical spectra stability at a maximum pump power of 290 mW.

Additionally, the obtained results demonstrated that the output performance is analogous to that of typical Q-switched generation that utilizes other nanomaterials, such as black phosphorus [34], graphene [189], and CNTs [190], in a ytterbium-doped fiber laser cavity.

It is normal behavior for the nonlinear process of FWM to have an unequal power distribution until reaching a certain value of input pump power. Also, a small amplitude variation was noticed among the multi-lines, which was ascribed to the spectral gain behavior of the YDF. The optimization of the cavity parameters, such as the nonlinearity and the gain spectrum, is supposed to further minimize the amplitude variation. Fig.(3.24) indicates that the proposed Ni-PVA SA can promote the good stability of the YDF multiwavelength Q-switched laser.

Then, the same sample was examined with a short YDFL of 0.6 m YDF. As the Ni-PVA is integrated inside the cavity, a CW operation with a considerable spectral broadening was observed at a threshold excited power of about 96 mW. The central wavelength was located at 1061.2 nm and the FWHM linewidth of the laser peak was determined to be 1.51 nm (Fig.(3.25)).

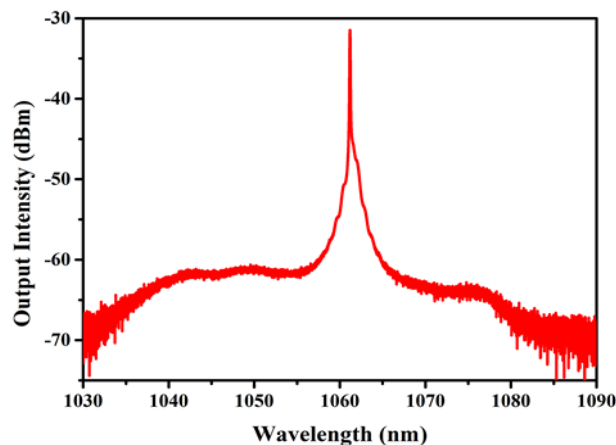


Fig.(3.25): The optical signal based Ni-PVA SA at threshold pump power.

Meanwhile, at the pump power of 121 mW, a self-starting Q-switched was begun with a repetition rate of about 16.82 kHz and pulse

duration of about $3.975\mu\text{s}$. At the stimulating power of 144 mW, the lasing peak shifted little to 1060.4 nm in the pulsed regime, as displayed in Fig. (3.26a). Fig. (3.26b) demonstrates the pulses train of Q-switched generation at exciting power of 144 mW. Dual-, and triple-line oscillations were observed namely 1037.8, 1038.4, and 1039.25 nm as the pump power attained 178.5 and 210 mW, respectively. But, as the pump power reached about 250 mW, the multiwavelength switched to mono-lasing peak, which was observed at 1037.8 nm. The emission spectra of the proposed YDFL for different pump powers are depicted in Fig.(3.27).

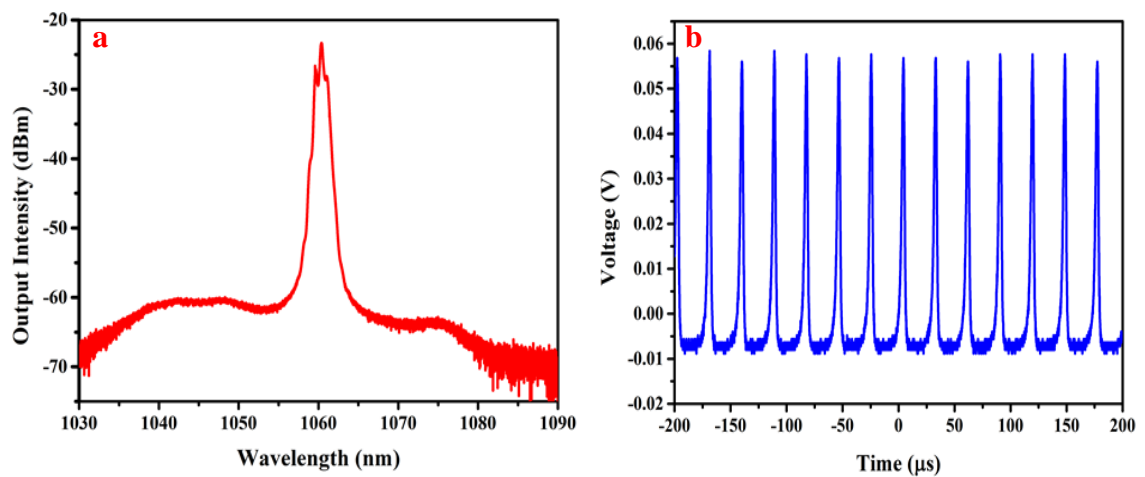


Fig.(3.26): (a) The optical, and (b) the temporal signals based Ni-PVA SA at 144 mW.

Notably, the switched single-, dual-, and triple-, peaks were realized in a tuning range around the 1040 nm and 1060 nm by just rising the pump level from 96 mW to 250 mW assisted with high nonlinearity of Ni-PVA without any intracavity. At the maximum pump power of 250 mW, the temporal signal possesses repetition rate increased linearly to 123.8 kHz and the pulse width narrowed to $1.146\mu\text{s}$. The oscilloscope trace and the RF spectrum at the utmost exciting power of 260 mW are illustrated in Fig. (3.28). Fig. (3.28c) demonstrations the RF spectrum at 260 mW of pump level. An SNR of ~ 60 dB was obtained at the fundamental frequency of 123.8 kHz which indicates a high level stability of the Q-switching.

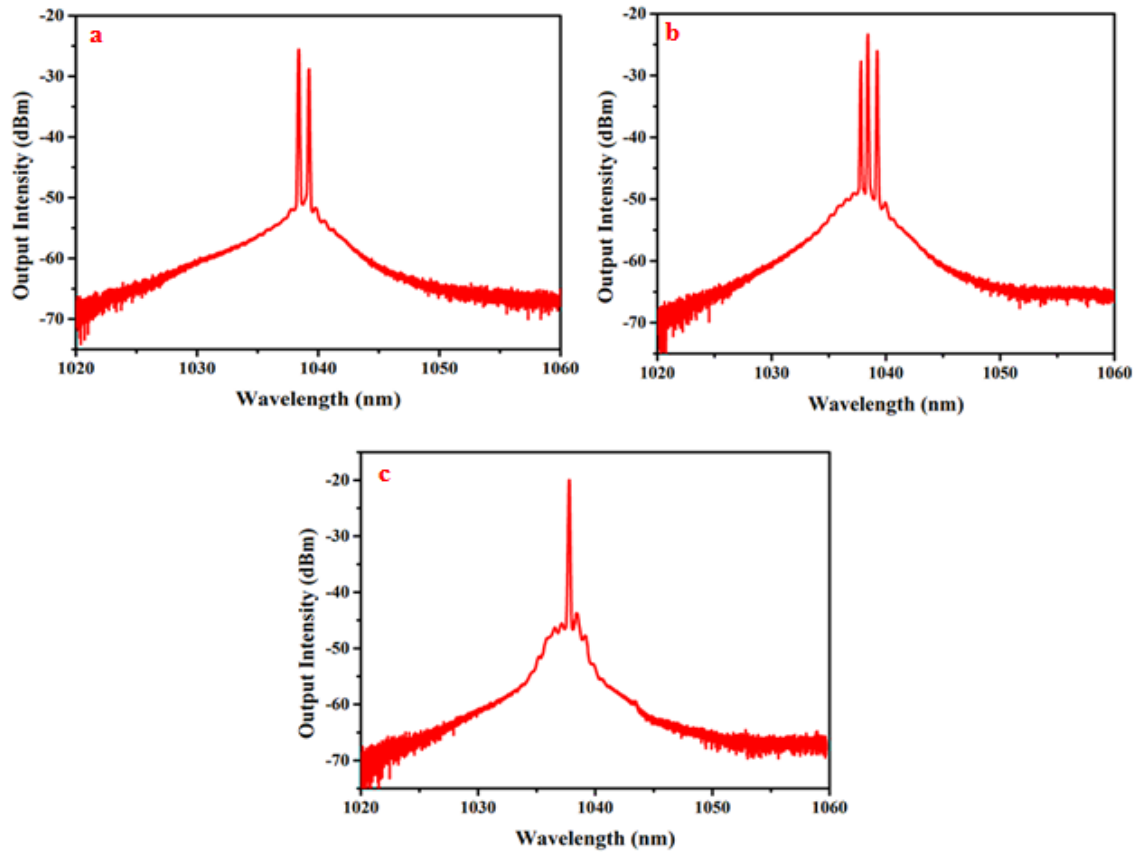


Fig.(3.27): Optical spectra at different pump powers: (a) 178.5 mW, (b) 210 mW, and (c) 250 mW.

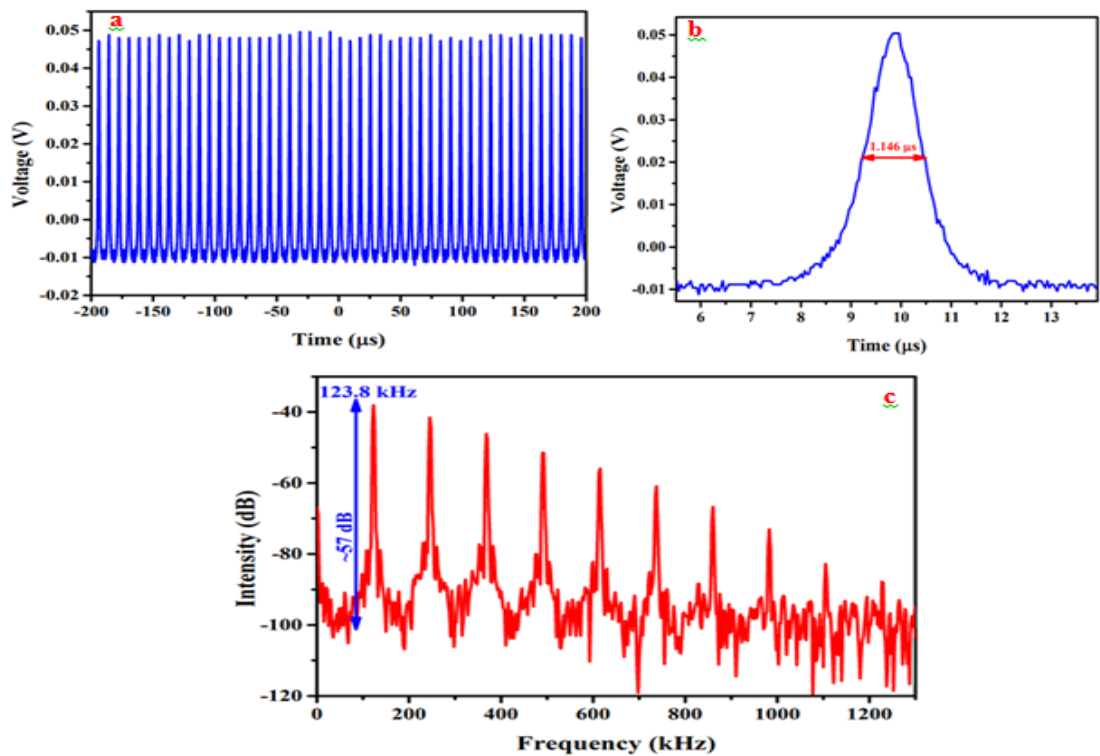


Fig. (3.28): (a) oscilloscope trace, (b) single pulse envelope, and (c) RF spectrum at 260 mW.

The inclusive estimation of the average power and pulse energy as the pump range is fine-tuned, illustrated in Fig. (3.29a). The largest recorded pulse energy was 9.54 nJ and the highest output power was 1.181 mW. The slope efficiency of the Q-switched fiber laser was 0.78 %. Also, the repetition rate and pulse width as a function of the pump power is depicted in Fig. (3.29b). These are distinctive characteristics of passive Q-switching that are ascribed to the nonlinear mechanisms in both the gain medium and the saturable absorber.

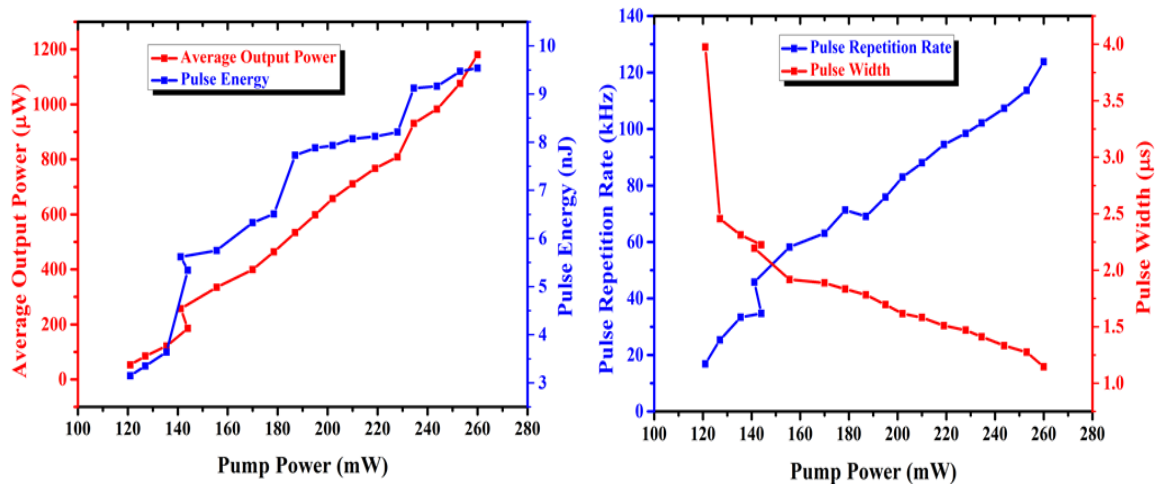


Fig.(3.29): (a) The average output power and pulse energy, and (b) the repetition rate and pulse width as a function of pump power.

3.3 Fe₂O₃ Optical Modulator

In this section, the functionality of Fe₂O₃ in YDFL based on 0.6 m of YDF is illustrated.

3.3.1 Fe₂O₃-PVA Freestanding Film

The Fe₂O₃-PVA thin film was inserted into the YDFL cavity via a fiber adaptor among two SMF pigtails as the optical equalizer and stabilizer due to their high nonlinearity. Through this work, as the pump power progressively raised between 102-170 mW and without any intracavity, six lasing lines were observed around 1040 nm with a bandwidth of about 4.5 nm (Fig.3.30)). Herein, it found that as the Fe₂O₃-PVA thin film incorporated inside the cavity, a blue-shifted lasing line centered at 1041.69 nm was detected at the threshold pump power of 102 mW. More gradually

rising the pump level to be about 170 mW, stable dual, triple, quadruple, and quintuple multiwavelength lasing channel were perceived at 1039.06, 1039.95, 1040.54, 1041.29, 1041.69, and 1042.54 nm inducing by the high nonlinear effect of Fe_2O_3 NPs. But, both the wavelength and power of lasing lines were suffered from some fluctuation due to the mode competition of the YDF spectrum.

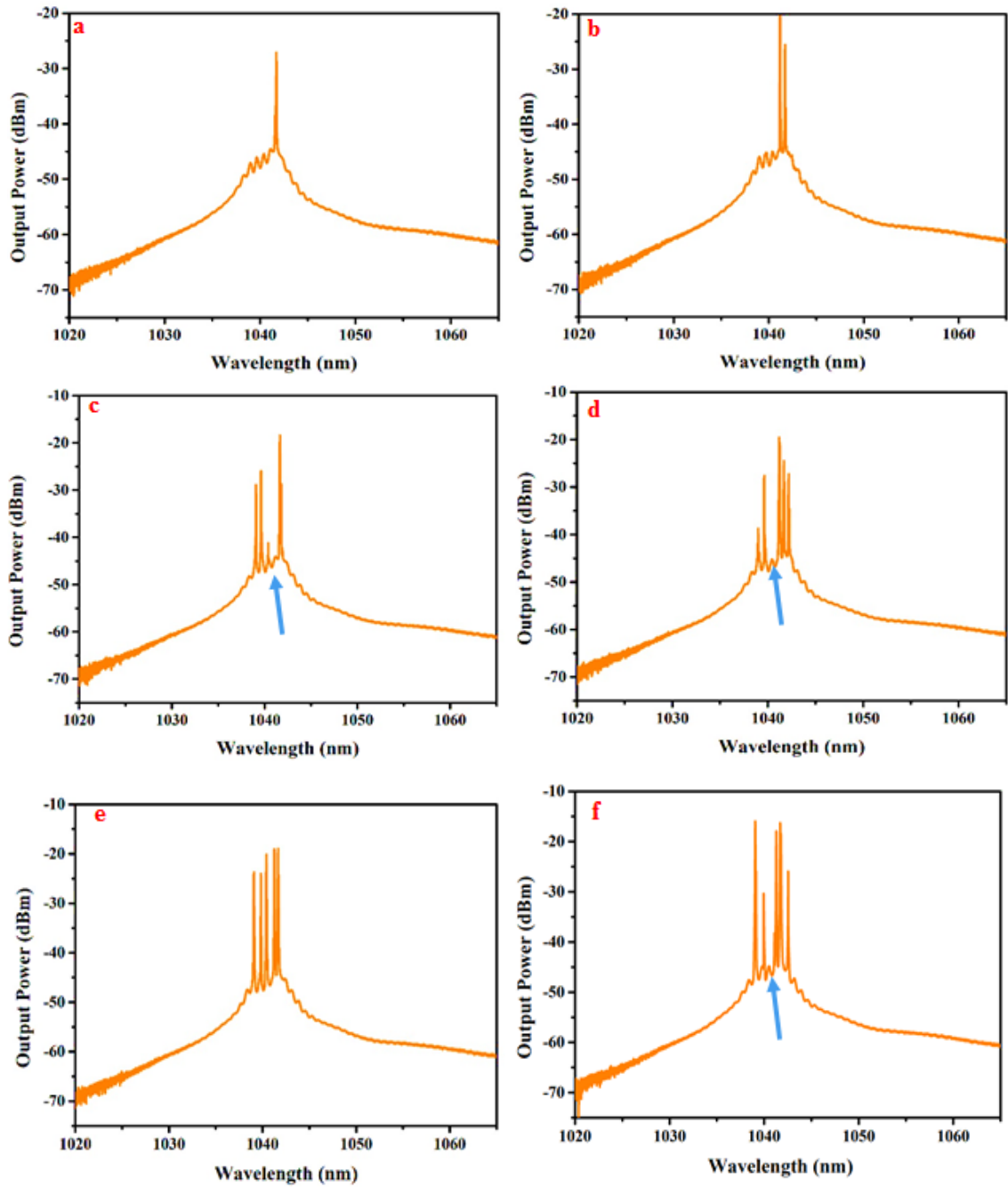


Fig. (3.30): Optical spectra of YDFL based on Fe_2O_3 -PVA thin film at (a) 102 mW, (b) 107.7 mW, (c) 117.4 mW, (d) 127 mW, (e) 135.5 mW, and (f) 170 mW.

Due to this experiment, no pulse signal is detected as there is no sign on the oscilloscope to suggest the existence of pulses, although the Fe_2O_3 -PVA thin film possesses the saturation absorption property (as noted in the characterization section in Fe_2O_3 -PVA to generate pulses by Q-switching or locking mode). The main subject in the understanding of the reason for accomplishing the CW lasing operation can be explaining as follow. It is recognized that the encouraging of pulse operation (Q-switched or mode-locked) demands a precise balance of the numerous parameters in the laser modulator especially the nonlinearity and dispersion effects. Therefore, in the present work, the conceivable reason is that the deposited thin film does not convene the necessities of the pulse laser operation.

3.3.2 Fe_2O_3 Thin Layer Based NF

The influence of Fe_2O_3 -NF on the YDF was examined. One and two consecutive layers of the coating were applied thru dipping the fiber tip into the NF and then followed by dehydration at room temperature. Firstly, one layer of Fe_2O_3 -NF was applied, which as boosting the exciting power to about 85 mW, laser light was emitted at a central wavelength of about 1065.7 nm. Then dual lasing lines were observed at 1051.7 and 1056.7 nm as the exciting power reached about 150 mW. The optical signals at threshold and 150 mW are presented in Fig.(3.31).

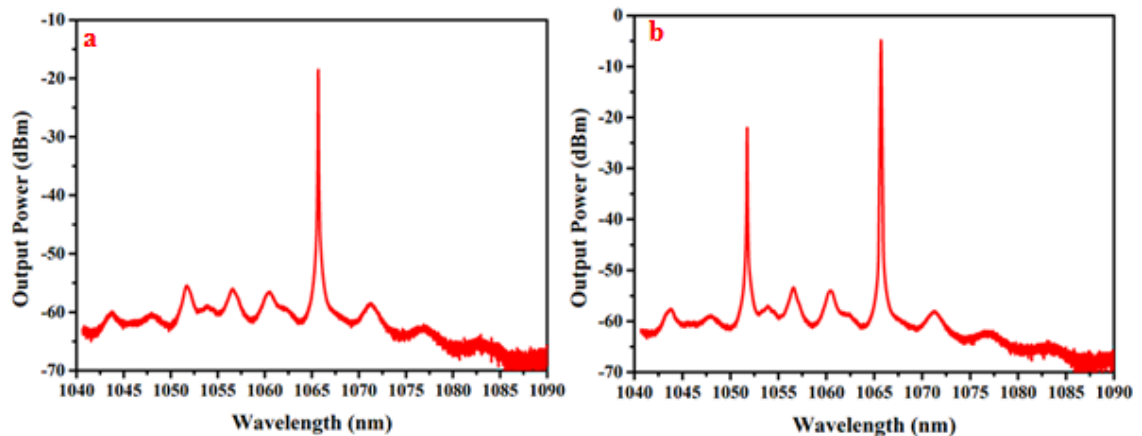


Fig. (3.31): Optical spectra of YDFL based on Fe_2O_3 -thin layer at (a) 85 mW, and (b) 150.

On the other side, the temporal examination proved that Fe_2O_3 -thin layer persuaded a pulse operation represented by the mode-locked signal as the bleaching power attained to about 120 mW. At 120 mW, stable mode-locked pulses were created as the rotational and compression forces of the in-line polarization controller was precisely adopted, which this polarization adaptation is necessitated owing to the polarization dependency gain/loss of the fiber oscillator and the polarization dependency of the Fe_2O_3 -thin layer optical modulator itself. Fig.(3.32) show the temporal and RF signal at the exciting power of about 120 mW, the characteristic pulse with a repetition frequency of 26.8 MHz that matched the cavity length (~ 7.5 m). Fig.(3.32b) displays the RF spectrum, in which a wide signal amplitude with a sampling rate of 26.8 MHz is noticed and more to ~ 38 dB of SNR is estimated. By zooming the mono-pulse, then ~ 18.6 ns is evaluated, as presented in Fig. (3.32c).

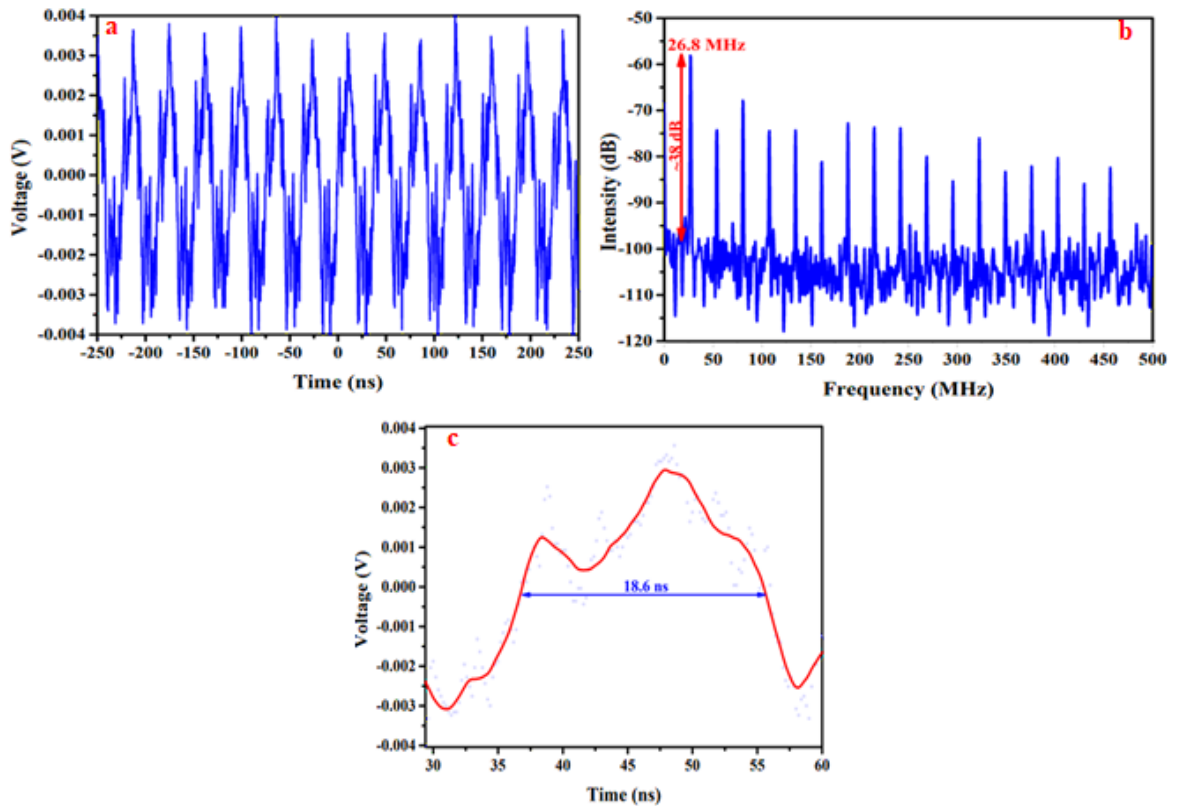


Fig. (3.32): (a) Oscilloscope trace, (b) RF spectrum, and (c) single pulse envelope at 120 mW.

Some ripple observed in the pulse, this due to the Q-switching instability. The reason for the switching instability effect is the following. Beginning from the steady-state of CW mode-locked, any little rise in the pulse energy causes greater saturation of the saturable absorption property of the optical modulator and consequently to a positive net gain. So, this cause to the exponential increase of the pulse energy pending this increase is stationary by gain saturation. Usually, fiber laser reveals a big gain saturation fluence, which might withstand several cavity round-trips. Then, the pulse energy declines much less than the steady-state level. The swaying around the steady-state is stopped only if gain saturation puts in quick enough, which leads ultimately to obtain the stable CW mode-locked. This obtained at the pump power reached about 200 mW, which dark mode-locked pulses were generated with a pulse width of about 6.6 ns was generated. The temporal and RF signals of the generated pulses at 200 mW are illustrated in Fig.(3.33).

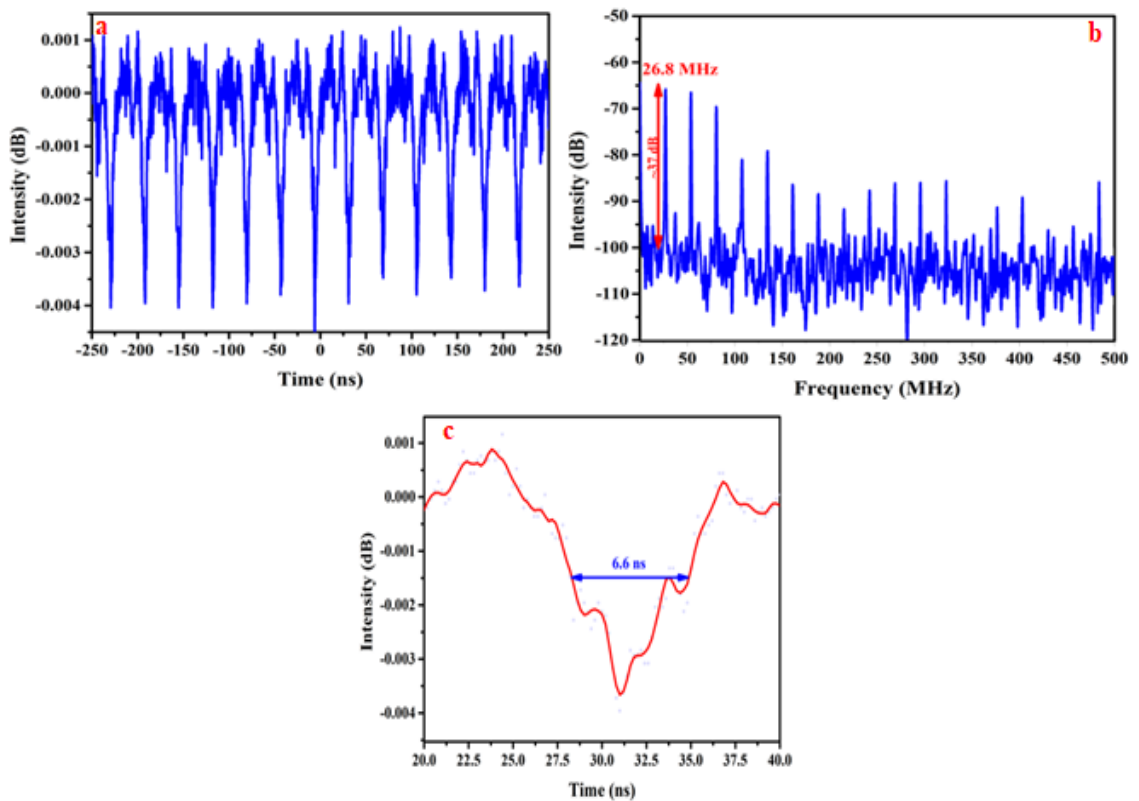


Fig. (3.33): (a) Oscilloscope trace, (b) RF spectrum, and (c) single pulse envelope at 200 mW.

Nanosecond pulses were obtained from this cavity owing to the cavity dispersion was not managed. Also, it should be noted that with no autocorrelator, the measured pulse width does not represent the true value. The average output power versus the pump power was also examined, as illustrated in Fig.(3.34). From this figure, it is noticeable to remark that the output power upsurges in the range 0.124-4.221 mW concerning to stimulating power uprising among the range of 85-250 mW. The slope efficiency of the proposed cavity is ~2.447%.

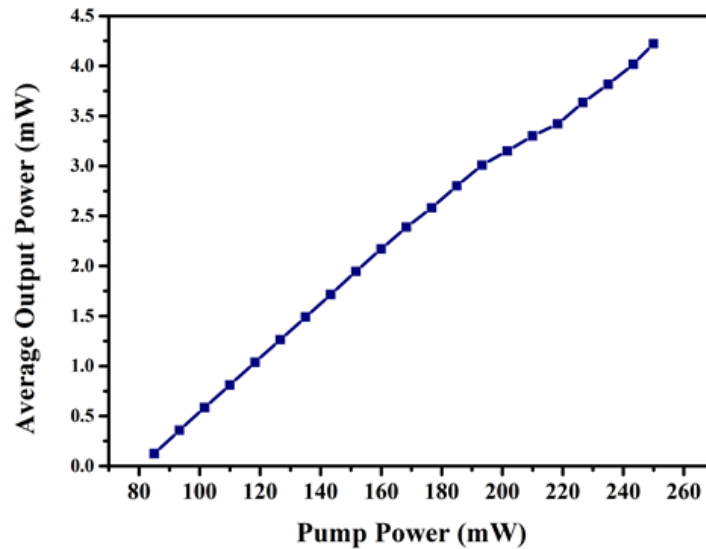


Fig. (3.34): Average power vs. the pump power.

Later, another layer was added above the first one using the same previous technique. Herein, the optical modulator properties (including the absorption, dispersion, modulation depth, etc.) could be changed with the dropped layer's number on the fiber tip. As the two-layer of Fe_2O_3 -thin layer is integrated within the YDFL, the emitted laser had been generated at a bleaching power of about 85 mW, centered at 1060.239 nm with a side-mode suppression ratio of about 24.1 dBm. Many side-modes were detected at this pump power centered at 1059.599 nm and 1063.099 nm, with peak power of about -39.876 dBm, and -44.549 dBm, respectively. Dual-lasing lines were observed at 1051.634 nm and 1064.632 nm as the pump power reached about 102 mW. As the pump power increased to

about 187 mW, triple-lasing lines centered at 1043.355 nm, 1051.147 nm, and 1064.671 nm were observed. Optical spectra at different pump powers are depicted in Fig.(3.35).

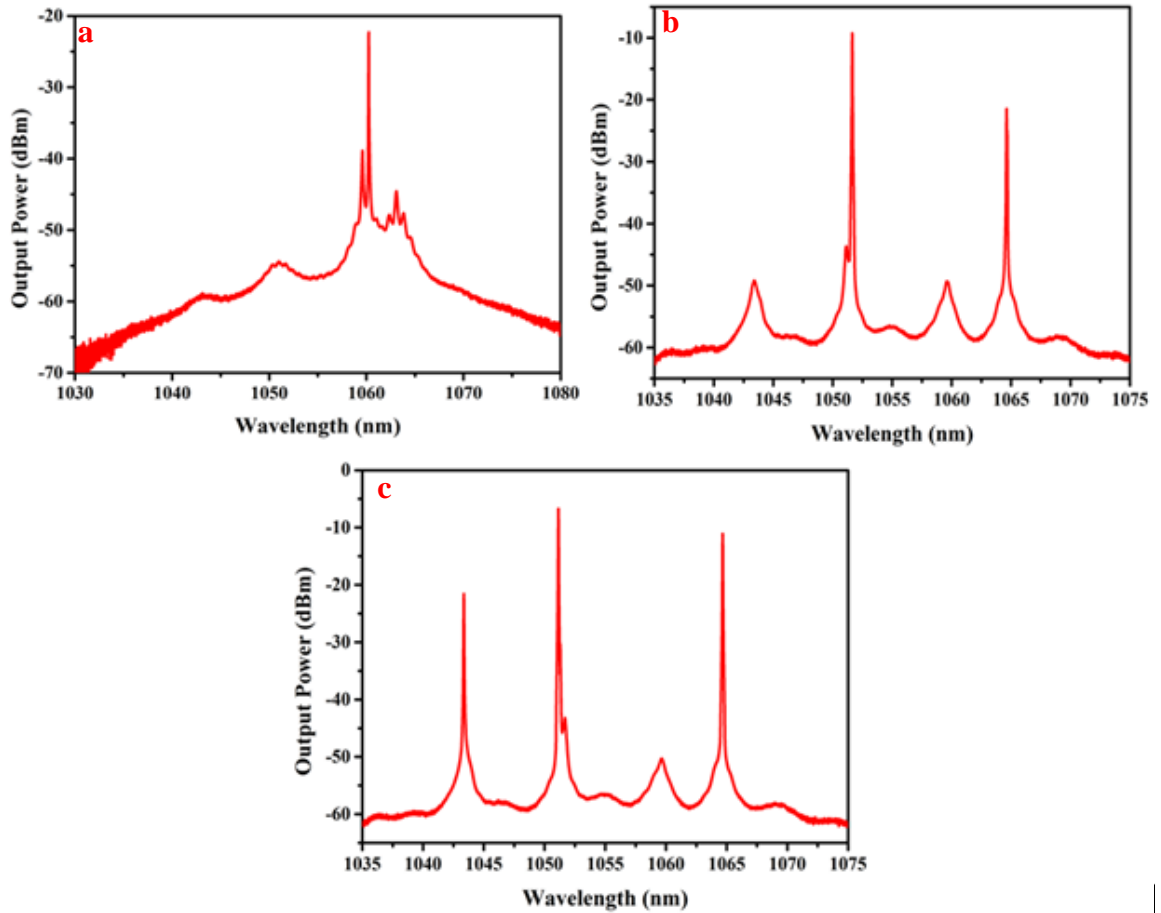


Fig. (3.35): Optical spectra of YDFL based on $\text{Fe}_2\text{O}_3\text{-NF}$ at (a) 85 mW, (b) 102 mW, and (c) 187 mW.

In the temporal examination part, the oscilloscope monitor showed that Fe_2O_3 -thin layer induces a pulse operation within the cavity represented by a mode-locked signal as the pump power reached about 110 mW. Herein, the polarization adjustment is requisite, so three puddles PC was integrated into the cavity. After several attempts to adjust the polarization within the cavity using the PC altogether with pump power, a bright mode-locked with second harmonics generation was observed. The oscilloscope trace, the single pulse envelope, and the RF spectrum are depicted in Fig. (3.36).

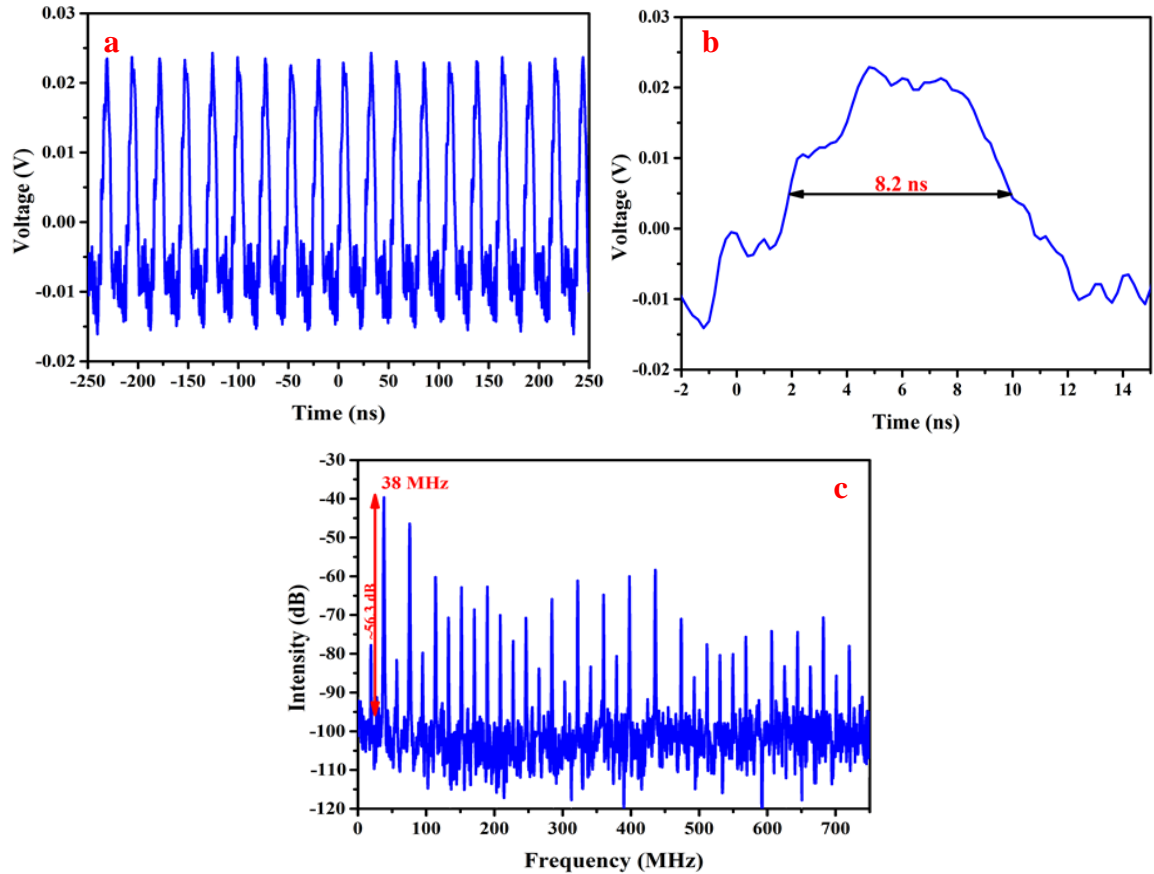


Fig. (3.36): (a) Oscilloscope trace, (b) single pulse envelope, and (c) RF spectrum at 250 mW.

On the other hand, the impact of the polarization state of the propagation signals is exported. With simultaneous changing of three puddles PC, both the intensity and the central wavelength deviation of the multiwavelength will be shifted, as shown in Fig. (3.37). At the maximum power of about 250 mW, single-line (1056.9 nm), dual-line (1056.8 nm and 1062.39 nm), triple-line (1039.19 nm, 1047.36 nm, and 1056.8 nm), and quadruple-line (1039.2 nm, 1047.36 nm, 1056.8 nm, and 1062.35 nm) were observed by simply adjusted the PC. More details about the effects of the three puddles PC on the YDF cavity have been explained in section 3.5.

Finally, the average output power versus the pump power was also examined, as illustrated in Fig.(3.38). From this figure, it is observable to distinguish that the output power upsurges in the range 75.06 μ W-4.426

mW associating to stimulating power uprising among the range of 85-250 mW. The slope efficiency of the proposed cavity is $\sim 2.628\%$.

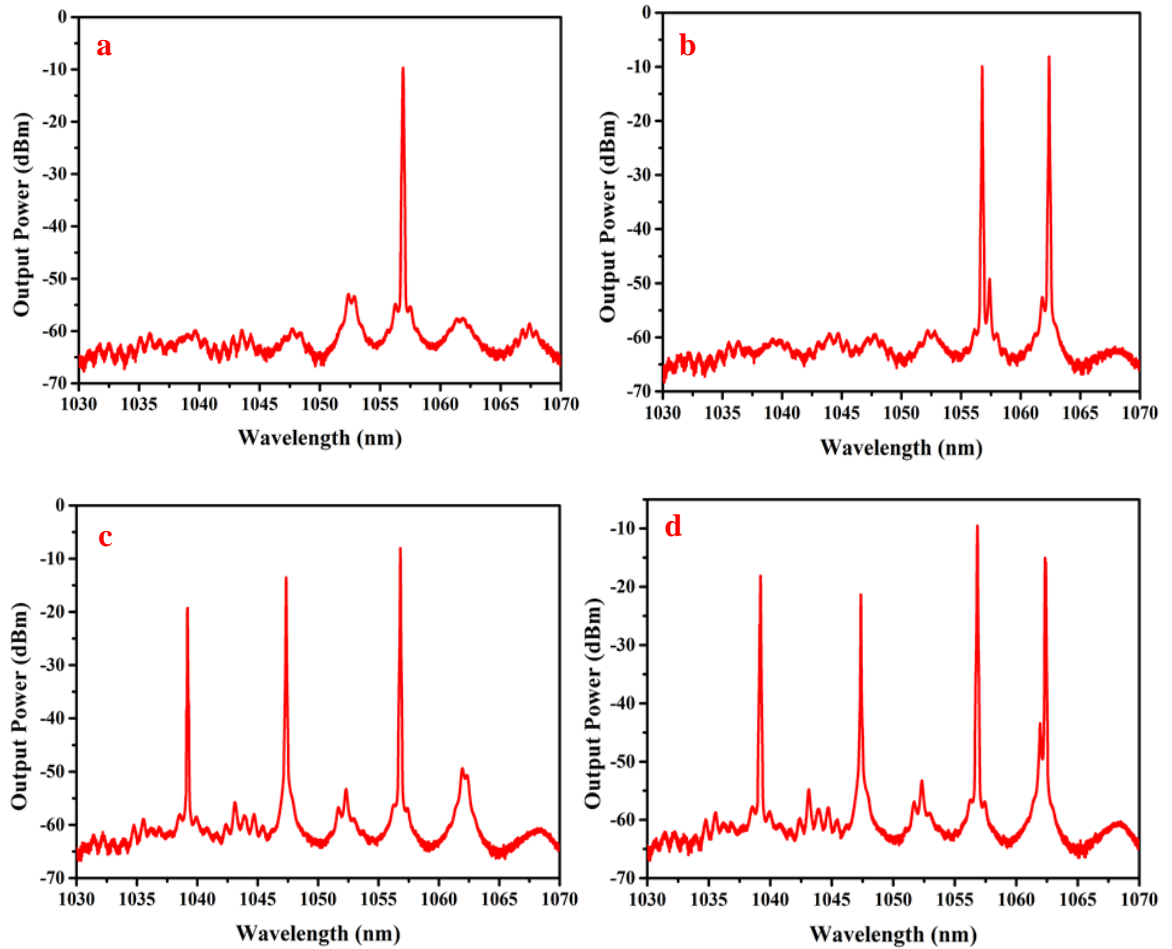


Fig. (3.37): Optical spectra of YDFL based on Fe_2O_3 -thin layer at 250 mW with different PC states.

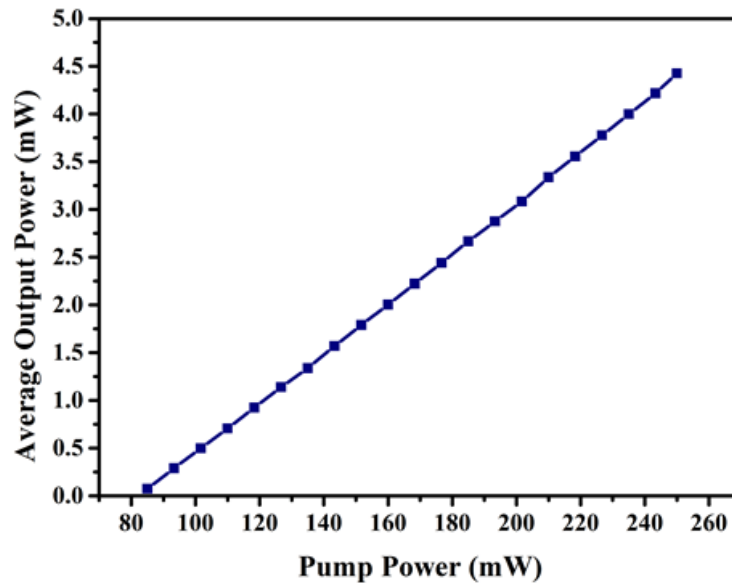


Fig. (3.38): Average power vs. the pump power.

3.4 SiO₂ Optical SA

In this section, the functionality of SiO₂ in YDFL based on 0.6 m of YDF has been illustrated.

3.4.1 SiO₂-PVA Freestanding Film

The spectral examination results of the YDFL based on SiO₂-PVA achieved in this experiment are displayed in Fig. (3.39). As the SiO₂-PVA thin film was inserted between the FC/PC fiber connector of the YDFL cavity based on 0.6 m of YDF, the CW laser was generated at a bleaching power of about 90.7 mW.

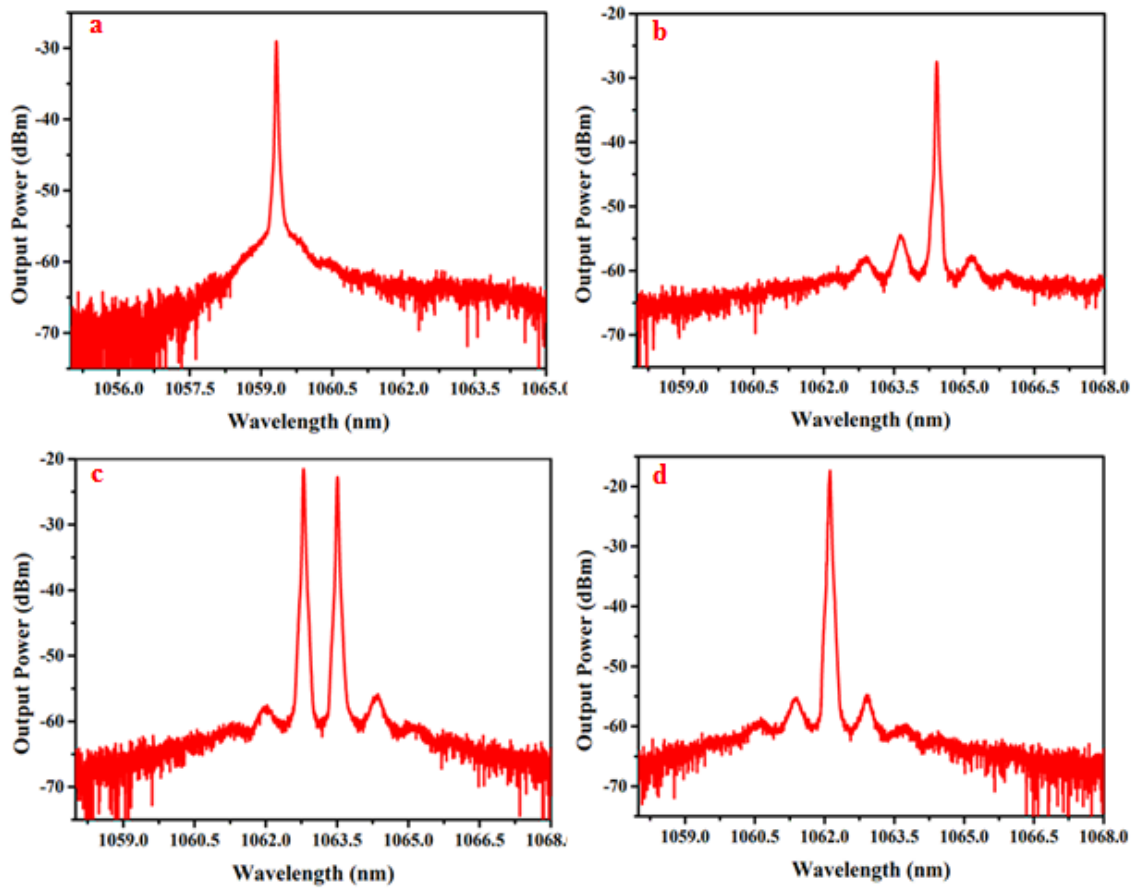


Fig. (3.39): Optical spectra of YDFL based on SiO₂/PVA thin film at (a) 90.7 mW, (b) 102 mw, (c) 121.3 mW, and (d) 170 mW.

This figure reveals the optical spectra of the generated laser at different pump powers, which designates that the YDFL based on SiO₂-PVA functioned as a switchable wavelength as the pump power varied between 90.7 mW and 170 mW. The center wavelength of the generated

laser at the threshold pump power of 90.7 mW is 1059.328 nm with a 3 dB spectral width of about 0.12 nm and SNR of about 31.4 dBm. As the pump power reached about 102 mW, the central wavelength was switched to a location of 1064.412 nm, while as the pump power increased more to 121.3 mW, dual-wavelength centered at 1062.796, 1063.508 nm were observed. Moreover, at 170 mW, the optical spectrum of the generated laser shown in Fig.(3.39d) proved that the output wavelength switched to 1062.116 nm central wavelength, with SNR of about 43.6 dBm and 3 dB spectral width of about 0.21. Through this work, no pulse signal has been noticed as there is no sign on the oscilloscope to suggest the existence of pulses, which might be attributed to that the deposited thin film does not convene the necessities of the laser pulse generation.

3.4.1 SiO₂ Thin Layer Based-NF

For more examination, a drip of SiO₂-NF was placed on the fiber end and then left to dry for several minutes after placed the fiber in vertical form. The laser started as the pump power reached 85 mW. The CW operation was generated at a central wavelength of 1064.46 nm with an SNR of about 29.1 dBm. While as the pump power increased to 96.4, 102, and 170 mW, dual-, triple-, and quadruple-lasing lines were emitted at 1062.9, 1063.7, 1064.5, 1065.3 nm, respectively, with constant line spacing of about 0.8 nm. These multiwavelength generations were realized with constant spacing with the assistance of the FWM effect. It can be noticed that the multiple-lasing lines are uneven (Fig (3.40)); it is normal behavior for the nonlinear process of FWM to have an unequal power distribution until reaching a certain value of input pump power. On the other side, at the pump power of 93.5 mW, it can be perceived that there a pulse signal was monitored on the oscilloscope. This pulse operation still unstable despite that the power increased to maximum available pump power. To powerfully augment the mode-locked lasing efficiency via fulfilling a

suitable regulating of the polarization-reliance gain/loss within the laser oscillator, the PC was employed to detune the polarization condition of the travelling wave in the YDFL cavity and to lessen polarization mode rivalry. The temporal signal still suffers instability but it looked like a Q-switched mode-locked laser generation, as shown in Fig(4.41).

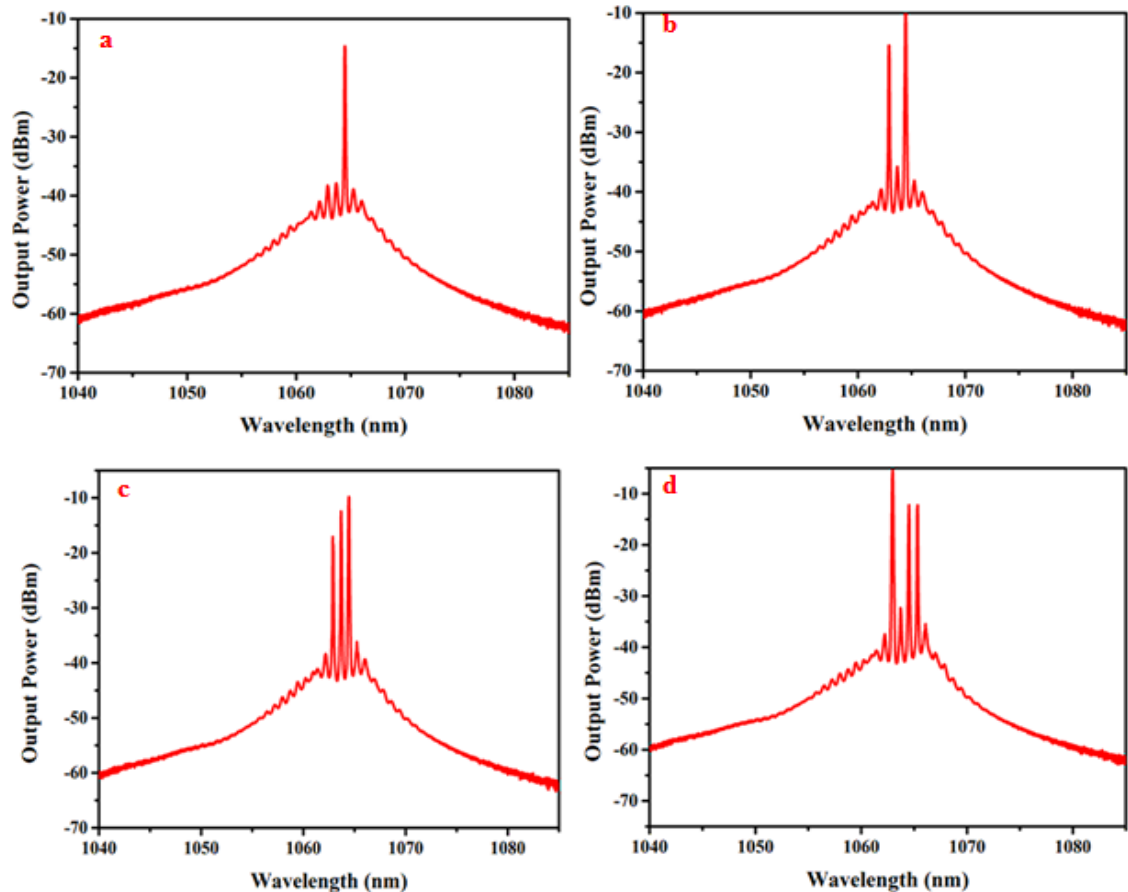


Fig. (3.40): Optical spectra of YDFL based on SiO₂ suspension at (a) 90.7 mW, (b) 102 mw, (c) 121.3 mW, and (d) 170 mW.

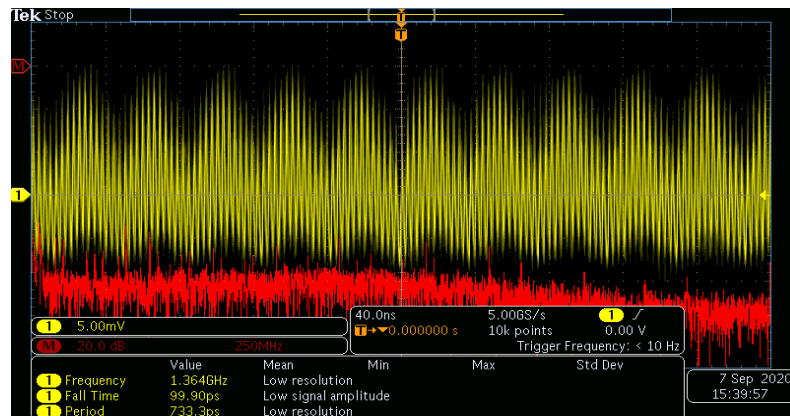


Fig.(3.41): Oscilloscope trace of YDFL based on SiO₂ suspension.

Among the utilized nanomaterials in the present thesis, the SiO_2 exhibits a large influence on the polarization state. As the polarization controller integrated with a presently utilized cavity, the bleaching power was increased to about 90.7 mW and the laser radiated was shifted to wavelength around 1061.24 nm, as shown in Fig (3.42a). Then triple-wavelength located at 1055.53, 1061.24, and 1066.35 nm were observed as the pump power increased to about 102. But, as the pump power reached about 170 mW, and with carefully adjusted the PC, quadruple-wavelength located at 1054.46, 1060.39, 1061.46, 1065.97 were detected. The optical spectra at different pump power are depicted in Fig.(3.42).

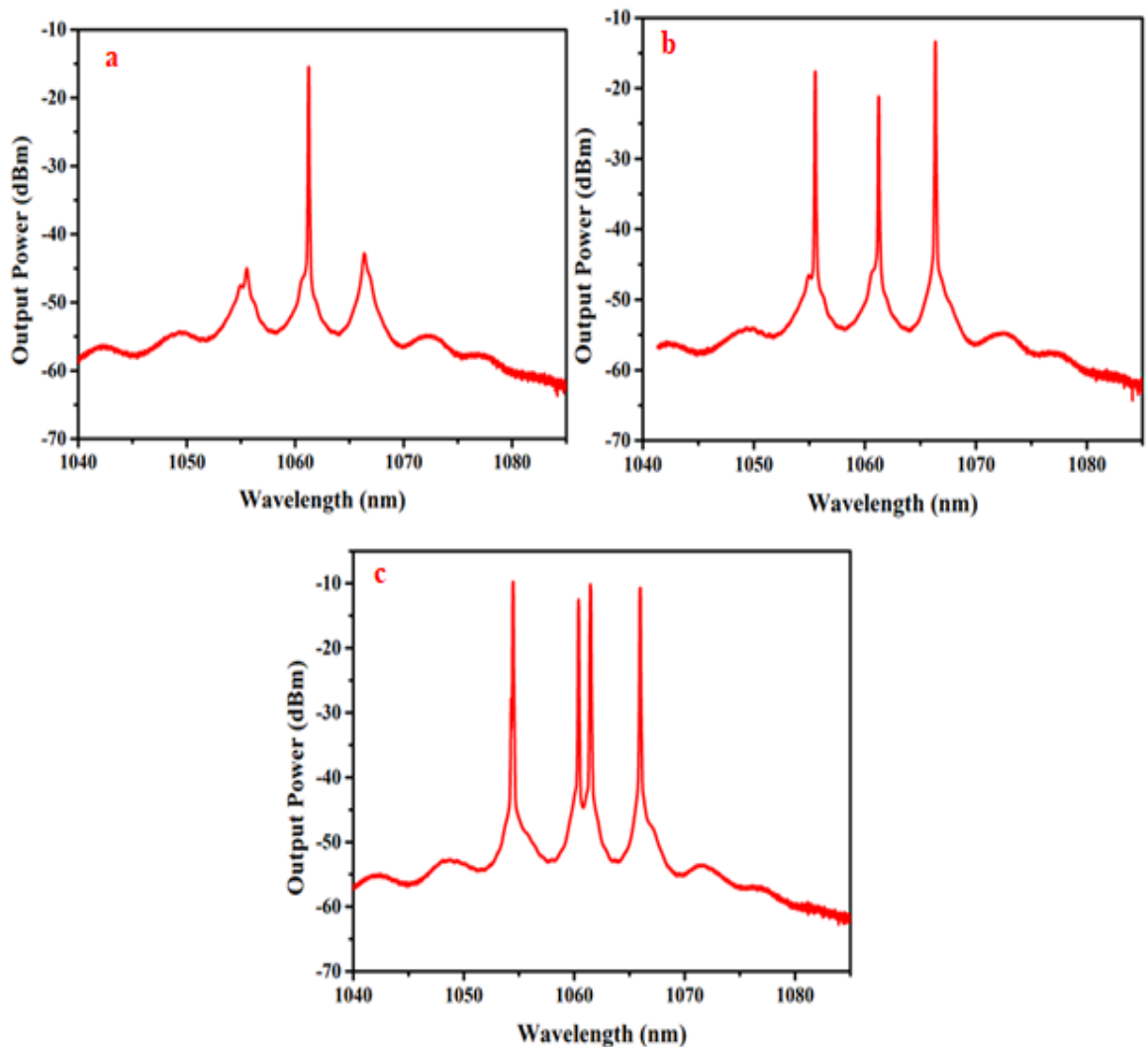


Fig. (3.42): Optical spectra of YDFL based on SiO_2 suspension and polarization controller at (a) 90.7 mW, (b) 102 mw, (c) 121.3 mW, and (d) 170 mW.

Notably, the optimization of the polarization state of light inside the cavity can act a job in the spectral gain of the fiber lasers and assist with passive/active effect to minimize the mode competition and achieve multiwavelength generation. Herein, the intensity-dependent loss produced by adjusting the PC can be employed to efficiently mitigate the mode competition, as well as the intensities and lasing line locations of multiwavelength, which are mostly determined by the spectrum function of the cavity birefringence. Through the fine-tuning of the PC that causes the adaptations of the cavity birefringence, the quadruple lasing-lines could be achieved. So, the line spacing of the multiple-lasing lines corresponds to cavity birefringence. In this work, other wavelength lines could also be achieved thru adopting the PC; however, the most stable lasing lines were presented here. Generally, the relative strength of the temporal signal and the line spacing among the lasing lines could be altered thru fine-adjust the PC, in which the lasing pulses must instantaneously fulfill both the mode-locking condition and the spectral function of the gain equalizer. However, the mode-locking stability condition was not satisfied in this experiment, which this cavity needs some dispersion management process. In our lab, not have the HI-1060 fiber that is used in dispersion management in this wavelength region.

Finally, the average output power versus the pump power was examined for the YDF laser based on both the SiO₂-PVA and SiO₂-thin layer samples. This laser cavity reveals slope efficiencies of about 2.576% and, 3.037% based on SiO₂/PVA and SiO₂-thin layer samples, respectively. The relation between the input power and average output power based on these samples is illustrated in Fig.(3.43).

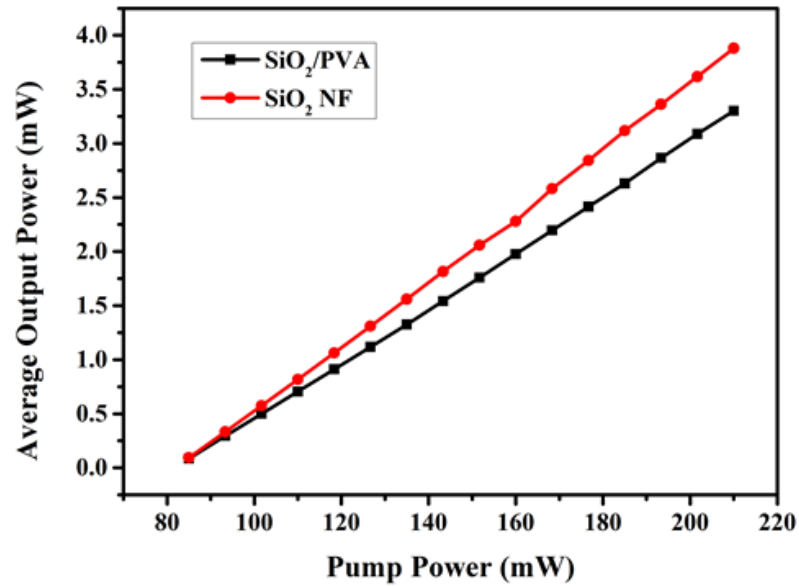


Fig. (3.43): Average power vs. the pump power.

3.5 Fe₂O₃/SiO₂ Optical Modulator

Nanocomposites are recently applied to improve the linear and nonlinear optical properties inconsequent to other physical and mechanical properties. On the other side, the dielectric media such as silica glass containing ferroelectric nanoparticles are being a new approach that is proposed to realize unique optoelectronic features under field coupling. Also, it was proved that the random parts of the distribution of nanoparticles cause giant variation in the local electromagnetic field. Herein, the blend effects and the good optical properties of both Fe₂O₃ and SiO₂ nanoparticles have been exploited, which extra nonlinear effect inside the cavity might appear.

As the Fe₂O₃/SiO₂ nanocomposite film was incorporated inside the laser cavity, a CW lasing was observed at a central wavelength around 1058.15 nm when threshold pump power was set to about 85 mW. After that, the pump power was raised gradually. As diode pump power reached about 93 mW, dual lasing lines located at 1058.2 nm and 1058.9 nm were observed. Subsequently, quadruple lasing lines (1058.2, 1059.7, 1061.4, and 1062.3 nm) with many lasing modes (1058.98, 1060.5, and 1063.1 nm)

were detected at exciting power of about 127 mW. These multiple-lines generated owing to the increase raise of YDF gain concerning rising pump power. This condition permits considerable wave energy for the FWM influence induces by the nonlinearity of $\text{Fe}_2\text{O}_3/\text{SiO}_2$ nanocomposite to produce new lines at the neighborhood lasing lines, which absorbs photons from these waves to produce new photons at new various frequencies. At 162 mW of exciting power, the mode competition and mode hopping appeared clearly inside the cavity, which led to disappeared one wavelength and appeared another. At this pump power, the lasing lines were observed at 1058.2 nm, 1063.9 nm, and 1064.7 nm. Also, multiple lasing modes located at 1057.4 nm, 1058.98 nm, 1059.7 nm, 1063.15 nm, and 1065.5 nm appeared in the emission spectrum. For more examination, the pump power increased slowly to 187 mW. Herein, the multiple-line oscillations were detected at 1058.2 nm, 1058.99 nm, 1063.11 nm, 1063.9 nm, and 1064.7 nm. More lasing modes centered at 1057.5 nm, 1059.7 nm, 1062.4 nm, and 1065.5 nm were observed.

Now, it can be concentrating on the examination of the generated multiwavelength performance. The lasing lines and lasing modes were detected at 1057.4, 1058.2, 1058.9, 1059.7, 1060.5, 1061.4, 1062.3, 1063.1, 1063.9, 1064.7, and 1065.5 nm, as the pump power varied between 85 and 187 mW, as shown in Fig.(3.44). It can be observed that the line spacing between these lasing lines is not uniform, which the spacing between the neighboring wavelengths was around 0.7, 0.8, and 0.9 nm. Notably, the line spacing is determined by the birefringence of both the cavity and the $\text{Fe}_2\text{O}_3/\text{SiO}_2$ nonlinear material as well as by the cavity length. However, the motives about the non-uniform line spacing between the generated wavelengths might be credited to: (1) the spectral hole-burning influence inside the cavity [191]. (2) When the gain of the cavity for some lasing lines is sufficiently big, while the gain of the other lines is adequately tiny,

so the cavity will strengthen the lines owing big gain nonetheless alleviate the other one [192].

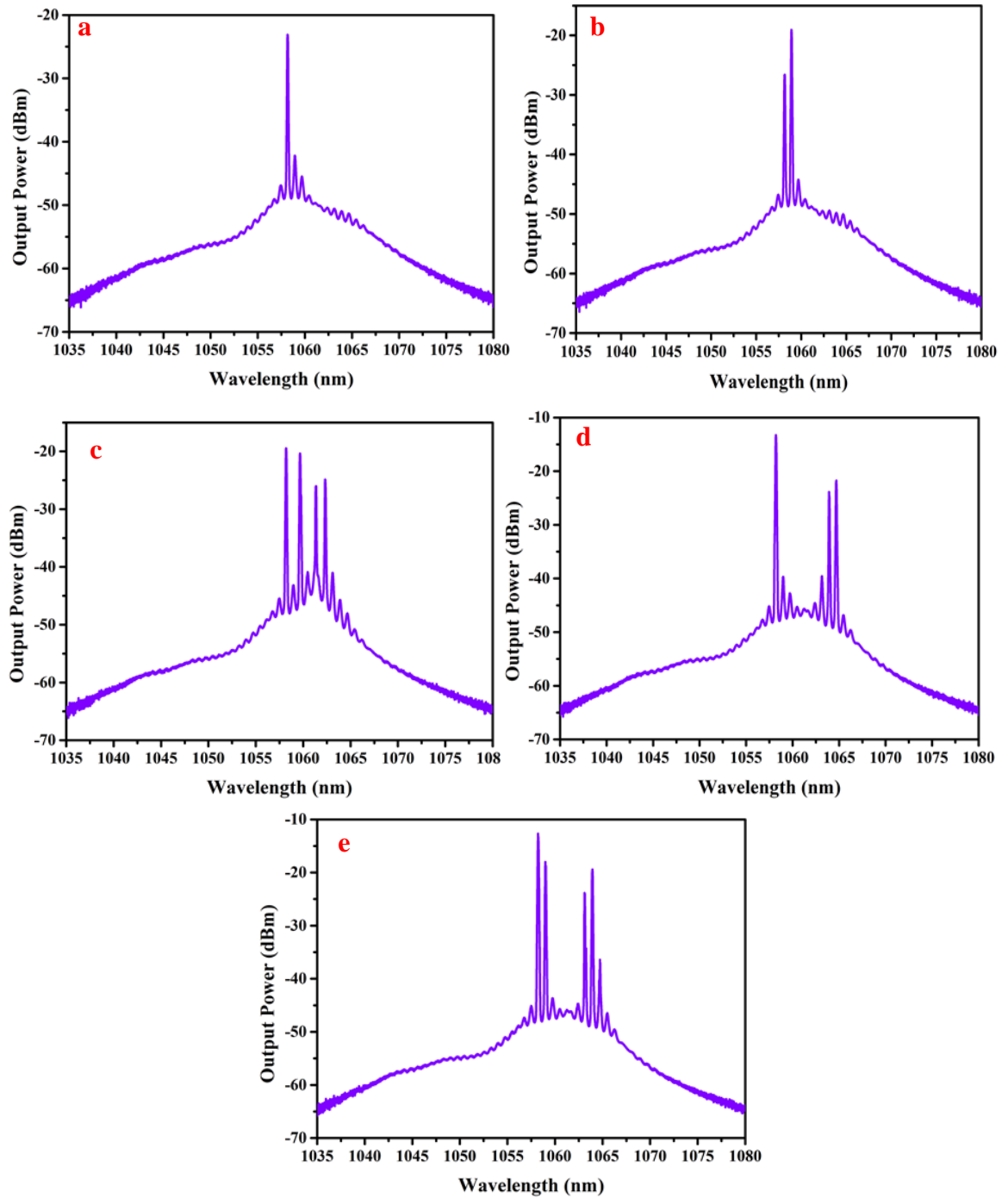


Fig.(3.44): Optical spectra of YDFL based on $\text{Fe}_2\text{O}_3/\text{SiO}_2$ nanocomposite film at (a) 85 mW, (b) 93 mW, (c) 127 mW, (d) 162 mW, and (e) 187 mW.

The multiwavelength performance including the lasing lines number and spacing between the lines could be further improved via enhancing the FWM efficiency thru optimizing the nonlinear material parameters (such as

the thickness of thin-film and the concentration of the nanomaterials) and lessening the cavity loss as well as inserting intra-cavity devices [193,194].

In the meantime, the typical oscilloscope signal of the multiwavelength YDFL output based on $\text{Fe}_2\text{O}_3/\text{SiO}_2$ nanocomposite film is illustrated in Fig.(3.45). Unstable pulse form was noticed, proving that the $\text{Fe}_2\text{O}_3/\text{SiO}_2$ nanocomposite film induces a pulse operation, but the cavity and the thin film need some optimization to produce a stable pulse laser signal.

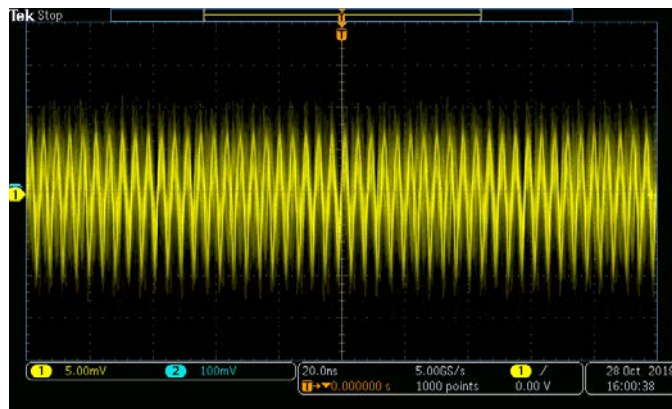


Fig.(3.45): Oscilloscope trace of YDFL based on $\text{Fe}_2\text{O}_3/\text{SiO}_2$ nanocomposite film.

After that, the impact of the polarization state of the propagation signals is exported. By inserting three puddles PC and simultaneous changing of its three puddles, the amplitude maxima of the laser dynamic gain will be shifted. According to this system, a CW multiwavelength lasing was observed at a central wavelength around 1060.804 nm when threshold pump power set to about 93 mW, The channel peaks have 0.58 nm spacing, as shown in Fig.(3.46a).

Fig.(3.46) shows the dependence of the generated multiwavelength line components on the pump power. Well localized and stabilized laser spectra with the smooth line were generated as the pump power exceeds 93 mW. As the pump power increased to about 202 mW, the laser spectrum contains dual various groups of channels created around 1060 nm and 1066 nm as shown in Fig. (3.46e).

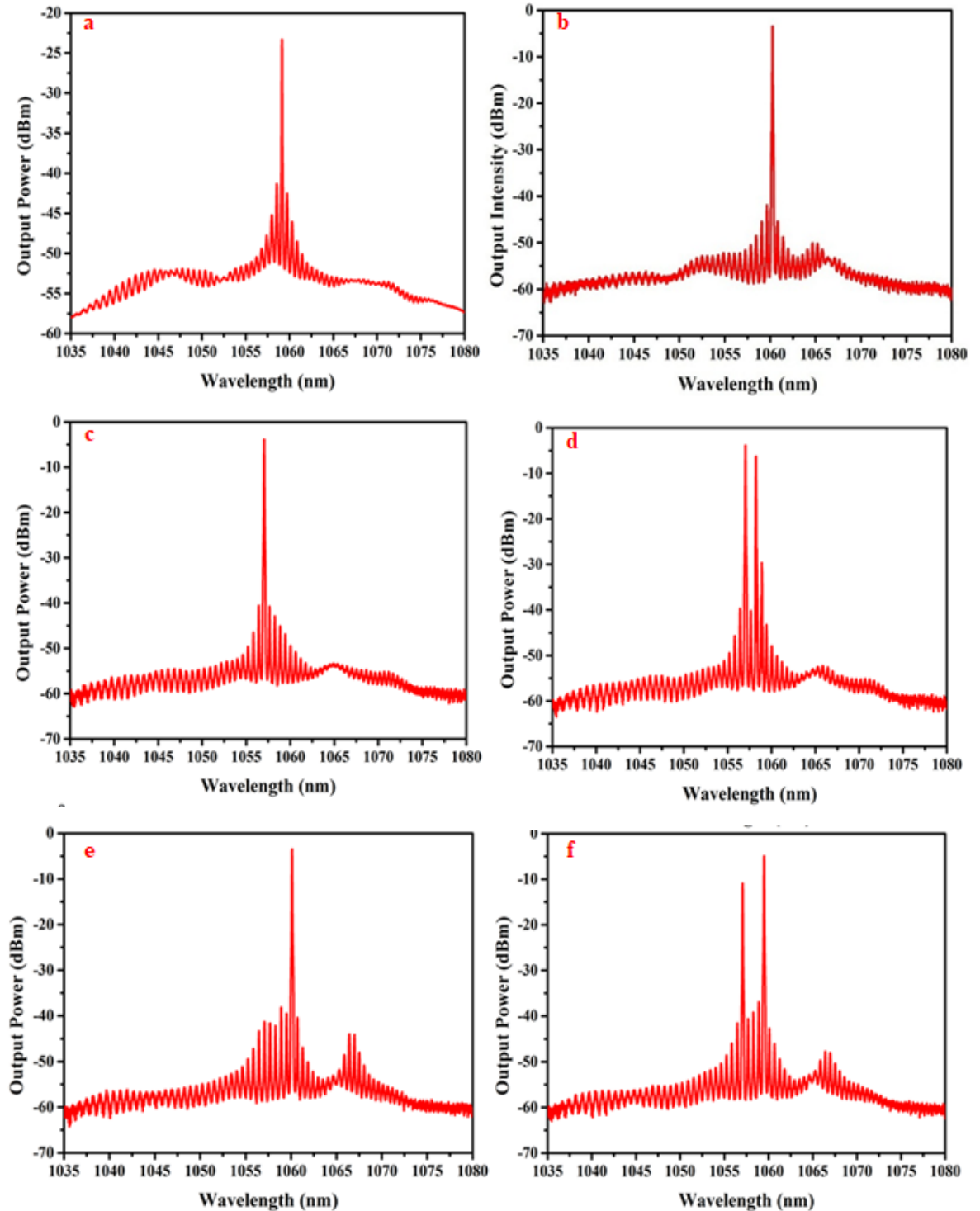


Fig. (3.46): Multiwavelength spectrum at a different power of (a) 93 mW, (b) 110 mW, (c) 152 mW, (d) 187 mW, (e) 202 mW, and (d) 250 mW.

As adjusting the pump power to about 290 mW (Fig.(3.47a)), about 10 lasing lines with many lasing side modes were observed. After then, the three puddles of the PC were adjusted which more lasing lines and more

side mode lasing with switching in the multiple lasing lines groups were built up, as shown in Fig.(3.47).

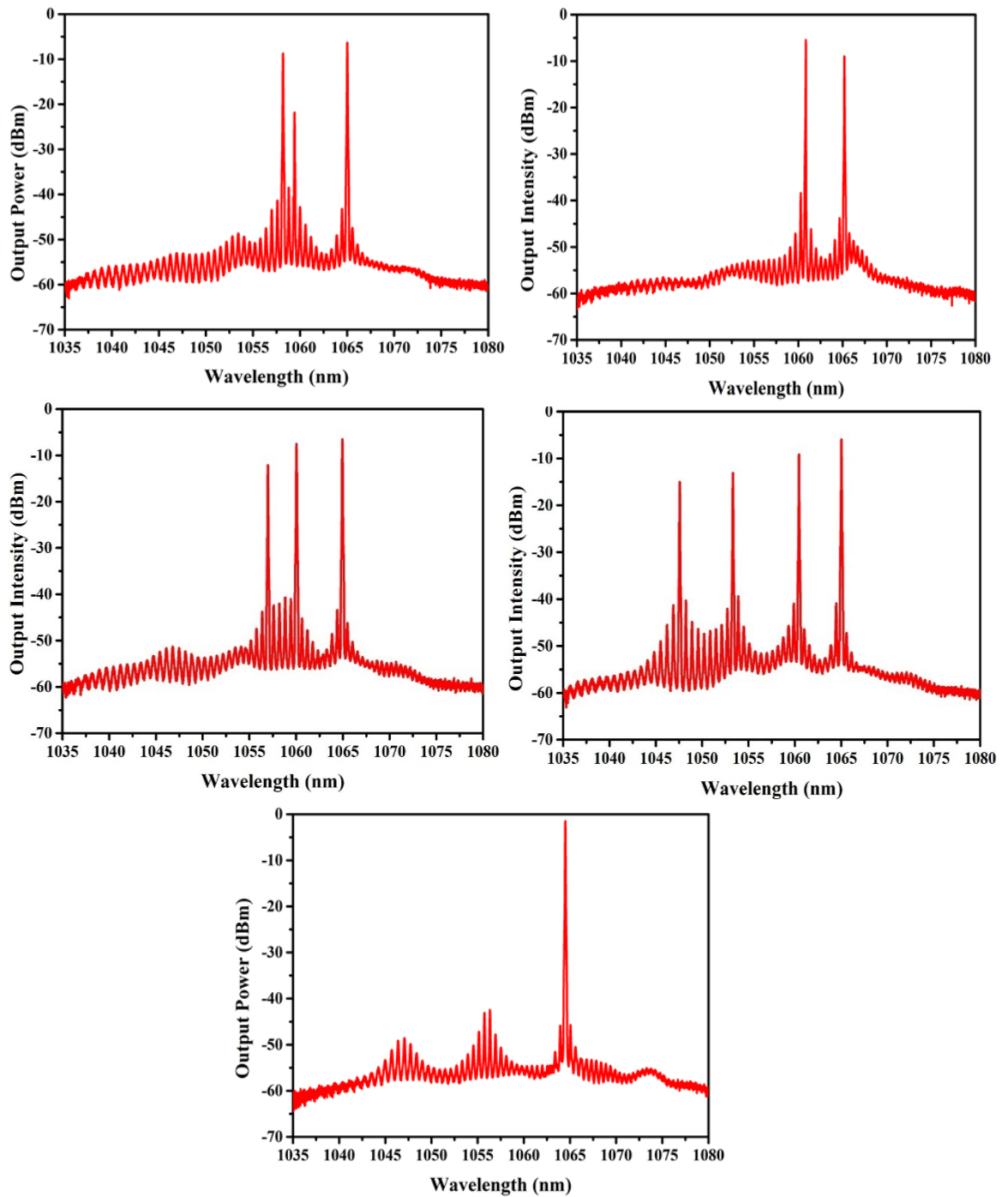


Fig.(3.47): Polarization dependence on multiwavelength at 290 mw.

In the present work, the variation of polarization state plays a key issue with vital significance to the dynamical character of the laser output. So, the effect of polarization state on the multiwavelength emission lines and the SNR were studied at the maximum available pump power of 290

mW by detuning the polarization state of the circulated laser inside the cavity. With the adjusting of the three puddles, stable multiwavelength of more than 20 lines with SNR between 9 dB and 46 dB with many numbers of side modes lasing were detected. Fig.(3.47b-e) displays the multiwavelength with different polarization states. This asymmetric gain can also be ascribed to many reasons. Firstly, polarization hole burning influence intrinsic in YDF itself. Notably, the generated line is modulated by the uneven feature spectrum from the ASE of the doped fiber. Additionally, the polarization condition of various spectral lines in the doped fiber could be varied via adopting the PC, so creating the polarization dependent gain and encouraging hole burning influence. Also, a strong polaritonic phenomenon is influenced on the phase-matching conditions of the nonlinear effects. Thus, as the fiber laser functions in other output conditions, it is challenging to adjust it constantly owing to the influence of the previous mentioned effects [193,194].

The multiwavelength generation in the present cavity is based on the cascaded structure of large-core fiber induced Fabry-Perot filter with the assistance of $\text{Fe}_2\text{O}_3/\text{SiO}_2$ nanocomposite induced FWM. Now, it can be more concentrating on the examination of the generated multiwavelength performance. There are many different effects induced inside the cavity. First, the YDF possesses a 4 μm core fiber, and all the other components of the laser cavity have been built from a basic mode fiber with 6.2 μm core fiber excluding the bending SMF possesses a core diameter of about 9 μm . So, this configuration can shape the Fabry-Perot filter, which works to build standing wave interference inside the fiber cavity [25]. Second, a three-puddles PC having a 3.5 m of SMF-28 bending on a spool with a loop diameter of about 4.5 cm. Taking into consideration that the SMF-28 is not exhibiting single-mode in the 1 μm , so transverse mode combining will maybe happen among the LP_{01} and LP_{11} modes [195–197].

It worthy to note, these multiwavelength lines can be also seeded by an FWM phenomenon induced by the high nonlinearity of $\text{Fe}_2\text{O}_3\text{-SiO}_2$ nanocomposite. On the other hand, multiple scattering excited by refractive index inhomogeneities of $\text{Fe}_2\text{O}_3\text{-SiO}_2$ nanocomposite might be provided an optical gain together with in-cavity YDF. So, the nonlinear interaction of various spectral components induced a multiwavelength generation with a narrow linewidth of about 0.5 nm, as depicted in Fig. (3.46-47). The ultranarrow emission modes might be attributed due to the interference effects of the multiple modes which these effects give rise to distinct sharp lines with a linewidth of less than 1 nm overlaid on the output lasing spectrum.

In the meantime, the characteristic oscilloscope pulse signal of the multiwavelength YDFL output based on $\text{Fe}_2\text{O}_3\text{-SiO}_2$ nanocomposite is presented in Fig.(3.48). The pulse behavior proving that the multiwavelength YDFL output is in the situation of mode-locked operation. This is attributed to the effect of high nonlinear refraction and absorption influences of $\text{Fe}_2\text{O}_3\text{-SiO}_2$ nanocomposite, as well as the effect of the interferometer.

In addition to that, the polarization adopting via the PC alignment can initiate a spectral gain-reliant amplitude variation. So, the temporal dynamics of the generated fiber laser get different profiles with various pulse shapes and intervals via adjusting the PC condition, which various polarization orientations can regulate the time dynamics form of the generated laser. In the present work, the operation regime between the CW and pulsed operation can be switched by just fine-tuning the state of the PC. Also, with a proper PC alignment the fiber laser can also exhibit harmonic mode-locking. Fig.(3.48a-b) shows the oscilloscope trace and the zoomed-in mono-pulse, which the time pulse duration equal to ~ 27.4 ns. The RF spectrum was also examined, which the central frequency was estimated ~ 18.75 MHz, SNR > 56.3 dB at the 30 Hz resolution, as

displayed in Fig.(3.48c). This denotes that the generated mode-locking possesses relatively small peak value variations and well-behaved stability.

Also, the measured average output power is given in Fig.(3.49) which indicates an approximately linear relation with excited power. Besides, the largest realized pulse energy is ~ 0.309 nJ which associates to a largest peak power of 5.801 mW. This laser cavity reveals a slope efficiency of about 2.875 %.

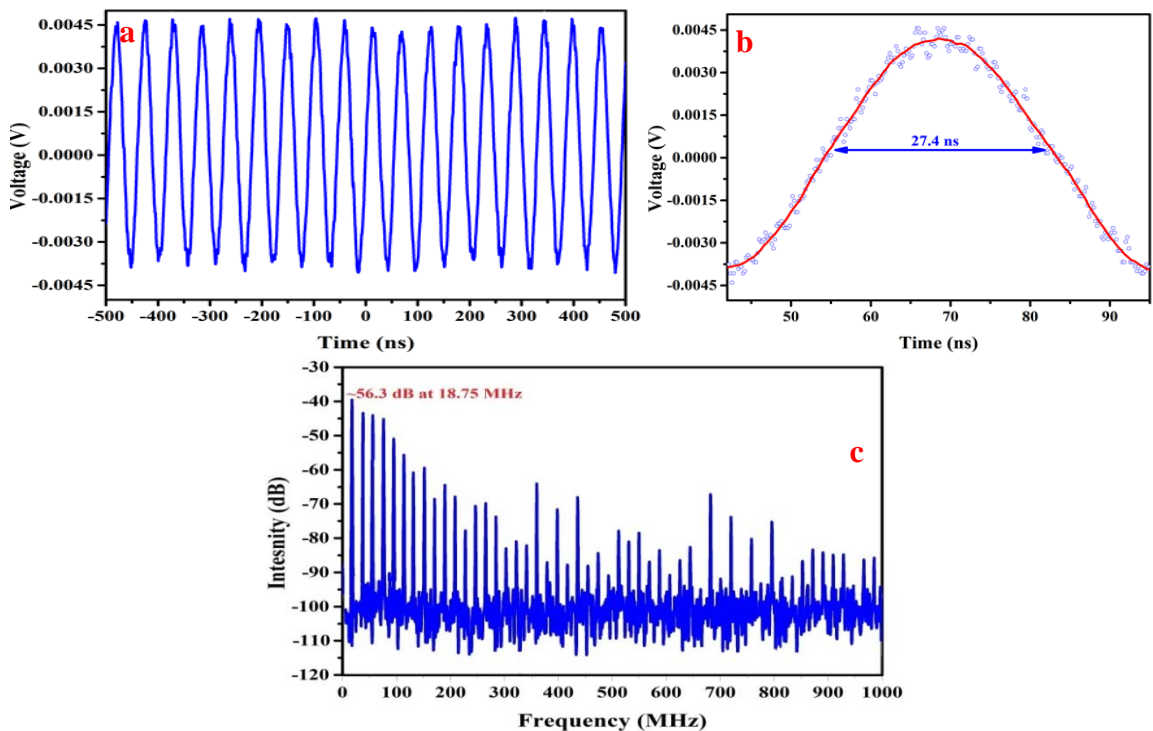


Fig.(3.48): The characterization of temporal behavior, (a) the recorded pulsed train, (b) the corresponding single pulse profile (c), and (d) RF spectrum of the laser at different polarization states.

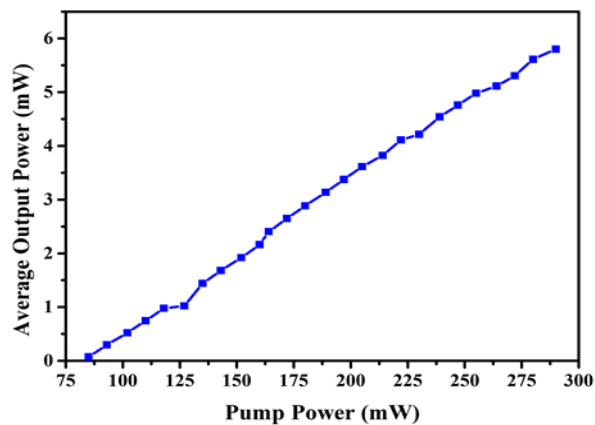


Fig. (3.49): Average power vs. the pump power.

CHAPTER FOUR

Results and Discussion:

Multiwavelength Erbium Doped

Fiber Laser

Chapter Four

Results and Discussion: Multiwavelength Erbium Doped Fiber Laser

4.1 Introduction

Generally, the C- and L-band spectrum (1530–1625) nm has attracted a lot of interest in optical telecommunications due to the low attenuation loss of silica fibers in this region and high transmission capacity. The multiwavelength EDF offers various advantages such as a low polarization-dependent gain, narrow linewidth, flat gain spectrum, high conversion efficiency, and low lasing threshold. However, EDF experiences a strong homogeneous broadening gain at room temperature, which leads to severe mode competition and consequently affects the laser stability. To date, different approaches have been proposed and demonstrated to generate stable multiwavelength fiber lasers which can be classified as active or passive techniques. The active nonlinear effects in optical fibers such as the stimulated scattering effects and four-wave mixing (FWM) can be achieved to generate multiwavelength laser. In this chapter, active nonlinear effects based on FWM using highly nonlinear nanomaterial have been exploited to produce a steady multiwavelength EDFL with various temporal generations.

4.2 Ni-NPs Optical Modulator

This section includes the details about the results, and discussion of the proposed multiwavelength EDFL based on Ni-NPs.

4.2.1 Nickel Thin Layer Based-NF:

First, the lasing output spectrum of the EDFL was tested without Ni-NF. A CW laser at a central wavelength of 1567.508 nm was observed when reaching a threshold pump power of ~ 72.4 mW as shown in

Fig.(4.1a). The cavity nonlinearity was enhanced after embedding the Ni-thin layer inside the EDFL, and FWM processes were achieved at a low pump power of about 38.4 mW. CW output with a redshift of the lasing wavelengths towards 1596.8 nm (L-band region) was observed as shown in Fig.(4.1b).

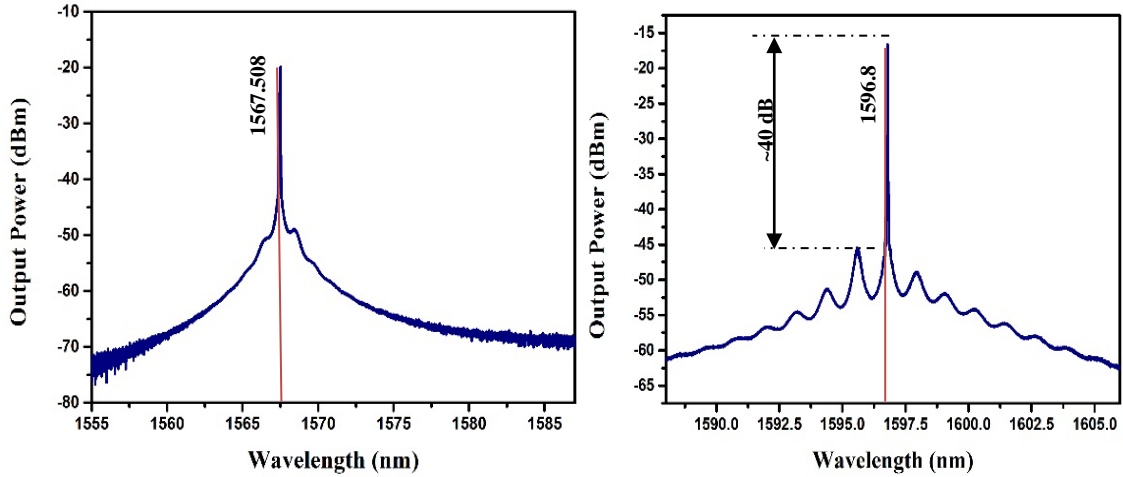


Fig.(4.1): The optical spectrum of EDFL (a) without and, (b) with Ni-NF.

With the increase of pump power, dual, triple, and quadruple wavelengths were observed at 1595.6 nm, 1596.8 nm, 1598 nm, and 1599.2 nm respectively. Figs. (4.2a-c) depict the measured spectra under pump powers of 52, 88, and 101.6 mW, respectively. As the pump power reaches a maximum value of 300 mW, the SMSR increases to about 43 dBm and the peak power of the four peaks becomes more stable. One side-mode is observed at 1594.4 nm with peak power of about -39.966 dB at the maximum pump power [Fig.(4.2e)].

The induced FWM leading to the mitigation of the mode competition in the EDFL is due to the high third-order nonlinearity of Ni-thin layer. The redshift in wavelength is out of our expectation at first glance as the EDF gain in the L-band is about 10 times lower than that in the C-band. Compared with the C-band region, EDF requires a long length with a large doping concentration, and high threshold pump power to generate a laser in the L-band [14,198–200].

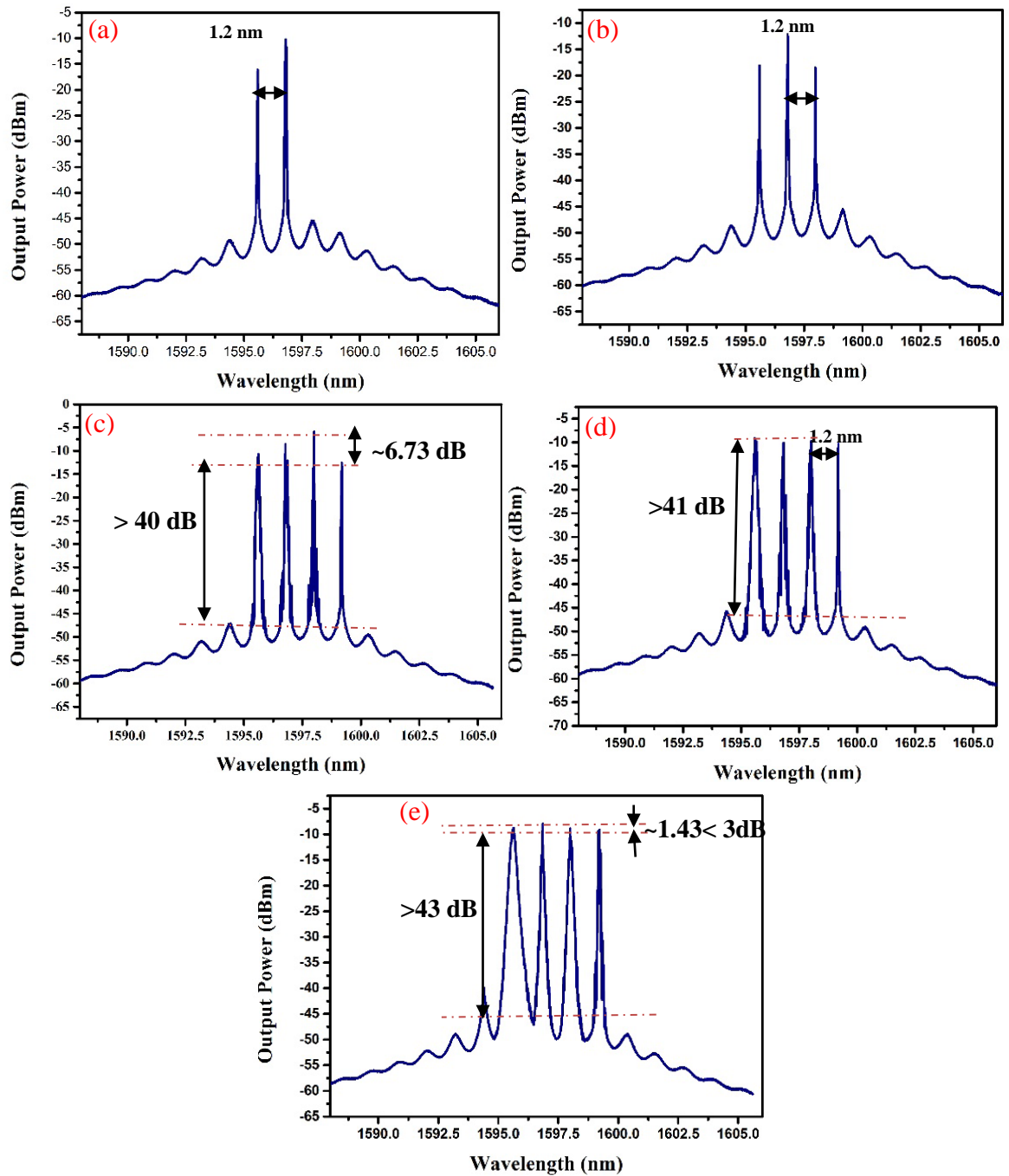


Fig.(4.2): The optical spectrum of EDFL at a different pump power (a) 52 mW, (b) 88 mW (c) 101.6 mw, (d) 160 mW, and (e) 300 mW.

Meanwhile, FWM efficiency mainly depends on the nonlinear coefficient γ , the pump power P , and the effective fiber length L (as $\eta_{\text{FWM}} \propto \gamma PL$). More importantly, the nonlinear coefficient γ (which is governed by $2\pi n_2 / A_{\text{eff}} \lambda$) plays a dominant role in enhancing the FWM effect. Additionally, the contribution of the dispersion effect is very small and can

be ignored, which results in a high FWM conversion efficiency. The proposed fiber laser operates in continuous mode as no pulse operation was observed. The possible reason is that the deposited Ni-NF as a thin layer inside the ring cavity does not meet the prerequisites of the pulse laser operation [28,171].

In order to investigate the stability of the proposed multiwavelength fiber laser, the laser spectra were scanned at 5 min intervals for half an hour at a maximum pump power of 300 mW as shown in Fig.(4.3).

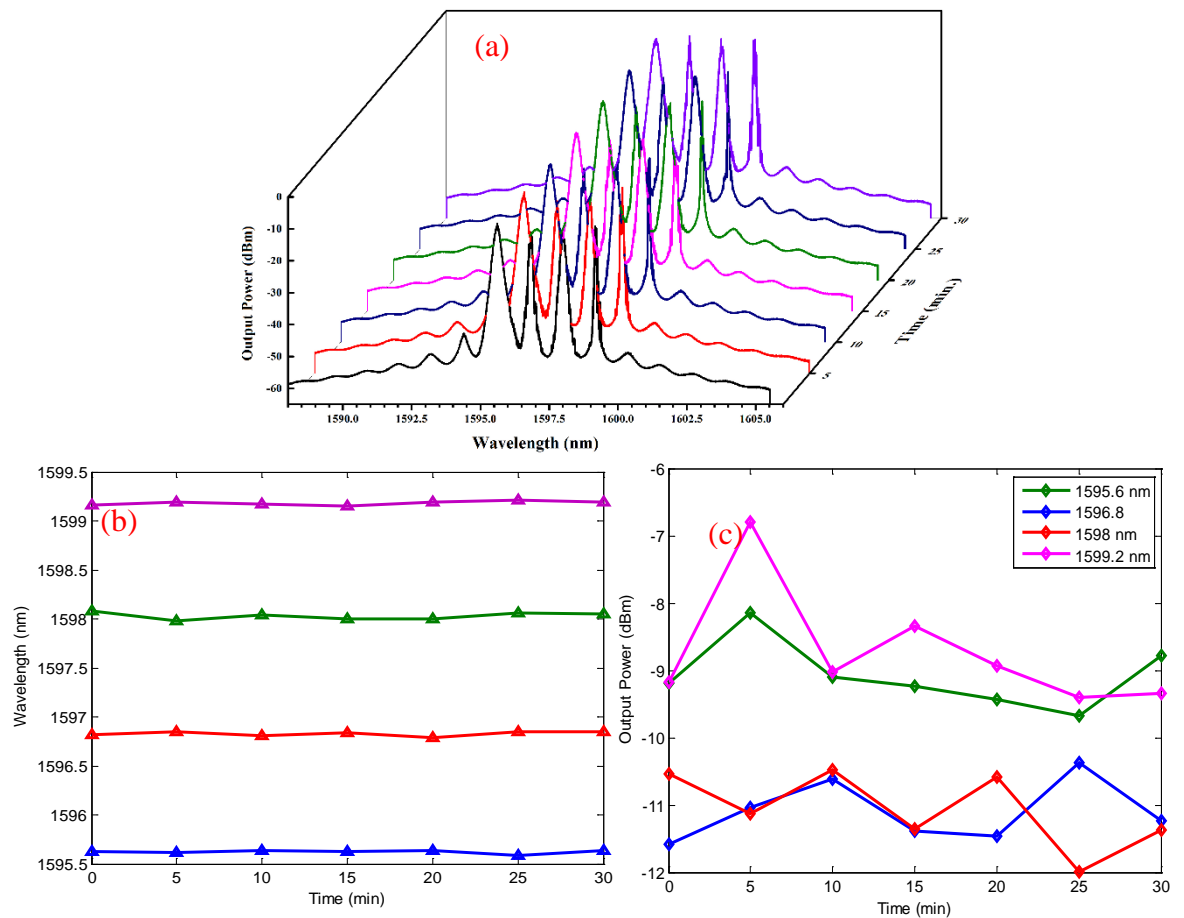


Fig.(4.3): (a) Output spectra measured with 30 minutes, (b) wavelength shift, and (c) Power fluctuations.

It has been found that the power fluctuation is less than 3 dBm, and the wavelength drift is less than 0.07 nm, which confirms high stability at room temperature without using a polarization controller or other intracavity filters. Besides, to investigate the stability, the power fluctuation

of the obtained peaks at maximum output power is shown in Figs. (4.3b) and (4.3c).

The performance of the proposed multiwavelength EDFL was compared with recently reported multiwavelength lasers based on FWM induced with different approaches such as graphene, black phosphorus, Bi-EDF, DSF, and HNLF. The main parameters of them are listed in Table (4.1). The table illustrates that Ref. [28] has the lowest threshold pump power but it is more compact which is based on graphene and a polarization-maintaining fiber Sagnac loop mirror. Therefore, the proposed laser is a cost-effective fabrication with lower pump power than most previous works.

Table (4.1): The output performance comparison of multiwavelength fiber lasers based on FWM.

Material	Central wavelength (nm)	Channel spacing (nm) at a maximum pump power	Threshold pump power (mW)	Singles peak extinction ratio (dB)	Ref.
Graphene /polarization-maintaining fiber sagnac loop mirror	1530	0.54	7	57	[28]
Bi-EDF	1615.5	0.41	147	30	[201]
Black phosphorus/micro-fiber coil	1882.5	0.54	116	40	[184]
DSF+HNLF	1595	0.9	40	30	[20]
Nickel	1596.8	1.2	38.4	40	Our work

4.2.2 Ni-PVA Freestanding Film (0.35% volume):

The EDFL cavity based on 2 m of doped fiber was configured to operate with the Ni-PVA film to examine this functionality in the 1.5 μm region. As the Ni-PVA SA is integrated inside the cavity, a CW operation with a considerable spectral broadening was observed at a threshold exciting power of about 77 mW. The emitted laser (1567.51 nm) exhibited a blue shift property in comparison with this cavity without Ni-PVA, this might be attributed to the insertion loss added by the Ni-PVA SA, whereas the broadening effect can be attributed to the SPM effect in the EDFL ring oscillator that arises owing to the high intensive light generated in the oscillator. Once the pump power reached 85 mW, self-started Q-switching pulses were generated with pulse duration of 4.9 μs and a repetition frequency of 20.5 kHz. Fig.(4.4) shows the optical spectra of the CW laser in comparison with Q-switched pulsed at threshold pump power. As the exciting power was gradually boosted to an utmost value of 275 mW, the repetition frequency was linearly raised to 56.79 kHz and the pulse duration was lessened to 1.5 μs .

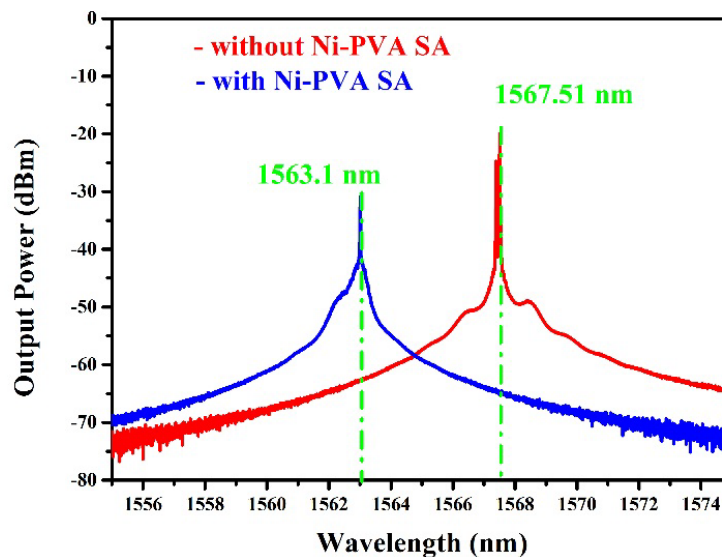


Fig.(4.4): The optical spectra of the CW laser in comparison with Q-switched pulsed at threshold pump power.

The temporal descriptions of the pulsed EDFL at the threshold and utmost excited power are depicted in Fig.(4.5). The Q-switching pulses were stable and no major amplitudes modulation was noticed in the pulses train and maintained an almost uniform shape and pulse intensity. From this figure, the pulse-to-pulse amplitude fluctuation at the maximum pump power is approximately 0.2%.

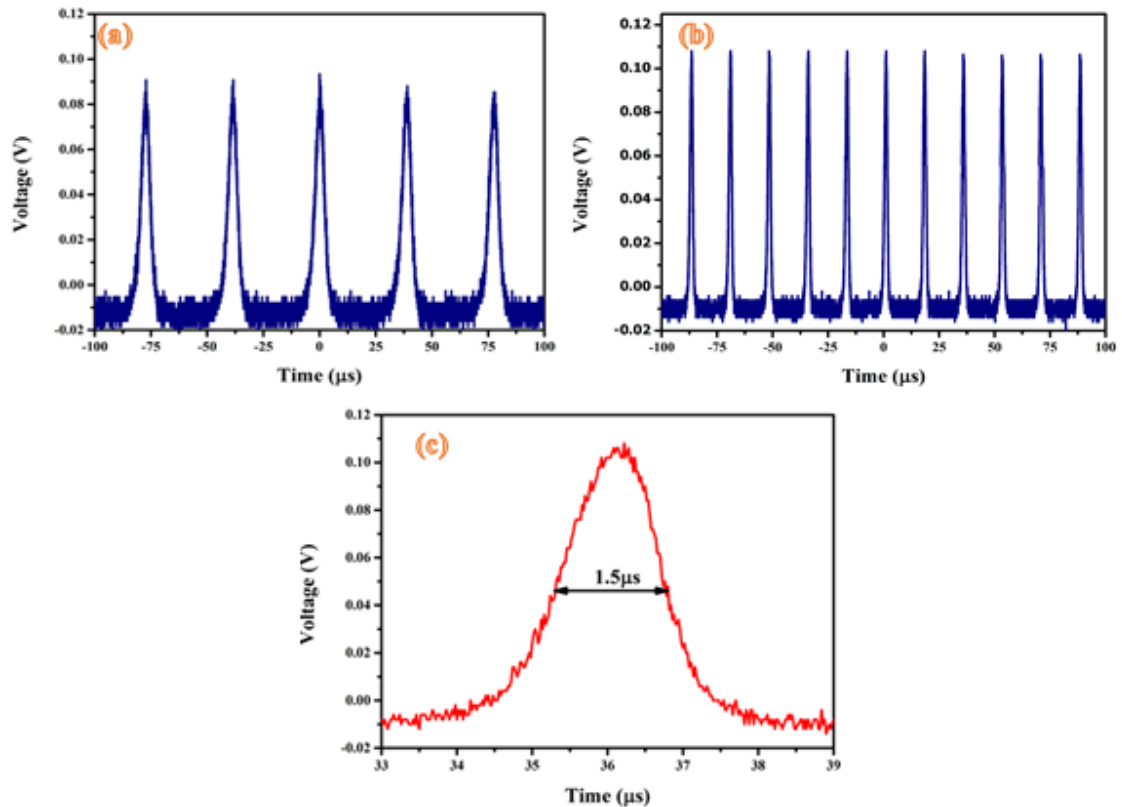


Fig.(4.5): Oscilloscope trace at (a) 85 mW, (b) 275 mW, and (c) single pulse profile at 275 mW.

Fig.(4.6) shows the frequency characteristics of the Q-switching pulses at a pump power of 275 mW. The fundamental RF at maximum output pulse of about 56.79 kHz which matched the repetition rate of Fig.(4.5b), SNR of more than 44 dB with no spectral modulation, and more than 12 harmonics frequency was observed with a span resolution bandwidth of 800 kHz, which confirms the stability of the Q-switching

pulses. The pulse repetition rate and pulse width of the Q-switched EDFL as a function of pump power are depicted in Fig.(4.7a).

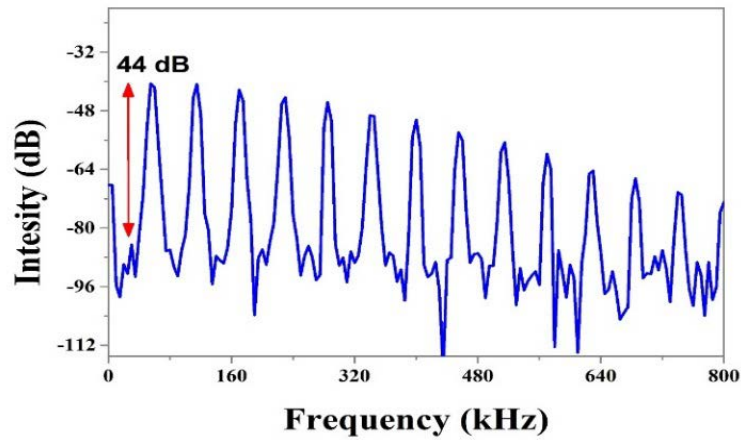


Fig.(4.6): RF spectrum at maximum pump power.

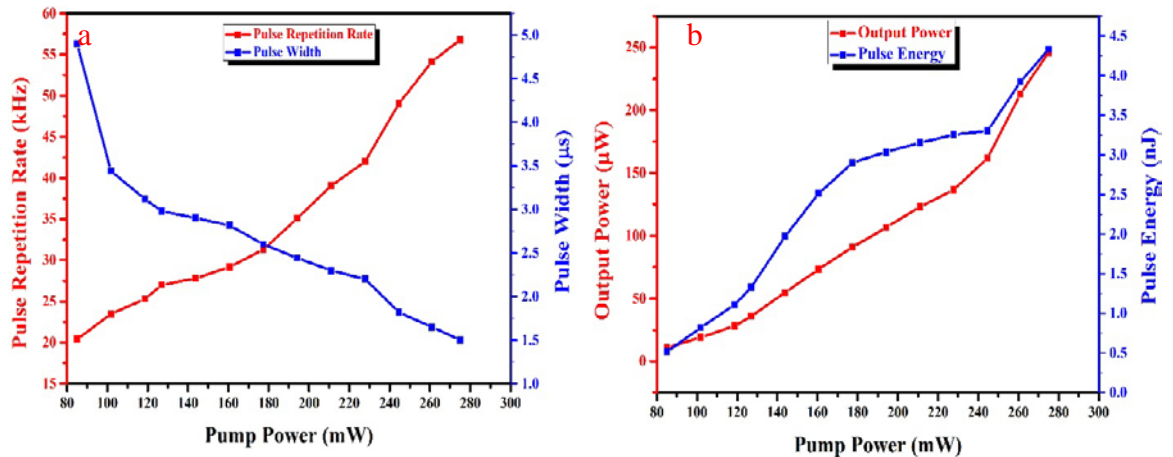


Fig.(4.7): (a) Pulse width and pulse repetition rate, and (b) Output power and pulse energy as a function of pump power.

The minimum pulse duration is related to the properties of the SA (e.g. modulation depth, recovery time), active medium, cavity length, and exciting power. While the exciting power boosted, the pulse repetition rate is increased because the additional gain is supplied to the cavity leads to the rapid saturation time in both the laser active medium and the SA at maximum pump power. The average output power and pulse energy of the proposed laser as a function of the input pump power is depicted in Fig.(4.7b). This result shows that as the exciting power upsurges from 85 to 275 mW leads to an increase in the average output power and the pulse

energy between 10 and 245.9 μW and 0.515–4.33 nJ respectively. The performance of generated pulses can be more enhanced by the adjusting of the laser cavity parameters.

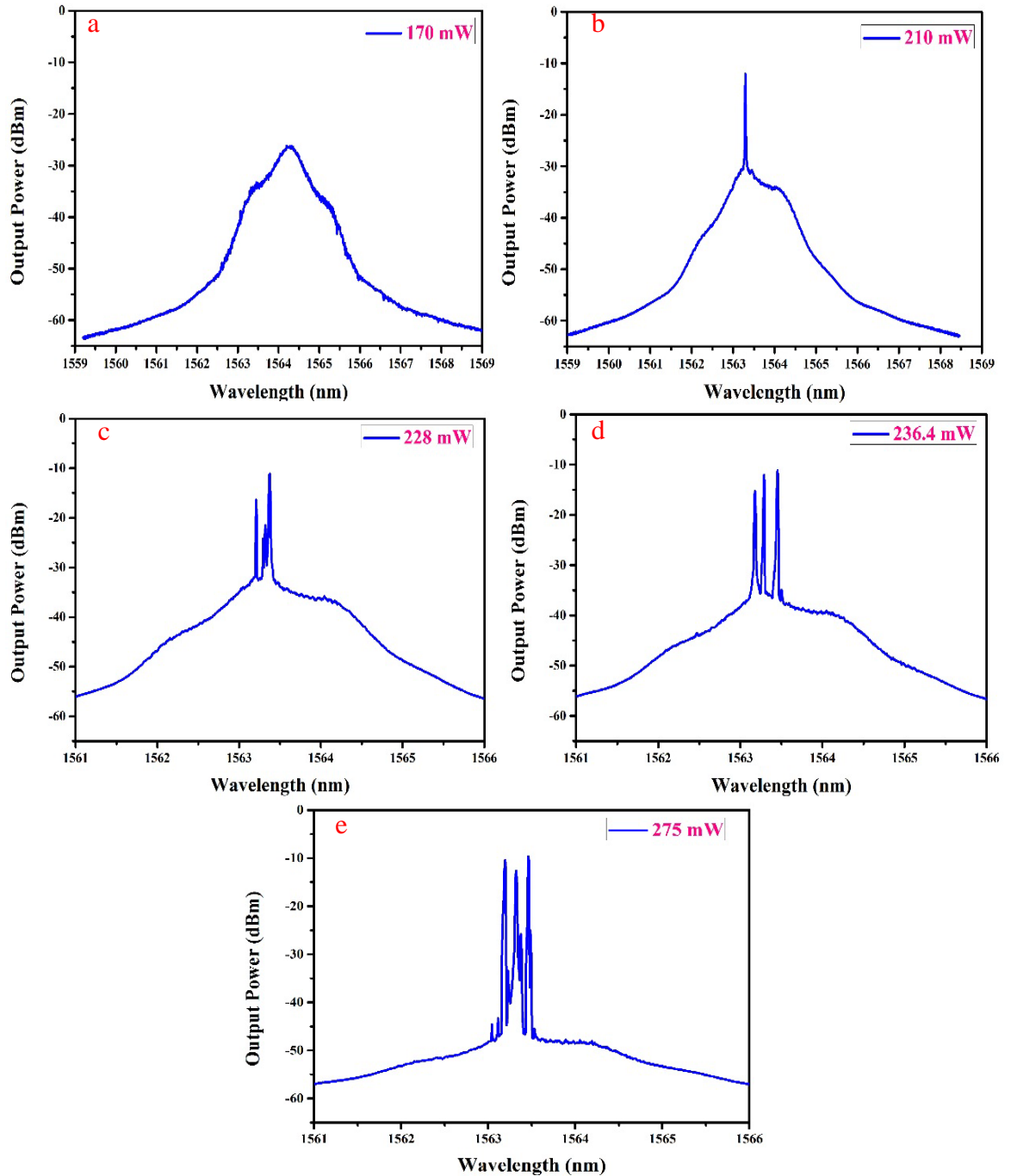


Fig.(4.8): The optical spectra at different pump power.

On the other hand, the optical spectra of emitted laser were tested under different pump power of 170, 210, 228, 236.4, and 275 mW, these results show in Fig.(4.8). As shown in the figure, it can be observed that as

the pump power raised to 228 and 236.4 m, the number of lines increased to dual and triple. The result indicates that Ni-NPs have the ability to generate multiwavelength laser due to their high nonlinearity. The generated wavelengths lasing are observed at 1563.1, 1563.3, and 1563.4 nm. The optical SMSR of the multiwavelength Q-switched EDFL output spectrum is estimated to be about 49 dBm.

In order to investigate the stability of the generated multiwavelength laser, the laser spectra were scanned each 5 min interval for half an hour at a maximum pump power of 275 mW as shown in Fig.(4.9). It has been found that the wavelength drift and power fluctuations are less than 0.03 nm and 2.4 dBm, respectively, which confirms that the operation is stable at room temperature. Further enhancements, such as more lasing lines, better mode suppression, and wavelength selectivity can be achieved by optimizing the cavity parameters, as well as by adding the comb-like filter to the ring cavity.

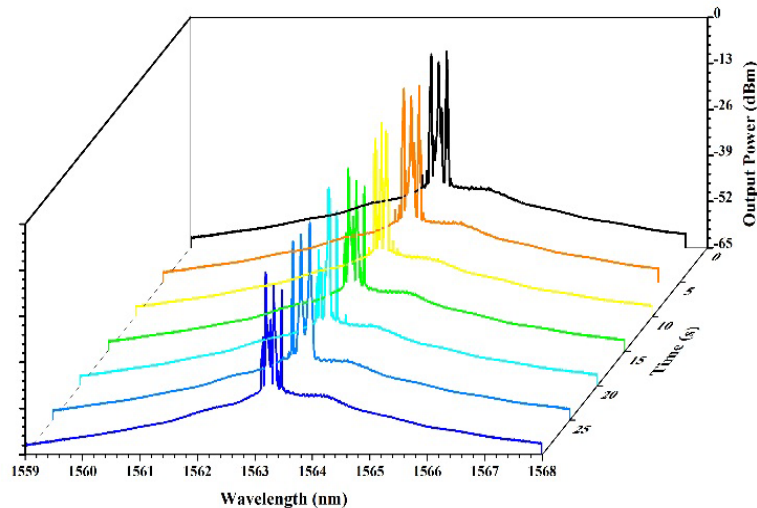


Fig.(4.9): Output spectra measured at the maximum pump power of 275 mW for 30 minutes.

Table (4.2) offers a brief on the results of lately published researches for both the nonlinear optical properties of different SAs nanomaterials and the corresponding EDFL operating situations with the Q-switched laser

output features when optical modulator matter integrated inside the oscillator. From the results in Table (4.2), the current manufactured fiber laser based on Ni-NPs optical modulator has a promising Q-switching performance of the smallest pulse width, a higher modulation depth, and relatively low pump power. The nonlinear optical properties of the saturable absorber such as modulation depth and the third-order susceptibility will determine the feasibility of Q-switching operation. The high third-order susceptibility of Ni-NPs is 1.29×10^{-5} esu which is superior to other SA's such as gold nanoparticles, copper oxide, and carbon nanotubes. This work clearly indicates that Ni-NPs is a good SA candidate to be used as a modulator for a fast and ultrafast pulse generation at low pump power.

Table (4.2): Performance comparison of different types of saturable absorbers in Q-switched EDFL.

Saturable absorber	Threshold pump power (mW)	Maximum Pulse repetition rate (kHz)	Minimum Pulse width (μ s)	α_0 %	χ (esu)	I_{sat} MW /cm ²	Ref.
Carbon nanotube	40	47	4.6	-	10^{-8} - 10^{-9}	222	[127]
Copper oxide	70	83	2.6	3.5	10^{-8} - 10^{-9}	3.3	[41, 202]
Aluminum	156	48.8	2.17	7	$\sim 10^{-6}$	15×10^{-4}	[29, 203]
Gold	114.8	58.1	1.78	7.8	$\sim 10^{-6}$	19.9	[204, 205]
Silver	19.9	58.5	2.4	18.5	$\sim 10^{-5}$	75	[39, 206]
Ni-NPs	77	56.79	1.5	15	$\sim 10^{-5}$	200	Our work

4.3 Fe₂O₃ Optical Modulator

At the first stage of the work, the laser functioned in CW operation as the exciting power was boosted beyond the threshold of 73 mW. As the Fe₂O₃ thin film was inserted inside the cavity, the laser was emitted as the pump power reached about 91 mW, which lasing peak was centered at a 1563.192 nm wavelength with about 2.9 nm 3dB bandwidth and 28.6 dB peak intensity (Fig.(4.10)). As the pump power exceeded the 107.7 mW, a self-starting and stable passively Q-switched was observed with a pulse width of 13.07 μ s and pulse repetition rate of 15.81 kHz. The generated pulse train stayed stable as the exciting power was increased up to 164.3 mW. By raising the pump power to more than 164.3 mW, the pulses turn into unstable and then disappeared, this might be attributed due to that the Fe₂O₃ optical modulator exhibited an over-saturated without any thermal damage. As the exciting power returned to decreased less than 164.3 mW, the Q-switched pulses were retuned with a stable phase.

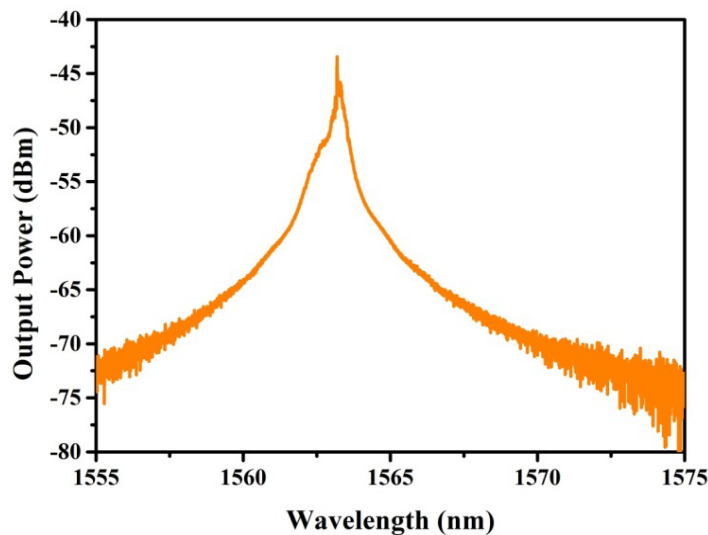


Fig.(4.10): The optical spectrum of EDFL based on Fe₂O₃ thin film at threshold pump power.

The pulse width reduced from 13.07 to 7.18 μ s at the same exciting power values, which corresponds to the normal feature of a Q-switched

laser. While the pump power increased, the pulse repetition rate is increased because the additional gain is supplied to the cavity leads to the rapid saturation time in both the laser active medium and the SA at maximum pump power. The minimum pulse duration is related to the properties of the SA (e.g. modulation depth, recovery time), active medium, cavity length, and pump power. It can be expected for shortening the pulse duration and an improved whole Q-switching regime could be attained via decreasing the overall length of the laser oscillator, improving the birefringence of the oscillator, and decreasing the oscillator losses. Fig.(4.11) depicts the oscilloscope trace of the Q-switching pulse in EDFL at the threshold of 107.7 mW and the maximum applied pump power of 164.3 mW pump power. The pulse train preserved an even intensity distribution without noticeable oscillation or amplitude alteration.

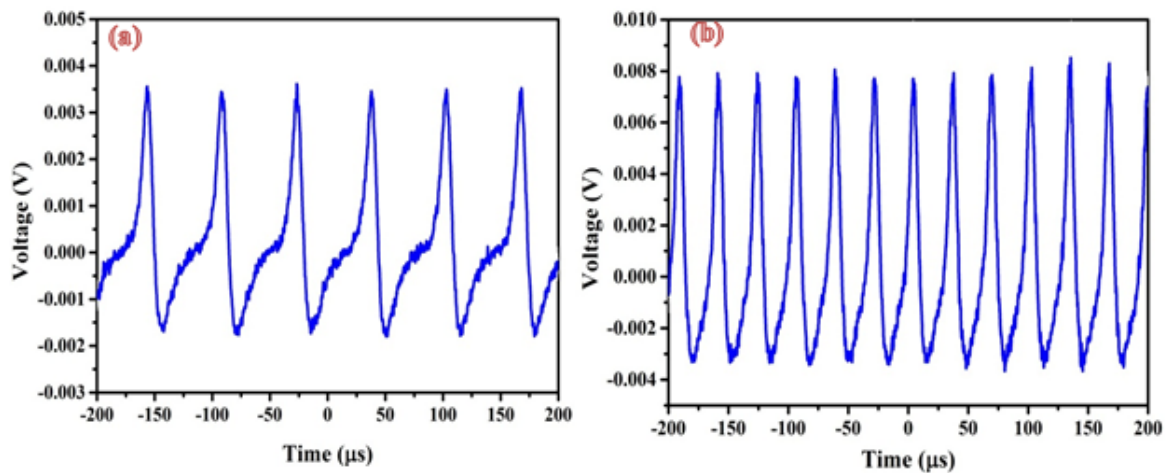


Fig.(4.11): Oscilloscope trace at (a) threshold pump power and (b) maximum applied pump power.

The reliance of pulse repetition frequency and the pulse duration on the input exciting power is revealed in Fig.(4.12a). While the average output power and pulse energy of the planned laser versus the pump power is illustrated in Fig.(4.12b). These figures demonstrate that as the pump power rises from 107.7 to 164.3 mW leads to a rise in the average output

power and the pulse energy between 47.8 and 160.8 μW and 3.02–5.23 nJ, respectively, with an efficiency of 0.4221 %. The performance of produced pulses can be more enhanced by the adopting of the laser cavity parameters.

To ensure the stability of the produced pulsed operation, the RF spectrum of the output signal was examined at the maximum pump power with a 500 kHz span. Fig.(4.143a) displays the fundamental RF amplitude at 30.74 kHz with a span of 500 kHz. Fig.(4.13 b) displays the corresponding single pulse profile of the generated pulse. It shows the full half-width at full maximum of about 7.18 μs . The SNR is 47.3 dB at the fundamental frequency, which shows good Q-switching stability.

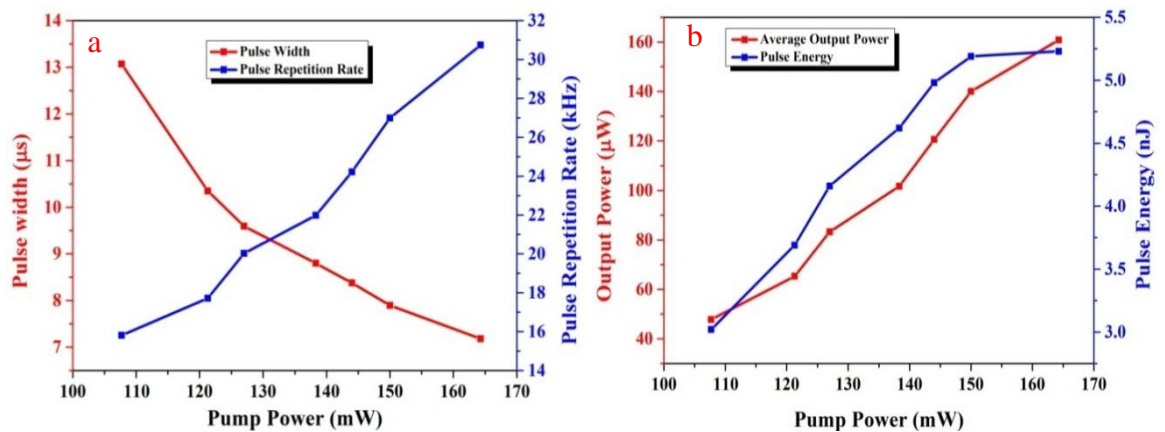


Fig.(4.12): (a) Pulse width and pulse repetition rate, and (b) Output power and pulse energy as a function of pump power.

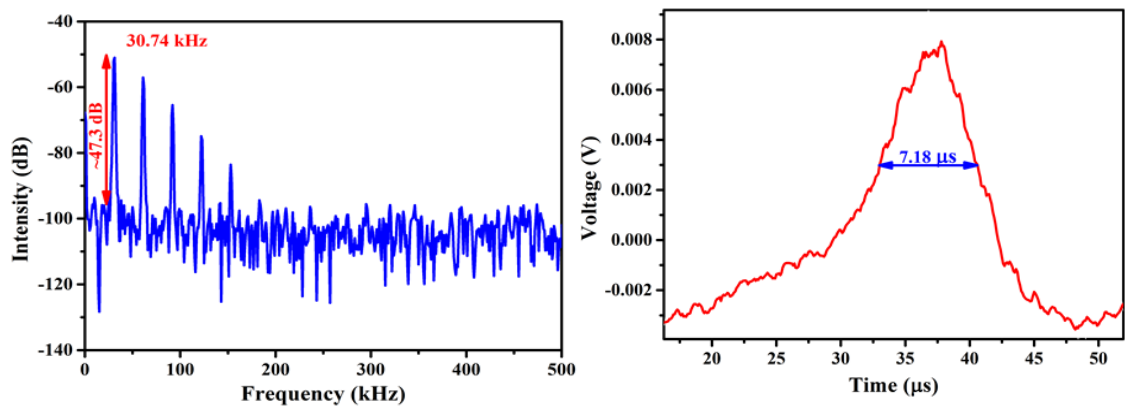


Fig.(4.13): (a) RF spectrum, and (b) single pulse profile at maximum exciting power.

On the other side, multi-peaks were detected in the optical spectrum at pump power reached about 160 mW. So, the optical spectrum at 164.3 mW is shown in and Fig.(4.14). This designates that two lasing lines are oscillating at the same time, centered at 1563.21 nm and 1563.46 nm.

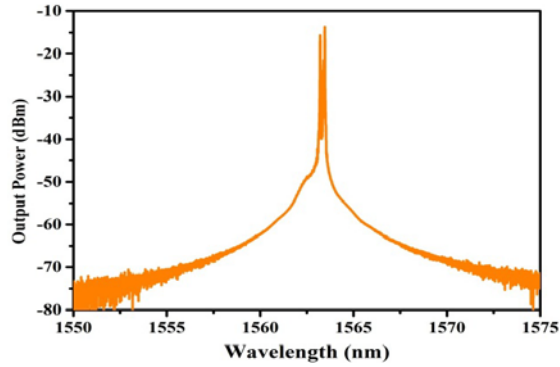


Fig.(4.14): The optical spectrum of EDFL based on Fe_2O_3 thin film at threshold pump power.

4.4 SiO_2 Optical Modulator

In this section, the function of the SiO_2 thin film in a 1.5 μm band using EDF as a gain medium is verified. The SiO_2 thin film was incorporated in the laser cavity as an optical modulator by sandwiching it among dual fiber ferrules thru a fiber adopter in the oscillator. As SiO_2 thin film inserted in the cavity, and the pump power reached about 85 mW, the laser light was initiated at a central wavelength of 1563.4 nm as shown in Fig.(4.15). The 3-dB bandwidth was estimated to ~ 0.16 nm, while optical SNR of the generated laser was determined to ~ 27.8 dBm.

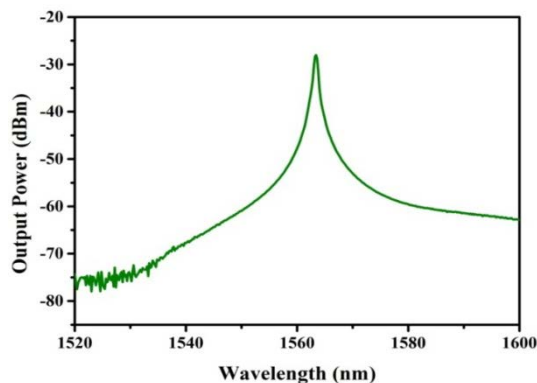


Fig.(4.15): The optical spectrum of EDFL based on SiO_2 thin film at threshold pump power.

While the pulse generation representing by the Q-switching pulses train was self-started as the exciting power exceeded the 90.7 mW. Fig.(4.16a) demonstrates the relation of the repetition rate and pulse width versus the pump power as it adjusts from 90.7 mW to 170 mW. The repetition frequency upsurges in the range 17.74 kHz-30.81 kHz as the excited power upsurges among the mentioned range. Simultaneously, the pulse duration lessens from 13.55 μ s to 4.025 μ s. Finally, the produced pulsed performances versus exciting power were also examined and the relation is demonstrated in Fig.(4.16b), which this figure displays the pulse energy/output power of the pulsed EDFL at diverse exciting powers. Under 90.7 to 170 mW exciting power span, the average output power was calculated to change from 8.92 μ W to 155.6 μ W. Together, pulse energy was determined and possesses that the generated Q-switched covers the optical energy varying from 0.503 nJ to 5.05 nJ.

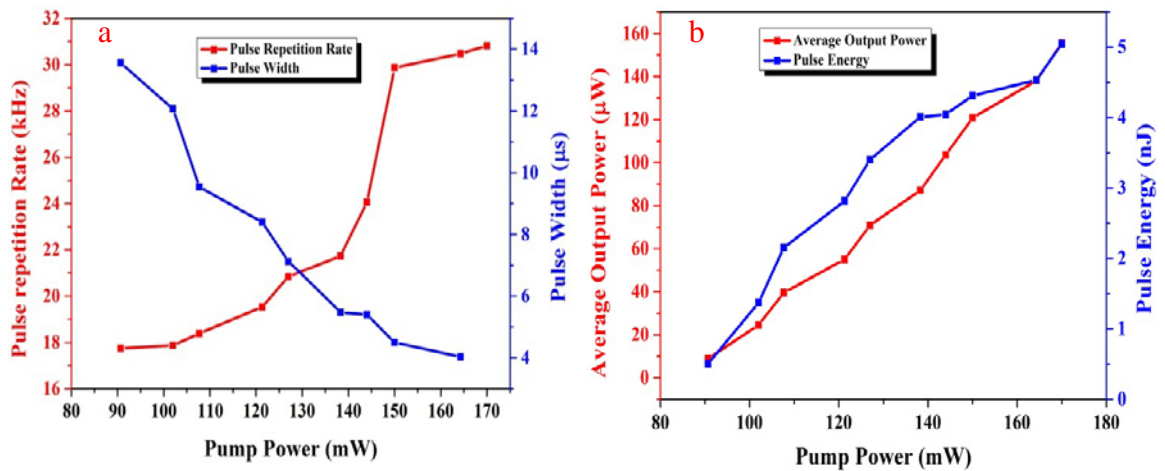


Fig.(4.16): (a) Pulse width and pulse repetition rate, and (b) Output power and pulse energy as a function of pump power.

The pulse trains of Q-switched that correspond to the threshold and maximum input pump power level are illustrated in Fig.(4.17). A single envelope of a pulse train that exhibiting the pulse duration value at the maximum pump power ranks was demonstrated in Fig.(4.18a). To confirm the pulse stability, the RF spectrum recorded as depicted in Fig.(4.18b). From this figure, it can be observed that the fundamental frequency peaked

at 30.81 kHz having a SNR of 50 dB with no spectral modulation; also an obvious trend of 14 harmonics frequency is shown. This denotes the stability of the pulsed operation as an SNR > 30 dB.

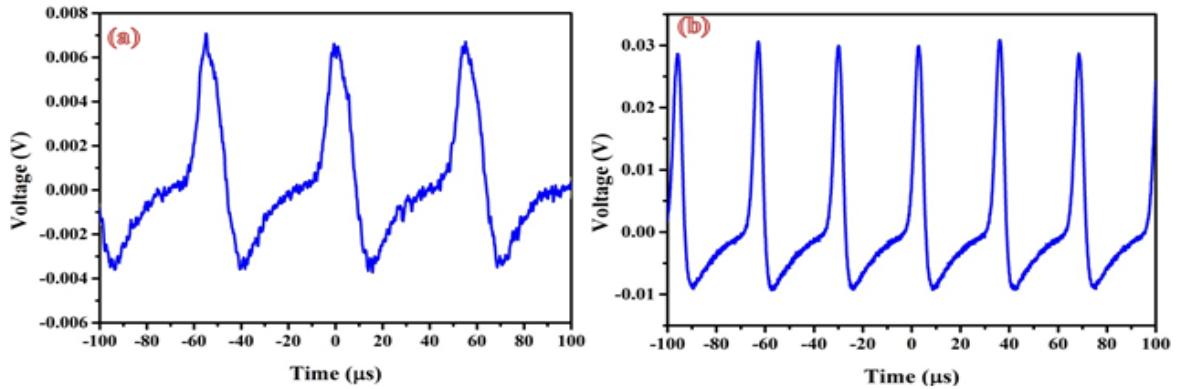


Fig.(4.17): Oscilloscope trace at (a) threshold pump power and (b) maximum applied pump power.

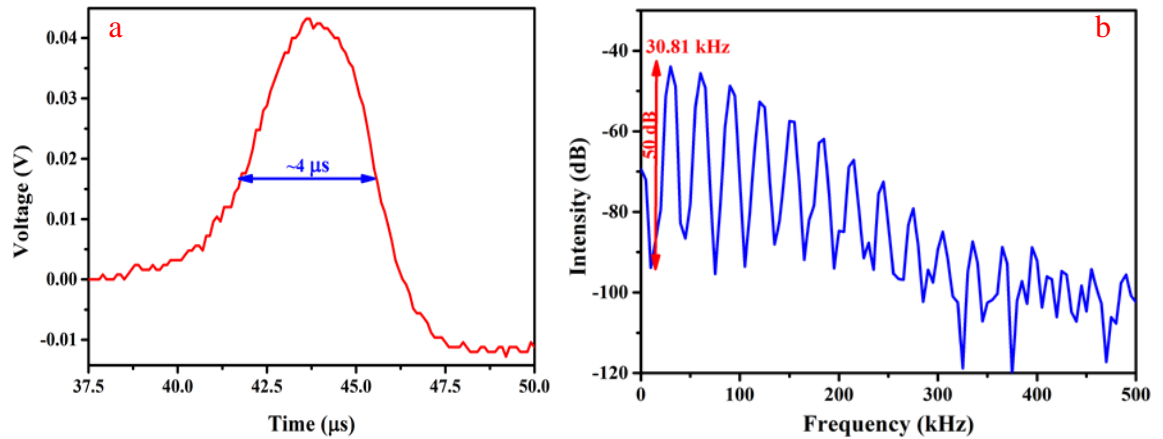


Fig. (4.18): (a) Single pulse envelope, and (b) RF spectrum of EDFL based on SiO₂-thin layer.

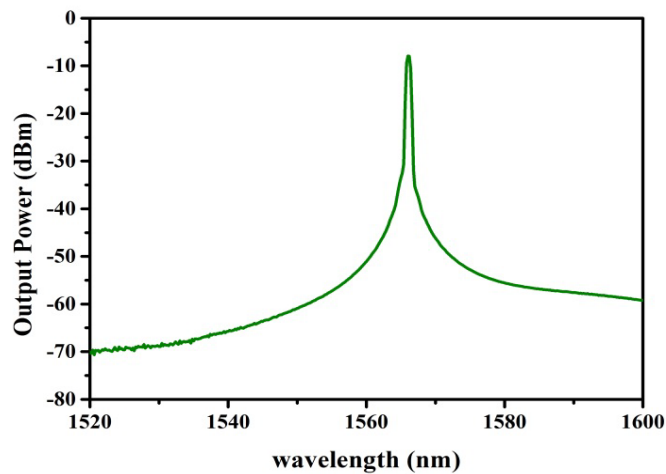


Fig.(4.19): The optical spectrum of EDFL based on SiO₂ thin film at threshold pump power.

Finally, the output optical spectrum at the maximum was also recorded, which this spectrum presents that a single peak located at 1566 nm which no multiple-peaks were observed, as shown in Fig.(4.19).

4.5 Fe₂O₃/SiO₂ Optical Modulator

Finally, the functionality of the Fe₂O₃/SiO₂ for optical modulation has been verified. As a thin piece of the prepared Fe₂O₃/SiO₂ thin film was integrated into the laser cavity, the lasing light was started as the pump power reached about 96.3 mW. As exciting power was increased to 121 mW, the EDFL began lasing with the passive Q-switching regime. A stable pulse train was noticeable on the oscilloscope. To more examine the performance of the Q-switching generation, the pump power was improved progressively from 121 to 250 mW. As the pump power exceeded the 210 mW, the pulse signal became unstable and also suffered from the fluctuation. In the range of 121-210 mW of the pump power, the repetition rate tuned from 22.51 to 46.18 kHz, whereas the pulse width varied between 9.85 to 2.8 μs, the pulse train at the threshold level and 210 mW are demonstrated in Fig. (4.20).

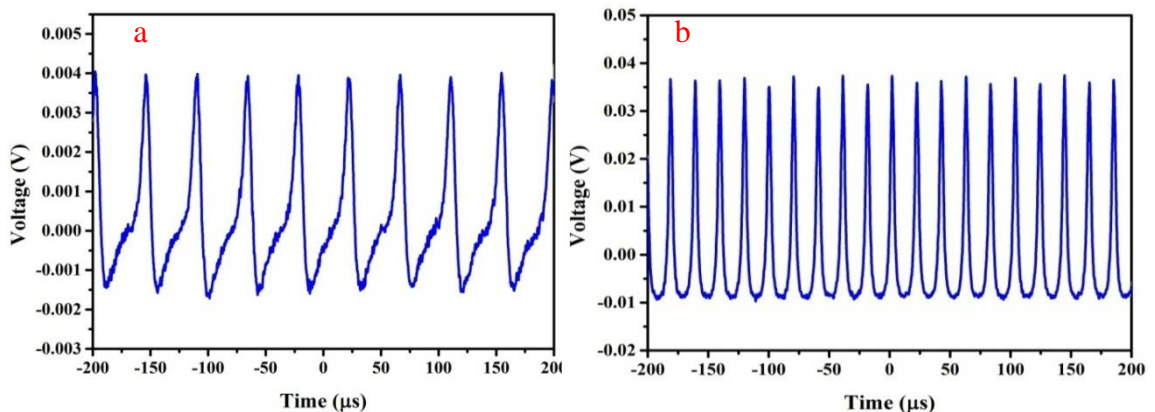


Fig.(4.20): Oscilloscope trace at (a) threshold pump power and (b) maximum applied pump power.

Fig.(4.21a) illustrates a monotonic increase of repetition frequency between the values 22.51-46.18 kHz and then progressively decrease of the pulse duration as the exciting power was raised from 121 to 210 mW. This

figure proves a characteristic behavior of a Q-switched pulse. Boosting the input exciting power caused in additional gain supply to saturate the optical modulator matter. Accordingly, the bleaching energy accumulated in the active matter was gotten earlier, producing to an upsurge in the repetition frequency and a lessening in the pulse duration. On the other side, the dependence of average output power and pulse energy of the proposed laser on the input pump power is illustrated in Fig.(4.21b), which this figure shows a near-linear reliance of the average output power and the pulse energy on the pump power. The recorded output power upsurges linearly up to 179 μW , while the pulse energy changed from 1.94 nJ to 3.88 nJ as the pump power was improved across the range 120–210 mW.

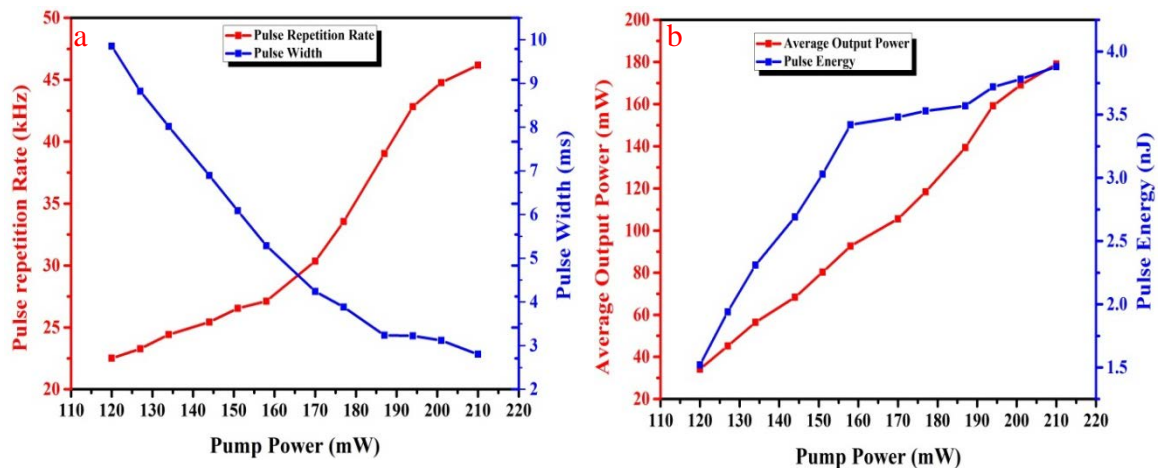


Fig.(4.21): (a) Pulse width and pulse repetition rate, and (b) Output power and pulse energy as a function of pump power.

Additionally, the stability of this laser system was examined by monitoring the RF output spectrum. Fig.(4.22a) demonstrates the frequency characteristics of the Q-switching pulses at a pump level of 210 mW. At maximum pump power, the fundamental RF was observed at 46.18 kHz with a SNR of about 61.6 dB with no spectral modulation. Fig.(4.22b) demonstrates the resultant single-pulse envelope, which displays a symmetrical, Gaussian-like shape.

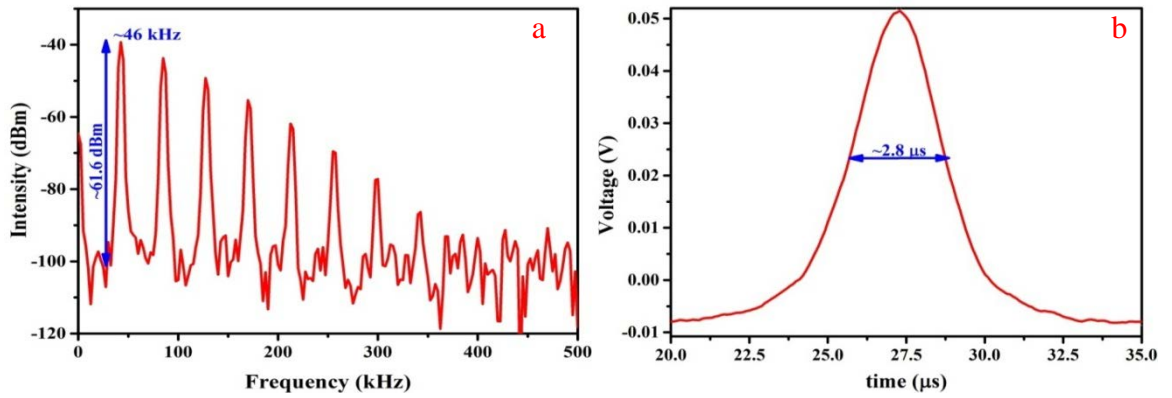


Fig. (4.22): (a) Single pulse envelope, and (b) RF spectrum of EDFL based on $\text{Fe}_2\text{O}_3/\text{SiO}_2$ thin film.

As the pump power reached 250 mW level, an obvious mode-locked signal appeared. By adjusting the polarization controller, a fundamental frequency of 26.5 MHz and a pulse width of about 4.6 ns, as shown in Fig.(4.23). Still, these mode-locked pulses suffered from some fluctuation.

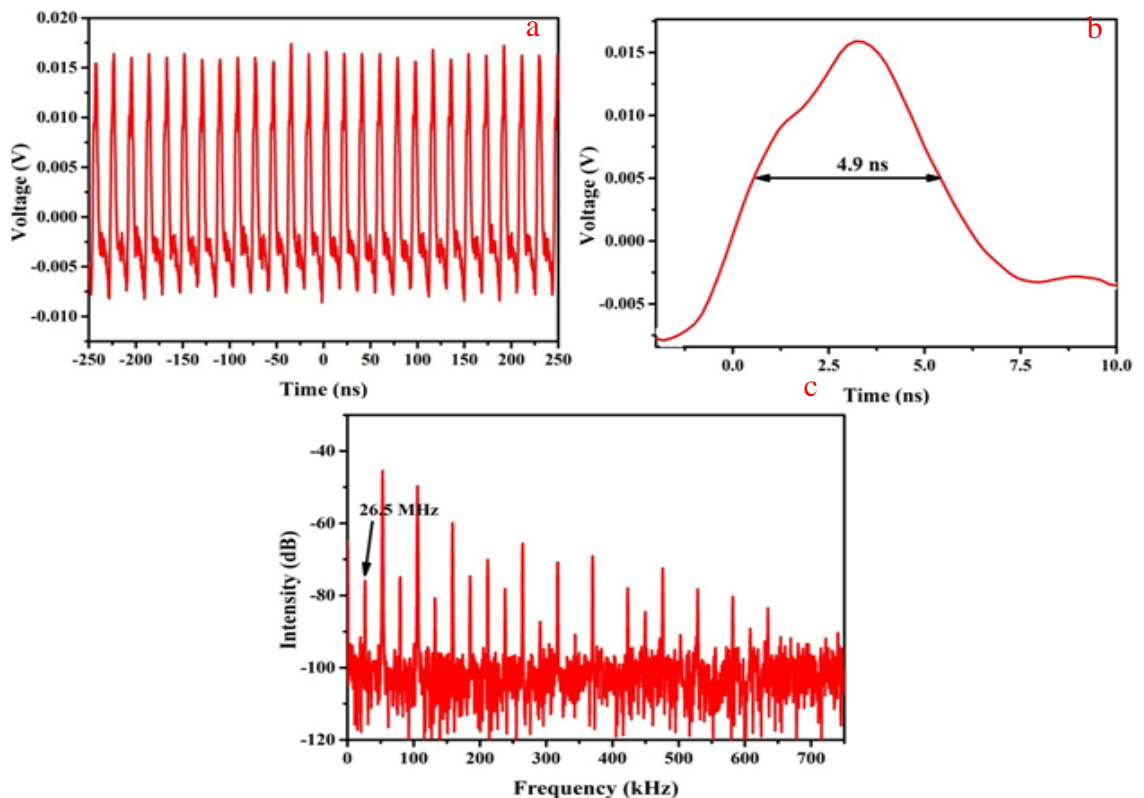


Fig. (4.23): (a) Oscilloscope trace, (b) single pulse envelope, and (c) RF spectrum of EDFL based on $\text{Fe}_2\text{O}_3/\text{SiO}_2$ thin film at 250 mW of pump power.

The related optical spectra of the proposed EDFL for various pump powers (96.3, 144, and 250) are showed in Fig.(4.24). The single-(1563.7), dual-(1562.7, 1563.3) line oscillations were observed as the pump power varied from the threshold of 96.3 mW to 144 mW.

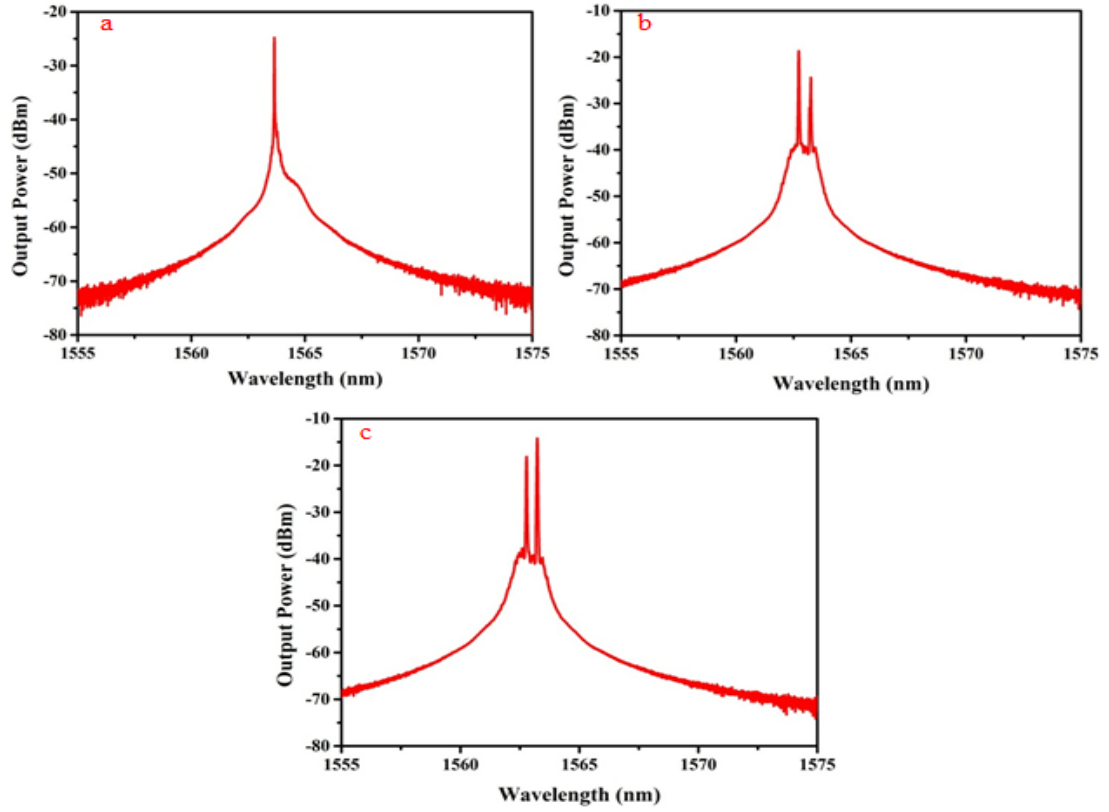


Fig (4.24): Optical spectra of EDFL based on Fe₂O₃/SiO₂ thin film at pump power of: (a) 96.3 mW, (b) 144 mW, and (c) 250 mW.

CHAPTER FIVE
CONCLUSIONS AND
SUGGESTIONS FOR FUTURE
WORK

Chapter Five

Conclusions and Suggestions for Future Work

5.1 Conclusions

In conclusion, we proposed and experimentally demonstrated a simple, compact and low cost multiwavelength from both ytterbium-doped fiber laser and erbium-doped fiber laser by utilizing three different types of nanomaterials (Ni-NPs, Fe₂O₃-NPs, and SiO₂-NPs) as optical modulator. Our study may pave an innovative method to produce multiwavelength lasing by employing new nonlinear materials at low threshold pumping with a short length cavity.

From this work, the following conclusions are drawn:

1. The Z-scan technique reveals that Ni-NPs, Fe₂O₃-NPs, SiO₂-NPs, and Fe₂O₃/SiO₂ nanocomposite possess strong third-order susceptibility. The remarkable optical efficiency of these nanoparticles is equivalent to several kilometers of high nonlinear fiber, which significantly reduces the cavity length and the required pump power.
2. Utilizing Ni-thin layer; high stable CW multiwavelength was simply generated in the L-band and 1 μ m and without utilizing any supplementary optical elements. Besides, mode-locking behavior was realized in YDFL too.
3. When a small piece of fabricated Ni-PVA was integrated into a ring cavity of both EDFL and YDFL, passively Q-switching multiwavelength with pulse duration of a range between several nanoseconds to few microseconds have been realized.
4. The Fe₂O₃-PVA thin film has been assisted to realize multiwavelength operated in CW regime around 1040 nm region, and operated in Q-switching regime around 1563 nm.

5. Fe_2O_3 -thin layer assists to generate multiple-channel oscillation operated in the mode-locked regime at 1 μm region.
6. SiO_2 -NPs assist to generate CW multiwavelength and pulse multiwavelength in the 1 μm region using SiO_2/PVA and $\text{SiO}_2\text{-NF}$, respectively.
7. In a 1.5 μm region, SiO_2 -NPs induced a multiple lasing line emitted in the Q-switching regime with pulse duration of few μs by SiO_2/PVA .
8. Multiwavelength assisted by FWM in 1 and 1.5 μm regions with mode-locked and CW operations were realized from YDFL and EDFL based on $\text{Fe}_2\text{O}_3/\text{SiO}_2$ nanocomposite, respectively.

5.2 Suggestions for Future Work:

To enhance the multiwavelength fiber laser performance and to improve more effective nonlinear optical modulator materials, we suggest the following future work:

1. Examination of CW and pulsed multiwavelength operation in thulium and holmium doped fibers at 2 μm band.
2. Realization of flat-gain multiwavelength operation by using multiple cascaded filters in EDFL and YDFL.
3. Exploring other innovative ways to achieve new high NL materials. Nanocomposites present an adaptable and specific approach to tailor the bandgap and non-linear properties of the materials. So, by adjusting the composition of metal (Ni-NPs), with metal oxide (Fe_2O_3 -NPs) and/or dielectric nanoparticles (SiO_2), binary and ternary composite can be attained with tunable characteristics.
4. The spin coating technique can be used to fabricate thinner and evenly surface nanocomposite polymeric film. That will minimize beam divergence and scattering losses and thus reducing the non-saturable loss and improving the laser performance.
5. The optimization of the laser cavity should be carried out by more reducing the total cavity length, and by optimizing the pumping scheme, also the optimization of the cavity out-coupling is vital via altering the coupling ratio other than that of 90:10. This will improve the laser output performance and increase efficiency.
6. Higher pumping power must be considered to obtain efficient nonlinear phenomena. Pump power in the range of 1 W is sufficient for fiber-based NL applications.
7. We can extend our work in the visible range.

- [1] T. Maiman, "Stimulated optical radiation in ruby", *Nature*. vol.187, p.493–494, 1960.
- [2] E. Snitzer, "Optical maser action of Nd^{3+} in a barium crown glass", *Physical Review Letters*. vol.7, p.444, 1961.
- [3] E. Snitzer, "Proposed fiber cavities for optical masers", *Journal of Applied Physics*. vol.32, p.36–39, 1961.
- [4] C. Koester, E. Snitzer, "Amplification in a fiber laser", *Applied Optics*. vol.3, p.1182–1186, 1964.
- [5] V. Ter-Mikirtychev, "Fundamentals of fiber lasers and fiber amplifiers", Springer, 2014.
- [6] D. Funk, J. Carlson, J. Eden, "Room temperature upconversion ultraviolet (381 nm) and violet (412 nm) laser in Nd^{3+} : ZBLAN fiber, in: *UV and Visible Lasers and Laser Crystal Growth*", International Society for Optics and Photonics, Vol. 2380, pp. 108–114, 1995.
- [7] J. Schneider, "Fluoride fibre laser operating at 3.9/spl mu/m", *Electronics Letters*. vol. 31, p.1250–1251, 1995.
- [8] L. Dong, B. Samson, "Fiber Lasers: Basics, Technology, and Applications", Crc Press, 2016.
- [9] B. Meggitt, K. Grattan, "Optical Fiber Sensor Technology", Springer, 1998.
- [10] S. Xiao, Q. Zeng, J. Wang, J. Xu, Y. Wang, "Realization of multiwavelength label optical packet switching", *IEEE Photonics Technology Letters*. vol.15, p. 605–607, 2003.
- [11] A. Salman, A.H. Al-Janabi, "Q-switching near-infrared multiwavelength generation by intracavity tungsten-oxide-induced four-wave mixing in an erbium-doped fiber laser", *Applied Optics*. vol.58, p.4332–4336, 2019.
- [12] X. Du, H. Zhang, X. Wang, X. Wang, P. Zhou, Z. Liu, "Multiwavelength Raman fiber laser based on polarization maintaining fiber loop mirror and random distributed feedback", *Laser Physics Letters*. vol.12, p.45106, 2015.
- [13] S. Sugavanam, Z. Yan, V. Kamynin, A.S. Kurkov, L. Zhang, D. V Churkin, "Multiwavelength generation in a random distributed feedback fiber laser using an all fiber Lyot filter", *Optics Express*. vol.22, p.2839–2844, 2014.
- [14] X. Liu, L. Zhan, S. Luo, Z. Gu, J. Liu, Y. Wang, Q. Shen, "Multiwavelength erbium-doped fiber laser based on a nonlinear amplifying loop mirror assisted by un-pumped EDF", *Optics Express*. vol.20, p.7088–7094, 2012.

- [15] P. Wang, D. Weng, K. Li, Y. Liu, X. Yu, X. Zhou, "Multi-wavelength Erbium-doped fiber laser based on four-wave-mixing effect in single mode fiber and high nonlinear fiber", *Optics Express*. vol.21 p.12570–12578, 2013.
- [16] W. Khaleel, A.H. Al-Janabi, "Erbium-doped fiber ring laser with wavelength selective filter based on non-linear photonic crystal fiber Mach–Zehnder interferometer", *Laser Physics*. vol.27, p.105104, 2017.
- [17] S. Yamashita, K. Hotate, "Multiwavelength erbium-doped fibre laser using intracavity etalon and cooled by liquid nitrogen", *Electronics Letters*. vol.32, p.1298–1299, 1996.
- [18] A. Salman, A.H. Al-Janabi, "Multiwavelength Q-switched erbium-doped fibre laser-based aluminum nanoparticles saturable absorber and sagnac loop filter, *Laser Physics*". vol.29, p.65103, 2019.
- [19] Y. Yuan, Y. Yao, M. Yi, B. Guo, J. Tian, "Multiwavelength fiber laser employing a nonlinear Brillouin optical loop mirror: experimental and numerical studies", *Optics Express*. vol.22, p.15352–15363, 2014.
- [20] Suchita, S. Sarbadhikari, and R. Vijaya, "Spectral broadening due to intra-cavity four-wave mixing at low pump powers in erbium-doped fiber ring laser", *International Journal of Modern Physics B*. vol.28, p.1442008, 2014.
- [21] L. Wang, X. Dong, P.P. Shum, H. Su, "Tunable erbium-doped fiber laser based on random distributed feedback", *IEEE Photonics Journal*. vol.6, p.1–5, 2014.
- [22] A. Al-Alimi, M. Yaacob, A.F Abas, M. Mahdi, M. Al-Mansoori, M. Mokhtar, "Simple multiwavelength Brillouin–Erbium-doped fiber laser structure based on short SSMF", *Optics Communications*. vol.300, p.8–11, 2013.
- [23] J. Liu, Y. Chen, Y. Li, H. Zhang, S. Zheng, S. Xu, "Switchable dual-wavelength Q-switched fiber laser using multilayer black phosphorus as a saturable absorber", *Photonics Research*. vol.6 p.198–203, 2018.
- [24] A.A. Salman, A. Al-Janabi, "Triple-wavelength Q-switched ytterbium-doped fiber laser based on tungsten oxide as saturable absorber", *Microwave and Optical Technology Letters*. vol.62, p.2257–2262, 2020.
- [25] A. Al-Masoodi, M. Ahmed, H. Arof, S. Harun, "Multi-Wavelength Q-Switched Ytterbium-Doped Fiber Laser with Multi-Walled Carbon Nanotubes", *Fiber and Integrated Optics*. vol.37, p.92–102, 2018.
- [26] L. Li, R. Lv, S. Liu, Z. Chen, J. Wang, Y. Wang, W. Ren, W. Liu, "Ferroferric-oxide nanoparticle based Q-switcher for a 1 micro m region", *Optical Materials*

- Express. vol.9, p.731–738, 2019.
- [27] Y. Zhao, A. Dunn, J. Lin, D. Shi, "Chapter 13 - Photothermal Effect of Nanomaterials for Efficient Energy Applications", *Novel Nanomaterials for Biomedical, Environmental and Energy Applications* (Eds.), Micro and Nano Technologies, Elsevier, p.415–434, 2019.
- [28] Z. Luo, M. Zhou, Z. Cai, C. Ye, J. Weng, G. Huang, H. Xu, "Graphene-Assisted Multiwavelength Erbium-Doped Fiber Ring Laser", *IEEE Photonics Technology Letters*. vol.23, p.501–503, 2011.
- [29] A. Salman, A.H. Al-Janabi, "Aluminum nanoparticles saturable absorber as a passive Q-switcher for erbium-doped fiber laser ring cavity configuration", *Laser Physics*. vol.29, p.45102, 2019.
- [30] S. Sadeq, S. Harun, A.H. Al-Janabi, "Ultrashort pulse generation with an erbium-doped fiber laser ring cavity based on a copper oxide saturable absorber", *Applied Optics*. vol.57, p.5180–5185, 2018.
- [31] Z. Kang, X. Guo, Z. Jia, Y. Xu, L. Liu, D. Zhao, G. Qin, W. Qin, "Gold nanorods as saturable absorbers for all-fiber passively Q-switched erbium-doped fiber laser", *Optical Materials Express*. vol.3, p.1986–1991, 2013.
- [32] G. Sobon, J. Sotor, I. Pasternak, A. Krajewska, W. Strupinski, K.M. Abramski, "Multilayer graphene-based saturable absorbers with scalable modulation depth for mode-locked Er- and Tm-doped fiber lasers", *Optical Materials Express*. vol.5, p.2884–2894, 2015.
- [33] Z. Qin, G. Xie, H. Zhang, C. Zhao, P. Yuan, S. Wen, L. Qian, "Black phosphorus as saturable absorber for the Q-switched Er:ZBLAN fiber laser at 2.8 μm ", *Optics Express*. vol.23, p.24713–24718, 2015.
- [34] F. Rashid, S. Azzuhri, M. Salim, R. Shaharuddin, M. Ismail, M. Ismail, M. Razak, H. Ahmad, "Using a black phosphorus saturable absorber to generate dual wavelengths in a Q-switched ytterbium-doped fiber laser", *Laser Physics Letters*. vol.13, p.85102, 2016.
- [35] R. Woodward, R. Howe, T. Runcorn, G. Hu, F. Torrisi, E. Kelleher, T. Hasan, "Wideband saturable absorption in few-layer molybdenum diselenide (MoSe_2) for Q-switching Yb-, Er- and Tm-doped fiber lasers", *Optics Express*. vol.23, p.20051–20061, 2015.
- [36] H. Liu, A. Luo, F. Wang, R. Tang, M. Liu, Z. Luo, W. Xu, C. Zhao, H. Zhang, "Femtosecond pulse erbium-doped fiber laser by a few-layer MoS_2 saturable

- absorber", *Optics Letters*. vol.39, p.4591–4594, 2014.
- [37] H. Zhang, S. Lu, J. Zheng, J. Du, S. Wen, D. Tang, K Loh, "Molybdenum disulfide (MoS_2) as a broadband saturable absorber for ultra-fast photonics", *Optics Express*. vol.22, p.7249–7260, 2014.
- [38] B. Chen, X. Zhang, K. Wu, H. Wang, J. Wang, J. Chen, "Q-switched fiber laser based on transition metal dichalcogenides MoS_2 , MoSe_2 , WS_2 , and WSe_2 ", *Optics Express*. vol.23, p.26723–26737, 2015.
- [39] H. Guo, M. Feng, F. Song, H. Li, A. Ren, X. Wei, Y. Li, X. Xu, J. Tian, "Q-Switched Erbium-Doped Fiber Laser Based on Silver Nanoparticles as a Saturable Absorber", *IEEE Photonics Technology Letters*. vol.28, p.135–138, 2016.
- [40] A. Muhammad, M. Ahmad, R. Zakaria, H. Rahim, S. Yusoff, K. Hamdan, H. Yusof, H. Arof, S. Harun, "Q-Switching Pulse Operation in 1.5- μm Region Using Copper Nanoparticles as Saturable Absorber", *Chinese Physics Letters*. vol.34 p.34205, 2017.
- [41] S. Sadeq, S. Al-Hayali, S. Harun, A. Al-Janabi, "Copper oxide nanomaterial saturable absorber as a new passive Q-switcher in erbium-doped fiber laser ring cavity configuration", *Results in Physics*. vol.10, p.264–269, 2018.
- [42] S. Al-Hayali, D. Mohammed, W. Khaleel, A. Al-Janabi, "Aluminum oxide nanoparticles as saturable absorber for C-band passively Q-switched fiber laser", *Applied Optics*. vol.56, p.4720–4726, 2017.
- [43] S. Al-Hayali, A. Al-Janabi, "Triple-wavelength passively Q-switched ytterbium-doped fibre laser using zinc oxide nanoparticles film as a saturable absorber", *Journal of Modern Optics*. vol.65, p.1559–1564, 2018.
- [44] A. Nady, M. Ahmed, A. Latiff, A. Numan, C. Raymond Ooi, S. Harun, "Nickel oxide nanoparticles as a saturable absorber for an all-fiber passively Q-switched erbium-doped fiber laser", *Laser Physics*. vol.27, p.65105, 2017.
- [45] D. Wu, H. Lin, Z. Cai, J. Peng, Y. Cheng, J. Weng, H. Xu, "Saturable Absorption of Copper Nanowires in Visible Regions for Short-Pulse Generation", *IEEE Photonics Journal*. vol.8, p.1–7, 2016.
- [46] J. Zhang, C. Noguez, "Plasmonic Optical Properties and Applications of Metal Nanostructures", *Plasmonics*. vol.3, p.127–150, 2008.
- [47] X. Wang, Z. Luo, H. Liu, N. Zhao, M. Liu, Y. Zhu, J. Xue, A. Luo, W. Xu, "Gold nanorod as saturable absorber for Q-switched Yb-doped fiber laser",

- Optics Communications. vol.346, p.21–25, 2015.
- [48] G. Villanueva Ibáñez, "Continuous wave and pulsed erbium-doped fiber lasers for microwave photonics applications", Doctoral dissertation, Universitat Politècnica de València, 2012.
- [49] R. Menzel, "Photonics: linear and nonlinear interactions of laser light and matter", Springer Science & Business Media, 2013.
- [50] G. Agrawal, "Chapter 8 - Stimulated Raman Scattering", in: G.B.T.-N.F.O. (5th E.), Optics and Photonics, Academic Press, Boston, pp. 295–352, 2013.
- [51] N. Abidin, M. Bakar, Y. Kamil, A. Abas, M. Alresheedi, M. Mahdi, "Open Cavity Hybrid Raman-Erbium Random Fiber Laser With Common Pump", IEEE. vol.7, p.85867–85874, 2019.
- [52] X. Tong, "Advanced materials for integrated optical waveguides", Springer, 2014.
- [53] M. Digonnet, "Rare-earth-doped fiber lasers and amplifiers, revised and expanded", CRC press, 2001.
- [54] F. Mitschke, F. Mitschke, "Fiber Optics", Springer, 2016.
- [55] M. Azadeh, "Fiber optics engineering", Springer, 2009.
- [56] A. Al-Azzawi, "Fiber optics: principles and practices", CRC Press, 2017.
- [57] R. Paschotta, "Field guide to optical fiber technology", in: SPIE, 2010.
- [58] A. GHATAK, A. Ghatak, K. Thyagarajan, K. Thyagarajan, "An introduction to fiber optics", Cambridge university press, 1998.
- [59] A. Juárez, I. Huerta, J. Asomoza, M. del Rocío Gómez Colín, "Photonic components for analog fiber links", Optical Communication. 2012.
- [60] T. Plc, "PLC-900 Fiber Polarization Controller", from Thorlab. com. web.
- [61] C. Barnard, P. Myslinski, J. Chrostowski, M. Kavehrad, "Analytical model for rare-earth-doped fiber amplifiers and lasers", IEEE Journal of Quantum Electronics. vol.30, p.1817–1830, 1994.
- [62] D.D. Michel, "Linear-cavity tunable fibre lasers employing an Opto-VLSI processor and a MEMS-based device", 2012.
- [63] J. Causado-Buelvas, N. Gomez-Cardona, P. Torres, "Practical Method for engineering Erbium-doped fiber lasers from step-like pulse excitations", in: Journal of Physics: Conference Series, IOP Publishing, p. 12017, 2011.
- [64] S. Ali, K. Al-Khateeb, B. Bouzid, "Comparison of the effect structure on ring and linear cavity lasers of Er-doped optical fibers", in: 2008 International Conference

- on Computer and Communication Engineering, IEEE, pp. 546–549, 2008.
- [65] H. Pang, H. Lian, R. Zhao, T. Liu, B. Hu, H. Cui, Y. Wang, "Design of an erbium-doped fiber laser based on ring cavity", in: 4th International Symposium on Advanced Optical Manufacturing and Testing Technologies: Advanced Optical Manufacturing Technologies, International Society for Optics and Photonics, p. 72822P, 2009.
- [66] R. Pérez-Herrera, M. Quintela, M. Fernández-Vallejo, A. Quintela, M. López-Amo, J. López-Higuera, "Stability comparison of two ring resonator structures for multiwavelength fiber lasers using highly doped Er-fibers", *Journal of Lightwave Technology*. vol.27, p.2563–2569, 2009.
- [67] S. Harun, H. Arof, "Current developments in optical fiber technology", *BoD–Books on Demand*, 2013.
- [68] N. Langford, "OPTICAL FIBER SENSOR TECHNOLOGY" Vol.2, Springer, 1998.
- [69] R. Mary, D. Choudhury, A. Kar, "Applications of fiber lasers for the development of compact photonic devices", *IEEE Journal of Selected Topics in Quantum Electronics*. vol.20, p.72–84, 2014.
- [70] L.B. Glebov, "Linear and nonlinear photoionization of silicate glasses", *Glass Science And Technology-Frankfurt Am Main*. vol.75, p.1–6, 2004.
- [71] A. Razif, B. Muhammad, "Development Of Metal Based Saturable Absorber For Pulsed Laser Generator" Faculty Of Engineering, University Of Malaya, Kuala Lumpur, 2018.
- [72] S. Tanabe, "Rare-earth-doped glasses for fiber amplifiers in broadband telecommunication", *Comptes Rendus Chimie*. vol.5, p.815–824, 2002.
- [73] N. Langford, "Optical fiber lasers", in: *Optical Fiber Sensor Technology*, Springer, p. 37–98, 1998.
- [74] W. Zhu, L. Qian, A. Helmy, "Implementation of three functional devices using erbium-doped fibers: An advanced photonics lab", *Laser*. vol. 1520, p.1570nm, 2007.
- [75] E. Desurvire, "Amplifiers, Principles and Applications", Wiley, 1994.
- [76] N. Ngo, "Ultra-fast fiber lasers: principles and applications with MATLAB® models", CRC Press, 2010.
- [77] T. Pfeiffer, H. Schmuck, H. Bulow, "Output power characteristics of erbium-doped fiber ring lasers", *IEEE Photonics Technology Letters*. vol.4, p.847–849,

1992.

- [78] A. Naji, B. Hamida, X. Cheng, M. Mahdi, S. Harun, S. Khan, W. Al-Khateeb, A. Zaidan, B. Zaidan, H. Ahmad, "Review of erbium-doped fiber amplifier", *International Journal of Physical Sciences*. vol.6, p.4674–4689, 2011.
- [79] P. Franco, M. Midrio, A. Tozzato, M. Romagnoli, F. Fontana, "Characterization and optimization criteria for filterless erbium-doped fiber lasers", *JOSA B*. vol.11, p.1090–1097, 1994.
- [80] G.P. Agrawal, "Nonlinear Fiber Optics: Formerly Quantum Electronics", Academic press, 2013.
- [81] K. Okamoto, "Fundamentals of optical waveguides", Academic press, 2006.
- [82] R. Boyd, "Nonlinear Optics" 3rd E., elsevier, 2008.
- [83] G. Agrawal, "Applications of nonlinear fiber optics", Academic press, 2020.
- [84] D. Wu, Z. Guo, Z. Wu, P. Shum, "900 nm waveband four wave mixing generation in highly nonlinear photonic crystal fiber", *Journal of Optics*. vol.20, p.35501, 2018.
- [85] L. Zhang, T. Tuan, H. Kawamura, T. Suzuki, Y. Ohishi, "Optical parametric oscillator based on degenerate four-wave mixing in suspended core tellurite microstructured optical fiber", *Optics Express*. vol.23, p.26299–26304, 2015.
- [86] H. Sun, X. Liu, L. Wang, X. Li, D. Mao, "Spacing-tunable multi-wavelength fiber laser based on cascaded four-wave mixing in highly nonlinear photonic-crystal fiber", *Laser Physics*. vol.20, p.1994–2000, 2010.
- [87] R. Parvizi, S. Harun, N. Shahabuddin, Z. Yusoff, H. Ahmad, "Multi-wavelength bismuth-based erbium-doped fiber laser based on four-wave mixing effect in photonic crystal fiber", *Optics & Laser Technology*. vol.42, p.1250–1252, 2010.
- [88] U. Keller, K. Weingarten, F. Kartner, D. Kopf, B. Braun, I. Jung, R. Fluck, C. Honninger, N. Matuschek, J. Der Au, "Semiconductor saturable absorber mirrors (SESAM's) for femtosecond to nanosecond pulse generation in solid-state lasers", *IEEE Journal of Selected Topics in QUANTUM ELECTRONICS*. vol.2, p.435–453, 1996.
- [89] Y. Han, Y. Guo, B. Gao, C. Ma, R. Zhang, H. Zhang, "Generation, optimization, and application of ultrashort femtosecond pulse in mode-locked fiber lasers", *Progress in Quantum Electronics*. p.100264, 2020.
- [90] P. Zhou, X. Wang, H. Xiao, Y. Ma, J. Chen, "Review on recent progress on Yb-doped fiber laser in a variety of oscillation spectral ranges", *Laser Physics*.

- vol.22, p.823–831, 2012.
- [91] R.S. Quimby, "Photonics and lasers: an introduction", John Wiley & Sons, 2006.
- [92] R. Paschotta, "Field guide to laser pulse generation", SPIE press Bellingham, 2008.
- [93] Y. Ouyang, T. You, Q. Zhou, M. Liu, H. Hou, X. Liu, W. Liu, "Layered AuTe₂Se_{4/3} for a stable nanosecond Q-switched fiber laser", *Optik*. vol.204, p.164231, 2020.
- [94] O. Svelto, D.C. Hanna, "Principles of lasers", Springer, 2010.
- [95] P.W. Milonni, J.H. Eberly, "Laser resonators and Gaussian beams", *Laser Physics*, 1st E.; John Wiley and Sons, 2010.
- [96] U. Keller, "Recent developments in compact ultrafast lasers", *Nature*. vol.424, p.831–838, 2003.
- [97] T. Hasan, Z. Sun, F. Wang, F. Bonaccorso, P. Tan, A. Rozhin, A. Ferrari, "Nanotube–polymer composites for ultrafast photonics", *Advanced Materials*. vol.21, p.3874–3899, 2009.
- [98] S. De Silvestri, P. Laporta, O. Svelto, "The role of cavity dispersion in cw mode-locked dye lasers", *IEEE Journal of Quantum Electronics*. vol.20, p.533–539, 1984.
- [99] R. Woodward, "Exploiting nonlinearity in optical fibres and nanomaterials for short-pulse laser technology", *Doctoral Thesis, the Diploma of Imperial College London*, 2015.
- [100] I.N. Duling III, I.N. Duling, "Compact sources of ultrashort pulses", *Cambridge University Press*, 1995.
- [101] M. Ahmed, N. Ali, Z. Salleh, A. Rahman, S. Harun, M. Manaf, H. Arof, "All fiber mode-locked Erbium-doped fiber laser using single-walled carbon nanotubes embedded into polyvinyl alcohol film as saturable absorber", *Optics & Laser Technology*. vol.62, p.40–43, 2014.
- [102] M. Zhang, R. Howe, R. Woodward, E. Kelleher, F. Torrisi, G. Hu, S. Popov, J. Taylor, T. Hasan, "Solution processed MoS₂-PVA composite for sub-bandgap mode-locking of a wideband tunable ultrafast Er: fiber laser", *Nano Research*. vol.8, p.1522–1534, 2015.
- [103] S. ZOOZ, "Development Of Dual-Wavelength And Pulsed Fiber Lasers Based On Thulium-Doped Fibers", *Faculty Of Engineering, University Of Malaya, Kuala Lumpur*, 2015.

- [104] S. Yamashita, "A Tutorial on Nonlinear Photonic Applications of Carbon Nanotube and Graphene", *Journal of Lightwave Technology*. vol.30, p.427–447, 2012.
- [105] S. Hussain, "Discovery of several new families of saturable absorbers for ultrashort pulsed laser systems", *Scientific Reports*. vol.9, p.1–9, 2019.
- [106] M. Zhang, G. Hu, G. Hu, R. Howe, L. Chen, Z. Zheng, T. Hasan, "Yb-and Er-doped fiber laser Q-switched with an optically uniform, broadband WS₂ saturable absorber", *Scientific Reports*. vol.5, p.17482, 2015.
- [107] J. Jeon, J. Lee, J.H. Lee, "Numerical study on the minimum modulation depth of a saturable absorber for stable fiber laser mode locking", *JOSA B*. vol.32, p.31–37, 2015.
- [108] M. Zhang, E. Kelleher, S. Popov, J. Taylor, "Ultrafast fibre laser sources: examples of recent developments", *Optical Fiber Technology*. vol.20, p.666–677, 2014.
- [109] I. Jung, F. Kärtner, N. Matuschek, D. Sutter, F. Morier-Genoud, Z. Shi, V. Scheuer, M. Tilsch, T. Tschudi, U. Keller, "Semiconductor saturable absorber mirrors supporting sub-10-fs pulses", *Applied Physics B: Lasers & Optics*. vol.65, 1997.
- [110] C. Hönniger, R. Paschotta, F. Morier-Genoud, M. Moser, U. Keller, "Q-switching stability limits of continuous-wave passive mode locking", *JOSA B*. vol.16, p.46–56, 1999.
- [111] G.J. Spühler, R. Paschotta, R. Fluck, B. Braun, M. Moser, G. Zhang, E. Gini, U. Keller, "Experimentally confirmed design guidelines for passively Q-switched microchip lasers using semiconductor saturable absorbers", *Journal of the Optical Society of America B*. vol.16, p.376–388, 1999.
- [112] M. Fermann, A. Galvanauskas, G. Sucha, "Ultrafast lasers: technology and applications", CRC Press, 2002.
- [113] S. Maidur, P. Patil, "Linear optical and third-order nonlinear optical properties of anthracene chalcone derivatives doped PMMA thin films", *Optik*. vol.190, p.54–67, 2019.
- [114] J. Ma, S. Lu, Z. Guo, X. Xu, H. Zhang, D. Tang, D. Fan, "Few-layer black phosphorus based saturable absorber mirror for pulsed solid-state lasers", *Optics Express*. vol.23, p.22643–22648, 2015.
- [115] T. Schibli, K. Minoshima, H. Kataura, E. Itoga, N. Minami, S. Kazaoui, K.

- Miyashita, M. Tokumoto, Y. Sakakibara, "Ultrashort pulse-generation by saturable absorber mirrors based on polymer-embedded carbon nanotubes", *Optics Express*. vol.13, p.8025–8031, 2005.
- [116] X. Liu, H. Yang, Y. Cui, G. Chen, Y. Yang, X. Wu, X. Yao, D. Han, X. Han, C. Zeng, "Graphene-clad microfiber saturable absorber for ultrafast fiber lasers", *Scientific Reports*. vol.6, 26024, 2016.
- [117] A. El-Korashy, H. El-Zahed, M. Radwan, "Optical studies of $[N(CH_3)_4]_2CoCl_4$, $[N(CH_3)_4]_2MnCl_4$ single crystals in the normal paraelectric phase", *Physica B: Condensed Matter*. vol.334, p.75–81, 2003.
- [118] S. Kimiagar, F. Abrinaei, "Effect of temperature on the structural, linear, and nonlinear optical properties of MgO-doped graphene oxide nanocomposites", *Nanophotonics*. vol.7, p.243–251, 2018.
- [119] E. Van Stryland, M. Sheik-Bahae, "Z-scan measurements of optical nonlinearities", *Characterization Techniques and Tabulations for Organic Nonlinear Materials*. vol.18, p.655–692, 1998.
- [120] G.D. Houser, E. Garmire, "Balanced detection technique to measure small changes in transmission", *Applied Optics*. vol.33, p.1059–1062, 1994.
- [121] J. Du, M. Zhang, Z. Guo, J. Chen, X. Zhu, G. Hu, P. Peng, Z. Zheng, H. Zhang, "Phosphorene quantum dot saturable absorbers for ultrafast fiber lasers", *Scientific Reports*. vol.7, p.42357, 2017.
- [122] C. Zhao, H. Zhang, X. Qi, Y. Chen, Z. Wang, S. Wen, D. Tang, "Ultra-short pulse generation by a topological insulator based saturable absorber", *Applied Physics Letters*. vol.101, p.211106, 2012.
- [123] K. Wang, J. Wang, J. Fan, M. Lotya, A. O'Neill, D. Fox, Y. Feng, X. Zhang, B. Jiang, Q. Zhao, H. Zhang, J.N. Coleman, L. Zhang, W.J. Blau, "Ultrafast Saturable Absorption of Two-Dimensional MoS_2 Nanosheets", *ACS Nano*. vol.7, p.9260–9267, 2013.
- [124] H. Yang, X. Feng, Q. Wang, H. Huang, W. Chen, A. Wee, W. Ji, "Giant Two-Photon Absorption in Bilayer Graphene", *Nano Letters*. vol.11, p.2622–2627, 2011.
- [125] X. Li, Y. Wang, Y. Wang, W. Zhao, X. Yu, Z. Sun, X. Cheng, X. Yu, Y. Zhang, Q.J. Wang, "Nonlinear absorption of SWNT film and its effects to the operation state of pulsed fiber laser", *Optics Express*. vol.22, p.17227–17235, 2014.
- [126] S.Y. Set, H. Yaguchi, Y. Tanaka, M. Jablonski, "Laser Mode Locking Using a

- Saturable Absorber Incorporating Carbon Nanotubes", *Journal of Lightwave Technology*. vol.22, p.51, 2004.
- [127] D. Mohammed, A. Al-Janabi, "Passively Q-switched erbium doped fiber laser based on double walled carbon nanotubes-polyvinyl alcohol saturable absorber", *Laser Physics*. vol.26, p.115108, 2016.
- [128] A. Al-Masoodi, M. Ismail, F. Ahmad, N. Kasim, Y. Munajat, H. Ahmad, S. Harun, "Q-switched Yb-doped fiber laser operating at 1073 nm using a carbon nanotubes saturable absorber", *Microwave and Optical Technology Letters*. vol.56, p.1770–1773, 2014.
- [129] S. Al-Hayali, A. Al-Janabi, "Dual-wavelength passively Q-switched ytterbium-doped fiber laser using Fe₃O₄-nanoparticle saturable absorber and intracavity polarization", *Laser Physics*. vol.28, p.35103, 2018.
- [130] X. Bai, C. Mou, L. Xu, S. Wang, S. Pu, X. Zeng, "Passively Q-switched erbium-doped fiber laser using Fe₃O₄-nanoparticle saturable absorber", *Applied Physics Express*. vol.9, p.42701, 2016.
- [131] S. Al-Hayali, S. Selleri, A. Al-Janabi, "Dual-Wavelength Passively Q-Switched Ytterbium-Doped Fiber Laser Based on Aluminum Oxide Nanoparticle Saturable Absorbers", *Chinese Physics Letters*. vol.34, p.114201, 2017.
- [132] N. Aziz, A. Latiff, M. Lokman, E. Hanafi, S. Harun, "Zinc Oxide-Based Q-Switched Erbium-Doped Fiber Laser", *Chinese Physics Letters*. vol.34, p.44202, 2017.
- [133] H. Ahmad, S. Reduan, Z. Ali, M. Ismail, N. Ruslan, C. Lee, R. Puteh, S. Harun, "C-Band Q-Switched Fiber Laser Using Titanium Dioxide (TiO₂) As Saturable Absorber", *IEEE Photonics Journal*. vol.8, p.1–7, 2016.
- [134] D. Mohammed, W. Khaleel, A. Al-Janabi, "Tunable Q-switched erbium doped fiber laser based on metal transition oxide saturable absorber and refractive index characteristic of multimode interference effects", *Optics & Laser Technology*. vol.97, p.106–110, 2017.
- [135] A. Stepanov, "Optical Properties of Polymer Nanocomposites With Functionalized Nanoparticles", in: K. Pielichowski, T.M.B.T.-P.C. with F.N. Majka (Eds.), *Micro and Nano Technologies*, Elsevier, pp. 325–355, 2019.
- [136] S. Srivastava, M. Haridas, J. Basu, "Optical properties of polymer nanocomposites", *Bulletin of Materials Science*. vol.31, p.213–217, 2008.
- [137] H. Guo, M. Feng, F. Song, H. Li, A. Ren, X. Wei, Y. Li, X. Xu, J. Tian, "Q-

- Switched Erbium-Doped Fiber Laser Based on Silver Nanoparticles as a Saturable Absorber", *IEEE Photonics Technology Letters*. vol.28, p.135–138, 2016.
- [138] K. Wang, Y. Feng, C. Chang, J. Zhan, C. Wang, Q. Zhao, J. Coleman, L. Zhang, W. Blau, J. Wang, "Broadband ultrafast nonlinear absorption and nonlinear refraction of layered molybdenum dichalcogenide semiconductors", *Nanoscale*. vol.6, p.10530–10535, 2014.
- [139] F. Davar, Z. Fereshteh, M. Salavati-Niasari, "Nanoparticles Ni and NiO: Synthesis, characterization and magnetic properties", *Journal of Alloys and Compounds*. vol.476, p.797–801, 2009.
- [140] K. Musza, M. Szabados, A. Ádám, Z. Kónya, Á. Kukovecz, P. Sipos, I. Pálinkó, "Mechanochemically modified hydrazine reduction method for the synthesis of nickel nanoparticles and their catalytic activities in the Suzuki–Miyaura cross-coupling reaction", *Reaction Kinetics, Mechanisms and Catalysis*. vol.126, p.857–868, 2018.
- [141] B. Sun, Y. Zhang, R. Zhang, H. Yu, G. Zhou, H. Zhang, J. Wang, "Nonlinear optical response during the electron transition process originated from 3D spin-orbit splitting in NiO nanosheets", *Optics Express*. vol.26, p.1230–1236, 2018.
- [142] L. Zhao, Z. Yang, Q. Cao, L. Yang, X. Zhang, J. Jia, Y. Sang, H.-J. Wu, W. Zhou, H. Liu, "An earth-abundant and multifunctional Ni nanosheets array as electrocatalysts and heat absorption layer integrated thermoelectric device for overall water splitting", *Nano Energy*. vol.56, p.563–570, 2019.
- [143] L. Fan, J. Khodadadi, "Thermal conductivity enhancement of phase change materials for thermal energy storage: A review", *Renewable and Sustainable Energy Reviews*. vol.15, p.24–46, 2011.
- [144] Y. Terada, K. Ohkubo, T. Mohri, T. Suzuki, "Thermal conductivity in nickel solid solutions", *Journal of Applied Physics*. vol.81, p.2263–2268, 1997.
- [145] R. Eluri, B. Paul, "Synthesis of nickel nanoparticles by hydrazine reduction: mechanistic study and continuous flow synthesis", *Journal of Nanoparticle Research*. vol.14, p.800, 2012.
- [146] N. Roselina, A. Azizan, K. Hyie, A. Jumahat, M. Bakar, "Effect of pH on Formation of Nickel Nanostructures through Chemical Reduction Method", *Procedia Engineering*. vol.68, p.43–48, 2013.
- [147] T.S. Soliman, S. Vshivkov, S. Elkalashy, "Structural, linear and nonlinear optical

- properties of Ni nanoparticles–Polyvinyl alcohol nanocomposite films for optoelectronic applications", *Optical Materials*. vol.107, p.110037, 2020.
- [148] H. Fan, G. You, Y. Li, Z. Zheng, H. Tan, Z. Shen, S. Tang, Y. Feng, "Shape-controlled synthesis of single-crystalline Fe₂O₃ hollow nanocrystals and their tunable optical properties", *The Journal of Physical Chemistry C*. vol.113, p.9928–9935, 2009.
- [149] D. Mao, X. Cui, Z. He, H. Lu, W. Zhang, L. Wang, Q. Zhuang, S. Hua, T. Mei, J. Zhao, "Broadband polarization-insensitive saturable absorption of Fe₂O₃ nanoparticles", *Nanoscale*. vol.10, p.21219–21224, 2018.
- [150] H. Zhou, A. Mito, D. Kundu, I. Honma, "Nonlinear Optical Susceptibility of Fe₂O₃ Thin Film Synthesized by a Modified Sol-Gel Method", *Journal of Sol-Gel Science and Technology*. vol.19, p.539–541, 2000.
- [151] S. Hua, K. Du, H. Wang, X. Cui, W. Zhang, T. Mei, "Study of the third-order nonlinear optical properties of Fe₂O₃ nanoparticles using the femtosecond intensity scan technique", In *Eleventh International Conference on Information Optics and Photonics (CIOP 2019)*, International Society for Optics and Photonics, vol.11209, p.112093R, 2019.
- [152] T. Hashimoto, T. Yamada, T. Yoko, "Third-order nonlinear optical properties of sol-gel derived α -Fe₂O₃, γ -Fe₂O₃, and Fe₃O₄ thin films, *Journal of Applied Physics*. vol.80, p.3184–3190, 1996.
- [153] F. Cui, C. Feng, R. Xie, Z. Hua, H. Ohtsuka, Y. Sakka, J. Shi, "Magnetic field-induced off-resonance third-order optical nonlinearity of iron oxide nanoparticles incorporated mesoporous silica thin films during heat treatment", *Optics Express*. vol.18, 2010.
- [154] M.J. Pulikkathumbayil, G. Govindaraj, "Unusual combination of conduction and dielectric relaxations in nanocrystalline α -Fe₂O₃", *Materials Letters*. vol.264, p.127314, 2020.
- [155] M. Joya, J. Barón-Jaimez, J. Barba-Ortega, "Preparation and characterization of Fe₂O₃ nanoparticles", *Journal of Physics: Conference Series*. vol.466, p.12004, 2013.
- [156] M. Rashad, "Tuning optical properties of polyvinyl alcohol doped with different metal oxide nanoparticles", *Optical Materials*. vol.105, p.109857, 2020.
- [157] D.E. Fouad, C. Zhang, H. El-Didamony, L. Yingnan, T. Mekuria, A. Shah, "Improved size, morphology and crystallinity of hematite (α -Fe₂O₃)

- nanoparticles synthesized via the precipitation route using ferric sulfate precursor", *Results in Physics*. vol.12, p.1253–1261, 2019.
- [158] G. Chatzikyriakos, K. Iliopoulos, A. Bakandritsos, S. Couris, "Nonlinear optical properties of aqueous dispersions of ferromagnetic γ -Fe₂O₃ nanoparticles", *Chemical Physics Letters*. vol.493, p.314–318, 2010.
- [159] M. Ando, K. Kadono, M. Haruta, T. Sakaguchi, M. Miya, "Large third-order optical nonlinearities in transition-metal oxides", *Nature*. vol.374, p.625–627, 1995.
- [160] P. Thomas, P. Sreekanth, K. Abraham, "Nanosecond and ultrafast optical power limiting in luminescent Fe₂O₃ hexagonal nanomorphotype", *Journal of Applied Physics*. vol.117, p.53103, 2015.
- [161] X. Fu, F. Bei, X. Wang, X. Yang, L. Lu, "Surface-enhanced Raman scattering of 4-mercaptopyridine on sub-monolayers of α -Fe₂O₃ nanocrystals (sphere, spindle, cube)", *Journal of Raman Spectroscopy: An International Journal for Original Work in All Aspects of Raman Spectroscopy, Including Higher Order Processes, and Also Brillouin and Rayleigh Scattering*. vol.40, p.1290–1295, 2009.
- [162] W. Wang, G. Yang, Z. Chen, Y. Zhou, H. Lu, G. Yang, "Iron nanoparticles in amorphous BaTiO₃ thin films with large third-order optical nonlinearity", *Journal of Applied Physics*. vol.92, p.7242–7245, 2002.
- [163] L. Sirleto, A. Aronne, M. Gioffrè, E. Fanelli, G. Righini, P. Pernice, A. Vergara, "Compositional and thermal treatment effects on Raman gain and bandwidth in nanostructured silica based glasses", *Optical Materials*. vol.36, p.408–413, 2013.
- [164] L. Sirleto, A. Vergara, M.A. Ferrara, "Advances in stimulated Raman scattering in nanostructures", *Advances in Optics and Photonics*. vol.9, p.169–217, 2017.
- [165] V. Joudrier, P. Bourdon, F. Hache, C. Flytzanis, "Characterization of nonlinear scattering in colloidal suspensions of silica particles", *Applied Physics B*. vol.70, p.105–109, 2000.
- [166] L. Irimpan, B. Krishnan, V. Nampoore, P. Radhakrishnan, "Nonlinear optical characteristics of nanocomposites of ZnO–TiO₂–SiO₂", *Optical Materials*. vol.31, p.361–365, 2008.
- [167] X. Wang, Z. Luo, M. Liu, R. Tang, A. Luo, W. Xu, "Wavelength-switchable femtosecond pulse fiber laser mode-locked by silica-encased gold nanorods", *Laser Physics Letters*. vol.13, p.45101, 2016.
- [168] X. Wang, S. Yang, M. Sun, Q. Liang, S. Li, A. Luo, M. Liu, Z. Luo, "Versatile

- mode-locked patterns in a fiber laser using silica-coated gold nanorods as saturable absorber", *Laser Physics*. vol.30, p.65104, 2020.
- [169] X. Wang, A. Luo, H. Liu, N. Zhao, M. Liu, Y. Zhu, J. Xue, Z. Luo, W. Xu, "Nanocomposites with gold nanorod/silica core-shell structure as saturable absorber for femtosecond pulse generation in a fiber laser", *Optics Express*. vol.23, p.22602–22610, 2015.
- [170] S. Liu, R. Lv, Y. Wang, J. Wang, Y. Wang, H. Wang, "Passively Mode-Locked Fiber Laser with WS_2/SiO_2 Saturable Absorber Fabricated by Sol–Gel Technique", *ACS Applied Materials & Interfaces*. vol.12, p.29625–29630, 2020.
- [171] Z. Luo, M. Zhou, D. Wu, C. Ye, J. Weng, J. Dong, H. Xu, Z. Cai, L. Chen, "Graphene-Induced Nonlinear Four-Wave-Mixing and Its Application to Multiwavelength Q-Switched Rare-Earth-Doped Fiber Lasers", *Journal of Lightwave Technology*. vol.29, p.2732–2739, 2011.
- [172] M. Liu, H. Liu, X. Zheng, N. Zhao, A. Luo, Z. Luo, W. Xu, "Demonstration of multiwavelength erbium-doped fiber laser based on a microfiber knot resonator", *IEEE Photonics Technology Letters*. vol.26, p.1387–1390, 2014.
- [173] S. Li, Y. Yin, G. Ran, Q. Ouyang, Y. Chen, M. Tokurakawa, E. Lewis, S. Harun, P. Wang, "Dual-wavelength mode-locked erbium-doped fiber laser based on tin disulfide thin film as saturable absorber", *Journal of Applied Physics*. vol.125, p.243104, 2019.
- [174] P. Ma, W. Lin, H. Zhang, S. Xu, Z. Yang, "High-Power Large-Energy Raman Soliton Generations Within a Mode-Locked Yb-Doped Fiber Laser Based on High-Damage-Threshold CVD-MoS₂ as Modulator", *Nanomaterials*. Vol.9, p.1305, 2019.
- [175] G. Chen, Y. Yang, M. Tian, C. Li, Y. Huang, M. Lv, "Passively Q-switched mode-locked ytterbium-doped fiber laser based on an Fe₃O₄-nanoparticle saturable absorber", *Optical Materials Express*. vol.10, p.588–596, 2020.
- [176] C. Sun, H. Pan, A. Zhang, X. Shi, "Effects of dispersion on characterization of multi-wavelength Q-switched fiber laser", *Optics Communications*. vol.462, 125373, 2020.
- [177] W. Xu, P. Guo, X. Li, Z. Hui, Y. Wang, Z. Shi, Y. Shu, "Sheet-structured bismuthene for near-infrared dual-wavelength harmonic mode-locking", *Nanotechnology*. vol.31, p.225209, 2020.
- [178] S. Al-hayali, "Short Pulse Fiber Laser Based on Transition Metal Oxide

- Nanomaterial Saturable Absorber" Doctoral Thesis, University of Baghdad Institute of Laser for Postgraduate Studies, 2017.
- [179] W. Khaleel, "Generation of switchable and tunable wavelengths EDFL using ring cavity configuration", University of Baghdad, Institute of Laser for Postgraduate Studies, 2016.
- [180] D. Mohammed, "Tunable Q-Switched Er-Doped Fiber Laser", University of Baghdad, Institute of Laser for Postgraduate Studies, 2017.
- [181] N Avram, M. Brik, "Optical Properties of 3d-Ions in Crystals", Springer Berlin Heidelberg, springer, 2013.
- [182] L. Pan, I. Utkin, R. Fedosejevs, "Passively Q-switched Ytterbium-Doped Double-Clad Fiber Laser With a Cr⁴⁺:YAG Saturable Absorber", IEEE Photonics Technology Letters. vol.19, p.1979–1981, 2007.
- [183] H. Ahmad, M. Ismail, S. Hassan, F. Ahmad, M. Zulkifli, S. Harun, "Multiwall carbon nanotube polyvinyl alcohol-based saturable absorber in passively Q-switched fiber laser", Applied Optics. vol.53, p.7025–7029, 2014.
- [184] S. Li, Y. Yin, E. Lewis, G. Garrell, P. Wang, "A twelve-wavelength Thulium-doped fibre laser based on a microfibre coil resonator incorporating black phosphorus", Optics Communications. vol.437, p.342–345, 2019.
- [185] Z. Tiu, S. Tan, H. Ahmad, S. Harun, "Dark pulse emission in nonlinear polarization rotation-based multiwavelength mode-locked erbium-doped fiber laser", Chinese Optics Letters. vol.12, p.113202, 2014.
- [186] T. Wang, W. Zhang, X. Shi, J. Wang, X. Ding, K. Zhang, J. Peng, J. Wu, P. Zhou, "Black phosphorus-enabled harmonic mode locking of dark pulses in a Yb-doped fiber laser", Laser Physics Letters. vol.16, p.85102, 2019.
- [187] M. Ahmad, A. Muhammad, H. Haris, H. Rahim, R. Zakaria, H. Ahmad, S. Harun, "Q-switched Ytterbium doped fibre laser using gold nanoparticles saturable absorber fabricated by electron beam deposition", Optik. vol.182, p.241–248, 2019.
- [188] M. Liu, D. Zhou, Z. Jia, Z. Li, N. Li, S. Li, Z. Kang, J. Yi, C. Zhao, G. Qin, H. Song, W. Qin, "Plasmonic Cu_{1.8}S nanocrystals as saturable absorbers for passively Q-switched erbium-doped fiber lasers", Journal of Materials Chemistry C. vol.5, p.4034–4039, 2017.
- [189] J. Liu, S. Wu, Q. Yang, P. Wang, "Stable nanosecond pulse generation from a graphene-based passively Q-switched Yb-doped fiber laser", Optics Letters.

- vol.36, p.4008–4010, 2011.
- [190] A. Al-Masoodi, M. Ismail, F. Ahmad, N. Kasim, Y. Munajat, H. Ahmad, S. Harun, "Q-switched Yb-doped fiber laser operating at 1073 nm using a carbon nanotubes saturable absorber", *Microwave and Optical Technology Letters*. vol.56, p.1770–1773, 2014.
- [191] L. Zhang, F. Yan, T. Feng, Y. Guo, Q. Qin, H. Zhou, Y. Suo, "Switchable multi-wavelength Thulium-doped fiber laser employing a polarization-maintaining sampled fiber bragg grating", *IEEE Access*. vol.7, p.155437–155445, 2019.
- [192] R. Faris, S. Al-Hayali, A. Al-Janabi, "Au coated ZnO/MWCNTs nanocomposites film-induced four-wave-mixing effect for multi-wavelength generation in erbium-doped fiber laser", *Optics Communications*. vol.485, p.126746, 2021.
- [193] Y. Chang, L. Pei, T. Ning, J. Zheng, J. Li, C. Xie, "Switchable and tunable multi-wavelength fiber ring laser employing a cascaded fiber filter", *Optical Fiber Technology*. vol.58, p.102240, 2020.
- [194] F. Su-Chun, X. Ou, L. Shao-Hua, J. Shui-Sheng, "Switchable multi-wavelength erbium-doped fiber lasers based on a Mach–Zehnder interferometer using a twin-core fiber", *Chinese Physics Letters*. vol.26, p.64208, 2009.
- [195] S. Huang, Y. Wang, P. Yan, J. Zhao, H. Li, R. Lin, "Tunable and switchable multi-wavelength dissipative soliton generation in a graphene oxide mode-locked Yb-doped fiber laser", *Optics Express*. vol.22, p.11417–11426, 2014.
- [196] T. Walbaum, C. Fallnich, "Wavelength tuning of multimode interference bandpass filters by mechanical bending: experiment and theory in comparison", *Applied Physics B*. vol.108, p.117–124, 2012.
- [197] Q. Wang, G. Farrell, W. Yan, "Investigation on single-mode–multimode–single-mode fiber structure", *Journal of Lightwave Technology*. vol.26, p.512–519, 2008.
- [198] Y. Zhou, S. Lou, Z. Tang, T. Zhao, W. Zhang, "Tunable and switchable C-band and L-band multi-wavelength erbium-doped fiber laser employing a large-core fiber filter", *Optics & Laser Technology*. vol.111, p.262–270, 2019.
- [199] Z. Sun, A.G. Rozhin, F. Wang, V. Scardaci, W.I. Milne, I.H. White, F. Hennrich, A.C. Ferrari, "L-band ultrafast fiber laser mode locked by carbon nanotubes", *Applied Physics Letters*. vol.93, p.61114, 2008.
- [200] Y. Luo, B. Liu, Y. Xiang, Z. Yan, Y. Qin, Q. Sun, X. Tang, "L-Band Noise-Like Pulse Generation in a Bidirectional Mode-Locked Fiber Laser", *IEEE Photonics*

- Technology Letters. vol.30, p.1333–1336, 2018.
- [201] S.W. Harun, R. Parvizi, S. Shahi, H. Ahmad, "Multi-wavelength erbium-doped fiber laser assisted by four-wave mixing effect", *Laser Physics Letters*. vol.6, p.813–815, 2009.
- [202] M. Shahmiri, N. Ibrahim, N. Faraji, W. Yunus, N. Asim, N. Zainuddin, "Third-order nonlinear optical properties of chemically synthesized copper oxide nanosheets", *Physica E: Low-Dimensional Systems and Nanostructures*. vol.54, p.109–114, 2013.
- [203] Y. Xu, Y. Lu, Y. Zuo, F. Xu, D. Zuo, "Z-scan measurements of nonlinear refraction and absorption for aluminum-doped zinc oxide thin film", *Applied Optics*. vol.58, p.6112–6117, 2019.
- [204] D. Fan, C. Mou, X. Bai, S. Wang, N. Chen, X. Zeng, "Passively Q-switched erbium-doped fiber laser using evanescent field interaction with gold-nanosphere based saturable absorber", *Optics Express*. vol.22, p.18537–18542, 2014.
- [205] H. Liao, R. Xiao, J. Fu, P. Yu, G. Wong, P. Sheng, "Large third-order optical nonlinearity in Au:SiO₂ composite films near the percolation threshold", *Applied Physics Letters*. vol.70, p.1–3, 1997.
- [206] N. Zulina, I. Pavlovets, M. Baranov, I. Denisyuk, "Optical, structural and nonlinear optical properties of laser ablation synthesized Ag nanoparticles and photopolymer nanocomposites based on them", *Optics & Laser Technology*. vol.89, p.41–45, 2017.

PUBLICATIONS

The following publications prior to the thesis:

- [1] **Ansam M. Salman**, A.A. Salman, A. Al-Janabi, Stable L-band multiwavelength erbium-doped fiber laser based on four-wave mixing using nickel nanofluid, *Applied Optics*. 58 (2019) 6136–6143, published.
- [2] **Ansam M.Salman**, AbdulhadiAl-Janabi, Ni-NPs doped PVA: An efficient saturable absorber for generation multiwavelength Q-switched fiber laser system near 1.5 μm , *Optical Materials*. 98 (2019) 109418, published.
- [3] **Ansam M. Salman**, A. Al-Janabi, Nickel nanoparticles-based saturable absorber: Toward compact multiwavelength Yb-doped fiber pulsed lasers near 1 μm region, *Microwave and Optical Technology Letters*. 62 (2020) 984–992, published.
- [4] **Ansam M. Salman**, A. Al-Janabi, Nickel Nanoparticles Saturable Absorber for Multiwavelength Pulses Generation in Ytterbium-Doped Fiber Laser, *Fiber and Integrated Optics*. (2020) 1–13. doi:10.1080/01468030.2020.1768607, published.

In addition, the following papers were published during the period of PhD, but is beyond the scope of this thesis:

- [5] Dunia I. Al-Janabi, **Ansam M. Salman**, A. Al-Janabi, High sensitivity balloon-like thermometric sensor based on bent single mode fiber, *Measurement Science and Technology*. (2020), published.
- [6] D.I. Al-Janabi, **Ansam M. Salman**, A.H.M. Al-Janabi, All fiber,

- highly sensitive sensor based on gold nanoparticle-coated macrobent single mode fiber for human temperature monitoring, *Journal of Nanophotonics*. 14 (2020) 46013, published.
- [7] A.H. Abdalhadi, **Ansam M. Salman**, R.A. Faris, A. Al-Janabi, Titania-carbon nanocomposite as a saturable absorber for generation passively ytterbium-mode locked pulses, *Optical Materials*. 112 (2021) 110728, published.
- [8] S.K. Al-Hayali, **Ansam M. Salman**, A.H. Al-Janabi, High sensitivity balloon-like interferometric optical fiber humidity sensor based on tuning gold nanoparticles coating thickness, *Measurement*. 170 (2021) 108703, published.
- [9] S.K. Al-Hayali, **Ansam M. Salman**, A.H. Al-Janabi, Effect of hygroscopic polymer-coatings on the performance of relative humidity sensor based on macro-bend single-mode fiber, *Optical Fiber Technology*. 62 (2021) 102460, published.
- [10] Fay F. Ridha, **Ansam M. Salman**, A.H. Al-Janabi, STABLE EVANESCENT WAVE MODE-LOCKED LASER BASED ON A PHOTONICS CRYSTAL FIBER INDUCED-MACH-ZEHNDER FILTER AS GAIN-TILT EQUALIZER, *Applied Optics*, Vol. 60 No. 11, (2021) accepted.

الخلاصة

ركزت هذه الأطروحة على تصميم وتصنيع ليزر ليفي متعدد الأطوال يعمل في نطاقين رئيسيين متنوعين هما نطاق ١ ميكرومتر و ١.٥ ميكرومتر. تم بنجاح انجاز عدة أنواع من الليزرات الليفية متعددة الأطوال ذات أنظمة تشغيل مختلفة (الموجة المستمرة، ذي مفتاح عامل النوعية و قفل الانماط) باستخدام مواد نانوية غير خطية مطورة حديثاً كمعادل للكسب ومثبت. لتحقيق هذه الليزرات متعددة الأطوال الموجية ، تم تصنيع الجسيمات النانوية المعدنية (جزيئات النيكل النانوية ((Ni-NPs)) والجسيمات النانوية شبه الموصلة (أوكسيد الحديد (Fe_2O_3)) والجسيمات النانوية العازلة (السيليكا (SiO_2)) بطريقة بسيطة وفعالة من حيث التكلفة مع شكلين مختلفين: شكل سائل وشكل مركب بوليمر قائم بذاته لاستخدامه لاحقاً في تجويف الليزر. تم عمل مجموعة من القياسات لتوصيف العينات المحضرة مثل الخواص البصرية الخطية وغير الخطية.

من خلال العمل، تم إنشاء الطول الموجي المتعدد ببساطة في نطاق الطويل (L-band) و ١ ميكرومتر مع تباعد قناة ١.٢ نانومتر و ٠.٨ نانومتر عندما تم دمج سائل النيكل نانوي (Ni-NF) مع تجاويف اليترييوم والايبروم الحلقيان، على التوالي. تم توليد هذا الليزر متعدد الأطوال الموجية في كلا تجويف اليترييوم والايبروم بمساعدة خلط الأربع موجات. بعد ذلك ، تم دمج Ni-NPs في مصفوفة البوليمر (PVA) لتصنيع مُعدّل ضوئي رقيق قائم على الأغشية. عندما تم دمج قطعة صغيرة من العينة المصنعة في التجويف الحلقي لكل من اليترييوم والايبروم؛ تم تحقيق ليزر ذي مفتاح عامل النوعية متعدد الأطوال الموجية يملك مدة نبضة تتراوح بين عدة نانوثانية إلى بضعة ميكروثانية. إلى جانب ذلك ، تم تحقيق سلوك قفل النمط في اليترييوم أيضاً.

قناة ليزر متعددة الأطوال الخماسية ظهرت حول منطقة ١٠٤٠ نانومتر، تعمل في نظام الموجة المستمرة، وقناة ليزر مزدوجة تم اكتشافها حوال ١٥٦٣ نانومتر ، تعمل في نظام ذي مفتاح عامل النوعية مع الحد الأدنى من مدة النبضة ٧.١٨ مايكروثانية ومعدل التكرار الأقصى ٣٠.٧٤ كيلوهرتز تم الحصول عليها عند دمج الغشاء البلوميري لاوكسد الحديد في تجاويف اليترييوم والايبروم ، على التوالي. أيضاً ، تم اكتشاف أطوال موجية متعددة تعمل في نظام قفل النمط حول مناطق ١ ميكرومتر و ١.٥ ميكرومتر ، بسبب التأثير غير الخطي العالي لمادة اوكسيد الحديد النانوية.

فيما بعد، تم إنشاء نبضات نظام ذي مفتاح عامل النوعية ذات مدة النبضة الدنيا البالغة ٤ ميكرو ثانية و ٣.٤ ميكرو ثانية الناتجة عن غشاء السلكا البلومري وطبقة رقيقة من السيلكا السائل على التوالي من تجويف الايبروم. إلى جانب ذلك ، تحفز هذه المعدلات الطول الموجي المزدوج الموجة المستمرة والنبض الموجي الرباعي في النطاق ١ ميكرومتر. تم تحقيق الطول الموجي المتعدد المنبعث في الموجة المستمرة، ذي مفتاح عامل النوعية ، وكذلك القفل النمط، من الايبروم

على أساس المركب النانوي أوكسيد الحديد/سيليكيا. أيضًا ، تم تحقيق أكثر من ٢٠ طول موجي مع نسبة الإشارة إلى الضوضاء بين ٩ ديسيبل و ٤٦ ديسيبل مع العديد من الأوضاع الجانبية التي تعمل بالليزر في عملية قفل الوضع من الليتريوم استنادًا إلى المركب النانوي أوكسيد الحديد/سيليكيا. قد تمهد دراستنا طريقة مبتكرة لإنتاج ليزر متعدد الأطوال الموجية من خلال استخدام مواد غير خطية جديدة عند ضخ عتبة منخفضة مع تجويف قصير الطول.



وزارة التعليم العالي والبحث العلمي

جامعة بغداد

معهد الليزر للدراسات العليا

تعديل المواد النانوية لمتعدد الأطوال الموجية لليف البصري المشوب باليتريوم/الايربيوم

أطروحة مقدمة الى

معهد الليزر للدراسات العليا/جامعة بغداد/لاستكمال متطلبات نيل شهادة دكتوراه
فلسفة في الليزر/ الهندسة الالكترونية والاتصالات

من قبل

انسام ماجد سلمان

بكلوريوس هندسة الليزر والالكترونيات البصرية-٢٠٠٦

ماجستير هندسة الليزر والالكترونيات البصرية-٢٠٠٩

باشرف

الأستاذ الدكتور عبد الهادي مطشر الجنابي

٢٠٢١م

١٤٤٢هـ